Multiscale study of mouse preimplantation morphogenesis

Markus Schliffka

PSL UNIVERSITÉ PARIS

THÈSE DE DOCTORAT
DE L'UNIVERSITÉ PSL

Préparée à l'Institut Curie – Génétique et biologie du développement – UMR3215/U934

Multiscale study of mouse preimplantation morphogenesis
-
Etude multi-échelle de la morphogenèse de l'embryon préimplantatoire

Soutenue par
Markus Frederik SCHLIFFKA

Le 12 juin 2023

Ecole doctorale n° 515
Complexité du vivant

Spécialité
Biologie cellulaire et développement

Composition du jury :

Dr. Marie-Emilie TERRET Directrice de recherche, Collège de France	*Présidente*
Prof. Carien NIESSEN Professeur, Universität zu Köln	*Rapporteur*
Prof. Guillaume CHARRAS Professeur, University College London	*Rapporteur*
Dr. Jean-Léon MAITRE Chargé de recherche, Institut Curie	*Directeur de thèse*

institutCurie | PSL

ACKNOWLEDGEMENTS

During my time as a PhD student at the Institut Curie, I have been accompanied by many wonderful people, without who this undertaking would not have been possible. My biggest gratitude, of course, goes towards my thesis supervisor **Jean-Léon Maître**. I have been very fortunate to find in him an excellent PhD supervisor, both professionally and personally. I thank him for his guidance, support and advice in all scientific and career question, his always open door, and countless hours of discussion. I appreciate that he has been always approachable with questions and problems of all kind and open to my suggestions and ideas. His motivation and optimism have made my time as a PhD student in his lab a most valuable and enjoyable time.

Likewise, I thank my co-supervisors **Fabrice Schmitt** of Carl Zeiss SAS for giving me the opportunity to do my PhD in collaboration with Zeiss, and **Olivier Renaud** of the Imaging platform of the Genetics and Developmental Unit at the Institut Curie for his support and constant help.

I thank **Carien Niessen** and **Guillaume Charras** for agreeing to be the reviewers for this thesis, as well as jury members. I also thank **Marie-Emilie Terret** for agreeing to serve as a jury member.

I am very grateful to the members of my **Thesis Advisory Committee**, **Flora Llense**, **Arnaud Echard** and **Wolfgang Keil,** for their valuable discussions, input and support during my PhD.

I thank **Arghyadip Mukherjee** of the ENS/PSL for his collaboration on the inverse bleb project. I am grateful for our frequent discussions about the project and for his valuable input on our biophysical understanding of this phenomenon. I also thank him for his professional advice and support.

A big thank you goes to my wonderful colleagues of the **Maître lab**. Spending almost five years with them made my PhD an unforgettable time and I am very grateful for all the fun moments we spent in the lab, out of the lab or on retreats around France. Although most of my PhD happened during the COVID period, the great environment of the group helped me to successfully navigate my PhD project between confinements, travel bans, vaccine appointments and “attestations”.

Especially, I thank **Francesca Tortorelli**, who was my wonderful co-first author on the myosin project. I thank her for the most enjoyable time that we worked together on this project and for being an amazing friend and colleague. I also thank all other team members who contributed to this project.

I thank **Julien Dumortier** and **Diane Pelzer** for their collaboration in the inverse bleb project, and all other colleagues who contributed to the project.

I thank **Ludmilla de Plater** and **Adrien Eichmuller** for all their efforts involving our mouse work, without them my projects would not have been possible. I thank **Özge Özgüç** for her joint effort in the myosin project, for always having help and advice and for making every day in the lab great fun. I thank all other PhD students, **Julie Firmin**, **Louise Dagher** and **Shivani Dharmadikari**, and postdocs, **Edgar Delgado-Herrero**, **David Rozema** and **Peta Bradbury**, for being wonderful colleagues and making my time in the Maître lab so memorable. I also thank the members of the UMR3215/U934 at BDD, especially the Bardin lab.

I extend my gratitude towards the core facilities of the Institut Curie: I thank all members of the imaging platform of the Genetics and Developmental Biology Unit at the Institut Curie (**PICT-IBiSA@BDD**). Here, I thank again Olivier Renaud in his function as facility head, and especially **Olivier Leroy** for his help with custom scripts for live imaging and his frequent assistance with all microscopy related questions. I thank the **EOPS mouse facility** at the Institut Curie for their invaluable help with the animal experimentation, here especially **Celine Daviaud**, **Mickaël Garcia** and **Paul Bureau.**

Finally, I thank my wonderful friends and family for their love and help during my PhD. I thank my family members for all their support, Dominik for always being there for me, Antonia and Alexander for our friendship since our university days and having an open ear any time of the day and night.

I gratefully acknowledge funding of my PhD in the framework of a Convention Industrielle de Formation pour la Recherche (No 1113 2019/0253) between the **Agence Nationale de la Recherche** and **Carl Zeiss SAS**, and by **La Ligue contre le Cancer** with a 4th year contract. I also gratefully acknowledge support by **La Fondation des Treilles**.

SUMMARY

During development, embryos undergo a complex sequence of morphogenetic shape changes powered by cellular contractile forces which allow the embryo to correctly form tissues and organs. Contractile cellular forces in morphogenesis are chiefly generated by the actomyosin cytoskeleton. In the mammalian embryo, morphogenesis begins during preimplantation development, which commences with fertilization and leads up to the formation of the blastocyst, the structure that implants into the maternal uterus. During preimplantation development, the embryo undergoes a series of contractility-driven morphogenetic steps that culminate in the positioning of the first lumen of development in the blastocyst.

Here, we conducted the first study investigating the effect of complete contractility loss on preimplantation development. We performed single and double maternal-zygotic knockout of the non-muscle myosin heavy chain genes *Myh9* and *Myh10*, which allowed us to study the relative contribution of these two paralogs to contractility generation in preimplantation development. We found that MYH9 is the main contributor in this process, as its maternal-zygotic loss results in cell cycle delay, reduced cell number, compaction and differentiation. Loss of *Myh10* did not have a strong detectable impact compared to wildtype embryos. Nevertheless, a more severe phenotype could be observed in *Myh9* and *Myh10* double knockout embryos as cytokinesis failed in most cases, suggesting some compensation by MYH10 in *Myh9* single mutants. Despite severely reduced cell number, differentiation and lumen formation still somehow continued in double knockout embryos. In the most extreme cases, single-celled embryos accumulated fluid in intracellular compartments, indicating that the preimplantation developmental program is executed independently of cell number.

In WT embryos, the blastocyst forms in a process of hydraulic fracturing producing hundreds of microlumen followed by their coarsening into a single lumen surrounded by multiple cells. While the global mechanism of this process is understood, it remains unclear how cells regulate microlumen dynamics locally. Here, we describe inverse blebs at cell-cell contacts during microlumen formation. Inverse blebs are short-lived membrane protrusions expanding into the cytoplasm before being retracted by

actomyosin contraction. We show that inverse blebs form due to a global increase in intercellular fluid pressure and require local fluid confinement by cell-cell adhesion. We propose that inverse blebs serve as hydraulic pumps to push the fluid within the microlumen network, thereby supporting the coarsening of the first mammalian lumen. Together, these finding expand our molecular, cellular and physical understanding of how cell contractility shapes the early mammalian embryo.

TABLE OF CONTENTS

1. INTRODUCTION

1.1 Principles of morphogenesis in animal development

Animal embryogenesis is the process in which an organism develops from a zygote to its complete form. In order to correctly develop into a new organism, embryos undergo a tightly controlled program that relies on three principles [1]: Firstly, cell proliferation allows embryos to increase their cell number and grow in size. Secondly, differentiation leads to cell specialization in which cells acquire different fates that determine their properties and function in tissues. Thirdly, in the process of morphogenesis, embryos shape their cells into tissues and organs that fulfill specific functions in the organism. These principles are intertwined as developmental processes are ultimately controlled by the genetic program of a particular organism, but proliferative and morphogenetic processes feed back into gene expression [2,3].
Morphogenesis relies to a large extent on the physical properties of cells and tissues which can be modulated in space and time according to the developmental process. On a cellular level, cells can control their shape which allows them to adapt to various functions [4–6], ranging from long-stretched neurons to compact cuboidal epithelial cells. Cells can also leave their tissue context and migrate autonomously [7,8]. On the tissue level, important morphogenetic processes include shape changes such as tissue bending [9,10], cell sorting [1,11] and collective cell migration [8,12,13]. Complex tissue rearrangements occur in budding or branching morphogenesis, where tissues create tree-like architectures that enlarge the surface of organs such as the lung [14], glands [15] and the vasculature [16]. Another important principle of morphogenesis is the formation of lumens, which are fluid-filled spaces lined by cells. Lumens are an important structure that allow organisms to transport substances [17], fulfill signaling tasks [18] or serve as a basis for further tissue sculpting [19]. Fluid-filled lumens can either arise by fluid accumulation between cells leading to lumen opening [20], or by hollowing of the luminal space after apoptosis of cells in a process called cavitation [21,22]. Finally, the deposition of extracellular matrix can impact the physical properties and shaping of tissues, e.g. by causing epithelial buckling [23], regulating embryonic growth [24] or facilitating lumen opening [25]. Aberrations in morphogenesis are associated with a variety of pathologies in humans. Developmental morphogenetic errors can result in congenital malformations such as

spina bifida [26], cleft palate [27] or abnormal heart valve development [28], which are an important reason for infant mortality [29].

1.2 Organization of the cytoskeleton and the cell cortex

Animal morphogenesis relies on the ability of cells and thereby tissues to control their position and shape in space and time. This is possible due to the ability of cells to control their shape with the help of their cytoskeleton which, through interconnection of the cells, leads to structural changes in the entire tissue. The cytoskeleton is a complex network of protein filaments that provides structural support to cells and plays a crucial role in a wide range of cellular processes, including cell division, cell migration, intracellular transport, spatial organization of the cellular components and signal transduction. The cytoskeleton is composed of three main components: actin filaments, microtubules and intermediate filaments [30]. In each of these components, protein monomers dynamically (de-)polymerize to form filaments and ultimately networks. Motor proteins associated with the actin filaments and microtubules can rearrange the cytoskeletal filaments or use them as transport routes across the cell body. Typically, for actin filaments, these motor proteins are myosins, while for microtubules, the motor proteins have been defined as kinesins and dyneins, with myosins having been reported to bind microtubules as well in certain instances [31,32]. The components of the cytoskeleton interact extensively with each other and cooperate in cellular processes [33], most prominently during cell division, where microtubules organize and separate the chromosomes during mitosis and actin and myosin effect cytokinesis [34]. The actomyosin component of the cytoskeleton, located at the cell surface, is an important determinant of the cell shape and mechanical properties. It will therefore be the focus of further description.

The actomyosin cytoskeleton is a major generator of forces in the cell. In particular, its components enrich below the plasma membrane in a zone called the cell cortex, which is a highly dynamic meshwork of actin filaments, myosin molecules and associated proteins [35]. The cell cortex is attached to the plasma membrane by anchoring proteins, e.g. ankyrin, spectrin and ezrin [36,37]. Actin and myosin dynamics in the cortex are among the most important factors controlling the physical properties of cells,

namely their surface tension and viscoelasticity [35,38]. The tight regulation of tension and elasticity generates cellular contractility which is crucial for morphogenesis. The thickness, composition and dynamics of the cortex are highly dynamic and depend on the cell type and its physiological state. A cortex thickness of 50-400 nm has been reported depending on the sample and method used [39–43].

1.2.1 Molecular organization of actin filaments

Actin, which constitutes the basic building block of the actomyosin cytoskeleton, is an ubiquitously expressed structural protein. Its sequence is highly conserved across eukaryotic cells, highlighting its vital basic role as one of the basic systems of cellular organization [44]. The basic unit of the actomyosin cytoskeleton are actin monomers, also known as globular (G-)actin. G-actin dynamically assembles and disassembles in linear filamentous actin (F-actin) (Figure 1). This assembly is energy-dependent, as G-actin polymerization requires adenosine triphosphate (ATP) binding. F-actin formation is triggered by initial G-actin oligomerization mediated by actin nucleation factors, such as the actin related protein 2/3 (Arp2/3) complex working in concert with the Wiskott-Aldrich syndrome protein (WASP) or members of the formin protein family. F-actin filament elongation is then promoted by polymerization of further ATP-bound actin monomers [45]. Interestingly, this elongation occurs asymmetrically as the filament is polarized with an extending (+) end, and a shortening (-) end [46]. Filaments grow at the (+) end supported by the G-actin binding protein profilin, while ATP hydrolysis in the actin monomers at the (-) end promotes their dissociation [47]. This results in a process termed ‘treadmilling’, in which actin filaments stay roughly the same length, but show a spatial net displacement, which is important for cellular processes such as cell migration (Figure 1). In addition to actin monomer dissociation off the filament (-) end, actin depolymerizing factor/cofilin promotes filament shortening, while gelsolin/vilin proteins can sever actin filaments [48]. This contributes to a rapid turnover of actin filament in the cytoskeleton. Through the action of adaptor proteins, these actin filaments become assembled into higher-order structures such as bundled and branched structures, or the complex 3D networks that constitute the cell cortex. For instance, the Arp2/3 complex binds to existing actin filaments and

causes the branching off of a new, angled filament [49], and actin filaments can be linked or bundled by cross-linking proteins α-actinin and fascin [50].

While actin filaments are to a certain extent able to induce mechanical forces on their own (for example in pushing membrane protrusions [51,52]), myosins as the actin-associated motor proteins are necessary to exert the full array of cytoskeletal functions.

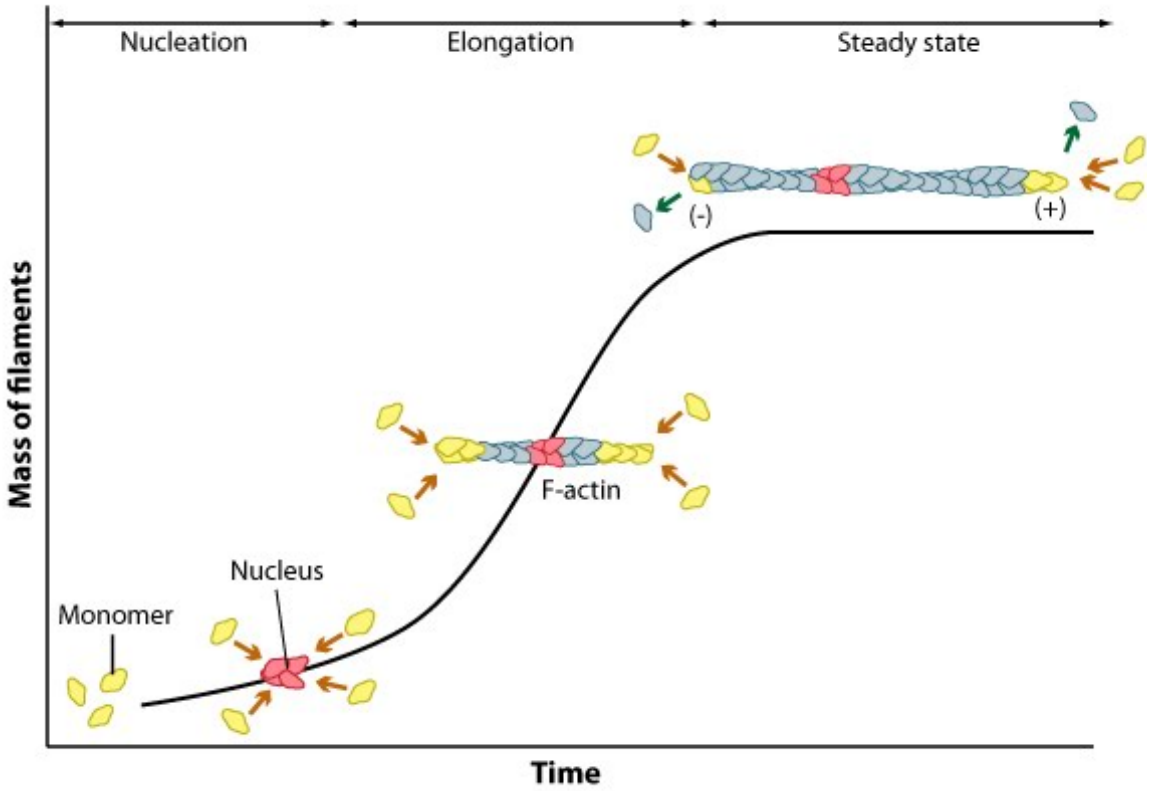

Figure 1: Actin filament dynamics. G-actin / actin monomers polymerize when cued by a nucleation factor and start extending. Net loss at the (-) end occurs due to monomer dissociation after ATP hydrolysis. The filament grows at the (+) end by addition of monomers into the filament. When polymerization and dissociation rates are equal, the filament displaces itself while keeping a constant length in the 'treadmilling process'. Image adapted from *www.mechanobio.info*.

1.2.2 Myosin: the motor molecule of the actin cytoskeleton

Myosins are the molecular motor proteins associated with actin filaments, which they can either displace, put under tension or use as a track to walk on. Myosins constitute a large superfamily of genes with over 15 subfamilies described to date [53] which are involved in diverse cellular processes such as intercellular transport, cortex organization, organelle tethering, cytokinesis, cell migration depending on their

subfamily, and even transcription regulation in case of nuclear myosins [53–56]. All myosin family members share their actin-binding capacity which is mediated by an N-terminal catalytic head domain that contains an ATP-binding site and effects the power stroke that allows myosin movement on or displacing of the actin filament. The C-terminal tail domain serves for assembly of multiple myosin molecules into myosin filaments or for cargo binding.

Members of the myosin II family (also known as conventional myosin) are responsible for creating contractile forces in cells. The best-known instance of this is muscle contraction, which is effected by skeletal, cardiac and smooth muscle myosin II [57]. Given the fact that animal morphogenesis does not depend on muscle movement, the properties of the non-muscle members of the myosin II family (non-muscle myosin II, NM II), which are ubiquitously expressed, will be considered in chapters 1.2.3 and 1.2.4.

1.2.3 Non-muscle myosin II generates cellular forces

NM II molecules are hexamers of two non-muscle myosin heavy chains (NMHC), two regulatory light chains (RLC) and two essential light chains (ELC) that ensure conformational stability (Figure 2) [58]. NMHCs consist of a motor domain, a neck domain where RLCs and ELCs bind, a coiled rod domain and a tail domain (seen from N-terminal to C-terminal). NMHCs dimerize at the rod domain in a helical structure which assembles the NM II hexamer. This helical rod domain also serves as a binding hub for NM II assembly in myosin mini-filaments. The N-terminal ATP-binding head domain effects the power stroke of the myosin complex, during which it binds and dissociates from the actin filaments depending on its nucleotide bound state, resulting in an effective movement along the filament. NM II hexamers can assemble via their rod domain into bipolar filaments that can link several actin filaments into larger structures.

The activity of NM II is regulated on the level of regulatory light chains and heavy chains. RLCs are phosphorylated by an array of kinases, most prominently myosin light chain kinase (MLCK or MRCK) under the control of calmodulin, and Rho-associated, coiled coil-containing kinase (ROCK) and citron kinase under the control

of the small regulatory GTPase Ras homolog family member A (RhoA) [59–62]. While these kinases can directly phosphorylate RLC and thus promote NM II activity, ROCK can also act by phosphorylating and inhibiting the negative regulator of RLC, protein phosphatase 1, thus increasing RLC phosphorylation levels [63]. Also, RLC phosphorylation by protein kinase C (PKC) promotes NM II activity. NMHCs are likewise regulated by kinases and phosphatases, however, the effects seem to be less clear than for RLCs [64]. NMHCs can be phosphorylated by PKC, casein kinase II and TRPM7 [65–67]. This might inhibit the assembly of NM II into mini-filaments [66].

NM II regulates a range of cellular processes pertaining to cellular movement, shaping, adhesion and division. In regard to morphogenesis, its main role is to create cell surface tension in the cell cortex and thus to confer contractility on the cell. How this physical cellular property translates to morphogenetic processes is discussed in chapter 1.3.

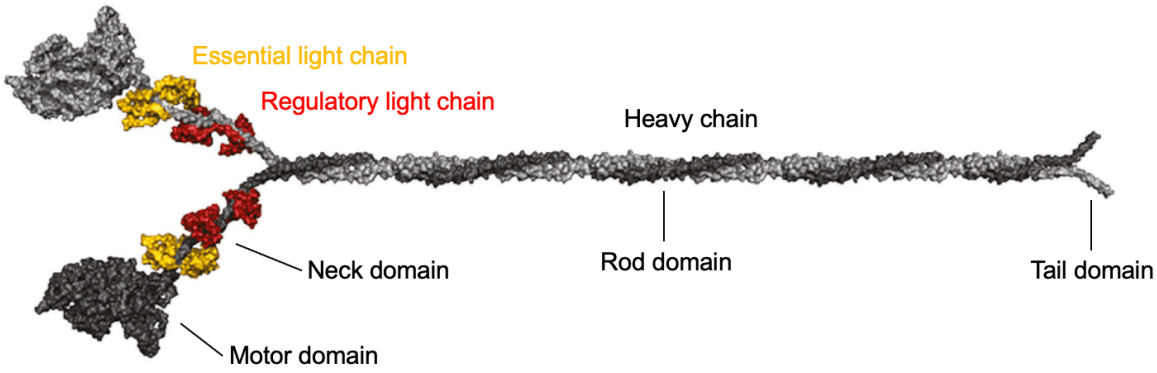

Figure 2: Structure of a non-muscle myosin II molecule. A hexameric NM II molecule consists of two heavy chains, essential light chains and regulatory light chains each. The hexameric complex binds to actin with the N-terminal motor domain containing the ATP binding site. The essential and regulatory light chains bind to the adjacent neck domain, which ensures conformational stability. The central part of the heavy chains is coiled into the rod domain, and finally the C-terminal tail domain. NM II molecules interact through their rod domains to form myosin filaments. Schematic adapted from [58].

1.2.4 The role of NMHC paralogs

Mammals possess three gene paralogs coding for the heavy chain of NM II (as opposed to one gene in *D. melanogaster* [68]): *Myh9*, *Myh10* and *Myh14*, which in their protein form are called NMHC A, B and C. For simplicity's sake, the protein forms

of the NMHC paralogs will hereafter be referred to following their gene names as MYH9, MYH10 and MYH14. Despite some redundant functions [69,70], a differential localization of the paralogs has been observed to a certain extent in endothelial and cultured cancer cells [71,72], and specific roles for the three NMHC paralogs could be delineated. On a molecular level, MYH9 and MYH10 show different actin binding kinetics and actin displacement speed [73–76]. MYH9 is the dominant paralog in cytokinesis after mitosis, providing cortical contractility while MYH10 stabilizes the cortex [77,78]. On the tissue scale, MYH9 and MYH10 both participate in organizing adherens junctions, with MYH9 organizing cadherin clustering and MYH10 effecting force transmission at the junction [79,80].

Beyond these molecular studies, knockout mouse lines have been created for each of the paralogs to study their role in embryonic development. Zygotic knockout of *Myh9* results in embryonic lethality at embryonic day (E) 7.5, caused by adhesion defects in the visceral endoderm [81]. Embryos knocked out zygotically for *Myh10* show embryonic lethality between E10.5 and birth, due to a range of developmental defects in the heart, brain and liver [82]. Finally, the third paralog *Myh14* shows no phenotype when knocked out, indicating that its functions are redundant with those of *Myh9/10* [83]. The partial redundancy of NMHC paralog functions was also shown on an organismic level by inserting the gene sequences of *Myh9* into the locus of *Myh10* (and the same approach for *Myh10*) which produced a less severe phenotype than the simple knockout, but ultimately could not rescue embryonic lethality [84,85].

1.2.5 Anchoring of the cytoskeleton by adhesion molecules

The organization of the actomyosin cytoskeleton on a cellular scale has been described in chapters 1.2.1 to 1.2.4. However, the cytoskeleton has to be connected and controlled within a multicellular tissue context by means of cell adhesions to effectively cause any tissue-level behavior. Cells directly adhere to each other or the surrounding matrix through different types of adhesion complexes, such as tight junctions, adherens junctions, desmosomes, gap junctions or focal adhesions, in which adhesion is mediated by different kinds of adhesion molecules.

In the context of actomyosin-driven morphogenesis, adherens junctions are the most essential type of cell-cell adhesions as they associate to actin filaments [86]. In adherens junctions, the cell-cell adhesion is mediated by cadherins (short for “calcium-dependent adhesion”). The classical cadherins found in adherens junction exist in cell type specific forms of two types: the type I forms epithelial cadherin (E-cadherin, CDH1), neural cadherin (N-cadherin, CDH2) and placental cadherin (P-cadherin, CDH3), and the type II forms CDH15, CDH5 and CDH6 [87].

Cadherins mediate cell-cell contacts by entering homophilic interaction with their extracellular part, which consist of five globular Ca^{2+}-binding domains. On the cytosolic side, cadherins assemble a protein complex at the core of which α-catenin and β-catenin mediate the interaction between the adhesion molecule and actin filaments [88]. The actomyosin cytoskeleton and cadherin cooperate in cell-cell contact formation, as actin polymerization is required for contact initiation [89], and NM II is required for cadherin clustering [90,91]. Signaling through the cadherin adhesion complex leads to a relaxation of the contact tension, which enables contact expansion [11,92]. The anchorage of the cytoskeleton to the cell contacts mechanically couples cell cortices of individual cells [11] and thereby allows transmission and integration of forces on a tissue scale, which is important for the coordination of morphogenetic events such as tissue constriction, bending or migration [93,94].

Tight junctions are another type of cell-cell contact which form between the apicobasally polarized cells of epithelial tissues. Tight junctions form a physical barrier between the lateral membranes of epithelial cells which adhere via tight junctions and the non-adhesive apical membrane [95]. In addition to mediating cell-cell contact, they also control paracellular substance transport as they form semipermeable seals which regulate diffusion of molecules across epithelial sheets. Within tight junctions, occludins and claudins establish the connection between cell membranes, and bind the cytosolic zonula occludens proteins, which mediate the connection between the tight junction and the actomyosin cortex [96]. This makes tight junctions a part of the mechanical adhesion complex in epithelia, as well as a regulator of actomyosin contractility [97,98].

In addition to cell-cell contacts, cells can be anchored in the extracellular matrix (ECM), e.g. fibroblasts in the connective tissue [99]. In this case, the adhesion complexes

mediating attachment are called focal adhesions in which integrins are the main adhesion molecules. Like adherens junctions, they interact with actin filaments which is a major factor in how cells sense and react to mechanical forces [100], migrate as a single cell or as a collective [101] and establish epithelial polarity [102].

1.3 Actomyosin contractility controls tissue morphogenesis

As described in chapter 1.2, the actomyosin cytoskeleton can produce contractile forces. This allows cells and tissues to control their shape and position in space and time. In this chapter, I will describe how actomyosin contractility can be employed by cells and tissues to effect morphogenetic processes.

1.3.1 Cell division

The most evident process controlled by actomyosin contractility is cell division. Following the segregation of chromosomes during mitosis mediated by microtubules, the two daughter cells are physically separated during cytokinesis. During mitosis, cells experience a shape change in the characteristic mitotic rounding [103] caused by increased surface tension due to a drastic reorganization of the actomyosin cortex [104,105]. During anaphase, a transient structure, the contractile ring, forms perpendicularly to the mitotic spindle. This structure, organized by signals involving the small regulatory GTPase RhoA, constricts and effects invagination of the cleavage furrow. As described in chapter 1.2.3, NM II is the driving force behind this process [106]. Beyond the single-cell level, the orientation of division can be influenced by tissue-level forces [107]. Conversely, cell elimination by apoptotic cell death also involves the action of actomyosin contractility in activating the apoptotic pathway [108], nuclear fragmentation [109] and cell extrusion from epithelia [110]. Thus, the action of the actomyosin cytoskeleton is critical for growing tissues and maintaining their homeostasis.

1.3.2 Cell and tissue shaping

Beyond these processes controlling cell number, the actomyosin cytoskeleton acts primarily to control the cell shape in a tissue and thus to ensure its correct function. Depending on its localization and function, the actomyosin cytoskeleton can adapt different configurations, ranging from branched networks of various density to unbranched filaments of various lengths and sizes, which confers different mechanical properties on the cytoskeleton [111]. Contractile forces resulting from these networks can control cell shape and interaction on the short timescale of seconds [112,113] and long timescale of minutes to hours [114,115]. The connection of the cytoskeleton to the cell surface by adhesion molecules and thus to the transmission of forces from the cell to the tissue scale can then effect tissue-level deformations that shape organs and ultimately the whole organism. A number of the most important morphogenetic principles are described in the following.

An important step in development is the correct sorting of cells to the target localization when two tissues separate. Historically, this was thought to occur due to differential adhesion of cell types which would result in their separation [1]. While differential adhesion plays indeed an important role in tissue sorting in many systems [116,117], it is now understood that differences in cortical tensions between cells are likewise an important factor in cell sorting which results in cell rearrangements according to their interfacial tension, e.g. during germ layer separation in the gastrulation process [11,115,118,119]. After sorting, high tension at the established boundary can ensure partitioning of the compartments by large-scale actomyosin networks, as for example observed in the separation of the dorso-ventral compartments of the imaginal wing disc during *Drosophila* development [120].

Actomyosin also controls the geometry of cell arrangement. For example, polarization of actomyosin activity leads to cell intercalation in the *Xenopus* mesoderm [121,122] or junctional remodeling of the *Drosophila* germ band cells [123]. This control of cell shape translates into deformations on the tissue scale such as convergent extension in which tissues concertedly extend in one axis while narrowing perpendicularly, a movement which is important for gastrulation and organogenesis [124].

In apicobasally polarized epithelial cell layers, actomyosin contractility plays an important role in tissue shaping in the process of apical constriction, which is one of the most important processes of 3D tissue morphogenesis [93]. In epithelia, the lateral membranes are held together by adherens junctions, while the basal membranes attach to a matrix with focal adhesions. This enables the non-adhesive apical membranes to change their surface area through the contraction of an apical junctional actomyosin network. Since epithelial cells are connected by adherens and tight junctions, shrinking of the apical domain exerts a force on the neighboring cells which ultimately leads to bending of the epithelial sheet. Epithelial bending by apical constriction drives important developmental events such as mesoderm invagination during gastrulation in *Drosophila* [125,126], endoderm invagination in ascidian embryos [127] and neural tube closure in vertebrates [128] or generally in the formation of epithelial tubes [129].

Apart from cell-cell interaction in tissue shaping, the interaction between cells with the ECM is an important factor enabling correct tissue shaping. It is an important factor in the budding and branching morphogenesis of epithelial organs such as the salivary gland in which epithelial folding depends on strong cell-ECM interactions, and less on cell-cell adhesions [130]. In this way, the ECM serves as a mechanical scaffold enabling tissue deformation.

1.3.3 Cell motility

In addition to the control of tissue shape and geometry, cell motility is another important factor of morphogenesis. Cells have the capacity to migrate based on mechanical and chemical cues provided by their environment. Such a migration process can be initiated for individual cells or cell cohorts as single cell migration or collective migration, respectively [8]. Cell migration can occur in different modes which differ in the type of cell protrusion that drives it: mesenchymal migration which is driven by polymerization-dependent protrusions, and amoeboid migration that relies on blebs as membrane protrusions [131].

Polymerization-dependent membrane protrusions containing lamellipodia and lamella in mesenchymal cell migration are one of the best-characterized instances of how the

actin cytoskeleton directs cell behavior. The lamellipodium is a dynamic network of branched actin filaments at the leading edge of a cell. Here, Arp2/3 causes branching and polymerization of new actin filaments which rapidly turn over, while the lamellum, located behind the leading edge, consists of more stable and larger actin bundles [64,132]. These actin networks connect to the substrate of migration via focal adhesions which form and mature at the leading edge and are disassembled at the posterior trailing edge. While myosin is not required for actin polymerization in the lamellipodium or focal adhesion initiation, NM II is required for adhesion maturation [133]. Then, the traction force exerted by actin filaments on these focal adhesions effects the translocation of the cell body [134].

1.3.4 Blebs in cell migration and other processes

A less well-understood migration mechanism is based on membrane blebs. Blebs are short lived, spherical membrane protrusions that locally extend from cells before being retracted by a reassembled actomyosin cortex on the timescale of 1-2 min [131,135]. Blebs form due to a local detachment of the cell and the cortex. The membrane rapidly extends devoid of actin for about 30 s to the maximal extension of the bleb, followed by the reassembly of the actomyosin cortex and bleb retraction within 2 min [136]. Several models have been proposed as the cause of bleb formation: (1) a local cortex disruption that leaves the membrane untethered, (2) a reduction in membrane-cortex linking proteins that facilitates membrane detachment, and (3) a local contraction of the actomyosin cortex that forces the membrane to protrude outward (Figure 3) [131]. Whatever the cause for their formation, bleb inflation seems to depend on the hydrostatic pressure of the cytosol [137,138] generated by global cortical contractility, as myosin inhibition stops bleb formation. The inflation of a bleb is followed by the reassembly of the actomyosin cortex. Actin, the membrane-cortex linking ezrin-radixin-moesin complex (ERM) and actin-crosslinking proteins such as α-actinin are recruited to the bleb membrane to constitute a new cortex. However, how cortex formation is initiated remains to be investigated as of now, as classical actin nucleation factors such as Arp2/3 or the important formin mDia are absent form blebs. Finally, NM II is recruited to the bleb with a delay of ca. 10 s relative to actin, and its activation

results in the contraction of the newly established actin network and the retraction of the bleb ca. 2 min after its initiation [135,136,139]. NM II-mediated bleb retraction presents an interesting instance of specific roles of NMHC paralogs in a biological process. MYH9 seems to be the dominant paralog in this instance, as *Myh9* knockdown inhibits bleb retraction, while no impact on the bleb retraction dynamics could be observed for *Myh10* and *Myh14* knockdown [140]. These principles of bleb-driven cell migration in a developmental context are exemplified in zebrafish primordial germ cell migration during which blebs form in response to a calcium gradient that causes local actomyosin contraction and thereby bleb formation which sets the leading edge of the migrating cells [141]. However, how exactly bleb formation drives cellular translocation is not yet completely understood; current models propose a bleb-mediated forward movement of cytoplasm or bleb-generated pushing forces as the mechanism of forward translocation [142]. Despite being widely observed in cell migration, blebs have been originally observed in apoptosis and necrosis, where they form as the cytoskeleton breaks down [143], and they have since been implied to function in several cellular processes such as signaling hubs in cancer cell survival [144], positioning the cytokinetic cleavage furrow [145], cell spreading [146] and viral infection [147]. Apart from their diverse biological functions, the de novo assembly of the actomyosin cortex after membrane protrusion makes them ideal to study cortex organization and dynamics, and constitutes an interesting example of how actomyosin contractility controls cell behavior on the timescale of seconds.

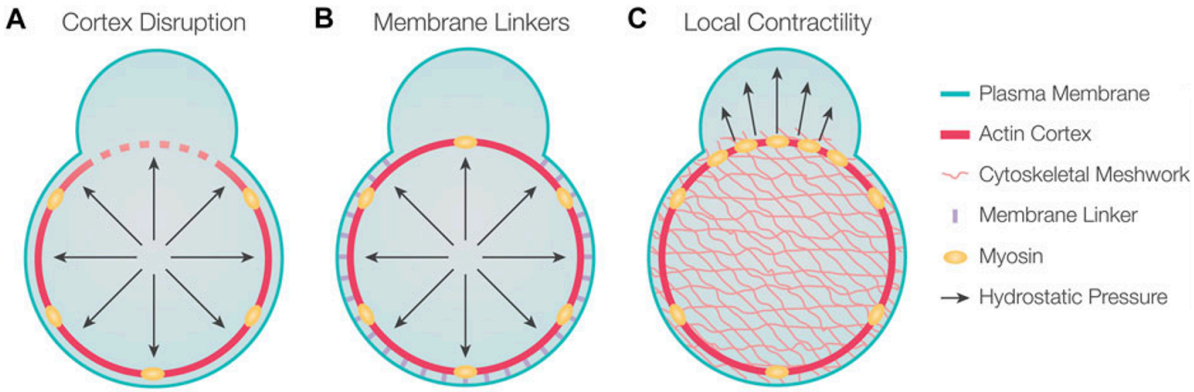

Figure 3: Three models of bleb formation: A) A local disruption of the actomyosin cortex under the membrane leads to its detachment and bleb protrusion. B) A local reduction in membrane-

cortex linking proteins leads to membrane detachment. C) A local cortical contraction leads to a pressure imbalance in the cytosol which causes bleb protrusion. Image adapted from [131].

How these principles result in animal morphogenesis has been studied in several model organisms, from invertebrates to mammals. The focus of this work lies on the preimplantation development of the mouse embryo, which is described in chapter 1.4 with focus on the actomyosin contractility-dependent morphogenetic steps of this first developmental period of mammalian development.

1.4 Mammalian preimplantation development

1.4.1 Preimplantation development as a model system to study mammalian morphogenesis

Mammalian preimplantation development comprises the initial phase of embryogenesis commencing at fertilization and concluding with the attachment of the embryo to the maternal endometrium upon implantation [148]. During this period, the embryo develops in an autonomous manner without support from the surrounding maternal tissues. This independence enables direct study of the embryo during preimplantation development as it can be isolated from the maternal developmental tract and cultured ex vivo [149]. As such, prolonged live imaging and embryo manipulations can be carried out, which is possible only to a limited extent at later developmental stages [150,151]. Preimplantation development features a series of morphogenetic events that occur together with cellular proliferation and the first differentiation events in development. Therefore, the preimplantation embryo is a good model system to study the cellular mechanisms underlying morphogenesis [152].
The mouse as the classic model organism for mammalian developmental biology [153] has yielded most insights into the process of preimplantation development [154]. However, embryos of other species such as rabbit [155,156], monkey [157–159] or cow [160,161] are also investigated today. Additionally, preimplantation development constitutes one of the few instances where human development can be studied directly on the human embryo, as regulations in many countries allow the culture of and experimentation on surplus human embryos donated from couples who completed their in vitro fertilization treatment [162–165]. Studying human preimplantation

development, and the associated developmental mechanisms that could cause developmental defects, is of high clinical relevance given that up to 30% of fertilized embryos fail to develop beyond the preimplantation phase [166,167]. Thus, a better understanding of preimplantation development and the potential failures could lay the basis for novel fertility treatments [168].

1.4.2 Mouse preimplantation development

As the studies presented in this PhD thesis have been conducted using the mouse embryo as a model system, the following description of mammalian preimplantation development refers to this developmental process in the mouse unless otherwise stated. Mouse preimplantation development is marked by a series of cleavage divisions that increase the number of cells, morphogenetic steps that shape the developing embryo and cell fate decisions that give rise to the first lineages of the embryo (Figure 4).

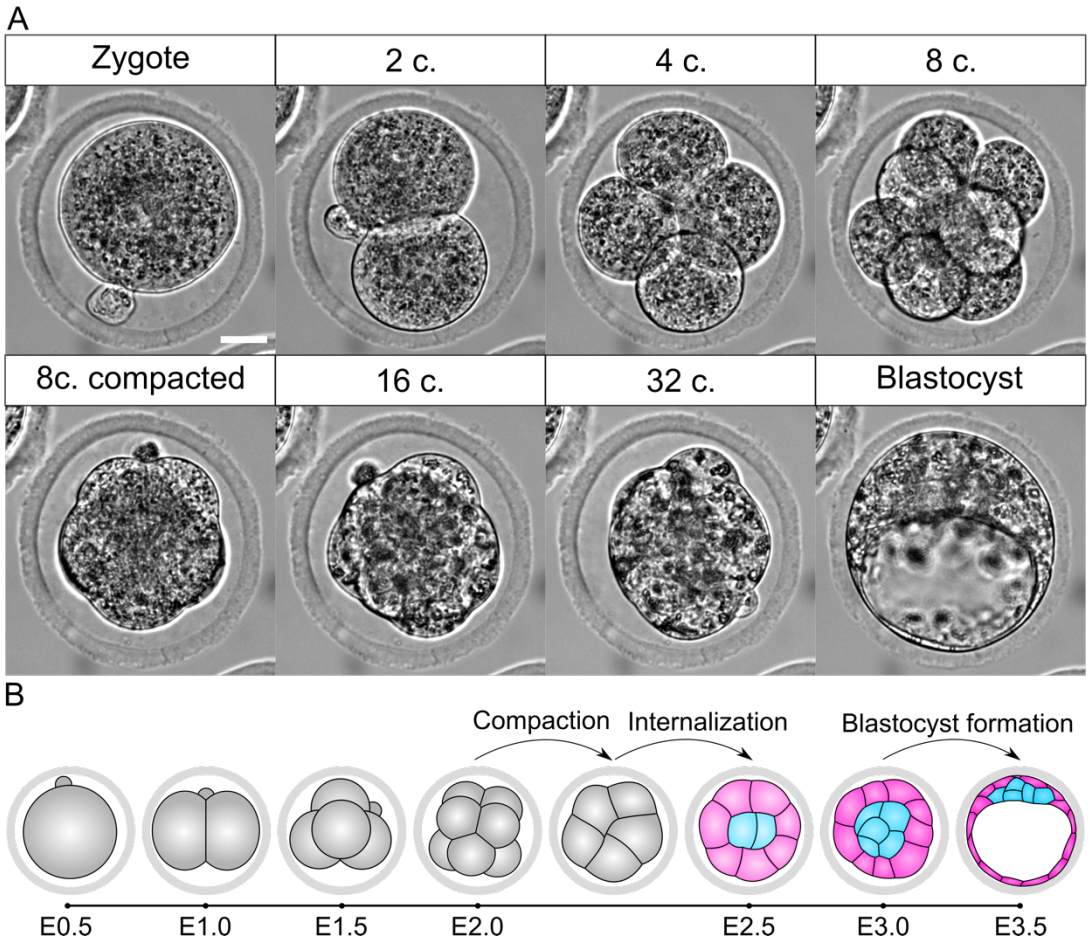

Figure 4: Overview of mouse preimplantation development. A) Bright-field images of the cleavages stages and morphogenetic events of mouse preimplantation development (Scale bar, 20 μm). B) Schematic representation of the developmental stages depicted in (A). Development

commences with the totipotent zygote. The embryo then undergoes three cleavage divisions through the 2-cell and 4-cell stages before morphogenesis begins at the 8-cell stage with the compaction process. During the fourth cleavage to the 16-cell stage, a portion of blastomeres is internalized into the center of the embryo, which initiates the first lineages differentiation in the mouse embryo. Surface blastomeres will acquire a trophectoderm fate (magenta), while internalized cells will become the inner cell mass (cyan). After another cleavage division which leads to further internalization of cells, the embryo forms the first lumen of mammalian development in which the inner cell mass is confined to one side of the trophectoderm, thus breaking the radial symmetry of the embryo. The zona pellucida can be seen in (A) as the circular layer surrounding the embryo. E indicates the days of embryonic development.

1.4.2.1 Fertilization and cleavage divisions

Preimplantation development commences with the fusion of the two gametes (sperm cell and oocyte) to form the totipotent zygote [169], which can give rise to all tissues of the embryo, including the embryo-derived extraembryonic lineages that form auxiliary extraembryonic tissues in mammals (yolk sac, chorion, amnion, allantois) [170]. During preimplantation development, the embryo is encased by the zona pellucida, a glycoprotein layer that is formed during oogenesis and is necessary for fertilization, but dispensable for further preimplantation development [171,172]. Interestingly, deformations of the zona pellucida can guide the orientation of the blastocyst when it inflates on E3.5 and thereby help setting the first symmetry axis of development [173,174]. During the first four days of development (fertilization to E3.5), the embryo undergoes a series of cleavage divisions leading to exponential cell number increase. However, the global embryonic volume remains constant during preimplantation development as cellular material is partitioned between sister blastomeres. The blastomeres retain the initial totipotency of the zygote until the 4-cell stage as the early mouse embryo is highly plastic in its developmental potential [175], meaning that the loss of a blastomere or dissociation of the embryo at the 2- or 4-cell stage can still result in a viable organism. Reciprocally, aggregation of embryos during the cleavage stages in a chimeric embryo does not negatively impact further development [176,177]. Single blastomeres retain their plasticity until the 8-cell stage, up until which they can contribute to the first two lineages of the embryo [178]. During the first three cleavage divisions from zygote to the 8-cell stage, no morphogenesis occurs [152,179] and blastomeres remain undistinguishable in their morphology and differentiation potential [180]. However, actomyosin contractility manifests itself

already at these stages in the form of periodic cortical waves of contraction which occur in blastomeres as the surface tension of blastomeres decreases [181,182]. These contractile waves travel around blastomeres with a period of ca. 80 s, showing how actomyosin contractility can act on vastly different timescales when compared with the following hour-long process of compaction.

1.4.2.2 Compaction

After the third cleavage division to the 8-cells stage on E2.5, the embryo undergoes its first morphogenetic event called compaction (Figure 5A) [183]. During compaction, the eight blastomeres, which are only loosely adhering following the third division, flatten against each other, thereby increasing their cell-cell contact area and minimizing the area exposed to the surrounding medium [152]. Cell-cell adhesion is mediated by cadherin-1 (CDH1, E-cadherin) which becomes confined to the cell-cell contacts from a prior even distribution [184,185]. This polarized CDH1-mediated cell-cell adhesion has been proposed to drive compaction, and indeed *Cdh1* perturbation prevents compaction [186–188], indicating an essential role for adhesion molecules in this process. It has been proposed, based on siRNA-mediated knockdown studies, that cadherin-containing filopodia at the cell surface effect compaction in a myosin X-dependent manner [189]. However, the genetic knockout of MYO10 failed to replicate this phenotype [190]. Instead, it was found that an increase of actomyosin mediated cell surface tension at the free cell-medium interface is responsible for effecting the compaction process (Figure 5) [181]. In this model, actomyosin concentrates at the cell-medium interface while simultaneously being excluded from the cell-cell contact due to CDH1 signaling, leading to a two-fold increase in the surface tension at the free surface and a relaxation of the contact tension [181]. This is supported by the failure of embryos to compact when myosin is inhibited or knocked out [115,181]. While the function of the compaction process is ultimately unknown, it has been hypothesized that the geometry of the compacted embryo energetically facilitates the internalization of cells after the next cleavage division [115]. In human preimplantation embryos, early compaction has been associated with successful implantation, suggesting a link between compaction timing and embryo quality [191]

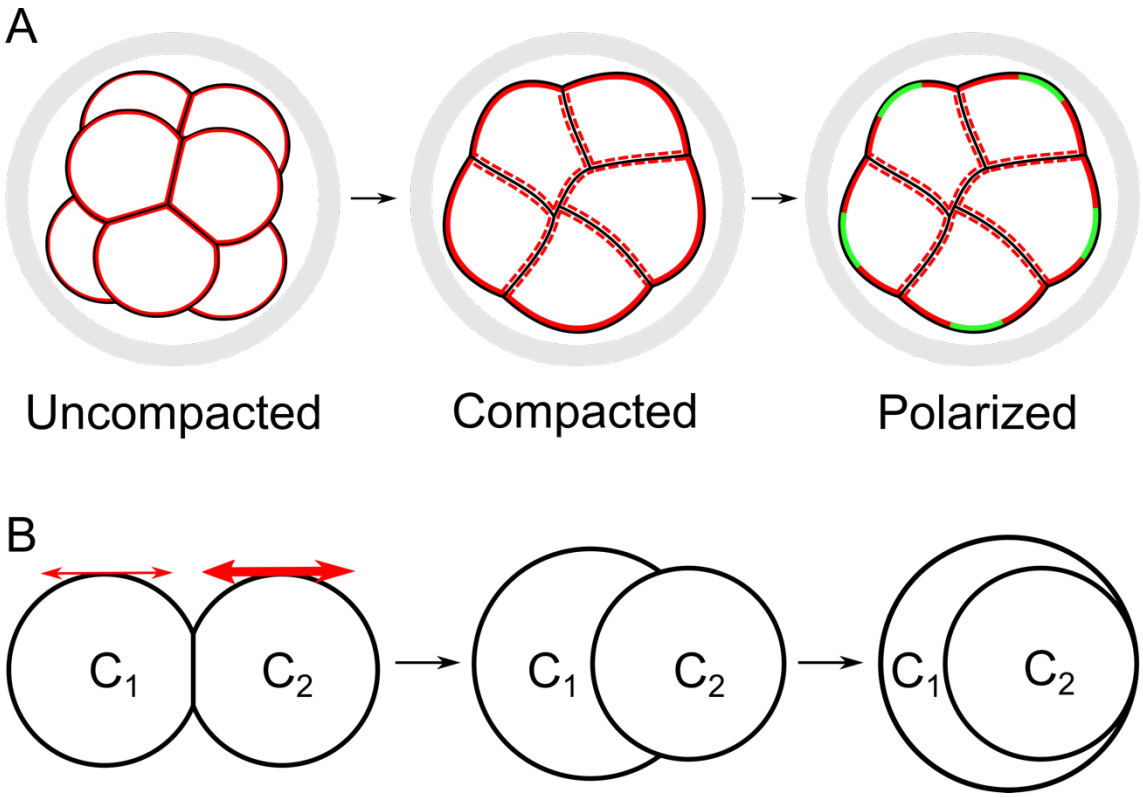

Figure 5: Principles of compaction and internalization. A) Schematic sequence of the compaction movement at the 8-cell stage. The embryo transitions from an uncompacted state in which actomyosin (red) is uniformly distributed at the blastomere surface (left), to the compacted state with actomyosin depletion at the contacts in favor of the contact-free surface (center). Finally, the formation of the apical domain (green) excluded actomyosin from the cell pole towards the apical junction (left). B) Principle of cell internalization due to tension differences illustrated on a cell doublet. Two contacting cells with different surface tensions (represented by red arrows, here: surface tension C_1 < surface tension C_2 (left)) will extend their contact area whereby the less contractile cell will envelop the more contractile cell (center). This leads to the complete internalization of the more contractile cell (right).

1.4.2.3 Blastomere polarization

The mammalian oocyte and zygote is not prepatterned in terms of a polarization of maternal determinants or cytosolic components, as is the case for many other species [192,193]. Polarization of the blastomeres initiates after the third cleavage division: Simultaneously to compaction at the 8-cell stage, the blastomeres start to polarize with the formation of an apical domain at the center of the contact-free membrane (Figure 5A) [194]. This polarization occurs in three steps: First, actomyosin localizes to the contact-free cell surface away from contacts, which drives compaction as described in

chapter 1.4.2.2. At the membrane level, this manifests as the appearance of a circular patch enriched in microvilli [195] which are organized by the ERM complex [196]. Subsequently, apical determinant proteins localize to the contact free surface, among them most importantly the Par complex [192], consisting of partitioning defective proteins 6 and 3 and atypical protein kinase C (PARD6-PARD3-aPKC) as its core components in the early mouse embryo [197]. Loss of these apical components leads to polarization defects [198,199]. Finally, the apical domain becomes depleted in actomyosin through negative regulation by the Par complex. This leads to a surface contractility asymmetry in 8-cell stage blastomeres, which is propagated to daughter blastomeres if the apical domain is inherited asymmetrically as described in chapter 1.4.2.4, which affects cell positioning and differentiation of the daughter cells. Cell-cell contacts support polarization by the exclusion of apical determinants, but they are dispensable as polarization can occur in an isolated 8-cell stage blastomere [188,199,200]. In subsequent divisions, the apical domain can be asymmetrically inherited (see chapter 1.4.2.4). Interestingly, compaction and apical polarization can occur independently despite coinciding temporally, highlighting independent underlying mechanisms [201,202].

1.4.2.4 Internalization

During the fourth cleavage division, blastomere internalization occurs, which is the first cell sorting event of mammalian development. A fraction of cells is allocated to the center of the morula and thereby lose their contact with the surrounding medium, while the other fraction remains on the morula surface. Internalization relies on two principles: asymmetric divisions and tension-dependent sorting [152]. Asymmetric divisions occur when the cleavage plane of an 8-cell stage blastomere is oriented parallel to the surface of the morula. As a result, one of the daughter cells is retained in the center of the morula, while the other one stays on the surface. This also results in an asymmetric inheritance of the apical domain to the outer cell, which is relevant for subsequent differentiation [115]. An asymmetric division can be induced by the perpendicular orientation of the mitotic spindle relative to the morula surface, resulting in the parallel division plane. The apical domain can orient the spindle perpendicularly

by anchoring one spindle pole [199], but it is unclear whether asymmetric divisions occur in a controlled way [199,203] or stochastically [204].

However, some cleavage divisions at the 8-cell stage do not occur asymmetrically, resulting in two daughter cells at the embryonic surface. In this case, a cell can be allocated to the morula center by tension-dependent sorting (Figure 4, Figure 5B) [115,205]: a blastomere internalizes when its cortical tension is higher than those of its neighbors. In 16-cell stage doublets, the threshold for complete internalization was determined to be a 1.5-fold tension asymmetry between blastomeres. Below that, both blastomeres will stay exposed to the surface and potential internalization can happen after another division cycle [115]. These differences in tension arise from unequal inheritance of apical material which contains less actomyosin and confers distinct surface tensions to the daughter cells [115,206]. Thus, more contractile blastomeres sort to the center of the embryo, while less contractile blastomeres stay on the surface as a result of apical signals.

1.4.2.5 TE/ICM differentiation: the first lineage segregation in mammalian development

The allocation of cells into an inner and outer fraction also triggers the first lineage differentiation of mouse development into the pluripotent inner cell mass (ICM) and the epithelial trophectoderm (TE) on the embryo surface (Figure 4B). Historically, two hypotheses have been put forward explaining this first lineage segregation: the inside-out hypothesis, which proposed that the position and microenvironment of blastomeres in the morula decide their fate [207], and the polarity hypothesis, which proposed that apicobasal polarization would be the deciding factor in differentiation [200].

Our current understanding of TE-ICM differentiation unifies these two concepts in that cell fate seems to be driven by position-dependent yes-associated protein 1 (YAP) activity (initially identified as downstream effector of the HIPPO pathway, which is involved in mechanosensitive signal transduction) [208]. In this model, the transcription coregulator YAP is expressed in all blastomeres, but can only exercise its transcriptional function dependent on its phosphorylation state: In its phosphorylated state, YAP remains in the cytosol, while the unphosphorylated form

can translocate into the nucleus and causes transcriptional activation in cooperation with its cofactor TAZ and the transcriptional regulator TEA domain transcription factor 4 (TEAD4) [209–213]. Nuclear localization of YAP results in a TE fate, while in the ICM, YAP is sequestered in the cytosol. Phosphorylation and thus localization of YAP is controlled by the HIPPO pathway component large tumor suppressor (LATS) kinase [214], which localizes to adherens junctions [215] and functions in cooperation with Angiomotin proteins (AMOT) [216,217]. However, in outer, apicobasally polarized cells, AMOT is sequestered to the apical, adhesion free membrane, which prevents YAP phosphorylation and permits nuclear translocation. In inner cells, there is no apical domain and they contact their neighbors with adherens junctions. Here, AMOT colocalizes with LATS kinase at the adherens junctions and effects YAP phosphorylation, thus sequestering YAP in the cytosol [201]. This mechanism shows how position and polarity each contribute the first fate decision. Indeed, loss of the apical domain, e.g. by aPKC knockout, leads to impaired TE differentiation [199]. On the flipside, ICM differentiation depends on the proper formation of CDH1-mediated adherens junctions, since in maternal-zygotic *Cdh1* knockout embryos, blastomeres adopt a global TE fate [188], presumably due to the disturbed HIPPO pathway.

Other factors of the cellular microenvironment have been shown in vitro to influence YAP localization independently of the HIPPO pathway, such as cell shape, ECM stiffness and contractility [218–220]. Of these factors, inhibition of actomyosin contractility was shown to perturb YAP localization in the mouse preimplantation embryo [115]. Also, blastomere geometry influences YAP localization: the size of the apical domain correlates with nuclear YAP levels, showing a quantitative influence of exposed surface area in the differentiation process.

The cooperation of factors such as cell position, polarization and contractility constitutes an interesting interplay in the first cell differentiation event of the mouse embryo. Differential YAP signaling in the TE and ICM leads to a differential expression of transcription factors that reinforce lineage fate [221]. The first lineage determinants, CDX2 and SOX2, are expressed at low levels at the 8-cell stage, but their expression becomes restricted to the TE and ICM respectively [222]. In the TE, YAP signaling reinforces CDX2 expression, which in turn activates downstream TE genes [223,224]. In the ICM, SOX2, OCT4 and NANOG form a pluripotency gene regulatory network,

which has been extensively characterized in cultured, ICM derived embryonic stem cells [225]. Blastomeres retain some differentiation plasticity until the 32-cell stage, since after dissociation and reaggregation, they can contribute to both lineages. Final fate determination in the TE seems to occur during the late 32-cell stage, as TE cells isolated at this point cannot regenerate ICM cells. Contrarily, ICM cells isolated from the late 32-cell stage can regenerate entire blastocysts, showing that ICM fate can remain malleable to some extent [178,226]. Thus, cell fate is induced at the 16-cell stage, but remains malleable until the 32-cell stage. During further development, the ICM will give rise to all fetal tissues as well as to most extraembryonic tissues such as the amnion and allantois, while the TE will contribute to the chorion and the parietal yolk sac [170].

As part of the TE differentiation process, the surface blastomeres acquire characteristics of a squamous epithelium. At the 16-cell stage, the apical domain extends in what has been described as an actin-dependent zippering process from the cell pole to occupy the entire medium-exposed membrane [227]. TE cell recruit cytosolic factors such as the zonula occludens proteins ZO-1 and ZO-2 and cingulin to the apical contacts, which is sealed by transmembrane proteins claudin 4 and 6, occludin and junctional adhesion molecule-1 (JAM-1) [228]. Tight junctions form a semipermeable paracellular seal which enables subsequent lumen formation [229]. This step completes the epithelial polarization of blastomeres initiated at the 8-cell stage with the definite separation of the apical domain at the free blastomere surface and the basolateral domain at the adhesive cell-cell contacts [230].

1.4.2.6 Blastocyst formation I: Ion transport into the intercellular space

Following the 16-cell stage, the embryo undergoes its 5th cleavage division to the 32-cell stage at E3.0. This leads to further allocation of cells to the ICM by oriented asymmetric division as described in chapter 1.4.2.4. Tight junction formation, which is initiated at the 16-cell stage, results in the sealing of the intercellular space from the outside medium. The embryo now forms the blastocoel, the first lumen of mammalian development. Blastocoel formation constitutes an unusual case of lumen formation, as it forms at the basolateral side of an epithelium. In most other cases of lumen

formation during development, the lumen forms at the apical side of an epithelium [231]. In apical lumen formation, cells oppose their non-adhesive apical membrane, whose separation is often facilitated by the exocytosis of charge-repelling surface proteins [232], leading to a concerted lumen opening. In the case of the blastocyst, the lumen has to form against the basolateral cell-cell contacts which are held together by adhesion molecules. Both apical and basolateral lumen form by drawing water in the intercellular space by establishing an osmotic gradient. In the case of blastocoel formation, this is achieved by creating a trans-trophectodermal osmotic gradient between the outside medium and the space between the blastomeres. This osmotic gradient is chiefly established by unidirectional transport of sodium and chloride ions from the outside medium into the intercellular space while other ions are facultative [233]. Apical Na^+ import is achieved by the Na^+/H^+-exchanger NHE3 [234,235] as well as Na^+ channels [233,236] (Figure 6). Additionally, Na^+/glucose and Na^+/amino acid cotransporters have been implied in apical Na^+ import [233,237,238]. However, these transport proteins can only conduct Na^+ along a gradient. The step of this process requiring energy expenditure occurs at the basolateral membrane, where the ouabain-sensitive Na^+/K^+-ATPase exports Na^+ ions into the intercellular space in an ATP-dependent manner [239–243]. In addition to this crucial transport function, the Na^+/K^+-ATPase also seems to be required for tight junction integrity [244]. Cl^- ions accumulate following the Na^+ gradient. However, contradicting findings concerning the entry route of Cl^- have been reported: while some studies suggest a transcellular Cl^- route mediated by HCO_3^-/Cl^- exchangers and Cl^- channels [245], others have found no effect of blocking Cl^- transporters or channels on blastocyst formation and therefore proposing a paracellular Cl^- entry into the nascent lumen [233] (Figure 6). The osmotic pressure created by the ion gradient draws water into the intercellular space. However, it may not be sufficient to draw water directly through the lipid bilayer of the plasma membrane [246], wherefore the water influx is facilitated by transmembrane water channels called aquaporins (AQP). Specific aquaporins have been found in the mouse preimplantation embryo, namely AQP9 at the apical membrane and AQP3 and AQP8 at the basolateral membrane [247,248]. The knockout of single aquaporin genes results in viable mice [249], suggesting a redundancy between aquaporin paralogs which might also apply to preimplantation development. However, the global

pharmacological inhibition of aquaporins results in impaired blastocoel growth, highlighting the role of aquaporins in facilitating water entry into the nascent lumen [248] (Figure 6).

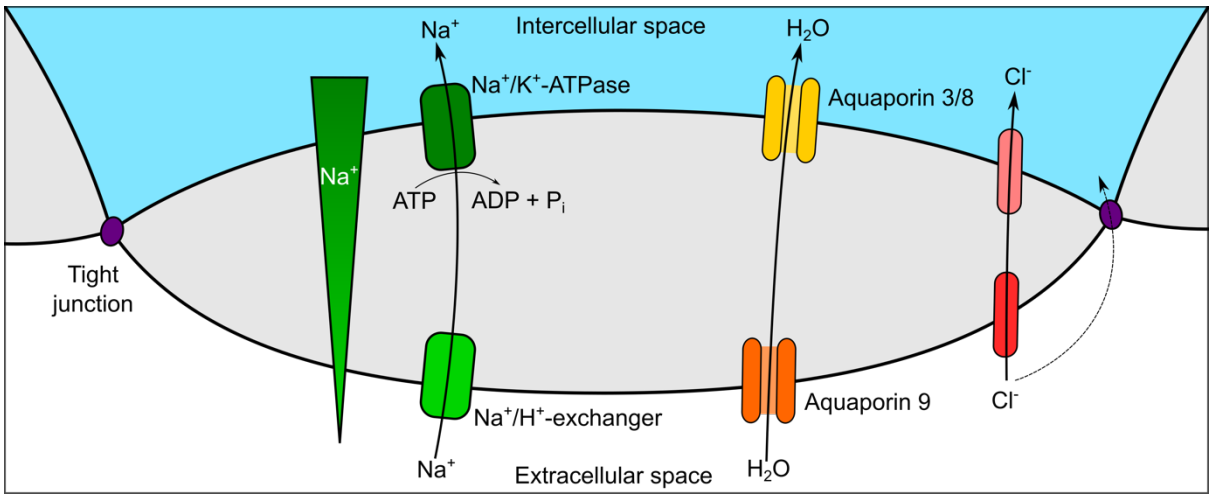

Figure 6: Ion transport mechanism in blastocyst formation. At the 32-cell stage, mouse embryos establish an osmotic gradient over the now fully epithelialized trophectoderm. This is achieved by an active, directed sodium import axis in which sodium ions are transported over the outer apical membrane by ion exchangers such as the Na^+/H^+-antiporter and other transporter and channels. The Na^+/K^+-ATPase effects the energy expenditure steps of ion transport by ATP-dependent Na^+ translocation over the basolateral membrane. Cl^- ions move passively into the intercellular space following the charge gradient of the active cation transport, with potential ingress of chloride ion through tight junctions. Water accumulation driven by the trans-epithelial osmotic gradient it facilitated by aquaporins which are specifically localized in the apical or basolateral membrane.

1.4.2.7 Blastocyst formation II: Mechanism of blastocoel formation

Once fluid starts accumulating in the intercellular space, the increase in hydrostatic pressure leads to local membrane separation throughout the embryo and the formation of hundreds of microlumens at all cell-cell contacts in the TE and ICM (Figure 7), which has been likened to a hydraulic fracturing process [250]. They can appear both at contact interfaces of two cells (bicellular microlumens) and at the contact points of three or more cells (multicellular microlumens). Microlumen formation leads to a rearrangement of adhesion molecules at the blastomere contacts from an even distribution in the closed state to a heterogeneous distribution in which CDH1 seems to accumulate at the edges microlumens. Microlumens grow globally for ca. 3 h after initial formation, before they eventually all start shrinking except one lumen which will

become the final blastocoel (Figure 7). This process, which takes another 3 h, has been likened to a coarsening process as observed in the coarsening of foams [251]. In this model, microlumens exchange fluid due to pressure differences and discharge their content into less pressurized compartments, until only one lumen remains [250]. The entire process from microlumen initiation to the final blastocoel happens during 5-6 h. Bicellular microlumen lose their fluid before multicellular microlumens, and the final blastocoel likely arises from a multicellular microlumen. This suggests differences in pressure between bi- and multicellular microlumens with the multicellular ones acting as pressure sinks. In the wild-type embryo, the blastocoel always forms at the interface of the TE and ICM, thereby confining the ICM to one side of the blastocoel cavity. However, there is no evidence for a prepatterning of the blastocyst formation site at this interface, highlighting the regulative nature of preimplantation morphogenesis [252].

Notwithstanding this observation, the position of the blastocoel can be controlled by patterning cell adhesion and contractility in the morula [250]. In WT/maternal *Cdh1*$^{+/-}$ chimeric embryos, the blastocoel will always form between the adhesion-deficient blastomeres. The fluid thus accumulates between the hydraulically more compliant cells where cell-cell contacts can be separated more easily. Similarly, in WT/maternal (m)*Myh9*$^{+/-}$ chimeras, the lumen forms in the less contractile half. While there is no evidence for adhesion patterning in the wild-type morula, surface tension has been found to be different between the TE and ICM [115]. Indeed, microlumens are asymmetrically shaped at the TE-ICM interface where they bulge more into the TE cell, underlining its lower contractility. Tension differences between TE and ICM might therefore guide the positioning of the blastocoel. However, how actomyosin contractility, which often manifests itself on the time scale of seconds rather than hours, controls the coarsening and positioning of the blastocoel is not yet fully understood.

Blastocoel formation breaks the radial symmetry of the mouse embryo and establishes the first symmetry axis of development between the embryonic (site of ICM localization) and abembryonic (TE opposite the ICM) pole. It also separates the TE into the polar (contacting the ICM) and mural (contacting the blastocoel) TE, which will

pursue different developmental paths after embryo implantation into the uterus [170,253,254].

Once the final blastocoel has been established, it expands by further fluid accumulation. However, this expansion results in a series of collapses and reinflations. Due to the increase in luminal pressure, the epithelial integrity of the TE cannot be maintained when TE cells enter mitosis, which leads to a loss of luminal fluid and blastocyst collapse. Continuous collapse and regrowth cycles set the final size of the embryo and contribute to the hatching from the zona pellucida [255–257].

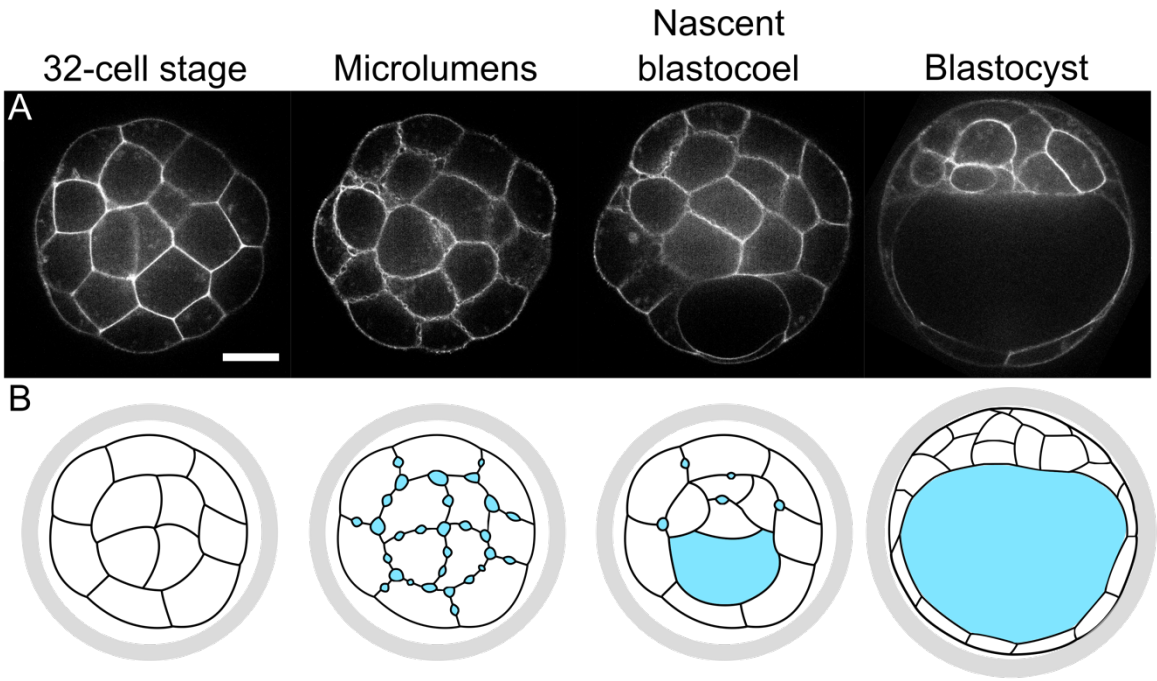

Figure 7: Mechanism of blastocyst formation. A) Equatorial plane of a mouse embryo with fluorescently labelled membrane (Scale bar, 20 μm) and B) schematic representation of the stages of blastocyst formation. After the fifth cleavage to reach the 32-cell stage, the embryo creates an osmotic gradient between the intercellular space and the outside medium which leads to fluid accumulation into the intercellular space and the appearance of hundreds of microlumens at all cell-cell contacts. These microlumens exchange fluid due to pressure differences in a coarsening process which results in the disappearance of all microlumens except one remaining lumen: the blastocoel. This process takes place over ca. 5 h. The blastocoel consistently forms between the trophectoderm and the inner cell mass, thus confining the latter to one side of the lumen. This breaks the radial symmetry of the embryo and sets the first symmetry axis of mouse development, which determines the dorsoventral axis of the embryo.

1.5 Mouse embryonic development beyond blastocyst formation

After blastocyst formation, the embryo undergoes another cell lineage differentiation. From the 64-cell stage onward, the ICM splits into two separate lineages: the primitive endoderm (PrE) and the epiblast (EPI), which are characterized by mutually exclusive expression of the transcription factors GATA6 and NANOG, respectively [258]. Initially, the precursor cells of these two lineages are located in random 'salt-and-pepper' manner in the ICM [259]. The two lineages eventually become spatially segregated with the PrE cells lining the blastocoel interface and the EPI cells being sandwiched between PrE and TE. The signaling events inducing PrE/EPI differentiation have been delineated: EPI cells start specifying prior to PrE cells [260,261] and secrete fibroblast growth factor 4 (FGF4) [262], which induces differentiation of the PrE precursors [254,263]. How the two cell populations spatially segregate is less clear. Various hypotheses include sorting due to differential adhesion or difference in cortical tension. While there is no evidence for a role of adhesion in this process, as sorting does not seem to depend on CDH1 [264–266], a role for actomyosin contractility has been proposed in the form of active cell migration [267] and recently in the form of dynamic surface fluctuations that would drive spatial PrE/EPI segregation [268]. Additionally, fine tuning of specific transcription factor levels according to cell position may help resolve the initially mixed cell population.

At E4.5, the embryo reaches the implantation stage. After hatching from the zona pellucida, it attaches to the maternal uterine endometrium with the mural TE at abembryonic pole [269]. The embryo then invades the maternal tissue and undergoes further morphogenetic rearrangements [253,270], which ultimately set the stage for gastrulation from E6.25 onward and subsequent fetal development [271].

1.6 Review article: Stay hydrated: The basolateral fluids shaping tissues

All tissues are immersed in extracellular fluid to a certain degree. Lumen formation is a common morphogenetic event in which fluid-filled space is created between previously densely packed cells. The transport and dynamics of fluid play an important role in animal development, as it can influence tissue morphogenesis and cell differentiation.

However, most attention has been given to lumens which form on the apical side of epithelia or endothelia. Indeed, these apical lumens are among the most well-studied events of tissue fluid accumulation [20,22]. They include many physiologically important structures such as the vasculature, the intestinal lumen or the renal tubules [274–276]. Also, animal morphogenesis sees the appearance of many transient lumens during development which ultimately disappear from the organism, but nevertheless fulfill indispensable functions during their respective developmental steps. Example for these transient developmental apical lumens are: the epiblast lumen in early mammalian development [277], the left-right organizers of vertebrate development (the node in mammals / Kupffer's vesicle in fish) [278,279], or yet apical lumen formation in zebrafish lateral line development [280].

Recent research has also demonstrated the relevance of fluid on the basolateral side of epithelia.
We decided to write this review to account for the growing evidence how intercellular fluid emerges as a factor driving morphogenesis. Highlighting various examples of basolateral fluids, we review the principles how these fluids contribute to animal morphogenesis.

Available online at www.sciencedirect.com

ScienceDirect

Current Opinion in Genetics & Development

Stay hydrated: basolateral fluids shaping tissues

Markus Frederik Schliffka[1,2] and Jean-Léon Maître[1]

During development, embryos perform a mesmerizing choreography, which is crucial for the correct shaping, positioning and function of all organs. The cellular properties powering animal morphogenesis have been the focus of much attention. In contrast, much less consideration has been given to the invisible engine constituted by the intercellular fluid. Cells are immersed in fluid, of which the composition and physical properties have a considerable impact on development. In this review, we revisit recent studies from the perspective of the fluid, focusing on basolateral fluid compartments and taking the early mouse and zebrafish embryos as models. These examples illustrate how the hydration levels of tissues are spatio-temporally controlled and influence embryonic development.

Addresses
[1] Institut Curie, PSL Research University, Sorbonne Université, CNRS UMR3215, INSERM U934, Paris, France
[2] Carl Zeiss SAS, Marly-le-Roi, France

Corresponding author: Maître, Jean-Léon (jean-leon.maitre@curie.fr)

Current Opinion in Genetics & Development 2019, **57**:70–77

This review comes from a themed issue on **Developmental mechanisms, patterning and evolution**

Edited by **Gáspár Jékely** and **Maria Ina Arnone**

For a complete overview see the Issue and the Editorial

Available online 21st August 2019

https://doi.org/10.1016/j.gde.2019.06.015

Fluid compartments

During animal development, the embryo changes its shape following a carefully orchestrated program. This transformation results from combined cellular processes such as cell growth, proliferation, deformation, neighbor exchange and migration [1,2]. Often, these movements lead cells to form coherent compartmentalizing structures [3]. These compartments are bounded by a barrier, typically an epithelial layer, and can then gain further complexity [4]. Additionally, all living cells are immersed in fluid, of which the volume, composition and movement are controlled within larger compartments such as lumens, organs or vessels. This fluid is crucial for cell and tissue homeostasis, as its properties determine many cellular functions, from metabolism to signaling [5,6••,7,8,9,10,11].

We define fluid compartments as units within which fluid freely permeates. Fluid compartments are bounded by a barrier, which controls the exchange of solutes and water (Figure 1). Typically, this barrier is made of epithelial or endothelial cells, which are apico-basally polarized and form tight junctions [12,13]. Apico-basal polarity allows for directed transport, while tight junctions between the barrier cells ensure that fluid and solutes cannot freely diffuse over the compartment barrier [14]. Together, apico-basal polarity and tight junctions permit the definition of chemically and physically distinct fluids in the apical and basolateral compartment (Figure 1). Thereby, tissues can confine chemical signaling to the apical or basolateral compartments [9,15,16]. For example, in the zebrafish lateral line, cells restrict FGF signals to a few cells of the organ, which share a small apical lumen of a few microns in diameter [17]. In other cases, such as in flat gastruloids, Nodal signaling can be perceived differently by cells if applied within the apical or basolateral compartments as a result of polarized receptor localization [15]. Similarly, physical signals, such as the shear stress produced by contraction-generated flows, can be confined to a compartment. For example, shear stress controls heart valve differentiation during zebrafish heart development [18,19]. Fluid flow in other contexts, for example, interstitial flow [20,21] or cilia-mediated flow also generate shear and may induce a cellular response if sufficiently strong [22]. Finally, osmotic and hydrostatic pressures are able to set distinct volumes to compartments and organs, such as the chick eye [23], zebrafish brain ventricle [24] or mouse blastocyst [25••].

Previous reviews thoroughly covered crucial aspects related to intercellular fluid such as apical lumen formation [12,29,30] or the generation and sensing of fluid flow [31,32]. Here, we focus on recent findings on fluid permeating the basolateral compartment. Unlike apical compartments, basolateral compartments typically contain less fluid and are populated with cells which adhere to each other and to the extracellular matrix [33]. In the following, we will discuss recent findings on how basolateral fluid is controlled and how it impacts the morphogenesis of the mouse blastocyst and of the zebrafish gastrula.

The mammalian blastocoel: a blueprint for basolateral lumens

The blastocoel is the first lumen to form during the early development of several groups of animals such as echinoderms, amphibians or mammals [34–36]. The blastocoel is a basolateral lumen, which may come across as unfamiliar when most studies on lumens focus on apical ones [12,29,30,37]. Yet, MDCK cells, a canonical model

Figure 1

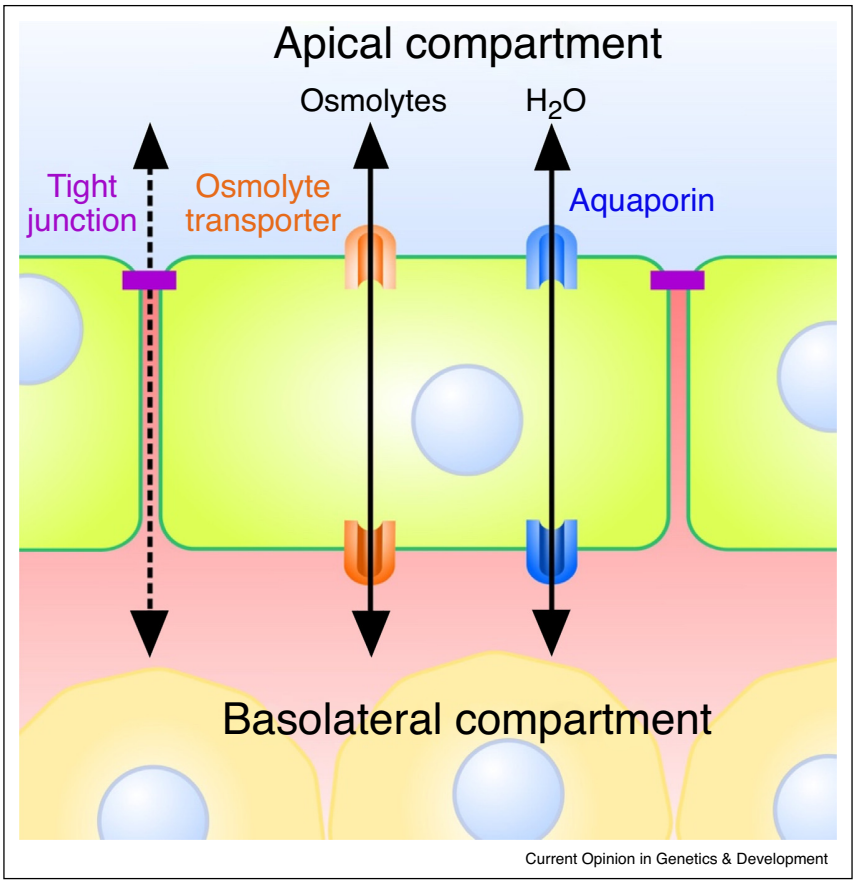

Cellular control of fluid compartments.
Fluid movement between compartments is controlled by barriers such as epithelia or endothelia. Transmembrane pumps, transporters and channels control the distribution of osmolytes in both compartments [26]. Water follows the osmotic gradient established across the cellular barrier by flowing through aquaporins, which are water-specific transmembrane channels [27,28]. The sealing of the cell barrier is maintained by tight junctions, which control paracellular exchange [14].

for apical lumen formation [30,38], can form 'inverted cysts' with a lumen on their basolateral side if cultured in suspension [39,40] or form domes when in a monolayer by pumping fluid towards their basolateral interface [41•]. Such epithelial structures with 'inverted' polarity may turn out not to be that uncommon in physiological and pathological settings [42]. Apical and basolateral cysts will likely share many features, with one key difference: basolateral lumens form at the adhesive interface of cells. To study this aspect, the mouse blastocyst, forming during preimplantation development, can serve as an ideal experimental system.

The blastocyst consists of an epithelial envelope, the trophectoderm (TE), enclosing the inner cell mass (ICM) and the blastocoel [43,44]. The blastocoel is a basolateral fluid compartment, in which cells from the ICM typically gather into a coherent structure, but can also be found dispersed throughout the embryo against the TE envelope, for example, in the elephant shrew [45]. Before blastocoel formation, the mouse embryo first compacts, pulling its cells into close contact and reducing intercellular fluid [46] (Figure 2). Then, surface cells acquire apico-basal polarity and seal their basolateral compartment by expanding their apical domain and fastening their tight junctions [47,48]. This allows polarized transport of osmolytes and fluid towards the basolateral compartment [49–51] (Figure 2).

At the onset of blastocoel formation, fluid accumulates in the intercellular space of the mouse embryo and cell–cell contacts become separated by hundreds of short-lived micron-size lumens [52••]. Analogous structures were previously described when fluid is flushed on the basolateral side of MDCK monolayers [53••]. The pressure of the fluid, in the range of hundreds of pascals, is able to fracture adherens junctions, resulting in short-lived fluid pockets between cell–cell contacts. In the blastocoel, the

Figure 2

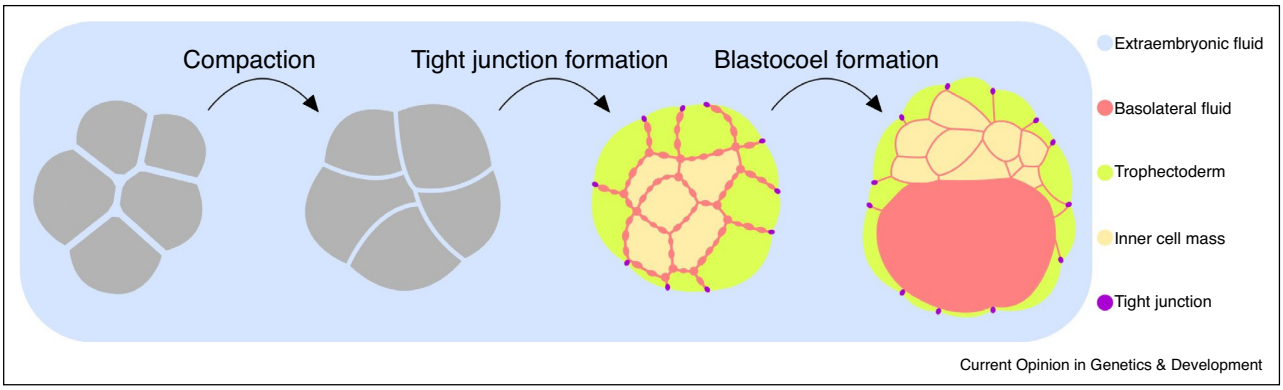

Basolateral lumen formation in the mouse blastocyst.
During compaction, the mouse embryo minimizes the amount of intercellular fluid between cells (blue). After the fourth cleavage, the embryo establishes tight junctions (purple) between surface cells as they become a polarized epithelium (green). This process separates the intercellular (red) and extraembryonic (blue) fluid compartments. Then, directed osmolyte and water transport leads to fluid accumulation in the basolateral compartment [49–51]. The pressurized fluid fractures cell–cell contacts into micron-size lumens. Tensile and adhesive mechanical properties of the tissue constrain the fluid into a single lumen, which becomes the blastocoel [52]. As the blastocoel expands, it mechanically challenges the integrity of the compartment by stretching the epithelial envelope and testing the tight junctions [25,55].

pressure is of similar magnitude, as measured in rabbit [49] and mouse embryos [25••,52••,54], suggesting that basolateral lumens forming at adhesive interfaces can nucleate by hydraulic fracturing of cell–cell contacts.

Micron-size lumens eventually disappear except for one that becomes the blastocoel [52••]. In epithelial monolayers *in vitro*, cracks formed by hydraulic fracturing seal back within minutes through a mechanism that depends on actomyosin contractility [53••]. Analogous fluid gaps can be seen in early Xenopus embryos when contractility is affected [56]. In the mouse embryo, differences in contractility, such as the one existing between TE and ICM cells [57], can guide the fluid towards the most deformable tissue, the TE [52••] (Figure 2). The ability of cell contractility to guide intercellular fluid appears as a general feature for apical [24,58,59] or basolateral compartments [52••]. In addition to contractility, other mechanical properties of tissues can direct basolateral fluid. During hydraulic fracturing, when the fluid percolates the material, it will follow the path of least resistance. When adhesion molecules are patterned, the fluid will collect in the least adhesive part of the embryo [52••]. Studies on the mechanical stability and molecular regulation of junctions under hydrostatic stresses will be needed to understand how basolateral fluids shape tissues. Additional mechanisms, such as localized fluid transport, could be at play and will require further studies. Optogenetic tools, such as light-gated ion channels [60], could constitute a prime instrument in this investigation.

Once the blastocoel is the last remaining lumen, it continues expanding as fluid continues accumulating. This expansion can be counteracted by leakage of the luminal fluid through defective tight junctions [61–63], leading to the collapse of the blastocyst [25••,64]. The origins of this leakage are manifold. Cell divisions can challenge the integrity of the epithelium [25••,54] as daughter cells need to assemble new adherens and tight junctions [65,66•]. Similar to the hydraulic fracturing of adherens junctions, excessive pressure could also rupture the tight junctions of the TE [48,66•]. In addition, the ability of TE cells to stretch could also be limiting, with unusual mechanical behaviors potentially at play to reduce this effect [41•]. Once compromised, the tightness of the epithelium and the homeostasis of the fluid compartments need to be restored, which can be achieved by modulating contractility in fractured adherens and tight junctions [53••,66•]. After tight junction resealing, the epithelium can proceed its expansion until the next collapse [25••,55••]. Cycles of swelling and collapse have been proposed to determine the size of fluid-filled lumens and organs. This principle has been studied in models such as the regenerating hydra [67,68] and the blastocyst [25••,55••]. With blastocysts reaching about 200 μm in diameter for the mouse [69] and up to 3 mm for the rabbit [70], the mammalian embryo constitutes an ideal playground to explore how fluid compartments control organ size.

The basolateral fluid compartment enabling zebrafish gastrulation

During gastrulation, cells sculpt the embryo by establishing the three germ layers and the three axes of the body plan. This process essentially relies on cell–cell contact rearrangements within tissues with varying degrees of cell density and mechanical properties [71,72]. In zebrafish,

this process takes place in a basolateral compartment, which to some extent corresponds to the blastocoel found in other groups of animals such as amphibians [73]. This compartment is bounded by the enveloping layer (EVL), a squamous epithelium which dynamically controls the composition and localization of intercellular fluid [74••,75]. The amount of fluid in this basolateral compartment varies among teleost species, with high cell density in zebrafish and comparably much fewer cells within a voluminous basolateral compartment in killifish [76]. We now discuss three sequential morphogenetic events occurring within the same basolateral fluid compartment delimited by the same boundary: the EVL.

Zebrafish gastrulation begins with doming, a process during which cells intercalate radially to form a dome-like structure on top of the yolk syncytial layer (Figure 3). Changes in the surface tension of the EVL power their rearrangement [74••,77]. Throughout doming, cell density is regulated in time and space. Importantly, cell divisions affect cell–cell contact stability differently at the animal pole and at the equator. Cells near the margin become more packed while those close to the animal pole of the embryo become less dense [78•]. This is accompanied by a redistribution of the intercellular fluid, which becomes more prominent at the animal pole (Figure 3). If the fluid compartment boundary, the EVL, does not function properly, fluid fails to accumulate at the animal pole and doming is impaired [74••,75]. What controls the redistribution of the fluid throughout the compartment and how it affects cell intercalation remain unclear. The friction between cells and the lubricating action of the fluid may constitute interesting aspects to investigate.

After doming is complete, the three germ layers form when mesoderm and endoderm cells break off inward and leave the ectodermal layer [71]. Differences in contractility among germ layer progenitors can drive their separation [79] by controlling cell–cell contact formation and stability [80]. These differences in cell contractility crucially

Figure 3

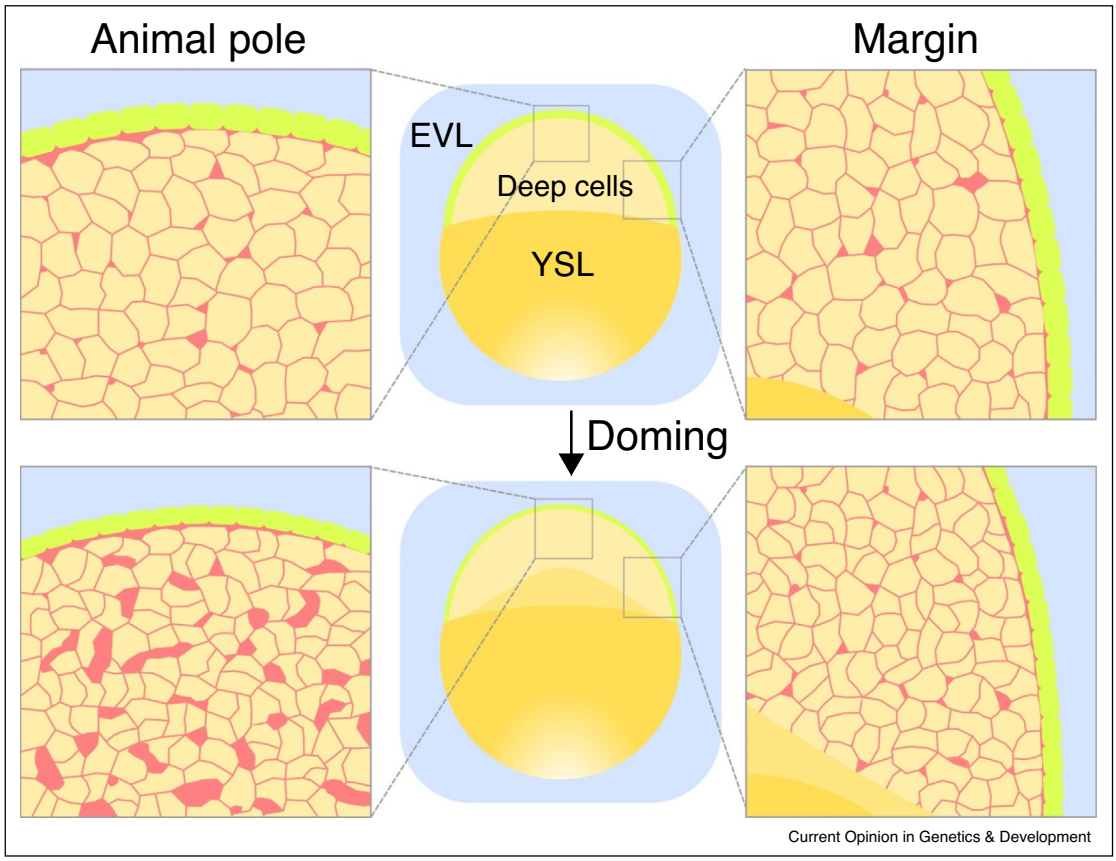

Intercellular fluid distribution during doming in zebrafish embryos.
At the onset of zebrafish gastrulation, surface cells become epithelial, separating the intercellular from the extraembryonic fluid. As this surface epithelium increases surface tension, deep cells are forced to rearrange radially [74] and intercellular fluid follows. However, because cell–cell adhesion is stronger at the margin of the tissue (right) than at the animal pole (left), fluid accumulates at the animal pole and the marginal tissues becomes less hydrated [78]. EVL: enveloping layer. YSL: yolk syncytial layer.

Figure 4

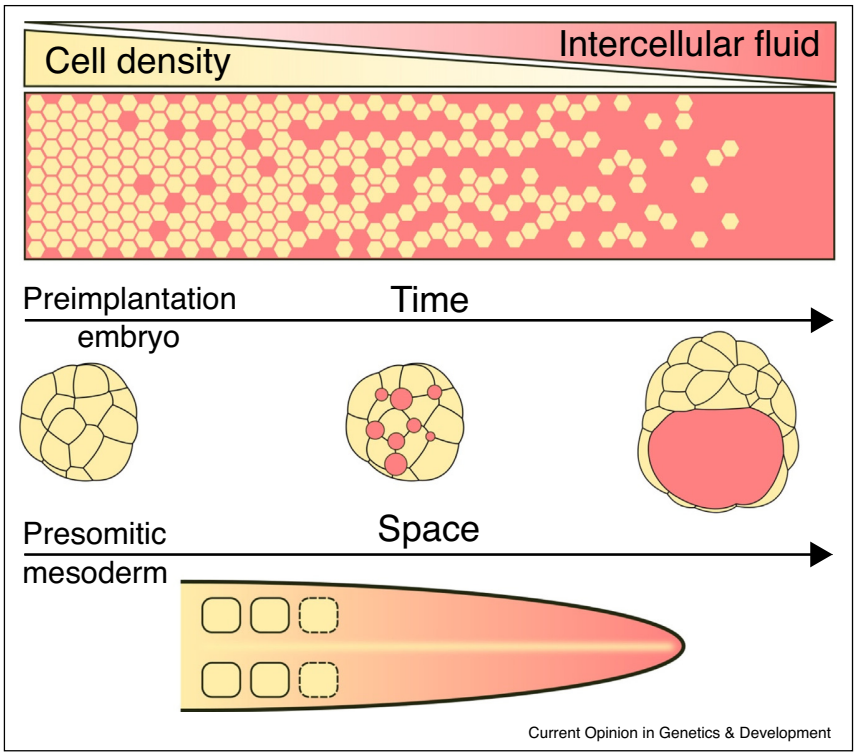

Spatial and temporal control of tissue hydration during morphogenesis.
The level of hydration of tissues changes in space and time during development. The inner cells of the mouse embryo are initially densely packed. Fluid accumulates inside the embryo and separates the inner cells until it begins to collect in one single pocket, which becomes the blastocoel [52]. The blastocoel is now considered a lumen, a purely fluid-filled compartment. Dense tissues such as anterior paraxial mesoderm contain less fluid between their cells than posterior presomitic mesoderm. Cell movement is facilitated in the hydrated posterior and jammed in the anterior [87].

depend on the composition of the intercellular fluid. Changing the osmolarity of the medium can impact cell mechanics [81,82], and osmolarity is a decisive parameter in the sorting of the zebrafish germ layers [6••]. How the composition of the intercellular fluid evolves and how this precisely impacts gastrulation remains to be determined. The function of the EVL in controlling the basolateral fluid composition and volume is likely to be key.

After germ layer separation, the embryo elongates its anteroposterior axis. Concomitantly, paraxial mesoderm cells from the elongating tailbud compact into somites [83,84] (Figure 4). As mesoderm cells progressively incorporate into the presomitic mesoderm, they become less motile [85]. Although cell density appears homogeneous, this translates into higher tissue stress in regions with lower cell–cell rearrangements [86]. This phenomenon was described as a jamming transition during which the tissue becomes frozen due to cells packing themselves into somites [87••]. Another way to describe this phenomenon is that when the tissue becomes too dry, the lack of lubrication prevents cells from rearranging and causes higher tissue stress. If cell–cell adhesion is defective, cells loosen up and the tissue becomes infiltrated with intercellular fluid, concomitantly with the lowering of the tissue stress [88••]. How fluid is managed throughout the tissue during this process and how the hydration state of the tissue favors cell movement will need further investigation. Importantly, changes in the amount of fluid between cells in space and time is concomitant with changes in the mechanical property of the entire tissue [74••,78•,87••]. The relative contribution of the fluid and of the cells to these properties remains to be determined.

Concluding remarks

In this review, we highlight the regulation and function of basolateral fluids during development. While previous research predominantly focused on forces generated directly by cells and tissues, comparably less attention has been given to the invisible fluid, in which cells are immersed. We gather that basolateral compartments can be more or less hydrated in space and time (Figure 4). For example, the tail of the zebrafish embryo becomes dryer as cells pack themselves anteriorly while the

preimplantation embryo becomes more and more hydrated over time until it forms a lumen. These changes in the level of hydration of the tissue impact numerous properties, from the ability of cells to rearrange to the diffusion of morphogens. We hope the recent advances such as the ones brought by studying the early mouse and fish embryos will motivate new research in this direction. This will require developing new tools to visualize the fluid properties and manipulate them, as well as new frameworks to precisely delineate the mechanisms by which tissue hydration controls development.

Conflict of interest statement

Nothing declared.

Acknowledgements

We thank Julien Dumortier, Diane Pelzer and Ines Cristo for fruitful discussions and comments on the draft of the review. Research in the lab of JLM is funded by the ATIP-Avenir program, an ERC-2017-StG 757557 and Labex DEEP (ANR-11-LBX-0044). MS is currently employed by Carl Zeiss SAS.

References

1. Navis A, Nelson CM: **Pulling together: tissue-generated forces that drive lumen morphogenesis**. *Semin Cell Dev Biol* 2016, **55**:139-147.

2. Heisenberg C-P, Bellaïche Y: **Forces in tissue morphogenesis and patterning**. *Cell* 2013, **153**:948-962.

3. Garcia-Bellido A, Ripoll P, Morata G: **Developmental compartmentalisation of the wing disk of Drosophila**. *Nat New Biol* 1973, **245**:251-253.

4. Honda H: **The world of epithelial sheets**. *Dev Growth Differ* 2017, **59**:306-316.

5. Olstad EW, Ringers C, Hansen JN, Wens A, Brandt C, Wachten D, Yaksi E, Jurisch-Yaksi N: **Ciliary beating compartmentalizes cerebrospinal fluid flow in the brain and regulates ventricular development**. *Curr Biol* 2019, **29**:229-241.

6. •• Krens SFG, Veldhuis JH, Barone V, Čapek D, Maître J-L, Brodland GW, Heisenberg C-P: **Interstitial fluid osmolarity modulates the action of differential tissue surface tension in progenitor cell segregation during gastrulation**. *Development* 2017, **144**:1798-1806

This study identifies the role of the osmolarity of intercellular fluid onto cells mechanical properties, which control germ layer separation.

7. Segal MB: **Extracellular and cerebrospinal fluids**. *J Inherit Metab Dis* 1993, **16**:617-638.

8. Pedersen RA, Spindle AI: **Role of the blastocoele microenvironment in early mouse embryo differentiation**. *Nature* 1980, **284**:550-552.

9. Sun G, Teh C, Shen H, Korzh V, Wohland T: **Modulating the expression level of secreted Wnt3 influences cerebellum development in zebrafish transgenics**. *Development* 2015, **142**:3721-3733.

10. Faubel R, Westendorf C, Bodenschatz E, Eichele G: **Cilia-based flow network in the brain ventricles**. *Science* 2016, **353**:176-178.

11. Moreau HD, Blanch-Mercader C, Attia R, Maurin M, Alraies Z, Sanséau D, Malbec O, Delgado M-G, Bousso P, Joanny J-F *et al.*: **Macropinocytosis overcomes directional bias in dendritic cells due to hydraulic resistance and facilitates space exploration**. *Dev Cell* 2019, **49**:171-188.

12. Blasky AJ, Mangan A, Prekeris R: **Polarized protein transport and lumen formation during epithelial tissue morphogenesis**. *Annu Rev Cell Dev Biol* 2015, **31**:575-591.

13. Overeem AW, Bryant DM, van IJzendoorn SCD: **Mechanisms of apical-basal axis orientation and epithelial lumen positioning**. *Trends Cell Biol* 2015, **25**:476-485.

14. Zihni C, Mills C, Matter K, Balda MS: **Tight junctions: from simple barriers to multifunctional molecular gates**. *Nat Rev Mol Cell Biol* 2016, **17**:564-580.

15. Etoc F, Metzger J, Ruzo A, Kirst C, Yoney A, Ozair MZ, Brivanlou AH, Siggia ED: **A balance between secreted inhibitors and edge sensing controls gastruloid self-organization**. *Dev Cell* 2016, **39**:302-315.

16. Müller P, Rogers KW, Jordan BM, Lee JS, Robson D, Ramanathan S, Schier AF: **Differential diffusivity of nodal and lefty underlies a reaction-diffusion patterning system**. *Science* 2012, **336**:721-724.

17. Durdu S, Iskar M, Revenu C, Schieber N, Kunze A, Bork P, Schwab Y, Gilmour D: **Luminal signalling links cell communication to tissue architecture during organogenesis**. *Nature* 2014, **515**:120.

18. Hove JR, Köster RW, Forouhar AS, Acevedo-Bolton G, Fraser SE, Gharib M: **Intracardiac fluid forces are an essential epigenetic factor for embryonic cardiogenesis**. *Nature* 2003, **421**:172-177.

19. Duchemin A-L, Chen M, Vermot J, Li L, Morrisey EE, Morley MP, Scherrer-Crosbie M, Frank DB, Jameson SC, Bamezai S *et al.*: **Hemodynamic forces sculpt developing heart valves through a KLF2-WNT9B paracrine signaling axis**. *Dev Cell* 2017, **43**:274-289.

20. Rutkowski JM, Swartz MA: **A driving force for change: interstitial flow as a morphoregulator**. *Trends Cell Biol* 2007, **17**:44-50.

21. Polacheck WJ, German AE, Kamm RD, Ingber DE, Mammoto A: **Mechanotransduction of fluid stresses governs 3D cell migration**. *Proc Natl Acad Sci U S A* 2014, **111**:2447-2452.

22. Ferreira RR, Vilfan A, Jülicher F, Supatto W, Vermot J: **Physical limits of flow sensing in the left-right organizer**. *eLife* 2017, **6**.

23. Coulombre AJ: **The role of intraocular pressure in the development of the chick eye: II. Control of corneal size**. *AMA Arch Ophthalmol* 1957, **57**:250-253.

24. Gutzman JH, Sive H: **Epithelial relaxation mediated by the myosin phosphatase regulator Mypt1 is required for brain ventricle lumen expansion and hindbrain morphogenesis**. *Development* 2010, **137**:795-804.

25. •• Chan CJ, Costanzo M, Ruiz-Herrero T, Mönke G, Petrie RJ, Bergert M, Diz-Muñoz A, Mahadevan L, Hiiragi T: **Hydraulic control of mammalian embryo size and cell fate**. *Nature* 2019, **571**:112-116

Chan *et al.* describe how epithelial stretching and cell division affect tight junction integrity of the blastocyst. They then evaluate how this controls the pressure and size of the blastocoel.

26. Dubyak GR: **Ion homeostasis, channels, and transporters: an update on cellular mechanisms**. *Adv Physiol Educ* 2004, **28**:143-154.

27. Verkman AS, Mitra AK: **Structure and function of aquaporin water channels**. *Am J Physiol Physiol* 2000, **278**:F13-F28.

28. Finn RN, Cerdà J: **Evolution and functional diversity of aquaporins**. *Biol Bull* 2015, **229**:6-23.

29. Sigurbjörnsdóttir S, Mathew R, Leptin M: **Molecular mechanisms of de novo lumen formation**. *Nat Rev Mol Cell Biol* 2014, **15**:665-676.

30. Datta A, Bryant DM, Mostov KE: **Molecular regulation of lumen morphogenesis**. *Curr Biol* 2011, **21**:R126-R136.

31. Cartwright JHE, Piro O, Tuval I: **Fluid dynamics in developmental biology: moving fluids that shape ontogeny**. *HFSP J* 2009, **3**:77-93.

32. Freund JB, Goetz JG, Hill KL, Vermot J: **Fluid flows and forces in development: functions, features and biophysical principles**. *Development* 2012:1229-1245.

33. Rodriguez-Boulan E, Macara IG: **Organization and execution of the epithelial polarity programme**. *Nat Rev Mol Cell Biol* 2014, **15**:225-242.

34. Müller H-AJ, Hausen P: **Epithelial cell polarity in early Xenopus development**. *Dev Dyn* 1995, **202**:405-420.

35. Danilchik M, Williams M, Brown E: **Blastocoel-spanning filopodia in cleavage-stage *Xenopus laevis*: potential roles in morphogen distribution and detection**. *Dev Biol* 2013, **382**:70-81.

36. Galileo DS, Morrill JB: **Patterns of cells and extracellular material of the sea urchin *Lytechinus variegatus* (Echinodermata; Echinoidea) embryo, from hatched blastula to late gastrula**. *J Morphol* 1985, **185**:387-402.

37. Shahbazi MN, Scialdone A, Skorupska N, Weberling A, Recher G, Zhu M, Jedrusik A, Devito LG, Noli L, Macaulay IC *et al.*: **Pluripotent state transitions coordinate morphogenesis in mouse and human embryos**. *Nature* 2017, **552**:239-243.

38. Peränen J, Rodríguez-Fraticelli AE, Martín-Belmonte F, Datta A, Mostov KE, Bryant DM: **A molecular network for de novo generation of the apical surface and lumen**. *Nat Cell Biol* 2010, **12**:1035-1045.

39. Wang AZ, Ojakian GK, Nelson WJ: **Steps in the morphogenesis of a polarized epithelium. I. Uncoupling the roles of cell-cell and cell-substratum contact in establishing plasma membrane polarity in multicellular epithelial (MDCK) cysts**. *J Cell Sci* 1990, **95**:137-151.

40. Wang AZ, Ojakian GK, Nelson WJ: **Steps in the morphogenesis of a polarized epithelium. II. Disassembly and assembly of plasma membrane domains during reversal of epithelial cell polarity in multicellular epithelial (MDCK) cysts**. *J Cell Sci* 1990, **95**:153-165.

41. • Latorre E, Kale S, Casares L, Gómez-González M, Uroz M, Valon L, Nair RV, Garreta E, Montserrat N, del Campo A *et al.*: **Active superelasticity in three-dimensional epithelia of controlled shape**. *Nature* 2018, **563**:203-208

During lumen expansion, epithelial cells stretch extensively thanks to non-linear elastic behaviors, such as superelasticity. Such an exotic mechanical property presumably relies on different types of cytoskeletons.

42. Zajac O, Raingeaud J, Libanje F, Lefebvre C, Sabino D, Martins I, Roy P, Benatar C, Canet-Jourdan C, Azorin P *et al.*: **Tumour spheres with inverted polarity drive the formation of peritoneal metastases in patients with hypermethylated colorectal carcinomas**. *Nat Cell Biol* 2018, **20**:296-306.

43. Maître JL: **Mechanics of blastocyst morphogenesis**. *Biol Cell* 2017, **109**:323-338.

44. Rossant J: **Making the mouse blastocyst: past, present and future**. *Curr Top Dev Biol* 2016, **117**:275-288.

45. Frankenberg SR, de Barros FRO, Rossant J, Renfree MB: **The mammalian blastocyst**. *Wiley Interdiscip Rev Dev Biol* 2016, **5**:210-232.

46. Maître J-L, Niwayama R, Turlier H, Nédélec F, Hiiragi T: **Pulsatile cell-autonomous contractility drives compaction in the mouse embryo**. *Nat Cell Biol* 2015, **17**:849-855.

47. Korotkevich E, Niwayama R, Courtois A, Friese S, Berger N, Buchholz F, Hiiragi T: **The apical domain is required and sufficient for the first lineage segregation in the mouse embryo**. *Dev Cell* 2017, **40**:235-247.

48. Zenker J, White MD, Gasnier M, Alvarez YD, Lim HYG, Bissiere S, Biro M, Plachta N: **Expanding actin rings zipper the mouse embryo for blastocyst formation**. *Cell* 2018, **173**:776-791.

49. Biggers JD, Borland RM, Powers RD: **Transport mechanisms in the preimplantation mammalian embryo**. *The Freezing of Mammalian Embryos*. Excerpta Medica, Elsevier/North-Holland Amsterdam; 1977:129-146.

50. Manejwala FM, Cragoe EJ, Schultz RM: **Blastocoel expansion in the preimplantation mouse embryo: role of extracellular sodium and chloride and possible apical routes of their entry**. *Dev Biol* 1989, **133**:210-220.

51. Borland RM, Biggers JD, Lechene CP: **Studies on the composition and formation of mouse blastocoele fluid using electron probe microanalysis**. *Dev Biol* 1977, **55**:1-8.

52. •• Dumortier J, Le Verge-Serandour M, Tortorelli A-F, Mielke A, de Plater L, Turlier H, Maitre J-L: **Hydraulic fracturing and active coarsening position the lumen of the mouse blastocyst**. *Science* 2019, **365**:465-468

Dumortier *et al.* propose a mechanism for basolateral lumen formation consisting in the hydraulic fracturing of cell–cell contacts, followed by contractility-directed fluid flow. This framework allows manipulating the positioning of the blastocoel by patterning adhesion or contractility *in vivo*.

53. •• Casares L, Vincent R, Zalvidea D, Campillo N, Navajas D, Arroyo M, Trepat X: **Hydraulic fracture during epithelial stretching**. *Nat Mater* 2015, **14**:343-351

Casares *et al.* describe for the first time hydraulic fracturing of epithelial tissues *in vitro* due to pressurized fluid. Fractures repair within minutes in a contractility-mediated process.

54. Leonavicius K, Royer C, Preece C, Davies B, Biggins JS, Srinivas S: **Mechanics of mouse blastocyst hatching revealed by a hydrogel-based microdeformation assay**. *Proc Natl Acad Sci U S A* 2018, **115**:10375-10380.

55. •• Ruiz-Herrero T, Alessandri K, Gurchenkov BV, Nassoy P, Mahadevan L: **Organ size control via hydraulically gated oscillations**. *Development* 2017, **144**:4422-4427

Through a combination of theoretical modeling and experiments, this study proposes a mechanism controlling fluid-filled organ size. They identify how cycles of abrupt leakage and repair lead to a steady-state lumen size.

56. Park TJ, Kim SK, Wallingford JB: **The planar cell polarity effector protein Wdpcp (Fritz) controls epithelial cell cortex dynamics via septins and actomyosin**. *Biochem Biophys Res Commun* 2015, **456**:562-566.

57. Maître J-L, Turlier H, Illukkumbura R, Eismann B, Niwayama R, Nédélec F, Hiiragi T: **Asymmetric division of contractile domains couples cell positioning and fate specification**. *Nature* 2016, **536**:344-348.

58. Alim K, Andrew N, Pringle A, Brenner MP: **Mechanism of signal propagation in Physarum polycephalum**. *Proc Natl Acad Sci U S A* 2017, **114**:5136-5141.

59. Forouhar AS, Liebling M, Hickerson A, Nasiraei-Moghaddam A, Tsai H-J, Hove JR, Fraser SE, Dickinson ME, Gharib M: **The embryonic vertebrate heart tube is a dynamic suction pump**. *Science* 2006, **312**:751-753.

60. Wietek J, Wiegert JS, Adeishvili N, Schneider F, Watanabe H, Tsunoda SP, Vogt A, Elstner M, Oertner TG, Hegemann P: **Conversion of channelrhodopsin into a light-gated chloride channel**. *Science* 2014, **344**:409-412.

61. Moriwaki K, Tsukita S, Furuse M: **Tight junctions containing claudin 4 and 6 are essential for blastocyst formation in preimplantation mouse embryos**. *Dev Biol* 2007, **312**:509-522.

62. Kim J, Gye MC, Kim MK: **Role of occludin, a tight junction protein, in blastocoel formation, and in the paracellular permeability and differentiation of trophectoderm in preimplantation mouse embryos**. *Mol Cells (Springer Sci Bus Media BV)* 2004, **17**:248-254.

63. Xu J, Kausalya PJ, Phua DCY, Ali SM, Hossain Z, Hunziker W: **Early embryonic lethality of mice lacking ZO-2, but not ZO-3, reveals critical and nonredundant roles for individual zonula occludens proteins in mammalian development**. *Mol Cell Biol* 2008, **28**:1669-1678.

64. Cole RJ: **Cinemicrographic observations on the trophoblast and zona pellucida of the mouse blastocyst**. *J Embryol Exp Morphol* 1967, **17**:481-490.

65. Pinheiro D, Hannezo E, Herszterg S, Bosveld F, Gaugue I, Balakireva M, Wang Z, Cristo I, Rigaud SU, Markova O *et al.*: **Transmission of cytokinesis forces via E-cadherin dilution and actomyosin flows**. *Nature* 2017, **545**:103-107.

66. • Stephenson RE, Higashi T, Erofeev IS, Arnold TR, Leda M, Goryachev AB, Miller AL: **Rho flares repair local tight junction leaks**. *Dev Cell* 2019, **48**:445-459

Stephenson *et al.* identify a novel mechanism of local tight junction repair. They characterize the sequence of molecular events that accompanies this repair process.

67. Kücken M, Soriano J, Pullarkat PA, Ott A, Nicola EM: **An osmoregulatory basis for shape oscillations in regenerating Hydra**. *Biophys J* 2008, **95**:978-985.

68. Fütterer C, Colombo C, Jülicher F, Ott A: **Morphogenetic oscillations during symmetry breaking of regenerating *Hydra vulgaris* cells**. *Europhys Lett* 2003, **64**:137-143.

69. Dickson AD: **The form of the mouse blastocyst**. *J Anat* 1966, **100**:335-348.

70. Lutwak-Mann C: **Some properties of the rabbit blastocyst**. *Development* 1954, **2**:1-13.

71. Williams MLK, Solnica-Krezel L: **Regulation of gastrulation movements by emergent cell and tissue interactions**. *Curr Opin Cell Biol* 2017, **48**:33-39.

72. Rohde LA, Heisenberg C: **Zebrafish gastrulation: cell movements, signals, and mechanisms**. *Int Rev Cytol* 2007, **261**:159-192.

73. Wolpert L, Tickle C: **Principles of Development**. OUP Oxford; 2011.

74. •• Morita H, Grigolon S, Bock M, Krens SFG, Salbreux G, Heisenberg C-P: **The physical basis of coordinated tissue spreading in zebrafish gastrulation**. *Dev Cell* 2017, **40**:354-366

Morita *et al.* characterize the respective roles of the EVL and the deep cells during the doming process. They reveal that the epithelial barrier function of the EVL is essential for the local fluid distribution.

75. Fukazawa C, Santiago C, Park KM, Deery WJ, Gomez de la Torre Canny S, Holterhoff CK, Wagner DS: **poky/chuk/ikk1 is required for differentiation of the zebrafish embryonic epidermis**. *Dev Biol* 2010, **346**:272-283.

76. Reig G, Cerda M, Sepúlveda N, Flores D, Castañeda V, Tada M, Härtel S, Concha ML: **Extra-embryonic tissue spreading directs early embryo morphogenesis in killifish**. *Nat Commun* 2017, **8**:15431.

77. Wallmeyer B, Trinschek S, Yigit S, Thiele U, Betz T: **Collective cell migration in embryogenesis follows the laws of wetting**. *Biophys J* 2018, **114**:213-222.

78. • Petridou NI, Grigolon S, Salbreux G, Hannezo E, Heisenberg C-P: **Fluidization-mediated tissue spreading by mitotic cell rounding and non-canonical Wnt signalling**. *Nat Cell Biol* 2019, **21**:169-178

This study reveals the impact of cell division and adhesion on tissue viscosity during zebrafish doming. The changes of tissue mechanical properties are accompanied by a redistribution of intercellular fluid.

79. Krieg M, Puech P, Käfer J, Graner F, Müller DJ, Heisenberg C: **Tensile forces govern germ-layer organization in zebrafish**. *Nat Cell Biol* 2008, **10**:429-436.

80. Maître J, Berthoumieux H, Frederik S, Krens G, Salbreux G, Jülicher F, Paluch E, Heisenberg C: **Adhesion functions in cell sorting by mechanically coupling the cortices of adhering cells**. *Science* 2012, **338**:253-257.

81. Stewart MP, Helenius J, Toyoda Y, Ramanathan SP, Muller DJ, Hyman AA: **Hydrostatic pressure and the actomyosin cortex drive mitotic cell rounding**. *Nature* 2011, **469**:226-230.

82. Charras GT, Mitchison TJ, Mahadevan L: **Animal cell hydraulics**. *J Cell Sci* 2009, **122**:3233-3241.

83. Pourquié O: **Somite formation in the chicken embryo**. *Int J Dev Biol* 2018, **62**:57-62.

84. Schröter C, Herrgen L, Cardona A, Brouhard GJ, Feldman B, Oates AC: **Dynamics of zebrafish somitogenesis**. *Dev Dyn* 2008, **237**:545-553.

85. Bénazéraf B, Francois P, Baker RE, Denans N, Little CD, Pourquié O: **A random cell motility gradient downstream of FGF controls elongation of an amniote embryo**. *Nature* 2010, **466**:248-252.

86. Serwane F, Mongera A, Rowghanian P, Kealhofer DA, Lucio AA, Hockenbery ZM, Campàs O: **In vivo quantification of spatially varying mechanical properties in developing tissues**. *Nat Methods* 2016, **14**:181-186.

87. •• Mongera A, Rowghanian P, Gustafson HJ, Shelton E, Kealhofer DA, Carn EK, Serwane F, Lucio AA, Giammona J, Campàs O: **A fluid-to-solid jamming transition underlies vertebrate body axis elongation**. *Nature* 2018, **561**:401-405

Mongera *et al.* model the motility gradient observed along the anterior–posterior axis of the presomitic mesoderm as a jamming transition. In this model, cell crowding is affected by cell–cell adhesion which prevents intercellular fluid accumulation, effectively drying the tissue.

1.7 Aims of the thesis

As laid out in chapter 1.4, the morphogenesis of the mammalian preimplantation embryo is to a large extent driven by the contractile forces of the actomyosin cytoskeleton. Previous studies focused on the role of actomyosin contractility in specific steps of the morphogenesis and employed methods that only partially reduce contractility in the preimplantation embryo, such as siRNA knockdown, pharmacological inhibition or partial knockout [115,272,273]. However, no complete genetic myosin knockout, taking into account the maternal and paternal contributions at the beginning of development, had been previously performed that would elucidate the effect of a virtually complete contractility loss on early mouse embryonic development. Therefore, the first aim of this thesis is to study how a complete loss of contractility, achieved by maternal-zygotic knockout of all expressed non-muscle myosin II heavy chain paralogs, will affect preimplantation development and morphogenesis in particular. This approach will also reveal to what extent different non-muscle myosin II heavy chain paralogs contribute to early morphogenesis, which is a question that had not been addressed with previous approaches.

The second part of this work focusses on the role of contractility during blastocoel formation, as its role during the microlumen phase and positioning of the first mammalian lumen is not yet well understood. While differences in blastomere contractility can account for the final positioning of the blastocoel [250], it remains unclear how contractility might affect fluid dynamics during the microlumen phase of blastocoel formation, as it often acts on the timescale of seconds and minutes. Therefore, the aim of this section of the thesis is to asses potential ways in which the actomyosin cytoskeleton might affect fluid exchange between microlumens on a very fast timescale and thereby could play a role in the formation of the first mammalian lumen.

2. RESULTS

2.1 Research paper A: Multiscale analysis of single and double maternal-zygotic *Myh9* and *Myh10* mutants during mouse preimplantation development

Background

Actomyosin is the main driver of mouse preimplantation morphogenesis. As detailed in the introduction, actomyosin contractility is mediated by NM II, whose heavy chains in turn exist as three gene paralogs in mice. In early mouse development, it is involved in processes such as cortical oscillations, compaction, polarization, internalization and blastocoel formation. Besides this, it is also required for cell division and has been implied in the first lineage specification in the mouse embryo.

Despite this important role of actomyosin contractility in early mouse development, no complete NM knockout has performed so far. Previous studies investigating the role of actomyosin contractility either relied on pharmacological blocking of myosin [281], siRNA-mediated knockdown [227], or only maternal knockout of one NMHC paralog [115].

Aim

In this publication, we addressed three questions:

- Which NMHC paralogs are expressed during mouse preimplantation development?
- How does the loss of either of these paralogs affect development?
- How does complete loss of actomyosin contractility affect development when all relevant NMHCs are knocked out?

During the preimplantation phase, the embryo relies on maternal contribution for certain genes [188], making a zygotic knockout only partially effective as its effect might be masked by maternal mRNA/protein. In order to maximally eliminate NMHCs, we employed a maternal-zygotic knockout strategy in this work.

Results

We found that MYH9 and MYH10 are expressed during mouse preimplantation development, with MYH9 being heavily maternally provided and MYH10 being expressed from the morula stage. Maternal-zygotic knockout of *Myh9* resulted in

embryos with reduced cell number, impaired compaction and reduced TE differentiation, while internalization and lumen formation were not impacted. Maternal-zygotic knockout of *Myh10* did not show any phenotype compared to WT. For both *Myh9* and *Myh10*, we did not find any differences in the embryo phenotype between maternal-zygotic and maternal knockout. This implies that the maternal contribution plays a dominant role in NMHC expression, and that the zygotic contribution plays a negligible part in establishing actomyosin contractility. Double maternal-zygotic knockout of *Myh9* and *Myh10* resulted in a drastically reduced cell number, even compared to *Myh9* knockout. Morphogenetic events, such as compaction and internalization, were heavily affected. However, embryos still managed to form a lumen and to correctly differentiate cells, albeit to a reduced degree. In the most extreme cases, double knockout embryos fail all cell divisions, resulting in a single-celled embryo. Nevertheless, single-celled embryos manage to accumulate fluid in intracellular compartments, analogously to blastocoel formation.

Our work elucidates the role of different NMHC paralogs during mouse preimplantation development. It shows how certain aspects of development (differentiation, blastocoel formation) are uncoupled from correct cell number, and can proceed even on a single-cell level. This highlights the robust and highly regulative nature of early mouse development.

Published as:

Markus Frederik Schliffka*, Anna Francesca Tortorelli*, Özge Özgüç, Ludmilla de Plater, Oliver Polzer, Diane Pelzer, Jean-Léon Maître (2021): **Multiscale analysis of single and double maternal-zygotic *Myh9* and *Myh10* mutants during mouse preimplantation development.** eLife 10:e68536
https://doi.org/10.7554/eLife.68536.

*equal contributions

Contributions to the manuscript:

For this manuscript, I and A.F.T. jointly performed all live imaging and immunostaining experiments of WT and *Myh* mutant embryos, as well as the immunostaining of MYH9 and MYH10.

Furthermore, I performed the experiments with MYH9-GFP embryos in Figure 1 - figure supplement 1 and established the blastomere fusion method used in Figure 8, Figure 2 - supplement 2, and Figure 8 - figure supplement 1.
I analyzed the data in Figure 3, Figure 4, Figure 6, Figure 7, Figure 8D,E, Figure 1 - figure supplement 1D, Figure 2 - figure supplement 1B,H,I, Figure 3 - figure supplement 1, Figure 3 - figure supplement 2 and Figure 8 - figure supplement 1D, and performed all statistical analyses. Furthermore, I participated in the writing and editing of the manuscript.

The movies referred to in the article can be found under this link: https://elifesciences.org/articles/68536.
Movie legends can be found together with the online movies, or after the manuscript.

RESEARCH ARTICLE

Multiscale analysis of single and double maternal-zygotic *Myh9* and *Myh10* mutants during mouse preimplantation development

Markus Frederik Schliffka[1,2†], Anna Francesca Tortorelli[1†], Özge Özgüç[1], Ludmilla de Plater[1], Oliver Polzer[1], Diane Pelzer[1], Jean-Léon Maître[1*]

[1]Institut Curie, PSL Research University, Sorbonne Université, Paris, France; [2]Carl Zeiss SAS, Marly-le-Roy, France

Abstract During the first days of mammalian development, the embryo forms the blastocyst, the structure responsible for implanting the mammalian embryo. Consisting of an epithelium enveloping the pluripotent inner cell mass and a fluid-filled lumen, the blastocyst results from a series of cleavage divisions, morphogenetic movements, and lineage specification. Recent studies have identified the essential role of actomyosin contractility in driving cytokinesis, morphogenesis, and fate specification, leading to the formation of the blastocyst. However, the preimplantation development of contractility mutants has not been characterized. Here, we generated single and double maternal-zygotic mutants of non-muscle myosin II heavy chains (NMHCs) to characterize them with multiscale imaging. We found that *Myh9* (NMHC II-A) is the major NMHC during preimplantation development as its maternal-zygotic loss causes failed cytokinesis, increased duration of the cell cycle, weaker embryo compaction, and reduced differentiation, whereas *Myh10* (NMHC II-B) maternal-zygotic loss is much less severe. Double maternal-zygotic mutants for *Myh9* and *Myh10* show a much stronger phenotype, failing most of the attempts of cytokinesis. We found that morphogenesis and fate specification are affected but nevertheless carry on in a timely fashion, regardless of the impact of the mutations on cell number. Strikingly, even when all cell divisions fail, the resulting single-celled embryo can initiate trophectoderm differentiation and lumen formation by accumulating fluid in increasingly large vacuoles. Therefore, contractility mutants reveal that fluid accumulation is a cell-autonomous process and that the preimplantation program carries on independently of successful cell division.

***For correspondence:** jean-leon.maitre@curie.fr

†These authors contributed equally to this work

Competing interest: See page 23

Funding: See page 23

Received: 18 March 2021
Accepted: 28 March 2021
Published: 19 April 2021

Reviewing editor: Edward E Morrisey, University of Pennsylvania, United States

Introduction

During embryonic development, cells execute their genetic program to build organisms with the correct cell fate, shape, position, and number. In this process, the coordination between cell proliferation, differentiation, and morphogenesis is crucial. In mice, the early blastocyst initially consists of 32 cells distributed among the trophectoderm (TE) and inner cell mass (ICM), with squamous TE cells enveloping the ICM and a lumen called the blastocoel (***Frankenberg et al., 2016***; ***Płusa and Piliszek, 2020***; ***Rossant, 2016***). Starting from the zygote, the early blastocyst forms after five cleavage divisions, three morphogenetic movements, and two lineage commitments (***Maître, 2017***; ***White et al., 2018***; ***Zhang and Hiiragi, 2018***). Differentiation and morphogenesis are coupled by the formation of a domain of apical material after the third cleavage (***Ziomek and Johnson, 1980***). The apical domain promotes differentiation into TE by counteracting signals from cell-cell contacts, which control the nuclear localization of the co-transcriptional activator Yap (***Hirate et al., 2013***; ***Nishioka et al., 2009***; ***Wicklow et al., 2014***). The apical domain also guides cell division orientation

(**Dard et al., 2009**; **Korotkevich et al., 2017**; **Niwayama et al., 2019**) and contact rearrangements (**Maître et al., 2016**), which is key for positioning cells at the embryo surface or interior. Morphogenesis and cleavages are concomitant and appear synchronized with compaction starting after the third cleavage, internalization after the fourth, and lumen opening after the fifth. Beyond this apparent coordination, the existence of a coupling between cleavages and morphogenesis requires further investigations.

Actomyosin contractility is a conserved instrument driving animal morphogenesis (**Heisenberg and Bellaïche, 2013**; **Lecuit and Yap, 2015**) and cytokinesis (**Ramkumar and Baum, 2016**). Recent studies have suggested key contributions of actomyosin contractility during all the morphogenetic steps leading to the formation of the blastocyst (**Özgüç and Maître, 2020**). During the 8-cell stage, increased contractility at the cell-medium interface pulls blastomeres together and compacts the embryo (**Maître et al., 2015**). Also, cells form an apical domain that inhibits actomyosin contractility (**Maître et al., 2016**; **Zhu et al., 2017**). During the fourth cleavage, the asymmetric inheritance of this domain leads sister cells to exhibit distinct contractility (**Anani et al., 2014**; **Maître et al., 2016**). This causes the most contractile blastomeres to internalize and adopt ICM fate, while weakly contractile cells are stretched at the surface of the embryo and become TE (**Maître et al., 2016**; **Samarage et al., 2015**). When the blastocoel fluid starts to accumulate, these differences in contractility between ICM and TE cells guide the fluid away from ICM-ICM cell-cell contacts (**Dumortier et al., 2019**). Finally, contractility has been proposed to control the size of the blastocoel negatively by increasing the tension of the TE and positively by reinforcing cell-cell adhesion via mechanosensing (**Chan et al., 2019**). Together, these findings highlight actomyosin as a major engine powering blastocyst morphogenesis.

To change the shape of animal cells, myosin motor proteins contract a network of cross-linked actin filaments, which can be tethered to the plasma membrane, adherens junctions, and/or focal adhesions (**Murrell et al., 2015**). This generates tension, which cells use to change shape and tissue topology (**Clark et al., 2013**; **Salbreux et al., 2012**). Among myosin motors, non-muscle myosin II are the key drivers of cell shape changes (**Zaidel-Bar et al., 2015**). Non-muscle myosin II complexes assemble from myosin regulatory light chains, myosin essential light chains, and non-muscle myosin heavy chains (NMHCs) (**Vicente-Manzanares et al., 2009**). NMHCs are responsible for generating the power stroke and exist in three distinct paralogs in mice and humans: NMHC II-A, II-B, and II-C, encoded by the genes *Myh9/MYH9*, *Myh10/MYH10,* and *Myh14/MYH14* (**Conti et al., 2004**). Distinct paralogs co-assemble into the same myosin mini-filaments (**Beach et al., 2014**) and, to some extent, seem to have redundant actions within the cells. However, several in vitro studies point to specific roles of NMHC paralogs. For example, MYH9 plays a key role in setting the speed of furrow ingression during cytokinesis (**Taneja et al., 2020**; **Yamamoto et al., 2019**) and is essential to drive bleb retraction (**Taneja and Burnette, 2019**). During cell-cell contact formation, MYH9 was found essential for cadherin adhesion molecule clustering and setting contact size while MYH10 would be involved in force transmissions across the junction and would influence contact rearrangements (**Heuzé et al., 2019**; **Smutny et al., 2010**).

These studies at the subcellular level and at a short timescale complement those at the organismal level and at a long timescale. In mice, the zygotic knockout of *Myh14* causes no obvious phenotype with animals surviving to adulthood with no apparent defect (**Ma et al., 2010**), whereas the loss of either *Myh9* (**Conti et al., 2004**) or *Myh10* (**Tullio et al., 1997**) is embryonic lethal. *Myh9* zygotic knockout embryos die at E7.5 due to visceral endoderm adhesion defects (**Conti et al., 2004**). *Myh10* zygotic knockout mice die between E14.5 and P1 because of heart, brain, and liver defects (**Tullio et al., 1997**). In addition, knocking out both *Myh10* and *Myh14* can lead to abnormal cytokinesis (**Ma et al., 2010**). Elegant gene replacement experiments have also revealed insights into partial functional redundancy between *Myh9* and *Myh10* during development (**Wang et al., 2010**). However, despite the prominent role of actomyosin contractility during preimplantation development (**Ma et al., 2010**), the specific functions of NMHC paralogs remain largely unknown. Previous genetic studies have relied on zygotic knockouts (**Conti et al., 2004**; **Ma et al., 2010**; **Tullio et al., 1997**), which do not remove the maternally deposited mRNA and proteins of the deleted genes. This often hides the essential functions of genes during preimplantation morphogenesis, as is the case, for example, with the cell-cell adhesion molecule CDH1 (**Stephenson et al., 2010**). Moreover, NMHCs could have redundant functions, and gene deletions may trigger compensation mechanisms, which would obscure the function of essential genes (**Rossi et al., 2015**).

In this study, we generated maternal-zygotic deletions of single or double NMHC genes to investigate the molecular control of contractile forces during preimplantation development. We used nested time-lapse microscopy to quantitatively assess the effect of maternal-zygotic deletions at different timescales. This reveals the dominant role of MYH9 over MYH10 in generating the contractility that shapes the mouse blastocyst. In addition, double maternal-zygotic *Myh9* and *Myh10* knockout reveals compensatory mechanisms provided by MYH10 in generating enough contractility for cytokinesis when MYH9 is absent. Moreover, the maternal-zygotic knockout of both *Myh9* and *Myh10* can cause embryos to fail all five successive cleavages, resulting in syncytial single-celled embryos. These single-celled embryos nevertheless initiate lineage specification and blastocoel formation by accumulating fluid into intracellular vacuoles. Therefore, double maternal-zygotic NMHC mutants reveal that fluid accumulation in the blastocyst is a cell-autonomous process. Finally, we confirm this surprising finding by fusing all blastomeres of wild-type (WT) embryos, thereby forming single-celled embryos, which accumulate fluid into inflating vacuoles.

Results

NMHC paralogs during preimplantation development

As in humans, the mouse genome contains three genes encoding NMHCs: *Myh9*, *Myh10*, and *Myh14*. To decipher the specific contributions of NMHC paralogs to preimplantation development, we first investigated the expression of *Myh9*, *Myh10*, and *Myh14*.

We performed real-time quantitative PCR (qPCR) at four different stages in order to cover the levels of transcripts at key steps of preimplantation development. We detected high levels of *Myh9* mRNA throughout preimplantation development (***Figure 1A***). Importantly, transcripts of *Myh9* are by far the most abundant among NMHCs at the zygote stage (E0.5), which suggests that *Myh9* is the main NMHC paralog provided maternally. *Myh10* mRNA is detected at very low levels in zygotes before it reaches comparable levels to *Myh9* mRNA at the morula stage (***Figure 1A***). We found that *Myh14* is not expressed during preimplantation stages (***Figure 1A***). Since *Myh14* homozygous mutant mice are viable and show no apparent defects (***Ma et al., 2010***), *Myh14* is unlikely to play an

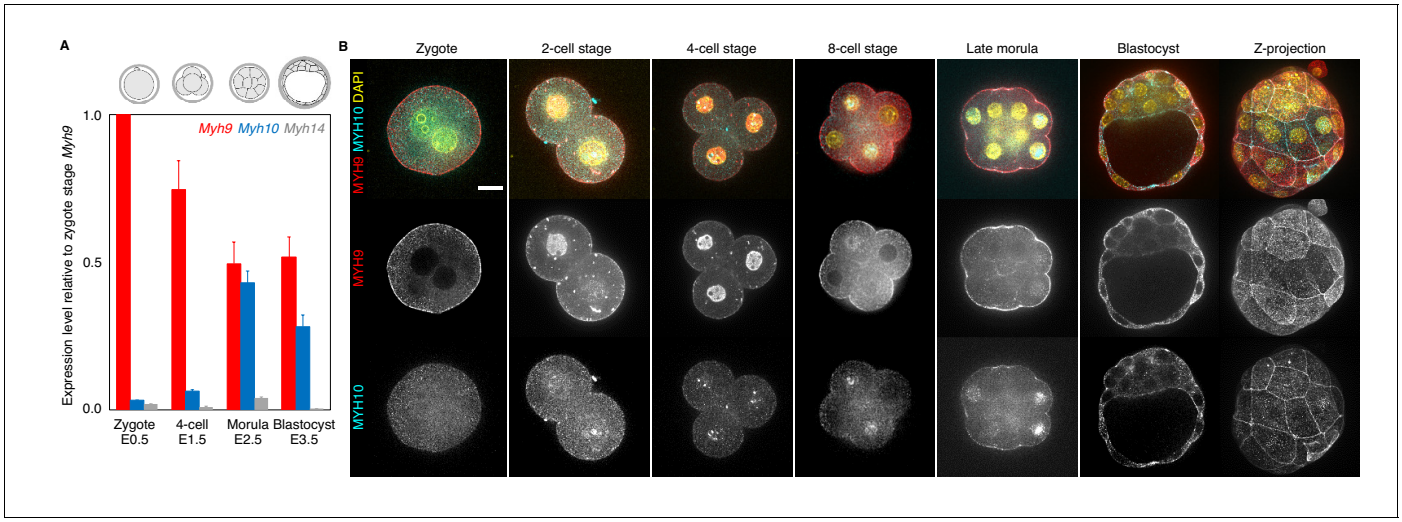

Figure 1. Expression of non-muscle myosin II heavy chain (NMHC) paralogs during preimplantation development. (**A**) RT-qPCR of *Myh9* (red), *Myh10* (blue), and *Myh14* (grey) at the zygote (E0.5, n = 234), four-cell (E1.5, n = 159), morula (E2.5, n = 189), and blastocyst (E3.5, n = 152) stages from six independent experiments. Gene expression is normalized to *Gapdh* and shown as the mean ± SEM fold change relative to *Myh9* at the zygote stage. (**B**) Representative images of immunostaining of NMHC paralogs MYH9 (red) and MYH10 (cyan) throughout preimplantation development. DAPI in yellow. Scale bar, 20 μm.

The online version of this article includes the following figure supplement(s) for figure 1:

Figure supplement 1. Analysis of the expression of non-muscle myosin II heavy chain (NMHC) paralogs during preimplantation development based on single cell RNA sequencing and MYH9-GFP fluorescence.

important role in preimplantation development. These qPCR measurements show similar trends to available mouse single cell RNA sequencing (scRNA-seq) data (***Figure 1—figure supplement 1A***; ***Deng et al., 2014***). In humans, scRNA-seq data indicate similar expression levels between *MYH9* and *MYH10* during preimplantation development and, as in mice, the absence of *MYH14* expression (***Figure 1—figure supplement 1B***; ***Yan et al., 2013***). This points to a conserved regulation of NMHC paralogs in mouse and human preimplantation development.

At the protein level, immunostaining of MYH9 becomes visible at the cortex of blastomeres from the zygote stage onwards (***Figure 1B***). On the other hand, MYH10 becomes detectable at the earliest at the 16-cell stage (***Figure 1B***). Finally, we used transgenic mice expressing endogenously tagged MYH9-GFP to assess the relative parental contributions of MYH9 protein (***Figure 1—figure supplement 1C–D***). Embryos coming from MYH9-GFP females show highest levels of fluorescence at the zygote stage, consistent with our qPCR measurement and scRNA-seq data (***Figure 1A***, ***Figure 1—figure supplement 1A***). MYH9-GFP produced from the paternal allele is detected at the 4-cell stage and increases until blastocyst stage, reaching levels comparable to blastocyst coming from MYH9-GFP females (***Figure 1—figure supplement 1C–D***).

Together, we conclude that MYH9 and MYH10 are the most abundant NMHCs during mouse and human preimplantation development and that MYH9 is heavily maternally provided at both the transcript and protein level in the mouse embryo (***Figure 1***, ***Figure 1—figure supplement 1***).

Preimplantation development of single maternal-zygotic *Myh9* or *Myh10* mutant embryos

Initial studies of *Myh9* or *Myh10* zygotic knockouts have reported that single zygotic knockouts are able to implant, suggesting they are able to form a functional blastocyst (***Conti et al., 2004***; ***Tullio et al., 1997***). A potential lack of phenotype could be due to maternally provided products, which are most abundant in the case of *Myh9* (***Figure 1***, ***Figure 1—figure supplement 1***). To eliminate this contribution, we used $Zp3^{Cre/+}$ mediated maternal deletion of conditional knockout alleles of *Myh9* and *Myh10*. This generated either maternal-zygotic (mz) homozygous or maternal only (m) heterozygous knockout embryos for either *Myh9* or *Myh10*. Embryos were recovered at E1.5, imaged throughout the rest of their preimplantation development, stained, and genotyped once WT embryos reached the blastocyst stage. We implemented a nested time-lapse protocol to image each embryo at the long (every 30 min for about 50 hr) and short (every 5 s for 10 min twice for each embryo around the time of their 8-cell stage) timescales. This imaging protocol allowed us to visualize the effect of actomyosin contractility at multiple timescales, as it is involved in pulsatile contractions, cytokinesis, and morphogenesis, which take place on timescales of tens of seconds, minutes, and hours, respectively (***Maître et al., 2015***; ***Maître et al., 2016***).

The first visible phenotype concerns the zona pellucida (ZP), which encapsulates the preimplantation embryo. WT and maternal *Myh10* mutants have a spherical ZP, whereas maternal *Myh9* mutants show an irregularly shaped ZP (***Figure 2—figure supplement 1A,B***). This suggests a previously unreported role of contractility in the formation of the ZP during oogenesis that is mediated specifically by maternal MYH9. The abnormally shaped ZP could cause long-term deformation of the embryo, as previous studies indicate that the ZP can influence the shape of the embryo at the blastocyst stage (***Kurotaki et al., 2007***; ***Motosugi et al., 2005***).

During compaction, angles formed at the surface of contacting cells increase as blastomeres are pulled into closer contact (***Figure 2A***). In WT embryos, contact angles increase from 87 ± 3˚ to 147 ± 2˚ during the 8-cell stage between the third and the fourth cleavage (mean ± SEM from the end of the last cleavage of the third wave to the first one of the fourth wave, 23 embryos, ***Figure 2A–B***, ***Appendix 1—table 1–2***, ***Figure 2—video 1***), as measured previously (***Maître et al., 2015***; ***Zhu et al., 2017***). In mz*Myh9* embryos, contact angles only grow from 85 ± 2˚ to 125 ± 4˚ (mean ± SEM, 15 embryos, ***Figure 2A–B***, ***Appendix 1—table 1–2***). This reduced ability to compact is in agreement with previous measurements on heterozygous m*Myh9* embryos, which generate a lower surface tension, and therefore cannot efficiently pull cells into closer contact (***Maître et al., 2016***). During the 8-cell stage, mz*Myh10* embryos initially grow their contacts from 87 ± 5˚ to 121 ± 4˚, similarly to mz*Myh9* embryos (mean ± SEM, 11 embryos, ***Figure 2A–B***, ***Appendix 1—table 1***). However, unlike mz*Myh9* embryos, mz*Myh10* embryos continue to increase their contact size and reach compaction levels identical to WT embryos by the end of the 16-cell stage (148 ± 4˚, mean ± SEM, 11 embryos, ***Figure 2A–B***, ***Appendix 1—table 1***). Importantly, heterozygous m*Myh9*

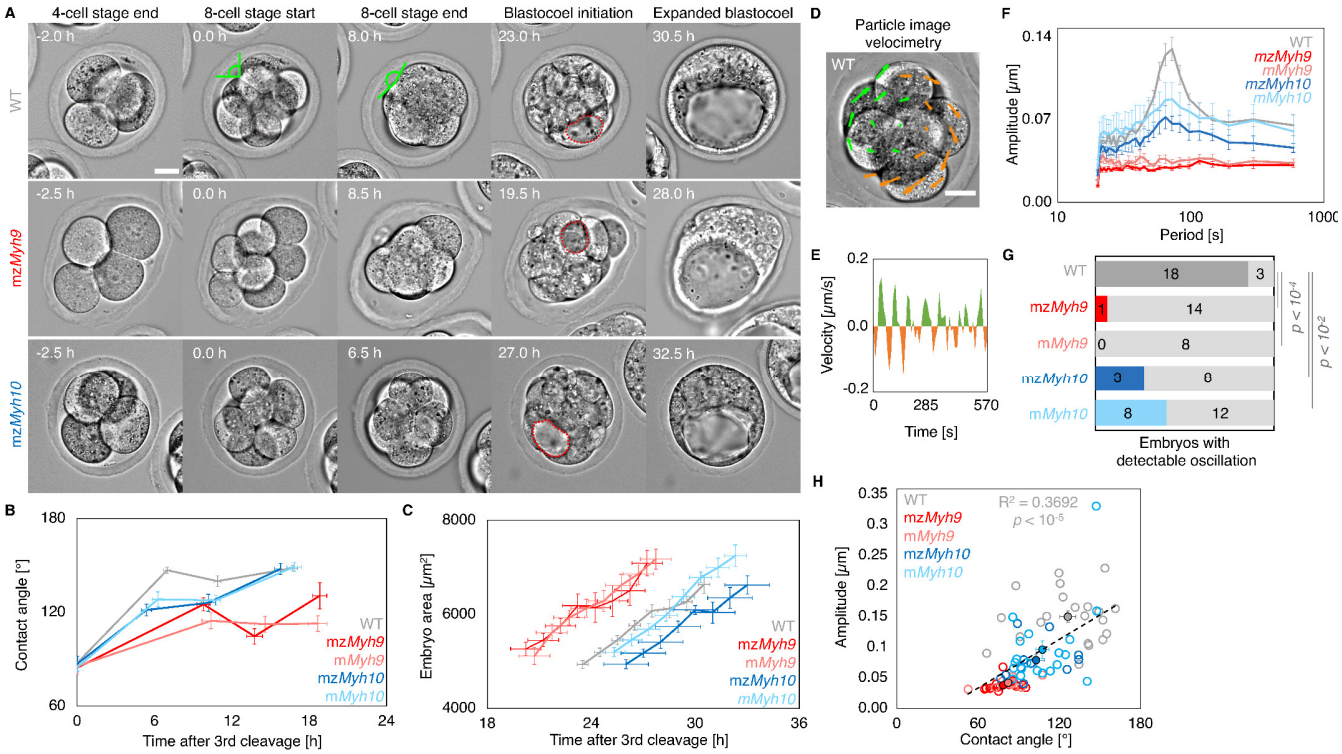

Figure 2. Multiscale analysis of morphogenesis in single maternal-zygotic *Myh9* or *Myh10* mutant embryos. (**A**) Representative images of long-term time-lapse of WT, mz*Myh9*, and mz*Myh10* embryos at the end of the 4-cell stage, start and end of the 8-cell stage, at the initiation of blastocoel formation and early blastocyst stage (see also ***Figure 2—video 1***). Scale bar, 20 μm. Time in hours after the third cleavage. Green lines mark the contact angles increasing during compaction. Dotted red lines indicate the nascent lumen. (**B**) Contact angle of WT (grey, n = 23, 23, 21, 22), mz*Myh9* (red, n = 15, 15, 10, 8), m*Myh9* (light red, n = 8, 8, 8, 3), mz*Myh10* (blue, n = 11, 11, 11, 11), and m*Myh10* (light blue, n = 20, 20, 20, 20) embryos after the third cleavage, before and after the fourth cleavage and before the fifth cleavage. Data show mean ± SEM. Statistical analyses are provided in ***Appendix 1—table 1–2***. (**C**) Embryo growth during lumen formation of WT (grey, n = 20), mz*Myh9* (red, n = 9), m*Myh9* (light red, n = 7), mz*Myh10* (blue, n = 7), and m*Myh10* (light blue, n = 13) embryos measured for seven continuous hours after a lumen of at least 20 μm in diameter is observed. Data show mean ± SEM. (**D**) Representative image of a short-term time-lapse overlaid with a subset of velocity vectors from Particle Image Velocimetry (PIV) analysis. Green for positive and orange for negative Y-directed movement. (**E**) Velocity over time for a representative velocity vector of embryo shown in D and ***Figure 2—video 2***. (**F**) Power spectrum resulting from Fourier transform of PIV analysis of WT (grey, n = 21), mz*Myh9* (red, n = 15), m*Myh9* (light red, n = 8), mz*Myh10* (blue, n = 11), and m*Myh10* (light blue, n = 20) embryos. Data show mean ± SEM. (**G**) Proportion of WT (grey, n = 21), mz*Myh9* (red, n = 15), m*Myh9* (light red, n = 8), mz*Myh10* (blue, n = 11), and m*Myh10* (light blue, n = 20) embryos showing detectable oscillations in their power spectrum (see 'Materials and methods'). Chi^2 p value comparing to WT is indicated. (**H**) Amplitude of oscillation as a function of the mean contact angle for WT (grey, n = 21), mz*Myh9* (red, n = 15), m*Myh9* (light red, n = 8), mz*Myh10* (blue, n = 11), and m*Myh10* (light blue, n = 20) embryos. Open circles show individual embryos and filled circles give mean ± SEM of a given genotype. Pearson's R^2 and p value are indicated. Statistical analyses are provided in ***Appendix 1—table 3***.

The online version of this article includes the following video and figure supplement(s) for figure 2:

Figure supplement 1. Macroscopic shape analysis of maternal-zygotic *Myh9* and *Myh10* mutant embryos.

Figure supplement 2. Morphogenesis of embryos with blastomeres fused at the 4-cell stage.

Figure 2—video 1. Preimplantation development of WT, mz*Myh9*, and mz*Myh10* embryos.
https://elifesciences.org/articles/68536#fig2video1

Figure 2—video 2. Periodic waves of contraction in WT, mz*Myh9*, mz*Myh10*, and mz*Myh9*;mz*Myh10* embryos.
https://elifesciences.org/articles/68536#fig2video2

Figure 2—video 3. Failed cleavage in mz*Myh9* embryos.
https://elifesciences.org/articles/68536#fig2video3

Figure 2—video 4. Preimplantation development of control, ¾, and ½ cell number embryos.
https://elifesciences.org/articles/68536#fig2video4

or m*Myh10* embryos show similar phenotypes to their respective homozygous counterparts (**Figure 2B**, **Appendix 1—table 1–2**), suggesting that maternal loss dominates for both NMHC paralogs and that the paternal allele makes little difference. Together, we conclude that maternal MYH9 is essential for embryos to compact fully, whereas MYH10 only regulates the rate of compaction.

During the 8-cell stage, contractility becomes visible on the short timescale as periodic contractions, which we can use to gauge the specific contribution of NMHCs (**Maître et al., 2015**; **Maître et al., 2016**). We performed particle image velocimetry (PIV) and Fourier analysis to evaluate the period and amplitude of periodic movements (**Figure 2D–F**; **Maître et al., 2015**). While 18/21 WT embryos displayed periodic contractions, these were rarely detected in *Myh9* mutants (1/15 mz*Myh9* and 0/8 m*Myh9* embryos) and occasionally in *Myh10* mutants (3/11 mz*Myh10* and 8/20 m*Myh10* embryos; **Figure 2G**, **Figure 2—video 2**). This suggests that contractility is reduced after maternal loss of *Myh10* and is greatly reduced following maternal loss of *Myh9*. This hierarchy in the phenotypes of the NMHC paralog mutants parallels the one observed on the long timescale during compaction (**Figure 2B**). In fact, we found that the amplitude of periodic contractions correlates with the contact angle across the genotypes we considered (**Figure 2H**, 75 embryos, Pearson's R = 0.608, $p < 10^{-5}$, **Appendix 1—table 3**). This analysis across timescales reveals the continuum between the short-term impact of *Myh9* or *Myh10* loss onto contractile movements and the long-term morphogenesis, as previously observed for internalizing ICM cells (**Maître et al., 2016**).

We also noted that the duration of the 8-cell stage is longer in embryos lacking maternal *Myh9* (9.8 ± 0.5 hr from the third to the fourth wave of cleavages, mean ± SEM, 15 embryos) as compared to WT (7.0 ± 0.3 hr, mean ± SEM, 23 embryos; **Figure 2A,B**, **Appendix 1—tables 1–2**, **Figure 2—video 1**). This is not the case for the duration of the fourth wave of cleavages or the ensuing 16-cell stage, which are similar in these different genotypes (**Appendix 1—table 2**). On the long timescale, longer cell cycles could affect the number of cells in *Myh9* mutants. Indeed, when reaching the blastocyst stage, mz*Myh9* embryos count less than half the number of cells than WT (58.1 ± 2.9 cells in 23 WT embryos, as compared to 25.2 ± 2.8 cells in 15 mz*Myh9* embryos, Mean ± SEM; **Figure 3B**). In the time-lapse movies, we did not observe cell death, which could, in principle, also explain a reduced cell number at the blastocyst stage. On the other hand, we did observe reverting cleavages in maternal *Myh9* mutants (**Figure 2—video 3**), effectively reducing cell number at the blastocyst stage. Loss of MYH9 is likely to cause difficulties during cytokinesis (**Taneja et al., 2020**; **Yamamoto et al., 2019**), which could in turn impact cell cycle progression (**Figure 2B**) and explain the significant reduction in cell number in mz*Myh9* embryos. As for mz*Myh10* embryos, we do not observe any cell cycle delay and count blastocysts with the correct cell number (**Figure 2B** and **Figure 3B**), indicating that MYH9 is the primary NMHC powering cytokinesis during mouse preimplantation development.

The second morphogenetic movement consists in the positioning of cells on the inside of the embryo after the fourth cleavage division to form the first lineages of the mammalian embryo. To see if this process is affected in NMHC mutants, we counted the number of inner and outer cells on immunostaining at the blastocyst stage (**Figure 3A–C**). Despite showing less than half the expected cell number, mz*Myh9* blastocysts show the same proportion of inner and outer cells as WT and mz*Myh10* embryos (**Figure 3C**). This suggests that the remaining contractility is sufficient to drive cell internalization or that oriented cell divisions can mitigate the loss of contractility-mediated internalization (**Korotkevich et al., 2017**; **Maître et al., 2016**; **Niwayama et al., 2019**). Outer and inner cells differentiate into TE and ICM, respectively. To assess whether differentiation is affected in NMHC mutants, we performed immunostaining of TE marker CDX2 and ICM marker SOX2 at the blastocyst stage (**Figure 3A**; **Avilion et al., 2003**; **Strumpf et al., 2005**). mz*Myh10* embryos display negligible reduction in CDX2 and SOX2 levels compared to WT embryos (**Figure 3E–G**). On the other hand, we found that mz*Myh9* embryos show lower levels of CDX2 in their outer cells, as measured here and previously for m*Myh9* embryos at the 16-cell stage (**Figure 3F**; **Maître et al., 2016**), and of SOX2 for inner cells compared to WT embryos (**Figure 3G**). This is caused in part by the presence of individual unspecified cells localized both inside and at the surface of mz*Myh9* embryos (**Figure 3D**). To assess whether delayed cell cycle progression may explain the reduced differentiation, we calculated the correlation between the duration of the 8-cell stage and the levels of CDX2 in the TE and of SOX2 in the ICM. This correlation is poor for all maternal *Myh9* mutants (Pearson's

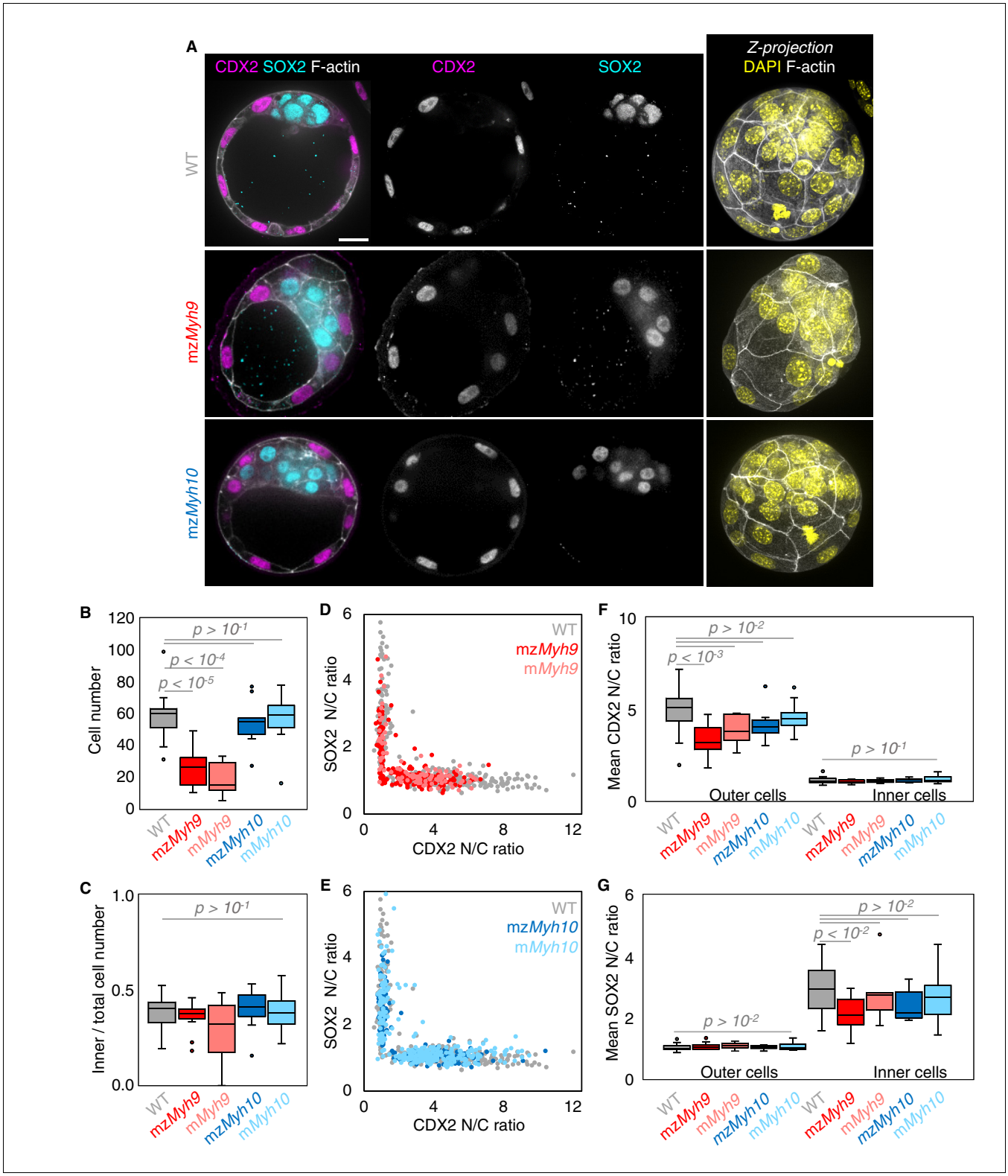

Figure 3. Analysis of TE and ICM lineages in single maternal-zygotic *Myh9* or *Myh10* mutant embryos. (**A**) Representative images of WT, mz*Myh9*, and mz*Myh10* embryos stained for TE and ICM markers CDX2 (magenta) and SOX2 (cyan), DAPI (yellow), and F-actin (grey). The same mutant embryos as in ***Figure 2A*** are shown. Scale bar, 20 µm. (**B-C**) Total cell number (**B**) and proportion of inner cells (**C**) in WT (grey, n = 23), mz*Myh9* (red, n = 15), m*Myh9* (light red, n = 8), mz*Myh10* (blue, n = 11), and m*Myh10* (light blue, n = 19) embryos. (**D-E**) Nuclear to cytoplasmic (N/C) ratio of CDX2 and SOX2

Figure 3 continued on next page

Figure 3 continued

staining for individual cells from WT (grey, n = 345), mz*Myh9* (red, n = 204), m*Myh9* (light red, n = 95), mz*Myh10* (blue, n = 160), and m*Myh10* (light blue, n = 300) embryos. (**F-G**) Average N/C ratio of CDX2 (**F**) and SOX2 (**G**) staining for outer (left) or inner (right) cells from WT (grey, n = 23), mz*Myh9* (red, n = 15), m*Myh9* (light red, n = 8), mz*Myh10* (blue, n = 11), and m*Myh10* (light blue, n = 19) embryos. Mann-Whitney *U* test p values compared to WT are indicated.

The online version of this article includes the following figure supplement(s) for figure 3:

Figure supplement 1. Analysis of YAP localization in maternal-zygotic *Myh9* and *Myh10* mutant embryos.

Figure supplement 2. Lineage specification of embryos with blastomeres fused at the 4-cell stage.

R = −0.193 for CDX2 and −0.076 for SOX2, 22 embryos, $p>10^{-2}$), which does not support reduced differentiation levels due to cell cycle delay.

To assess whether signalling upstream of CDX2 and SOX2 expression is affected in NMHC mutants, we stained embryos for the co-transcriptional activator YAP (***Hirate et al., 2013***; ***Nishioka et al., 2009***; ***Royer et al., 2020***; ***Wicklow et al., 2014***). In WT embryos, YAP is enriched specifically in the nuclei of TE cells (***Figure 3—figure supplement 1***; ***Hirate et al., 2013***; ***Nishioka et al., 2009***; ***Wicklow et al., 2014***). Consistent with CDX2 and SOX2 levels, YAP localization is unaffected in mz*Myh10* mutants and reduced in mz*Myh9* mutants (***Figure 3—figure supplement 1***), as observed previously in m*Myh9* mutants at the 16-cell stage (***Maître et al., 2016***). In the mouse preimplantation embryo, the nuclear localization of YAP is promoted by signals from the apical domain (***Hirate et al., 2013***). ML7 treatment, which inhibits the myosin light chain kinase, suggests that contractility may be required for apical domain formation (***Zhu et al., 2017***). However, immunostaining of apico-basal markers reveals that, as in WT, mz*Myh9* and mz*Myh10* embryos accumulate the apical marker PRKCz at the embryo surface (***Figure 4***; ***Hirate et al., 2013***). Also, basolateral markers such as the adhesion molecule CDH1 or members of the fluid transport machinery, such as the ATP1A1 subunit of the Na/K pump and aquaporin AQP3, are enriched at basolateral membranes of WT, mz*Myh9*, and mz*Myh10* embryos alike (***Figure 4***; ***Barcroft et al., 2003***; ***Barcroft et al., 2004***; ***Dumortier et al., 2019***; ***Stephenson et al., 2010***). Together, these findings suggest that MYH9-mediated contractility is required for the correct expression of lineage markers downstream of YAP but dispensable for the establishment of apico-basal polarity.

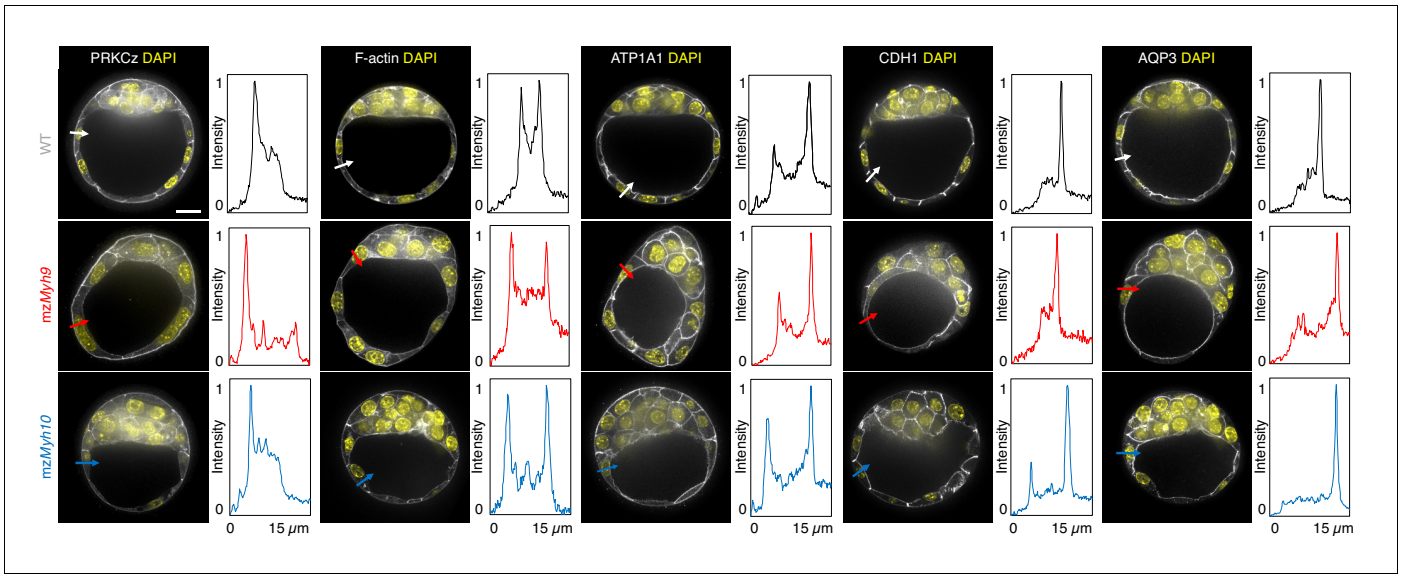

Figure 4. Apico-basal polarity of single maternal-zygotic *Myh9* or *Myh10* mutant embryos. Representative images of WT, mz*Myh9, and* mz*Myh10* embryos stained for apico-basal polarity markers. From left to right: PRKCz, F-actin, ATP1A1, CDH1, and AQP3 shown in grey. Nuclei stained with DAPI are shown in yellow. Intensity profiles of a representative 15 µm line drawn from the embryo surface towards the interior are shown next to each marker and genotype (arrows). Intensities are normalized to each minimal and maximal signals. Scale bar, 20 µm.

Apico-basal polarity is essential for the final morphogenetic step shaping the blastocyst: the formation of the first mammalian lumen. After the fifth cleavage, the growth of the blastocoel inflates and increases the projected area of WT embryos steadily at 3.9 ± 0.5 µm^2/min (mean ± SEM, 20 embryos; ***Figure 2C***, ***Figure 2—video 1***). During lumen formation, mz*Myh9* and mz*Myh10* embryos inflate at 3.9 ± 1.0 and 4.0 ± 0.5 µm^2/min, respectively, which is similar to WT embryos (mean ± SEM, 9 and 7 embryos; Student's *t* test compared to WT $p>10^{-2}$, ***Figure 2C***). This suggests that blastocoel expansion rate is unaffected in NMHC mutants. Importantly, we observe that the time of lumen opening in mz*Myh9* embryos is not delayed compared to WT embryos (***Figure 2A–C***). In fact, relative to the time of third cleavage, the lumen inflates on average at an earlier stage in mz*Myh9* embryos than in WT (***Figure 2C***). Some mz*Myh9* embryos begin inflating their lumen before the fifth wave of cleavages (5/11; ***Figure 2—video 1***), while all WT and mz*Myh10* embryos begin lumen formation after the first cleavages of the fifth wave. This argues against mz*Myh9* embryos having a global delay in their development, despite their longer cell cycles, lower cell number (***Figure 2B*** and ***Figure 3B***), and impaired differentiation (***Figure 3D,F–G***). Finally, when the lumen becomes sufficiently large, embryos come into contact with the ZP. 3D segmentation of blastocysts reveals that embryos with mutated maternal *Myh9* alleles become less spherical than those with a WT allele (***Figure 2—figure supplement 1C–F***). In fact, the shape of the ZP of mutant embryos at the 2-cell stage correlates with the shape of embryos at the blastocyst stage (***Figure 2—figure supplement 1G***; 67 embryos from all genotypes combined but WT, Pearson's R = −0.739, $p<10^{-2}$), which suggests that the misshapen ZP could deform the embryo. This is consistent with previous studies reporting on *Myh9* mutant embryos being more deformable than WT (***Maître et al., 2016***) and on the influence of the ZP on the shape of the blastocyst (***Kurotaki et al., 2007***; ***Motosugi et al., 2005***). Experimental deformation of the embryo was reported to affect cell fate (***Niwayama et al., 2019***; ***Royer et al., 2020***). In the range of deformation of the ZP observed in mutant embryos, we found weak correlations between the shape of the ZP and CDX2 or SOX2 levels (***Figure 2—figure supplement 1H–I***, CDX2 in outer cells of 77 embryos from all genotypes combined but WT, Pearson's R = 0.315, $p<10^{-2}$, SOX2 in the inner cells of 58 embryos, Pearson's R = 0.223, $p > 10^{-1}$). This suggests that defects in lineage specification of maternal *Myh9* mutant embryos do not simply result from the deformation of these blastocysts by their ZP. From this multiscale analysis, we conclude that maternal-zygotic loss of *Myh9* or *Myh10* has little impact on lumen formation and that maternal loss of *Myh9* impacts the shape of the blastocyst indirectly by its initial effect on the structure of the ZP.

Maternal *Myh9* mutants show defective cytokinesis and reduced cell number, which could constitute the cause for the defects in morphogenesis and lineage specification. To separate the effects of impaired contractility and defective cell divisions, we decided to reduce cell number by fusing blastomeres of WT embryos together. Reducing cell number by ¼ or ½ at the 4-cell stage results in embryos compacting with the same magnitude and forming a lumen concomitantly to control embryos (***Figure 2—figure supplement 2A–C***, ***Figure 2—video 4***, ***Figure 3—figure supplement 2B***). Also, embryos with reduced cell numbers differentiate into TE and ICM identically to control embryos as far as lineage proportions and fate marker levels are concerned (***Figure 3—figure supplement 2A,C–E***). Therefore, the morphogenesis and lineage specification defects observed in maternal Myh9 mutants are not likely to result simply from cytokinesis defects and their impact on cell number.

Together, these analyses reveal the critical role of MYH9 in setting global cell contractility on short and long timescales in order to effectively drive compaction, cytokinesis, and lineage specification. Comparably, the function of MYH10 during early blastocyst morphogenesis is less prominent. Importantly, the similarity of maternal homozygous and maternal heterozygous mutants indicates that the preimplantation embryo primarily relies on the maternal pools of MYH9. We conclude that maternally provided MYH9 is the main NMHC powering actomyosin contractility during early preimplantation development.

Preimplantation development of double maternal-zygotic *Myh9;Myh10* mutants

Despite MYH9 being the main NMHC provided maternally, the successful cleavages, shape changes, and differentiation observed in m*Myh9* and mz*Myh9* embryos suggest that some compensation by MYH10 could occur in these embryos. To test for compensations between the two NMHC paralogs

expressed during preimplantation development, we generated double maternal-zygotic *Myh9* and *Myh10* knockout (mz*Myh9*;mz*Myh10*) embryos.

Nested time-lapse revealed that mz*Myh9*;mz*Myh10* embryos fail most attempts of cytokinesis (***Figure 5A***, ***Figure 5—video 1***). In addition to failed cytokinesis, mz*Myh9*;mz*Myh10* embryos show increased cell cycle durations, which are more severe than those for mz*Myh9* embryos (***Figure 5A–B***, ***Appendix 1—table 1–2***). This results in mz*Myh9*;mz*Myh10* embryos with only 2.9 ± 0.5 cells when reaching the blastocyst stage (***Figure 6B***). In fact, they occasionally develop into blastocyst-stage embryos consisting of only one single cell (1/8 embryos). Of those which succeed in dividing at least once, compaction after the third cleavage is weak with contact angles for mz*Myh9*;mz*Myh10* embryos capping at 117 ± 4˚ compared to 147 ± 2˚ for WT (mean ± SEM, 3 and 23 embryos; ***Figure 5B***, ***Appendix 1—table 1***, ***Figure 5—video 1***). Consistent with previous observations, periodic contractions are undetectable in any of the double mutants that we analyzed (***Figure 5D–E***, ***Figure 2—video 2***). Together, this indicates that double maternal-zygotic *Myh9* and *Myh10* mutants generate extremely weak contractile forces compared to WT and single maternal-zygotic *Myh9* or *Myh10* mutants.

When investigating fate specification (***Figure 6***), CDX2 is present in 5/7 embryos as compared to all the 23 WT embryos we analyzed (***Figure 6F***). SOX2 is only detected when embryos succeed in internalizing at least one cell (***Figure 6A,C–E and G***). No maternal *Myh9;Myh10* mutant embryo consisting of only two cells contained an inner cell, half of embryos with 3–5 cells contained a single inner cell, and all embryos with six cells or more contained inner cells (***Figure 6D***). Moreover, the levels of CDX2 in outer cells are reduced compared to WT embryos, as observed previously for single maternal-zygotic *Myh9* mutants. Consistently, YAP is enriched in the nucleus of outer cells, albeit at lower levels than in WT (***Figure 3—figure supplement 1***). As for single mutants, the apical marker PRKCz, F-actin, the cell-cell adhesion molecule CDH1, and members of the fluid-pumping machinery ATP1A1 and AQP3 are correctly apico-basally polarized in double mutants (***Figure 7***). The presence of CDX2, nuclear YAP, and the correct organization of apico-basal polarity suggest that mz*Myh9;* mz*Myh10* embryos can initiate differentiation into TE, the epithelium responsible for making the blastocoel. The ability of mz*Myh9;*mz*Myh10* embryos to create de novo a functional polarized epithelium is further supported by the fact that they can eventually proceed with polarized fluid accumulation and create a blastocoel (***Figure 5A***, ***Figure 5—video 1***). As observed in single maternal *Myh9* mutants, mz*Myh9;*mz*Myh10* embryos are not delayed to initiate lumen formation despite their extended cell cycles (***Figure 5C***, ***Figure 5—video 1***). Also, we measure that mutant embryos grow at rates that are similar to WT ones (5.8 ± 1.5 and 3.9 ± 0.5 μm^2/min, mean ± SEM, 5 and 20 embryos, Student's *t* test $p>10^{-2}$; ***Figure 5C***). This indicates that contractility does not influence the initial growth rate of the blastocoel and that blastocoel formation does not require powerful actomyosin contractility.

Finally, we measure similar metrics for all single and double heterozygous *Myh9* and *Myh10* mutant embryos (***Figure 5***, ***Figure 6***, ***Appendix 1—table 1***), indicating once again that maternal contributions predominantly set the contractility for preimplantation development. We conclude that after the maternal loss of both *Myh9* and *Myh10*, contractility is almost entirely abolished. This effect is much stronger than that after the loss of maternal MYH9 only and suggests that, in single maternal *Myh9* mutants, MYH10 can compensate significantly, which we would not anticipate from our previous single mz*Myh10* knockout analysis. Therefore, despite MYH9 being the main engine of preimplantation actomyosin contractility, MYH10 ensures a substantial part of blastocyst morphogenesis in the absence of MYH9. The nature and extent of this compensation will need further characterization.

Preimplantation development of single-celled embryos

Embryos without maternal MYH9 and MYH10 can fail all successive cleavages when reaching the time of the blastocyst stage (18/53 embryos, all *Myh9* and *Myh10* mutant genotypes combined across seven experiments; ***Figure 8A***, ***Figure 8—video 1***). In single-celled embryos, multiple cleavage attempts at intervals of 10–20 hr can be observed, suggesting that the cell cycle is still operational in those embryos (***Figure 5—video 1***). This is further supported by the presence of multiple large nuclei in single-celled embryos, indicative of preserved genome replication (***Figure 8C***). Interestingly, these giant nuclei contain CDX2 and YAP, but no SOX2, suggesting that, in addition to the cell cycle, the lineage specification program is still partially operational (***Figure 8C–E***, ***Figure 3—***

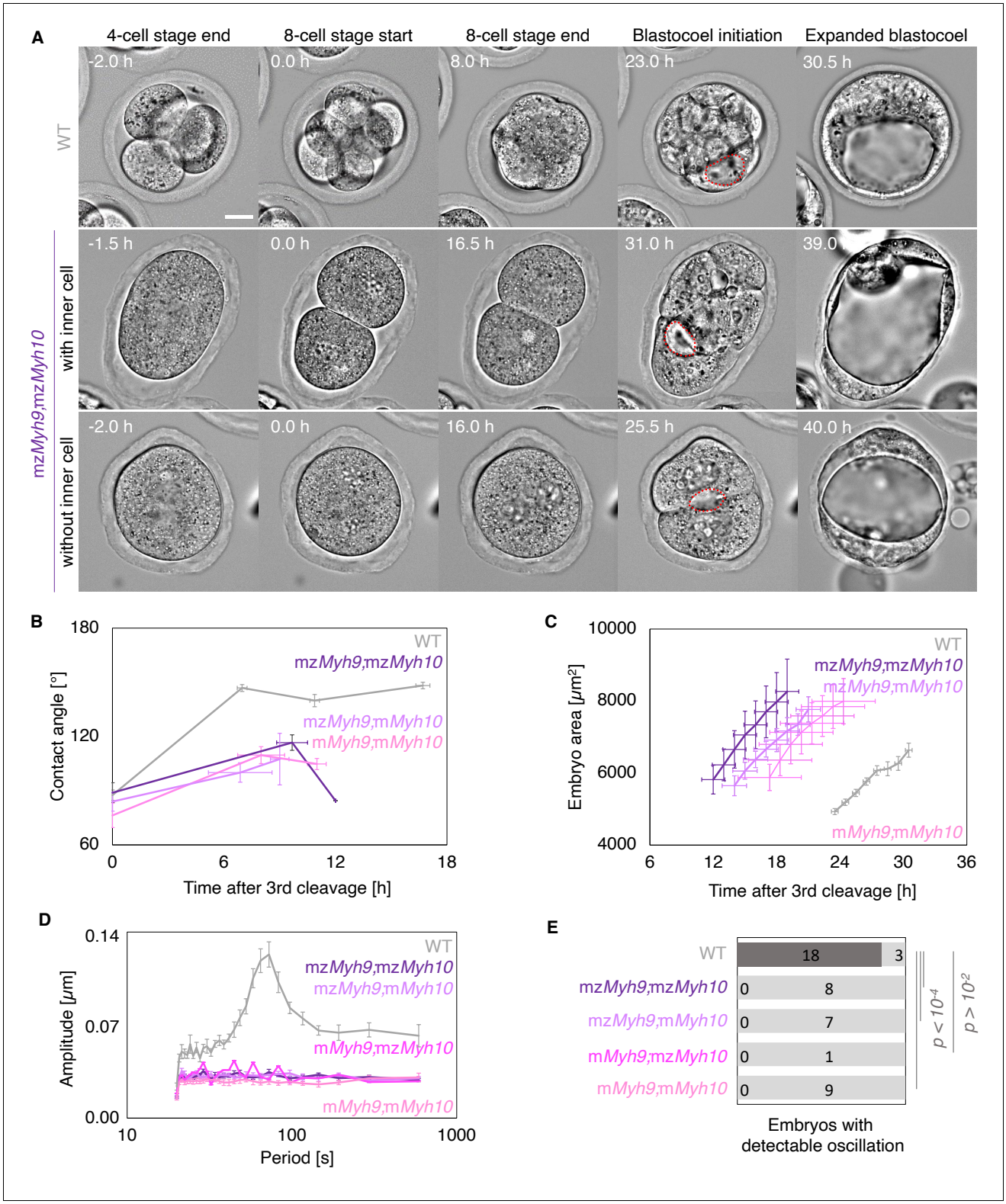

Figure 5. Multiscale analysis of morphogenesis in double maternal-zygotic *Myh9* and *Myh10* mutant embryos. (**A**) Representative images of long-term time-lapse of WT and mz*Myh9*;mz*Myh10* embryos at the end of the 4-cell stage, start and end of the 8-cell stage, at the initiation of blastocoel formation, and early blastocyst stage (***Figure 5—video 1***). The middle row shows an embryo that cleaved once at the time of the third cleavage and twice at the time of the fourth cleavage, which produces an embryo with one inner cell. The bottom row shows an embryo that cleaved once at the

Figure 5 continued on next page

Figure 5 continued

time of the fourth cleavage, which produces an embryo without inner cell. Scale bar, 20 µm. (**B**) Contact angle of WT (grey, n = 23, 23, 21, 22), mz*Myh9;*mz*Myh10* (purple, n = 7, 3, 1), mz*Myh9;*m*Myh10* (lilac, n = 7, 4, 2), and m*Myh9;*m*Myh10* (bubblegum, n = 7, 5, 3) embryos after the third cleavage, before and after the fourth cleavage, and before the fifth cleavage, when available. Data show mean ± SEM. Statistical analyses are provided in ***Appendix 1—table 1–2***. (**C**) Embryo growth during lumen formation for WT (grey, n = 20), mz*Myh9;*mz*Myh10* (purple, n = 5), mz*Myh9;*m*Myh10* (lilac, n = 6), and m*Myh9;*m*Myh10* (bubblegum, n = 6) embryos measured for seven continuous hours after a lumen of at least 20 µm is observed. Data show mean ± SEM. (**D**) Power spectrum resulting from Fourier transform of PIV analysis of WT (grey, n = 21), mz*Myh9;*mz*Myh10* (purple, n = 8), mz*Myh9;* m*Myh10* (lilac, n = 7), m*Myh9;*mz*Myh10* (pink, n = 1), and m*Myh9;*m*Myh10* (bubblegum, n = 9) embryos. Data show mean ± SEM. (**E**) Proportion of WT (grey, n = 21), mz*Myh9;*mz*Myh10* (purple, n = 8), mz*Myh9;*m*Myh10* (lilac, n = 7), m*Myh9;*mz*Myh10* (pink, n = 1), and m*Myh9;*m*Myh10* (bubblegum, n = 9) embryos showing detectable oscillations in their power spectrum. Chi^2 test p value compared to WT is indicated.

The online version of this article includes the following video for figure 5:

Figure 5—video 1. Preimplantation development of mz*Myh9;*mz*Myh10* embryos.
https://elifesciences.org/articles/68536#fig5video1

figure supplement 1). Strikingly, we also observed that at the time of blastocoel formation, single-celled maternal *Myh9* and *Myh10* mutant embryos begin to swell to sizes comparable to normal blastocysts (***Figure 8A–B***, ***Figure 8—video 1***). Single-celled embryos then form, within their cytoplasm, tens of fluid-filled vacuolar compartments, which can inflate into structures comparable in size to the blastocoel (***Figure 8A and C***, ***Figure 8—video 1***). The membrane of these cytoplasmic vacuoles contains the fluid pumping machinery ATP1A1 and AQP3, which is specific of basolateral membranes in multicellular embryos of all considered genotypes (***Figure 7***; ***Barcroft et al., 2003***; ***Barcroft et al., 2004***). This indicates that single-celled embryos are able to establish apico-basal polarity and to direct fluid pumping into a basolateral compartment despite the absence of neighbouring cells. When measuring the growth rates of single-celled embryos, we found that they are comparable to the ones of multiple-celled mutant embryos or WT (4.1 ± 0.8, 5.8 ± 1.5, and 3.9 ± 0.5 μm^2/min, mean ± SEM, 4, 5, and 20 embryos, Student's *t* test $p > 10^{-2}$; ***Figure 8B***), indicating that they are able to accumulate fluid as fast as embryos composed of multiple cells. Therefore, single-celled embryos are able to initiate TE differentiation and display some attributes of epithelial function. Unexpectedly, this also indicates that fluid accumulation during blastocoel formation is cell-autonomous. Together, this further indicates that the developmental program entailing morphogenesis and lineage specification carries on independently of successful cleavages.

To further test whether fluid accumulation is cell-autonomous without disrupting actomyosin contractility, we fused all blastomeres at the late morula stage before lumen formation (***Figure 8—figure supplement 1A***, ***Figure 8—video 2***). The nuclei from the fused cells displayed high CDX2 and low SOX2 levels, which indicates that fused embryos retain a TE phenotype (***Figure 8—figure supplement 1C–E***). Moreover, similarly to single-celled embryos resulting from the loss of contractility, single-celled embryos resulting from cell fusion grew in size at rates similar to those of control embryos while forming large fluid-filled vacuoles (3.3 ± 0.4 and 3.7 ± 0.4 μm^2/min, 7 and 8 embryos, Student's *t* test $p > 10^{-2}$; ***Figure 8—figure supplement 1A–B***, ***Figure 8—video 2***). This further confirms that the initiation of fluid accumulation and its rate during blastocoel morphogenesis can rely entirely on transcellular transport and are independent from cell-cell contacts and its associated paracellular transport.

Together, our experiments with single and double maternal-zygotic NMHC knockout embryos reveal that, while MYH9 is the major NMHC powering sufficient actomyosin contractility for blastocyst morphogenesis, MYH10 can significantly compensate the effect of MYH9 loss onto cytokinesis and compaction. Mutant and fused embryos also reveal that even blastocyst-stage embryos made out of a single cell can proceed with the preimplantation program in a timely fashion, as they differentiate into TE and build features of the blastocyst, such as the inflation of fluid-containing compartments. Finally, myosin mutants and fused embryos reveal that the developmental program entailing morphogenesis and lineage specification carries on independently of successful cleavages. This further demonstrates the remarkable regulative capacities of the early mammalian embryo.

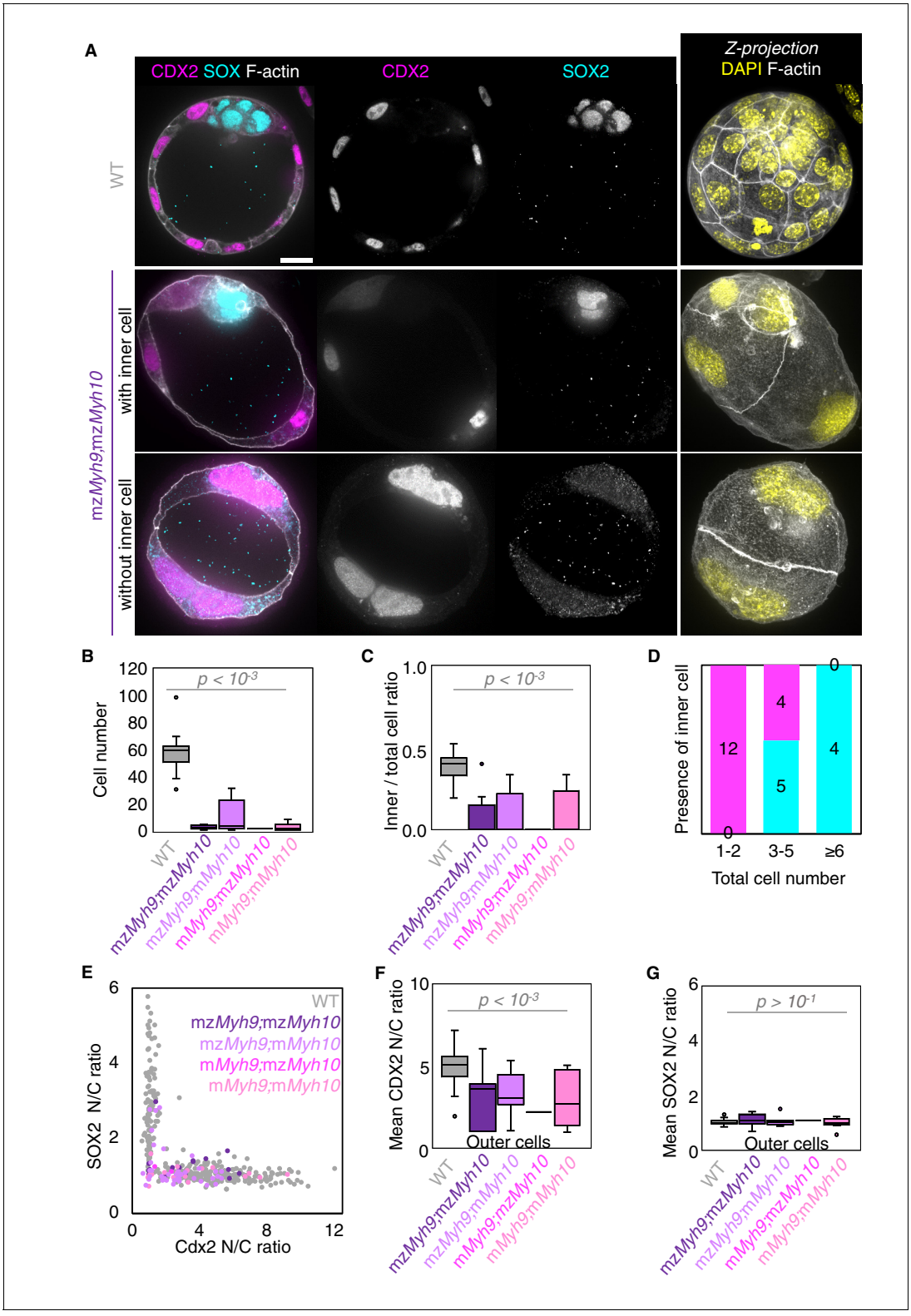

Figure 6. Analysis of TE and ICM lineage in double maternal-zygotic *Myh9* and *Myh10* mutant embryos. (**A**) Representative images of WT and mz*Myh9;*mz*Myh10* embryos stained for TE and ICM markers CDX2 (magenta) and SOX2 (cyan), DAPI (yellow), and F-actin (grey). The same mutant embryos as in ***Figure 5A*** are shown. Scale bar, 20 µm. (**B-C**) Total cell number (**B**) and proportion of inner cells (**C**) in WT (grey, n = 23), mz*Myh9;*mz*Myh10* (purple, n = 8), mz*Myh9;*m*Myh10* (lilac, n = 7), m*Myh9;*mz*Myh10* (pink, n = 1), and m*Myh9;*m*Myh10* (bubblegum, n = 9) embryos. (**D**) Number of maternal *Myh9;*

Figure 6 continued on next page

Figure 6 continued

Myh10 mutant embryos with (cyan) or without (magenta) inner cells as a function of the total number of cells. (**E**) Nuclear to cytoplasmic (N/C) ratio of CDX2 and SOX2 staining for individual cells from WT (grey, n = 345), mz*Myh9;*mz*Myh10* (purple, n = 17), mz*Myh9;*m*Myh10* (lilac, n = 41), m*Myh9;* mz*Myh10* (pink, n = 2), and m*Myh9;*m*Myh10* (bubblegum, n = 21) embryos. (**F-G**) N/C ratio of CDX2 (**F**) and SOX2 (**G**) staining for outer cells from averaged WT (grey, n = 23), mz*Myh9;*mz*Myh10* (purple, n = 8), mz*Myh9;*m*Myh10* (lilac, n = 7), m*Myh9;*mz*Myh10* (pink, n = 1), and m*Myh9;*m*Myh10* (bubblegum, n = 9) embryos. Mann-Whitney *U* test p values compared to WT are indicated.

Discussion

Recent studies have described the critical role of actomyosin contractility in establishing the blastocyst (***Anani et al., 2014***; ***Chan et al., 2019***; ***Dumortier et al., 2019***; ***Maître et al., 2015***; ***Maître et al., 2016***; ***Samarage et al., 2015***; ***Zenker et al., 2018***; ***Zhu et al., 2017***). To understand the molecular regulation of this crucial engine of preimplantation development, we have eliminated the maternal and zygotic sources of the NMHCs MYH9 and MYH10 individually and jointly. Maternal-zygotic mutants reveal that actomyosin contractility is primarily mediated by maternal MYH9, which is found most abundantly. Comparatively, loss of *Myh10* has a mild impact on preimplantation development. Nevertheless, double maternal-zygotic mutants reveal that in the absence of MYH9, MYH10 plays a critical role in ensuring sufficient contractility to power cleavage divisions. Furthermore, double maternal-zygotic mutants bring to light the remarkable ability of the preimplantation embryo to carry on with its developmental program even when reduced to a single-celled embryo. Indeed, single-celled embryos, obtained from NMHC mutants or from the fusion of all cells of WT embryos, display evident signs of differentiation and initiate lumen formation by accumulating fluid in a timely fashion. Therefore, NMHC mutants and fused embryos reveal that the developmental program entailing morphogenesis and lineage specification carries on independently of successful cleavages.

Despite the importance of contractility during the formation of the blastocyst, maternal-zygotic mutants of NMHCs are yet to be characterized. The phenotypes we report here further confirm some of the previously proposed roles of contractility during preimplantation development and provide molecular insights on which NMHC paralog powers contractility. We observed reduced compaction when *Myh9* is maternally deleted and slower compaction when *Myh10* is deleted (***Figure 2A–B***). This is in agreement with cell culture studies, in which *Myh9* knockdown reduces

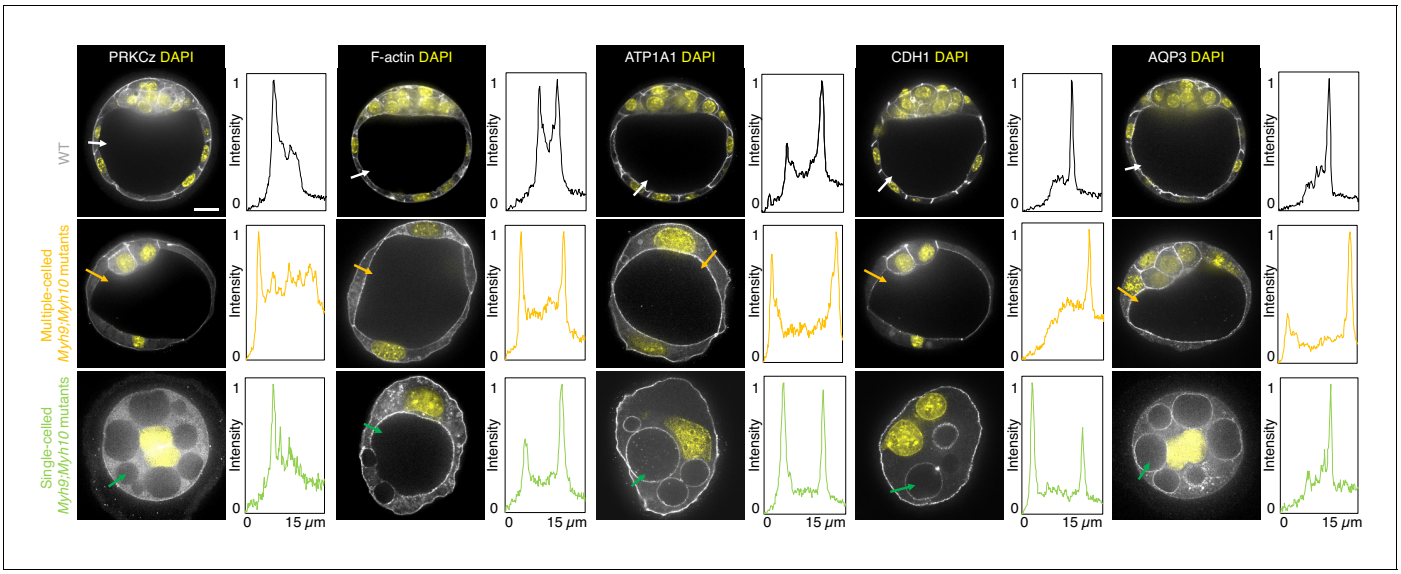

Figure 7. Apico-basal polarity of maternal *Myh9;Myh10* mutant embryos composed of multiple cells or a single cell. Representative images of WT, multiple- or single-celled *Myh9;Myh10* mutant embryos stained for apico-basal polarity markers. From left to right: PRKCz, F-actin, ATP1A1, CDH1, and AQP3 shown in grey. Nuclei stained with DAPI shown in yellow. Intensity profiles of a representative 15 µm line drawn from the embryo surface towards the interior are shown next to each marker and genotype (arrows). Intensities are normalized to each minimal and maximal signals. Scale bar, 20 µm.

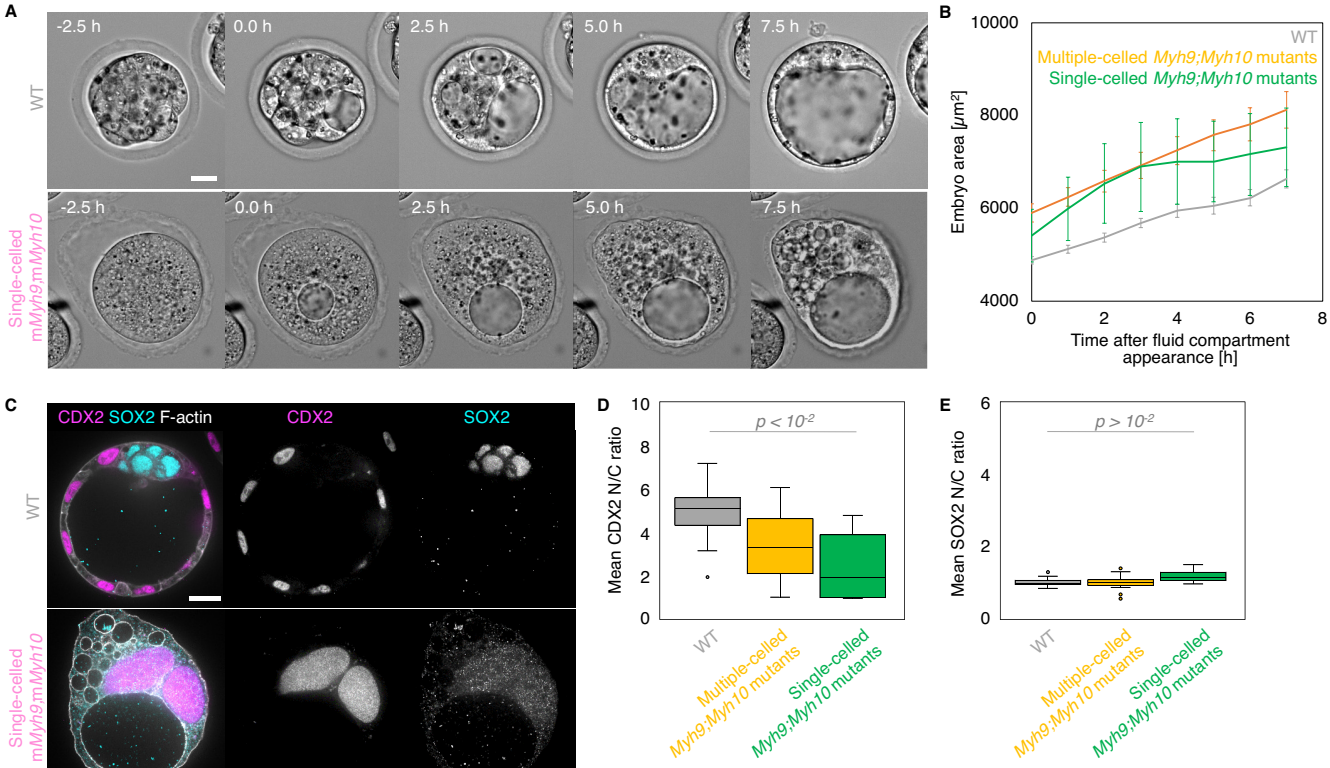

Figure 8. Single-celled embryos at the blastocyst stage. (**A**) Representative images of long-term time-lapse of WT and single-celled m*Myh9*;m*Myh10* embryos at the onset of fluid accumulation (***Figure 8—video 1***). Scale bar, 20 µm. (**B**) Embryo growth curves during fluid accumulation for WT (grey, n = 20) and multiple- (yellow, n = 13) or single-celled *Myh9;Myh10* (green, n = 4) mutant embryos measured for seven continuous hours after a lumen of at least 20 µm is observed. Data show mean ± SEM. (**C**) Representative images of WT and single-celled m*Myh9*;m*Myh10* embryos stained for TE and ICM markers CDX2 (magenta) and SOX2 (cyan), DAPI (yellow), and F-actin (grey). The same mutant embryos as in A are shown. Scale bar, 20 µm. (**D-E**) N/C ratio of CDX2 (**D**) and SOX2 (**E**) staining for outer cells from WT (grey, n = 23) and multiple- (yellow, n = 18) or single-celled *Myh9;Myh10* (green, n = 6) embryos. Mann-Whitney *U* test p values compared to WT are indicated.

The online version of this article includes the following video and figure supplement(s) for figure 8:

Figure supplement 1. Morphogenesis and lineage specification of embryos with all blastomeres fused at the late morula stage.

Figure 8—video 1. Preimplantation development of an m*Myh9*;m*Myh10* embryo failing all successive cleavages.
https://elifesciences.org/articles/68536#fig8video1

Figure 8—video 2. Fluid accumulation in control and single-celled fused embryos.
https://elifesciences.org/articles/68536#fig8video2

contact size whereas *Myh10* knockdown does not (***Heuzé et al., 2019***; ***Smutny et al., 2010***). This is also in agreement with previous studies using inhibitory drugs on the preimplantation embryo. Compaction is prevented, and even reverted, when embryos are treated with blebbistatin, a drug directly inhibiting NMHC function (***Maître et al., 2015***), or ML7, an inhibitor of the myosin light chain kinase (***Zhu et al., 2017***). However, zygotic injection of siRNA targeting *Myh9* did not affect compaction (***Samarage et al., 2015***; ***Zenker et al., 2018***), further indicating that MYH9 acts primarily via its maternal pool. Similarly, siRNA-mediated knockdown of a myosin regulatory light chain *Myl12b* did not affect compaction (***Zhu et al., 2017***). Therefore, for efficient reduction of contractility with molecular specificity, maternal depletion is required.

The phenotypes of the maternal-zygotic NMHC mutants can also appear in contradiction with other conclusions from previous studies. Drugs were used to test the role of contractility in apico-basal polarity establishment with contradictory results. ML7, but not blebbistatin, was reported to

block de novo cell polarization (**Zhu et al., 2017**). This discrepancy might be due to ML7 inhibiting other kinases than MLCK such as PKC (**Bain et al., 2003**), which is required for apical domain formation (**Zhu et al., 2017**). Also, blebbistatin was reported to block the maturation of the apical domain (**Zenker et al., 2018**). The apical domain is essential for TE differentiation and for polarized fluid transport (**Laeno et al., 2013**; **Hirate et al., 2013**). We observed that even the most severely affected NMHC mutant embryos are able to establish and maintain apico-basal polarity, specific expression of TE markers and, most importantly, a functional polarized fluid transport (**Figure 8**). This argues against the requirement of contractility for de novo polarization and apical domain maturation.

Besides compaction defects, reduced cell number is one of the major effects caused by reduced contractility in the maternal-zygotic knockout of NMHCs. Loss of MYH9 alone, but not of MYH10 alone, causes cytokinesis defects (**Figures 2–3**, **Figure 2—videos 1** and **3**). This could simply be explained by the higher levels of maternal MYH9 (**Figure 1**). In vitro studies also noted that MYH9, but not MYH10, is key to power the ingression of the cleavage furrow (**Taneja et al., 2020**). This recent study also noted that MYH10 can compensate the absence of MYH9 with increased cortical recruitment (**Taneja et al., 2020**). Consistently, we observed much more severe division failures when both *Myh9* and *Myh10* are maternally removed (**Figures 5**, **6** and **8**). This reveals significant compensation between NMHCs during preimplantation development. Whether this compensation takes place by a change in subcellular localization or by changes in expression level will require further studies.

Reduced cell number could have a major impact during very early development, when the zygote needs to produce enough cells for developmental patterning and morphogenesis. During normal development, the mouse embryo paces through the successive morphogenetic steps of compaction, internalization, and lumen formation at the rhythm of the third, fourth, and fifth waves of cleavage (**Maître, 2017**; **Płusa and Piliszek, 2020**; **Rossant, 2016**; **White et al., 2018**). Such concomitance may initially suggest that the preimplantation program is tightly linked to cleavages and cell number. However, seminal studies have established that the mammalian embryo is regulative and can build the blastocyst correctly with either supernumerary or fewer cells (**Smith and McLaren, 1977**; **Snow, 1973**; **Tarkowski, 1959**; **Tarkowski, 1961**; **Tarkowski and Wróblewska, 1967**). For example, aggregating multiple embryos results in compaction and lumen formation after the third and fifth cleavage, respectively, rather than when the chimeric embryos are composed of 8 and 32 cells (**Tarkowski, 1961**). Disaggregation leads to the same result with halved or quartered embryos compacting and forming a lumen at the correct embryonic stages rather than when reaching a defined cell number (**Tarkowski, 1959**; **Tarkowski and Wróblewska, 1967**). Contrary to disaggregated embryos, NMHC mutant embryos show reduced cell numbers without affecting the amount of cellular material (**Figure 2—figure supplement 1**). As observed in other species, the pace of development during mouse cleavage stages is thought to depend on the size ratio between the nucleus and the cytoplasm (**Tsichlaki and FitzHarris, 2016**). Evidences of nuclear divisions are visible even in the case of single-celled embryos (**Figure 8—video 1**), which suggests that the nuclear to cytoplasmic ratio may increase during the development of single-celled embryos. In line with these previous studies, the present experiments further confirm that compaction, internalization, and lumen formation take place without the expected cell number. Therefore, although cleavages and morphogenetic events are concomitant, they are not linked. Importantly, affecting blastocyst cell number through maternal *Myh9* loss or fusion of blastomeres at the 4-cell stage preserves the proportion of cells allocated to TE and ICM lineages (**Figure 3C** and **Figure 3—figure supplement 2D**). A recent study proposed that this proportion is controlled by the growth of the lumen (**Chan et al., 2019**). This is compatible with our observation that lumen growth is not affected by the loss of *Myh9* or cell fusion (**Figure 2C** and **Figure 2—figure supplement 2C**). However, lineage proportions break down when both *Myh9* and *Myh10* are maternally lost (**Figure 6C**). With about three cells on an average (**Figure 6C–D**), a majority of double mutants fail to internalize cells. As observed for doublets of 16-cell stage blastomeres, in principle, two cells should be enough to internalize one cell by an entosis-like process (**Maître et al., 2016**; **Overholtzer et al., 2007**). With extremely low contractility, double mutants may fail to raise contractility above the tension asymmetry threshold, enabling internalisation (**Maître et al., 2016**). As for oriented cell division (**Korotkevich et al., 2017**), this mechanism needs at least two cells to push one dividing cell within the cell-cell contact area. Together, this explains the absence of inner cells in mutant embryos with fewer than three cells.

Disaggregation experiments were key to reveal some of the cell-autonomous aspects of blastocyst formation: a single 8-cell stage blastomere can polarize (***Ziomek and Johnson, 1980***) and increase its contractility (***Maître et al., 2015***). Our observations on single-celled embryos reveal that fluid accumulation is also a cell-autonomous process (***Figure 8***). In fact, single-celled embryos inflate at rates similar to control embryos, implying that cell-cell contacts, closed by tight junctions at the embryo surface, are not required for accumulating fluid within blastomeres. Therefore, blastocoel components may be transported exclusively transcellularly, whereas paracellular transport through tight junctions may be negligible.

Whether single-celled embryos resulted from systematically failed cytokinesis or from cell fusion, these embryos grow at a similar rate, which is also the same as control embryos and other embryos composed of a reduced cell number (***Figure 2C***, ***Figure 5C***, ***Figure 8B***, ***Figure 8—figure supplement 1B***, and ***Figure 2—figure supplement 2C***). This suggests that fluid accumulation is a robust machinery during preimplantation development. Interfering with aquaporins, ion channels and transporters affect fluid accumulation, but the transcellular and paracellular contributions remain unclear (***Barcroft et al., 2003***; ***Kawagishi et al., 2004***; ***Schliffka and Maître, 2019***). Future studies will be needed to understand what sets robust transcellular fluid accumulation during preimplantation development. The ability of single cells to polarize and inflate a lumen was recently demonstrated in vitro by plating hepatocytes onto CDH1-coated substrates (***Zhang et al., 2020***). In this study, fluid accumulation in single-celled embryos does not result in the formation of a lumen but in the formation of inflating vacuoles. Vacuoles were also reported to appear occasionally in mutant mouse embryos with defective cell-cell adhesion (***Bedzhov et al., 2012***; ***Stephenson et al., 2010***). Similarly, vacuole formation in case of acute loss of cell-cell adhesion has been studied in vitro (***Vega-Salas et al., 1988***). When apical lumens are disrupted, the apical compartment is internalized, and this can result in fluid accumulation within the vacuolar apical compartment (VAC) (***Vega-Salas et al., 1988***). Analogous VACs were proposed to coalesce into the lumen of endothelial tubes upon cell-cell contact in vivo (***Kamei et al., 2006***). The molecular characteristics and dynamics of these structures and their empty counterparts, the so-called apical membrane initiation sites, have been extensively studied in vitro and proven helpful to better understand apical lumen formation (***Bryant et al., 2010***; ***Overeem et al., 2015***). In the case of the blastocyst, which forms a lumen on its basolateral side (***Dumortier et al., 2019***; ***Schliffka and Maître, 2019***), such vacuoles may constitute an equivalent *vacuolar basolateral compartment*. Similar to apical lumen, further characterization of the molecular identity and dynamic behaviors of these vacuoles may prove useful to better understand fluid accumulation during basolateral lumen formation. Studying transcellular fluid transport and the molecular machinery of basolateral lumen formation will be greatly facilitated by the fusion approach reported in the present study (***Figure 8—figure supplement 1***).

Materials and methods

Embryo work

Recovery and culture

All the animal works were performed in the animal facility at the Institut Curie, with permission from the institutional veterinarian overseeing the operation (APAFIS #11054–2017082914226001). The animal facilities are operated according to international animal welfare rules.

Embryos were isolated from superovulated female mice mated with male mice. Superovulation of female mice was induced by intraperitoneal injection of 5 international units (IU) pregnant mare's serum gonadotropin (Ceva, Syncro-part), followed by intraperitoneal injection of 5 IU human chorionic gonadotropin (MSD Animal Health, Chorulon) 44–48 hr later. Embryos at E0.5 were recovered from plugged females by opening the ampulla followed by a brief treatment with 37˚C 0.3 mg/mL hyaluronidase (Sigma, H4272-30MG) and washing in 37˚C FHM. Embryos were recovered at E1.5 by flushing oviducts and at E2.5 and E3.5 by flushing oviducts and uteri from plugged females with 37˚C FHM (Millipore, MR-122-D) using a modified syringe (Acufirm, 1400 LL 23).

Embryos were handled using an aspirator tube (Sigma, A5177-5EA) equipped with a glass pipette pulled from glass micropipettes (Blaubrand intraMark or Warner Instruments).

Embryos were placed in KSOM (Millipore, MR-107-D) supplemented with 0.1% BSA (Sigma, A3311) in 10 µL droplets covered in mineral oil (Acros Organics). Embryos are cultured in an incubator under a humidified atmosphere supplemented with 5% CO2 at 37˚C.

To remove the ZP, embryos were incubated for 45–60 s in pronase (Sigma, P8811).

Blastomeres were fused using the GenomONE-CF FZ SeV-E cell fusion kit (CosmoBio, ISK-CF-001-EX). HVJ envelope was resuspended following manufacturer's instructions and diluted in FHM for use. To fuse the blastomeres of embryos at the 4-cell stage, embryos were incubated in 1:60 HVJ envelope/FHM for 15 min at 37˚C followed by washes in KSOM. To fuse blastomeres at the morula stage, embryos were treated in the same manner in 1:50 HVJ envelope/FHM. Fusion typically completes ~30 min after the treatment.

For imaging, embryos were placed in 3.5 or 5 cm glass-bottom dishes (MatTek).

Mouse lines

Mice used were of 5 weeks old and above.

(C57BL/6xC3H) F1 hybrid strain was used for WT.

To remove LoxP sites specifically in oocytes, *Zp3*$^{Cre/+}$ *(Tg(Zp3-cre)93Knw)* mice were used (**de Vries et al., 2000**).

To generate mz*Myh9* embryos, *Myh9*^{tm5RSad} mice were used (**Jacobelli et al., 2010**) to breed *Myh9*$^{tm5RSad/tm5RSad}$; *Zp3*$^{Cre/+}$ females with *Myh9*$^{+/-}$ ±. To generate mz*Myh10* embryos, *Myh10*^{tm7Rsad} mice were used (**Ma et al., 2009**) to breed *Myh10*$^{tm7Rsad/tm7Rsad}$; *Zp3*$^{Cre/+}$ females with *Myh10*$^{+/-}$ ±. To generate mz*Myh9*;mz*Myh10* embryos, *Myh9*$^{tm5RSad/tm5RSad}$; *Myh10*$^{tm7Rsad/tm7Rsad}$; *Zp3*$^{Cre/+}$ females were mated with *Myh9*$^{+/-}$; *Myh10*$^{+/-}$ males. To generate embryos with a maternal *Myh9-GFP* allele, *Myh9*$^{tm8.1RSad}$ *(Gt(ROSA)26Sor*$^{tm4(ACTB-tdTomato,-EGFP)Luo}$*)* females were mated with WT males; to generate embryos with a paternal *Myh9-GFP* allele, WT females were mated with *Myh9*$^{tm8.1RSad}$ *(Gt(ROSA)26Sor*$^{tm4(ACTB-tdTomato,-EGFP)Luo}$*)* males (**Muzumdar et al., 2007**; **Zhang et al., 2012**). For fusion at the morula stage, *(Gt(ROSA)26Sor*$^{tm4(ACTB-tdTomato,-EGFP)Luo}$*)* mice were used (**Muzumdar et al., 2007**).

Mouse strain	RRID
(C57BL/6xC3H) F1	MGI:5650923
Tg(Zp3-cre)93Knw	MGI:3835429
Myh9$^{tm5RSad/tm5RSad}$	MGI:4838530
Myh10$^{tm7Rsad/tm7Rsad}$	MGI:4443040
Myh9$^{tm8.1RSad}$	MGI:5499741
Gt(ROSA)26Sor$^{tm4(ACTB-tdTomato,-EGFP)Luo}$	IMSR_JAX:007676

Immunostaining

Embryos were fixed in 2% PFA (Euromedex, 2000-C) for 10 min at 37˚C, washed in PBS, and permeabilized in 0.1% (SOX2, CDX2, and YAP primary antibodies) or 0.01% (all other primary antibodies) Triton X-100 (Euromedex, T8787) in PBS (PBT) at room temperature before being placed in blocking solution (PBT with 3% BSA) at 4˚C for 2–4 hr. Primary antibodies were applied in blocking solution at 4˚C overnight. After washes in PBT at room temperature, embryos were incubated with secondary antibodies, DAPI, and/or phalloidin in blocking solution at room temperature for 1 hr. Embryos were washed in PBT and imaged immediately after.

Primary antibodies	Dilution	Provider	RRID
CDX2	1:200	Abcam, ab157524	AB_2721036
SOX2	1:100	Abcam, ab97959	AB_2341193
YAP	1:100	Abnova, H00010413-M01	AB_535096
Phospho-MYH9 (Ser1943)	1:200	Cell Signaling, 5026	AB_10576567

Continued on next page

Continued

Primary antibodies	Dilution	Provider	RRID
MYH10	1:200	Santa Cruz, sc-376942	
PRKCz (H-1)	1:50	Santa Cruz, sc-17781	AB_628148
AQP3	1:500	Novusbio, NBP2-33872	
CDH1	1:500	eBioscience,14-3249-82	
ATP1A1	1:100	Abcam, ab76020	AB_1310695

Secondary antibodies and dyes	Dilution	Provider	RRID
Alexa Fluor Plus 488 anti-mouse	1:200	Invitrogen, A32723	AB_2633275
Alexa Fluor 546 anti-mouse	1:200	Invitrogen, A11003	AB_2534071
Alexa Fluor Plus 488 anti-rabbit	1:200	Invitrogen, A32731	AB_2633280
Alexa Fluor Plus 546 anti-rabbit	1:200	Invitrogen, A11010	AB_2534077
Alexa Fluor 633 anti-rat	1:200	Invitrogen, A21094	AB_141553
Alexa Fluor 488 anti-rat	1:200	Invitrogen, A11006	AB_2534074
Alexa Fluor 633 phalloidin	1:200	Invitrogen, A22284	
4′,6-diamidino-2-phenylindole (DAPI)	1:1000	Invitrogen, D1306	AB_2629482

Single embryo genotyping

DNA extraction was performed on single fixed embryos, in 10 µL of DNA extraction buffer containing 10 mM Tris-HCl (pH 8, Sigma, T2694), 50 mM KCl (Sigma, 60142), 0.01% gelatine (Sigma, G1393), 0.1 mg/mL proteinase K (Sigma, P2308) at 55˚C for 90 min, followed by deactivation of the proteinase K at 90˚C for 10 min. 2 µL of this DNA extract was used in PCR reactions.

To assess the *Myh9* genotype, a preamplification PCR was performed using forward (fw) primer GGGACCCACTTTCCCCATAA/reverse (rev) primer GTTCAACAGCCTAGGATGCG at a final concentration of 0.4 µM. The PCR program is as follows: denaturation at 94˚C 4 min; 35 cycles of 94˚C 1 min, 58˚C 1 min, 72˚C 3:30 min, 72˚C 1 min; final elongation step at 72˚C 7 min. Subsequently, 2 µL of the PCR product was directly used as a template for two independent PCR amplifications to detect either a 592 bp amplicon for the WT allele, with fw primer GGGACACAGTTGAATCCCTT/rev primer ATGGGCAGGTTCTTATAAGG or a 534 bp amplicon for a mutant allele, with fw primer GGGACACAGTTGAATCCCTT/rev primer CATCCTGTGGAGAGTGAGAGCAC at a final concentration of 0.4 µM. PCR program is as follows: denaturation at 94˚C for 4 min; 35 cycles of 94˚C 1 min, 58˚C 2 min, 72˚C 1 min; final elongation step at 72˚C 7 min.

To assess the *Myh10* genotype, a preamplification PCR was performed using fw primer GGCCCCCATGTTACAGATTA/rev primer TTTCCTCAACATCCACCCTCTG at a final concentration of 0.4 µM. The PCR program is as follows: denaturation at 94˚C for 4 min; 35 cycles of 94˚C 1 min, 58˚C 1 min, 72˚C 2 min, 72˚C 1 min; final elongation step at 72˚C 7 min. Subsequently, 2 µL of the PCR product was directly used as a template for a PCR amplification using fw primer 1 TAGCGAAGGTCTAGGGGAATTG/fw primer 2 GACCGCTACTATTCAGGACTTATC/rev primer CAGAGAAACGATGGGAAAGAAAGC at a final concentration of 0.4 µM. PCR program is as follows: denaturation at 94˚C for 4 min; 35 cycles of 94˚C 1 min, 58˚C 1:30 min, 72˚C 1 min; final elongation step at 72˚C 7 min, resulting in a 230 bp amplicon for a WT allele and a 630 bp amplicon for a mutant allele.

Quantitative RT-PCR

To extract total RNA, embryos were collected in 3 µL of PBS, frozen on ice or snap-frozen on dry ice and stored at −80˚C until further use. Total RNA extraction was performed using the PicoPure RNA Isolation Kit (ThermoFisher Scientific, KIT0204) according to manufacturer's instructions. DNase treatment was performed during the extraction, using RNase-Free DNase Set (QIAGEN, 79254).

cDNA was synthesized with random primers (ThermoFisher Scientific, 48190011), using the Super-Script III Reverse Transcriptase kit (ThermoFisher Scientific, 18080044) on all the extracted RNA, according to manufacturer's instructions. The final product could be used immediately or stored at −20˚C until further use.

All the RT-qPCR reactions were performed using the ViiA 7 Real-Time PCR machine (Applied Bio-Systems) according to the instruction of the manufacturer. For each target sample, amplifications were run in triplicate in 10 µL reaction volume containing 5 µL of 2x Power SYBR Green PCR Master Mix (Applied Biosystems, 4367659), 1.4 µL of cDNA, 0.5 µL of each primer at 2 µM, and 2.6 µL of nuclease-free water. The PCR program is as follows: denaturation at 95˚C 10 min; 40 cycles of 95˚C 15 s, 60˚C 1 min; 1 cycle of 95˚C 15 s, 60˚C 1 min, 95˚C 15 s. The last cycle provides the post PCR run melt curve, for assessment of the specifics of the amplification. Each couple of primers was designed in order to anneal on consecutive exons of the cDNA sequence, far from the exon-exon junction regions, except for the *Gapdh* gene. The size of amplicons varied between 84 bp and 177 bp. *Gapdh* housekeeping gene was used as internal control to normalize the variability in expression levels of each target gene, according to the $2^{-\Delta CT}$ method. For every experiment, data were further normalized to *Myh9* levels at the zygote stage.

Total RNA was extracted from 234, 159, 189, 152 embryos at zygote, four-cell, morula, and blastocyst stages, respectively, from six independent experiments.

Gene name	Primer sequence forward	Primer sequence reverse
Myh9 (ex7–ex8)	CAATGGCTACATTGTTGGTGCC	AGTAGAAGATGTGGAAGGTCCG
Myh10 (ex3–ex4)	GAGGGAAGAAACGCCATGAGA	GAATTGACTGGTCCTCACGAT
Myh14 (ex25–ex26)	GAGCTCGAGGACACTCTGGATT	TTTCTTCAGCTCTGTCACCTCC
Gapdh (ex6–ex7)	CATACCAGGAAATGAGCTTG	ATGACATCAAGAAGGTGGTG

Bioinformatic analysis

Mouse and human single cell RNA sequencing data were extracted from ***Deng et al., 2014*** and ***Yan et al., 2013***, analyzed as in ***De Iaco et al., 2017***. In brief, single cell RNAseq datasets of human and mouse embryos (GSE36552, GSE45719) were downloaded and analyzed using the online platform Galaxy (usegalaxy.org). The reads were aligned to the reference genome using TopHat (Galaxy Version 2.1.1; ***Kim et al., 2013***) and read counts generated with htseq-count (Galaxy Version 0.9.1; ***Anders et al., 2015***). Normalized counts were determined with limma-voom (Galaxy Version 3.38.3 + galaxy3; ***Law et al., 2014***).

Microscopy

For live imaging, embryos were placed in 5 cm glass-bottom dishes (MatTek) under a Celldiscoverer 7 (Zeiss) equipped with a 20x/0.95 objective and an ORCA-Flash 4.0 camera (C11440, Hamamatsu) or a 506 axiovert (Zeiss) camera.

Embryos were imaged from E1.5 to E3.5 until the establishment of a stable blastocoel in WT control embryos. Using the experiment designer tool of ZEN (Zeiss), we set up a nested time-lapse in which all embryos were imaged every 30 min at three focal planes positioned 10 µm apart for 40–54 hr and each embryo was subjected to two 10 min-long acquisitions with an image taken every 5 s at two focal planes positioned 10 µm apart that were set 12 and 19 hr after the second cleavage division of a reference WT embryo. Embryos were kept in a humified atmosphere supplied with 5% CO2 at 37˚C. After imaging, mutant embryos were tracked individually for immunostaining and genotyping.

Live MYH9-GFP embryos were imaged at the zygote, four-cell, morula, and blastocyst stages. Live imaging was performed using an inverted Zeiss Observer Z1 microscope with a CSU-X1 spinning disc unit (Yokogawa). Excitation was achieved using 488 and 561 nm laser lines through a 63x/1.2 C Apo Korr water immersion objective. Emission was collected through 525/50 and 595/50 band pass filters onto an ORCA-Flash 4.0 camera (C11440, Hamamatsu). The microscope was equipped with an incubation chamber to keep the sample at 37˚C and supply the atmosphere with 5% CO2.

Immunostainings were imaged on the same microscope using 405, 488, 561, and 642 nm laser lines through a 63x/1.2 C Apo Korr water immersion objective; emission was collected through 450/50 nm, 525/50 nm, 595/50 band pass or 610 nm low pass filters.

Data analysis

Time-lapse of preimplantation development

Based on the time-lapses of preimplantation development from E1.5 to E3.5, we assessed the timing of the third, fourth, and fifth cleavage divisions as well as the dynamics of compaction and lumen growth following these definitions:

(1)Cleavages are defined as part of the same wave when they occur within 30 min of the cleavage of another cell within the same embryo. As embryos are recovered at E1.5, time-lapse imaging starts around the time of the second cleavage. As cell divisions are affected by the mutations of *Myh9* and/or *Myh10*, the cell number of recovered embryos is not necessarily equal to WT cell number. Therefore, we used the entire time-lapse to determine whether the first observed division corresponds to thesecond, third, fourth, or fifth wave. Failed cytokinesis is counted as part of cleavage waves. (2) Timing of maximal compaction is defined as the time when embryos stop increasing their contact angles. (3) Timing of blastocoel formation is taken as the time when a fluid compartment with a diameter of at least 20 µm is visible.

The timings of all cleavage divisions and morphogenetic events were normalized to the end of the third cleavage division (beginning of the 8-cell stage in WT embryos).

Surface contact angles were measured using the angle tool in Fiji. Only the contact angles formed by two adjacent blastomeres with their equatorial planes in focus were considered. For each embryo, between one and six contact angles were measured after completion of the third cleavage, just before the onset of the fourth cleavage, after completion of the fourth cleavage, and just before the onset of the fourth cleavage.

Lumen growth was assessed by an increase in the area of the embryo. Using FIJI, an ellipse was manually fitted around the embryo every hour starting from the time of blastocoel formation (defined here as when a lumen of at least 20 µm becomes visible) until the end of the time-lapse. Growth rates of individual embryos were calculated over a 7 hr time window following the time of blastocoel formation. Measured projected areas from different embryos were synchronized to the time of blastocoel formation and averaged. For a fused single-celled embryo, the mean blastocoel formation time of the control embryos from each experiment was calculated to synchronize the fused embryos (1 hr of deviation from the mean blastocoel formation time can be allowed to accommodate cell divisions and sampling time). For control embryos, only blastocyst growing by at least 35% of their projected area were considered.

The shape of the zona pellucida was measured by fitting an ellipse on the outer edge of the zona pellucida and measuring the long and short axes.

Time-lapse of periodic contractions

Particle image velocimetry (PIV) analysis was performed using PIVlab 2.02 running on Matlab (***Thielicke and Stamhuis, 2020***; ***Thielicke and Stamhuis, 2014***). Similar to ***Maître et al., 2015***, time-lapse movies acquired every 5 s were processed using two successive passes through interrogation windows of 20/10 µm resulting in ~180 vectors per embryo. Vector velocities were then exported to Matlab for Fast Fourier Transform (FFT) analysis. The power spectrum of each embryo was then analyzed to assess the presence of a clear oscillation peak. The peak value between 50 and 120 s was taken as the amplitude, as this oscillation period range corresponds to the one where WT show oscillations (***Maître et al., 2015***; ***Maître et al., 2016***). An embryo is considered as oscillating when the amplitude peaks 1.7 above background (taken as the mean value of the power spectrum signal of a given embryo) to determine whether it has a detectable oscillation. Power spectra of embryos from the same genotype were averaged.

Time-lapse of Myh9-GFP embryos

Myh9-GFP intensity was measured in FIJI by fitting a circle with a radius of 50 µm over the sum projection of each embryo and measuring the mean gray value. Background intensity was measured in a

circular area with radius 5 µm and subtracted to the embryonic value. The corrected intensities were normalized to the zygote stage of maternal Myh9-GFP embryos.

Immunostaining

We used FIJI to measure the levels of SOX2, CDX2, and YAP expression and localization by measuring the signal intensity of immunostainings. For each embryo, 15 cells (five ICM, five polar TE, five mural TE) were measured. In case an embryo had fewer than five ICM cells, a corresponding number of TE cells were added. If the embryo had fewer than 15 cells, all cells were measured. For each cell, the signal intensity was measured in a representative 3.7 μm^2 circular area of the equatorial nuclear plane and in a directly adjacent cytoplasmic area. Mitotic and apoptotic cells were excluded from analysis. We then calculated the nuclear to cytoplasmic ratio.

To obtain apico-basal intensity profiles of polarity markers, we selected confocal slices cutting through the equatorial plane of a surface cell lining the blastocoel. We drew a 15-µm-long and 0.4-µm-thick line from the cell-medium interface through the cell into the cell-lumen or cell-vacuole interface. Lowest/highest intensity values were normalized to 0 and 1, respectively.

To count cell number, we used DAPI to detect nuclei and phalloidin staining to detect cells. Cells were considered outer cells if they were in contact with the outside medium.

To measure the 3D properties of blastocysts, we manually segmented the surface of the embryo and of the blastocoel using Bitplane Imaris. Volumes and ellipticity were obtained from Imaris. The cellular volume was obtained by subtracting the blastocoel volume from the total volume of the embryo.

Statistics

Mean, standard deviation, SEM, lower and upper quartiles, median, Pearson's correlation coefficients, unpaired two-tailed Welch's *t* test, Mann-Whitney *U* test, and Pearson's Chi^2 test with Yates's correction for continuity p values were calculated using Excel (Microsoft) and R (http://www.r-project.org). Pearson's correlation statistical significance was determined on the corresponding table. Statistical significance was considered when $p<10^{-2}$. Boxplots show the median (line), interquartile range (box), 1.5 x interquartile range (whiskers), and remaining outliers (dots).

The sample size was not predetermined and simply results from the repetition of experiments. No sample was excluded. No randomization method was used. The investigators were not blinded during experiments.

Acknowledgements

We thank the imaging platform of the Genetics and Developmental Biology unit at the Institut Curie (PICT-IBiSA@BDD), member of the French National Research Infrastructure France-BioImaging (ANR-10-INBS-04) for their outstanding support; the animal facility of the Institut Curie for their invaluable help. We thank Aurélie Teissendier for help with bioinformatic analysis, Victoire Cachoux for help with image analysis, and Yohanns Bellaïche for discussion and advice on the manuscript. Research in the lab of J-LM is supported by the Institut Curie, the Centre National de la Recherche Scientifique (CNRS), the Institut National de la Santé Et de la Recherche Médicale (INSERM), and is funded by grants from the ATIP-Avenir program, the Fondation Schlumberger pour l'Éducation et la Recherche via the Fondation pour la Recherche Médicale, the European Research Council Starting Grant ERC-2017-StG 757557, the European Molecular Biology Organization Young Investigator program (EMBO YIP), the INSERM transversal program Human Development Cell Atlas (HuDeCA), Paris Sciences Lettres (PSL) 'nouvelle équipe' and QLife (17-CONV-0005) grants and Labex DEEP (ANR-11-LABX-0044), which are part of the IDEX PSL (ANR-10-IDEX-0001–02). MFS is funded by a Convention Industrielle de Formation pour la Recherche (No 2019/0253) between the Agence Nationale de la Recherche and Carl Zeiss SAS. ÖÖ is funded from the European Union's Horizon 2020 research and innovation program under the Marie Skłodowska-Curie grant agreement No 666003 and benefits from the EMBO YIP bridging fund.

Additional information

Competing interests

Markus Frederik Schliffka: is employed by Carl Zeiss SAS via a public PhD programme Conventions Industrielles de Formation par la Recherche (CIFRE) co-funded by the Association Nationale de la Recherche et de la Technologie (ANRT). The other authors declare that no competing interests exist.

Funding

Funder	Grant reference number	Author
Association Nationale de la Recherche et de la Technologie	2019/0253	Markus Frederik Schliffka
H2020 Marie Skłodowska-Curie Actions	666003	Özge Özgüç
Fondation pour la Recherche Médicale		Özge Özgüç
Centre National de la Recherche Scientifique		Jean-Léon Maître
H2020 European Research Council	ERC-2017-StG 757557	Jean-Léon Maître
Schlumberger Foundation		Jean-Léon Maître
Université de Recherche Paris Sciences et Lettres	17-CONV-0005	Jean-Léon Maître
Agence Nationale de la Recherche	ANR-11-LABX-0044	Jean-Léon Maître
Institut National de la Santé et de la Recherche Médicale	HuDeCA	Jean-Léon Maître
European Molecular Biology Organization	Young Investigator Programme	Jean-Léon Maître
Agence Nationale de la Recherche	ANR-10-IDEX-0001-02	Jean-Léon Maître

The funders had no role in study design, data collection and interpretation, or the decision to submit the work for publication.

Author contributions

Markus Frederik Schliffka, Anna Francesca Tortorelli, Conceptualization, Resources, Data curation, Formal analysis, Validation, Investigation, Visualization, Methodology, Writing - review and editing; Özge Özgüç, Data curation, Software, Formal analysis, Visualization, Methodology, Writing - review and editing; Ludmilla de Plater, Resources, Methodology; Oliver Polzer, Formal analysis, Visualization; Diane Pelzer, Software, Formal analysis, Visualization, Writing - review and editing; Jean-Léon Maître, Conceptualization, Resources, Data curation, Software, Formal analysis, Supervision, Funding acquisition, Validation, Investigation, Visualization, Methodology, Writing - original draft, Project administration, Writing - review and editing

Author ORCIDs

Markus Frederik Schliffka https://orcid.org/0000-0002-5128-1653
Anna Francesca Tortorelli https://orcid.org/0000-0002-9995-9582
Özge Özgüç http://orcid.org/0000-0002-1545-1715
Ludmilla de Plater http://orcid.org/0000-0002-0982-5960
Oliver Polzer http://orcid.org/0000-0003-4970-6058

Diane Pelzer http://orcid.org/0000-0001-6906-2451
Jean-Léon Maître https://orcid.org/0000-0002-3688-1474

Ethics

Animal experimentation: All animal work is performed in the animal facility at the Institut Curie, with permission by the institutional veterinarian overseeing the operation (APAFIS #11054-2017082914226001). The animal facilities are operated according to international animal welfare rules.

Decision letter and Author response

Decision letter https://doi.org/10.7554/eLife.68536.sa1
Author response https://doi.org/10.7554/eLife.68536.sa2

Additional files

Supplementary files

- Transparent reporting form

Data availability

The microscopy data, ROI and analyses are available on the following repository under a CC BY-NC-SA license: https://ressources.curie.fr/mzmyh/.

The following previously published datasets were used:

Author(s)	Year	Dataset title	Dataset URL	Database and Identifier
Deng Q, Ramsköld D, Reinius B, Sandberg R	2014	Single-cell RNA-Seq reveals dynamic, random monoallelic gene expression in mammalian cells	https://www.ncbi.nlm.nih.gov/geo/query/acc.cgi?acc=GSE45719	NCBI Gene Expression Omnibus, GSE45719
Tang F, Qiao J, Li R	2013	Tracing pluripotency of human early embryos and embryonic stem cells by single cell RNA-seq	https://www.ncbi.nlm.nih.gov/geo/query/acc.cgi?acc=GSE36552	NCBI Gene Expression Omnibus, GSE36552

References

Anani S, Bhat S, Honma-Yamanaka N, Krawchuk D, Yamanaka Y. 2014. Initiation of Hippo signaling is linked to polarity rather than to cell position in the pre-implantation mouse embryo. *Development* **141**:2813–2824. DOI: https://doi.org/10.1242/dev.107276, PMID: 24948601

Anders S, Pyl PT, Huber W. 2015. HTSeq–a Python framework to work with high-throughput sequencing data. *Bioinformatics* **31**:166–169. DOI: https://doi.org/10.1093/bioinformatics/btu638, PMID: 25260700

Avilion AA, Nicolis SK, Pevny LH, Perez L, Vivian N, Lovell-Badge R. 2003. Multipotent cell lineages in early mouse development depend on SOX2 function. *Genes & development* **17**:126–140. DOI: https://doi.org/10.1101/gad.224503, PMID: 12514105

Bain J, McLauchlan H, Elliott M, Cohen P. 2003. The specificities of protein kinase inhibitors: an update. *The Biochemical journal* **371**:199–204. DOI: https://doi.org/10.1042/BJ20021535, PMID: 12534346

Barcroft LC, Offenberg H, Thomsen P, Watson AJ. 2003. Aquaporin proteins in murine trophectoderm mediate transepithelial water movements during cavitation. *Developmental biology* **256**:342–354. DOI: https://doi.org/10.1016/s0012-1606(02)00127-6, PMID: 12679107

Barcroft LC, Moseley AE, Lingrel JB, Watson AJ. 2004. Deletion of the Na/K-ATPase alpha1-subunit gene (Atp1a1) does not prevent cavitation of the preimplantation mouse embryo. *Mechanisms of development* **121**:417–426. DOI: https://doi.org/10.1016/j.mod.2004.04.005, PMID: 15147760

Beach JR, Shao L, Remmert K, Li D, Betzig E, Hammer JA, 2014. Nonmuscle myosin II isoforms coassemble in living cells. *Current biology : CB* **24**:1160–1166. DOI: https://doi.org/10.1016/j.cub.2014.03.071, PMID: 24814144

Bedzhov I, Liszewska E, Kanzler B, Stemmler MP. 2012. Igf1r signaling is indispensable for preimplantation development and is activated via a novel function of E-cadherin. *PLOS genetics* **8**:e1002609. DOI: https://doi.org/10.1371/journal.pgen.1002609, PMID: 22479204

Bryant DM, Datta A, Rodríguez-Fraticelli AE, Peränen J, Martín-Belmonte F, Mostov KE. 2010. A molecular network for de novo generation of the apical surface and lumen. *Nature cell biology* **12**:1035–1045. DOI: https://doi.org/10.1038/ncb2106, PMID: 20890297

Chan CJ, Costanzo M, Ruiz-Herrero T, Mönke G, Petrie RJ, Bergert M, Diz-Muñoz A, Mahadevan L, Hiiragi T. 2019. Hydraulic control of mammalian embryo size and cell fate. *Nature* **571**:112–116. DOI: https://doi.org/10.1038/s41586-019-1309-x, PMID: 31189957

Clark AG, Dierkes K, Paluch EK. 2013. Monitoring actin cortex thickness in live cells. *Biophysical journal* **105**:570–580. DOI: https://doi.org/10.1016/j.bpj.2013.05.057, PMID: 23931305

Conti MA, Even-Ram S, Liu C, Yamada KM, Adelstein RS. 2004. Defects in cell adhesion and the visceral endoderm following ablation of nonmuscle myosin heavy chain II-A in mice. *The Journal of biological chemistry* **279**:41263–41266. DOI: https://doi.org/10.1074/jbc.C400352200, PMID: 15292239

Dard N, Louvet-Vallée S, Maro B. 2009. Orientation of mitotic spindles during the 8- to 16-cell stage transition in mouse embryos. *PLOS ONE* **4**:e8171. DOI: https://doi.org/10.1371/journal.pone.0008171, PMID: 19997595

De Iaco A, Planet E, Coluccio A, Verp S, Duc J, Trono D. 2017. DUX-family transcription factors regulate zygotic genome activation in placental mammals. *Nature genetics* **49**:941–945. DOI: https://doi.org/10.1038/ng.3858, PMID: 28459456

de Vries WN, Binns LT, Fancher KS, Dean J, Moore R, Kemler R, Knowles BB. 2000. Expression of Cre recombinase in mouse oocytes: a means to study maternal effect genes. *Genesis* **26**:110–112. PMID: 10686600

Deng Q, Ramsköld D, Reinius B, Sandberg R. 2014. Single-cell RNA-seq reveals dynamic, random monoallelic gene expression in mammalian cells. *Science* **343**:193–196. DOI: https://doi.org/10.1126/science.1245316, PMID: 24408435

Dumortier JG, Le Verge-Serandour M, Tortorelli AF, Mielke A, de Plater L, Turlier H, Maître JL2019. Hydraulic fracturing and active coarsening position the lumen of the mouse blastocyst. *Science* **365**:465–468. DOI: https://doi.org/10.1126/science.aaw7709, PMID: 31371608

Frankenberg SR, de Barros FR, Rossant J, Renfree MB. 2016. The mammalian blastocyst. *Wiley interdisciplinary reviews. Developmental biology* **5**:210–232. DOI: https://doi.org/10.1002/wdev.220, PMID: 26799266

Heisenberg CP, Bellaïche Y. 2013. Forces in tissue morphogenesis and patterning. *Cell* **153**:948–962. DOI: https://doi.org/10.1016/j.cell.2013.05.008, PMID: 23706734

Heuzé ML, Sankara Narayana GHN, D'Alessandro J, Cellerin V, Dang T, Williams DS, Van Hest JC, Marcq P, Mège RM, Ladoux B. 2019. Myosin II isoforms play distinct roles in *adherens* junction biogenesis. *eLife* **8**: e46599. DOI: https://doi.org/10.7554/eLife.46599, PMID: 31486768

Hirate Y, Hirahara S, Inoue K, Suzuki A, Alarcon VB, Akimoto K, Hirai T, Hara T, Adachi M, Chida K, Ohno S, Marikawa Y, Nakao K, Shimono A, Sasaki H. 2013. Polarity-dependent distribution of angiomotin localizes Hippo signaling in preimplantation embryos. *Current biology : CB* **23**:1181–1194. DOI: https://doi.org/10.1016/j.cub.2013.05.014, PMID: 23791731

Jacobelli J, Friedman RS, Conti MA, Lennon-Dumenil AM, Piel M, Sorensen CM, Adelstein RS, Krummel MF. 2010. Confinement-optimized three-dimensional T cell amoeboid motility is modulated via myosin IIA-regulated adhesions. *Nature immunology* **11**:953–961. DOI: https://doi.org/10.1038/ni.1936, PMID: 20835229

Kamei M, Saunders WB, Bayless KJ, Dye L, Davis GE, Weinstein BM. 2006. Endothelial tubes assemble from intracellular vacuoles in vivo. *Nature* **442**:453–456. DOI: https://doi.org/10.1038/nature04923, PMID: 16799567

Kawagishi R, Tahara M, Sawada K, Morishige K, Sakata M, Tasaka K, Murata Y. 2004. Na+/H+ Exchanger-3 is involved in mouse blastocyst formation. *Journal of Experimental Zoology* **301A**:767–775. DOI: https://doi.org/10.1002/jez.a.90

Kim D, Pertea G, Trapnell C, Pimentel H, Kelley R, Salzberg SL. 2013. TopHat2: accurate alignment of transcriptomes in the presence of insertions, deletions and gene fusions. *Genome biology* **14**:R36. DOI: https://doi.org/10.1186/gb-2013-14-4-r36, PMID: 23618408

Korotkevich E, Niwayama R, Courtois A, Friese S, Berger N, Buchholz F, Hiiragi T. 2017. The Apical Domain Is Required and Sufficient for the First Lineage Segregation in the Mouse Embryo. *Developmental cell* **40**:235–247. DOI: https://doi.org/10.1016/j.devcel.2017.01.006, PMID: 28171747

Kurotaki Y, Hatta K, Nakao K, Nabeshima Y, Fujimori T. 2007. Blastocyst axis is specified independently of early cell lineage but aligns with the ZP shape. *Science* **316**:719–723. DOI: https://doi.org/10.1126/science.1138591, PMID: 17446354

Laeno AM, Tamashiro DA, Alarcon VB. 2013. Rho-associated kinase activity is required for proper morphogenesis of the inner cell mass in the mouse blastocyst. *Biology of Reproduction* **89**:122. DOI: https://doi.org/10.1095/biolreprod.113.109470, PMID: 23946538

Law CW, Chen Y, Shi W, Smyth GK. 2014. voom: Precision weights unlock linear model analysis tools for RNA-seq read counts. *Genome biology* **15**:R29. DOI: https://doi.org/10.1186/gb-2014-15-2-r29, PMID: 24485249

Lecuit T, Yap AS. 2015. E-cadherin junctions as active mechanical integrators in tissue dynamics. *Nature cell biology* **17**:533–539. DOI: https://doi.org/10.1038/ncb3136, PMID: 25925582

Ma X, Takeda K, Singh A, Yu ZX, Zerfas P, Blount A, Liu C, Towbin JA, Schneider MD, Adelstein RS, Wei Q. 2009. Conditional ablation of nonmuscle myosin II-B delineates heart defects in adult mice. *Circulation research* **105**:1102–1109. DOI: https://doi.org/10.1161/CIRCRESAHA.109.200303, PMID: 19815823

Ma X, Jana SS, Conti MA, Kawamoto S, Claycomb WC, Adelstein RS. 2010. Ablation of nonmuscle myosin II-B and II-C reveals a role for nonmuscle myosin II in cardiac myocyte karyokinesis. *Molecular biology of the cell* **21**: 3952–3962. DOI: https://doi.org/10.1091/mbc.E10-04-0293, PMID: 20861308

Maître JL, Niwayama R, Turlier H, Nédélec F, Hiiragi T. 2015. Pulsatile cell-autonomous contractility drives compaction in the mouse embryo. *Nature cell biology* **17**:849–855. DOI: https://doi.org/10.1038/ncb3185, PMID: 26075357

Maître JL, Turlier H, Illukkumbura R, Eismann B, Niwayama R, Nédélec F, Hiiragi T. 2016. Asymmetric division of contractile domains couples cell positioning and fate specification. *Nature* **536**:344–348. DOI: https://doi.org/10.1038/nature18958, PMID: 27487217

Maître JL. 2017. Mechanics of blastocyst morphogenesis. *Biology of the cell* **109**:323–338. DOI: https://doi.org/10.1111/boc.201700029, PMID: 28681376

Motosugi N, Bauer T, Polanski Z, Solter D, Hiiragi T. 2005. Polarity of the mouse embryo is established at blastocyst and is not prepatterned. *Genes & development* **19**:1081–1092. DOI: https://doi.org/10.1101/gad.1304805, PMID: 15879556

Murrell M, Oakes PW, Lenz M, Gardel ML. 2015. Forcing cells into shape: the mechanics of actomyosin contractility. *Nature reviews. Molecular cell biology* **16**:486–498. DOI: https://doi.org/10.1038/nrm4012, PMID: 26130009

Muzumdar MD, Tasic B, Miyamichi K, Li L, Luo L. 2007. A global double-fluorescent Cre reporter mouse. *Genesis* **45**:593–605. DOI: https://doi.org/10.1002/dvg.20335, PMID: 17868096

Nishioka N, Inoue K, Adachi K, Kiyonari H, Ota M, Ralston A, Yabuta N, Hirahara S, Stephenson RO, Ogonuki N, Makita R, Kurihara H, Morin-Kensicki EM, Nojima H, Rossant J, Nakao K, Niwa H, Sasaki H. 2009. The Hippo signaling pathway components Lats and Yap pattern Tead4 activity to distinguish mouse trophectoderm from inner cell mass. *Developmental cell* **16**:398–410. DOI: https://doi.org/10.1016/j.devcel.2009.02.003, PMID: 19289085

Niwayama R, Moghe P, Liu YJ, Fabrèges D, Buchholz F, Piel M, Hiiragi T. 2019. A Tug-of-War between cell shape and polarity controls division orientation to ensure robust patterning in the mouse blastocyst. *Developmental Cell* **51**:564–574. DOI: https://doi.org/10.1016/j.devcel.2019.10.012, PMID: 31735668

Overeem AW, Bryant DM, van IJzendoorn SC2015. Mechanisms of apical-basal axis orientation and epithelial lumen positioning. *Trends in cell biology* **25**:476–485. DOI: https://doi.org/10.1016/j.tcb.2015.04.002, PMID: 25941134

Overholtzer M, Mailleux AA, Mouneimne G, Normand G, Schnitt SJ, King RW, Cibas ES, Brugge JS. 2007. A nonapoptotic cell death process, entosis, that occurs by cell-in-cell invasion. *Cell* **131**:966–979. DOI: https://doi.org/10.1016/j.cell.2007.10.040, PMID: 18045538

Özgüç Ö, Maître JL. 2020. Multiscale morphogenesis of the mouse blastocyst by actomyosin contractility. *Current opinion in cell biology* **66**:123–129. DOI: https://doi.org/10.1016/j.ceb.2020.05.002, PMID: 32711300

Płusa B, Piliszek A. 2020. Common principles of early mammalian embryo self-organisation. *Development* **147**: dev183079. DOI: https://doi.org/10.1242/dev.183079, PMID: 32699138

Ramkumar N, Baum B. 2016. Coupling changes in cell shape to chromosome segregation. *Nature reviews. Molecular cell biology* **17**:511–521. DOI: https://doi.org/10.1038/nrm.2016.75, PMID: 27353479

Rossant J. 2016. Making the Mouse Blastocyst: Past, Present, and Future. *Current topics in developmental biology* **117**:275–288. DOI: https://doi.org/10.1016/bs.ctdb.2015.11.015, PMID: 26969983

Rossi A, Kontarakis Z, Gerri C, Nolte H, Hölper S, Krüger M, Stainier DY. 2015. Genetic compensation induced by deleterious mutations but not gene knockdowns. *Nature* **524**:230–233. DOI: https://doi.org/10.1038/nature14580, PMID: 26168398

Royer C, Leonavicius K, Kip A, Fortin D, Nandi K, Vincent A, Jones C, Child T, Coward K, Graham C, Srinivas S. 2020. Establishment of a relationship between blastomere geometry and YAP localisation during compaction. *Development* **147**:dev189449. DOI: https://doi.org/10.1242/dev.189449, PMID: 32928909

Salbreux G, Charras G, Paluch E. 2012. Actin cortex mechanics and cellular morphogenesis. *Trends in cell biology* **22**:536–545. DOI: https://doi.org/10.1016/j.tcb.2012.07.001, PMID: 22871642

Samarage CR, White MD, Álvarez YD, Fierro-González JC, Henon Y, Jesudason EC, Bissiere S, Fouras A, Plachta N. 2015. Cortical tension allocates the first inner cells of the mammalian embryo. *Developmental Cell* **34**:435–447. DOI: https://doi.org/10.1016/j.devcel.2015.07.004, PMID: 26279486

Schliffka MF, Maître JL. 2019. Stay hydrated: basolateral fluids shaping tissues. *Current opinion in genetics & development* **57**:70–77. DOI: https://doi.org/10.1016/j.gde.2019.06.015, PMID: 31445440

Smith R, McLaren A. 1977. Factors affecting the time of formation of the mouse blastocoele. *Journal of Embryology and Experimental Morphology* **41**:79–92.

Smutny M, Cox HL, Leerberg JM, Kovacs EM, Conti MA, Ferguson C, Hamilton NA, Parton RG, Adelstein RS, Yap AS. 2010. Myosin II isoforms identify distinct functional modules that support integrity of the epithelial zonula adherens. *Nature cell biology* **12**:696–702. DOI: https://doi.org/10.1038/ncb2072, PMID: 20543839

Snow MH. 1973. Tetraploid mouse embryos produced by cytochalasin B during cleavage. *Nature* **244**:513–515. DOI: https://doi.org/10.1038/244513a0, PMID: 4621127

Stephenson RO, Yamanaka Y, Rossant J. 2010. Disorganized epithelial polarity and excess trophectoderm cell fate in preimplantation embryos lacking E-cadherin. *Development* **137**:3383–3391. DOI: https://doi.org/10.1242/dev.050195

Strumpf D, Mao CA, Yamanaka Y, Ralston A, Chawengsaksophak K, Beck F, Rossant J. 2005. Cdx2 is required for correct cell fate specification and differentiation of trophectoderm in the mouse blastocyst. *Development* **132**:2093–2102. DOI: https://doi.org/10.1242/dev.01801, PMID: 15788452

Taneja N, Bersi MR, Baillargeon SM, Fenix AM, Cooper JA, Ohi R, Gama V, Merryman WD, Burnette DT. 2020. Precise tuning of cortical contractility regulates cell shape during cytokinesis. *Cell Reports* **31**:107477. DOI: https://doi.org/10.1016/j.celrep.2020.03.041, PMID: 32268086

Taneja N, Burnette DT. 2019. Myosin IIA drives membrane bleb retraction. *Molecular biology of the cell* **30**: 1051–1059. DOI: https://doi.org/10.1091/mbc.E18-11-0752, PMID: 30785846

Tarkowski AK. 1959. Experiments on the development of isolated blastomers of mouse eggs. *Nature* **184**:1286–1287. DOI: https://doi.org/10.1038/1841286a0, PMID: 13836947

Tarkowski AK. 1961. Mouse chimaeras developed from fused eggs. *Nature* **190**:857–860. DOI: https://doi.org/10.1038/190857a0, PMID: 13775333

Tarkowski AK, Wróblewska J. 1967. Development of blastomeres of mouse eggs isolated at the 4- and 8-cell stage. *Journal of embryology and experimental morphology* **18**:155–180. PMID: 6048976

Thielicke W, Stamhuis EJ. 2014. PIVlab – Towards User-friendly, Affordable and Accurate Digital Particle Image Velocimetry in MATLAB. *Journal of Open Research Software* **2**:jors.bl. DOI: https://doi.org/10.5334/jors.bl

Thielicke W, Stamhuis EJ. 2020. *PIVlab v2.36 - Time-Resolved Digital Particle Image Velocimetry Tool for MATLAB*. https://figshare.com/articles/code/PIVlab_version_1_35/1092508

Tsichlaki E, FitzHarris G. 2016. Nucleus downscaling in mouse embryos is regulated by cooperative developmental and geometric programs. *Scientific reports* **6**:28040. DOI: https://doi.org/10.1038/srep28040, PMID: 27320842

Tullio AN, Accili D, Ferrans VJ, Yu ZX, Takeda K, Grinberg A, Westphal H, Preston YA, Adelstein RS. 1997. Nonmuscle myosin II-B is required for normal development of the mouse heart. *PNAS* **94**:12407–12412. DOI: https://doi.org/10.1073/pnas.94.23.12407, PMID: 9356462

Vega-Salas DE, Salas PJ, Rodriguez-Boulan E. 1988. Exocytosis of vacuolar apical compartment (VAC): a cell-cell contact controlled mechanism for the establishment of the apical plasma membrane domain in epithelial cells. *The Journal of cell biology* **107**:1717–1728. DOI: https://doi.org/10.1083/jcb.107.5.1717, PMID: 3053735

Vicente-Manzanares M, Ma X, Adelstein RS, Horwitz AR. 2009. Non-muscle myosin II takes centre stage in cell adhesion and migration. *Nature reviews. Molecular cell biology* **10**:778–790. DOI: https://doi.org/10.1038/nrm2786, PMID: 19851336

Wang A, Ma X, Conti MA, Liu C, Kawamoto S, Adelstein RS. 2010. Nonmuscle myosin II isoform and domain specificity during early mouse development. *PNAS* **107**:14645–14650. DOI: https://doi.org/10.1073/pnas.1004023107, PMID: 20679233

White MD, Zenker J, Bissiere S, Plachta N. 2018. Instructions for Assembling the Early Mammalian Embryo. *Developmental cell* **45**:667–679. DOI: https://doi.org/10.1016/j.devcel.2018.05.013, PMID: 29920273

Wicklow E, Blij S, Frum T, Hirate Y, Lang RA, Sasaki H, Ralston A. 2014. HIPPO pathway members restrict SOX2 to the inner cell mass where it promotes ICM fates in the mouse blastocyst. *PLOS genetics* **10**:e1004618. DOI: https://doi.org/10.1371/journal.pgen.1004618, PMID: 25340657

Yamamoto K, Otomo K, Nemoto T, Ishihara S, Haga H, Nagasaki A, Murakami Y, Takahashi M. 2019. Differential contributions of nonmuscle myosin IIA and IIB to cytokinesis in human immortalized fibroblasts. *Experimental cell research* **376**:67–76. DOI: https://doi.org/10.1016/j.yexcr.2019.01.020, PMID: 30711568

Yan L, Yang M, Guo H, Yang L, Wu J, Li R, Liu P, Lian Y, Zheng X, Yan J, Huang J, Li M, Wu X, Wen L, Lao K, Li R, Qiao J, Tang F. 2013. Single-cell RNA-Seq profiling of human preimplantation embryos and embryonic stem cells. *Nature structural & molecular biology* **20**:1131–1139. DOI: https://doi.org/10.1038/nsmb.2660, PMID: 23934149

Zaidel-Bar R, Zhenhuan G, Luxenburg C. 2015. The contractome–a systems view of actomyosin contractility in non-muscle cells. *Journal of cell science* **128**:2209–2217. DOI: https://doi.org/10.1242/jcs.170068, PMID: 26021351

Zenker J, White MD, Gasnier M, Alvarez YD, Lim HYG, Bissiere S, Biro M, Plachta N. 2018. Expanding actin rings zipper the mouse embryo for blastocyst formation. *Cell* **173**:776–791. DOI: https://doi.org/10.1016/j.cell.2018.02.035

Zhang Y, Conti MA, Malide D, Dong F, Wang A, Shmist YA, Liu C, Zerfas P, Daniels MP, Chan CC, Kozin E, Kachar B, Kelley MJ, Kopp JB, Adelstein RS. 2012. Mouse models of MYH9-related disease: mutations in nonmuscle myosin II-A. *Blood* **119**:238–250. DOI: https://doi.org/10.1182/blood-2011-06-358853, PMID: 21908426

Zhang Y, De Mets R, Monzel C, Acharya V, Toh P, Chin JFL, Van Hul N, Ng IC, Yu H, Ng SS, Tamir Rashid S, Viasnoff V. 2020. Biomimetic niches reveal the minimal cues to trigger apical lumen formation in single hepatocytes. *Nature Materials* **19**:1026–1035. DOI: https://doi.org/10.1038/s41563-020-0662-3

Zhang HT, Hiiragi T. 2018. Symmetry Breaking in the Mammalian Embryo. *Annual review of cell and developmental biology* **34**:405–426. DOI: https://doi.org/10.1146/annurev-cellbio-100617-062616, PMID: 30095292

Zhu M, Leung CY, Shahbazi MN, Zernicka-Goetz M. 2017. Actomyosin polarisation through PLC-PKC triggers symmetry breaking of the mouse embryo. *Nature Communications* **8**:921. DOI: https://doi.org/10.1038/s41467-017-00977-8, PMID: 29030553

Ziomek CA, Johnson MH. 1980. Cell surface interaction induces polarization of mouse 8-cell blastomeres at compaction. *Cell* **21**:935–942. DOI: https://doi.org/10.1016/0092-8674(80)90457-2, PMID: 7438209

Appendix 1

Appendix 1—table 1. Statistical analysis of compaction data.
Mean contact angles and developmental times related to ***Figure 1B*** and ***Figure 3B*** with associated SEM, embryo number, and p value from unpaired two-tailed Welch's *t* test against WT.

		Time after last third cleavage				Time before intial fourth cleavage				Time after last fourth cleavage				Time before intial fifth cleavage			
		Mean	SEM	Embryos	p value	Mean	SEM	Embryos	p value	Mean	SEM	Embryos	p value	Mean	SEM	Embryos	p value
WT	Time after 3rd cleavage [h]	0	0	23	NA	7.0	0.3	23	NA	10.9	0.3	21	NA	16.7	0.4	22	NA
	Contact angle [°]	87	3		NA	147	2		NA	140	3		NA	148	2		NA
mzMyh9	Time after 3rd cleavage [h]	0	0	15	NA	9.8	0.5	15	*0.0001*	13.8	0.6	10	*0.002*	18.8	0.5	8	*0.01*
	Contact angle [°]	85	2		*0.5*	125	4		*0.00001*	104	5		*0.00001*	131	8		*0.02*
mMyh9	Time after 3rd cleavage [h]	0	0	8	NA	10.4	0.7	8	*0.001*	14.6	0.8	8	*0.002*	18.7	0.7	3	*0.002*
	Contact angle [°]	86	5		*0.5*	115	6		*0.0001*	112	7		*0.003*	113	21		*0.1*
mzMyh10	Time after 3rd cleavage [h]	0	0	11	NA	5.4	0.4	11	*0.004*	10.2	0.6	11	*0.2*	15.8	0.4	11	*0.1*
	Contact angle [°]	87	5		*0.8*	121	4		*0.0001*	126	5		*0.03*	148	4		*0.8*
mMyh10	Time after 3rd cleavage [h]	0	0	20	NA	6.3	0.4	20	*0.2*	10.8	0.3	20	*0.5*	16.8	0.6	20	*0.9*
	Contact angle [°]	85	3		*0.3*	128	5		*0.0004*	128	3		*0.006*	149	2.8		*0.5*
mzMyh9; mzMyh10	Time after 3rd cleavage [h]	0	0	7	NA	9.7	0.8	3	*0.07*	12	NA	1	NA	NA			
	Contact angle [°]	89	6		*0.8*	117	4		*0.006*	84.5	NA		*NA*				
mzMyh9; mMyh10	Time after 3rd cleavage [h]	0	0	7	NA	6.9	1.7	4	*1.0*	9	0.5	2	*0.1*	12	NA	1	NA
	Contact angle [°]	83	5		*0.6*	100	5		*0.002*	108	14		*0.07*	113	NA		*NA*
mMyh9; mMyh10	Time after 3rd cleavage [h]	0	0	7	NA	8	1.3	5	*0.5*	11	0.5	3	*1.0*	NA			
	Contact angle [°]	76	7		*0.1*	110	5		*0.0006*	105	3		*0.002*				

Appendix 1—table 2. Statistical analysis of cell cycle duration data.
Mean durations of 8-cell stage, fourth wave of cleavage, and 16-cell stage related to ***Figures 2B*** and ***5B*** with associated SEM, embryo number, and p value from unpaired two-tailed Welch's *t* test against WT.

	Duration of 8-cell stage [h]				Duration of fourth wave of cleavages [h]				Duration of 16-cell stage [h]			
	Mean	SEM	Embryos	p value	Mean	SEM	Embryos	p value	Mean	SEM	Embryos	p value
WT	7.0	0.3	23	NA	4.0	0.3	23	NA	5.5	0.4	23	NA
mzMyh9	9.8	0.5	15	*0.0001*	4.8	0.7	15	*0.3*	5.7	0.8	14	*0.8*
mMyh9	10.4	0.7	8	*0.001*	4.2	1.2	8	*0.9*	7.0	1.1	8	*0.1*
mzMyh10	5.4	0.4	11	*0.004*	4.8	0.8	11	*0.2*	5.6	0.5	11	*0.9*
mMyh10	6.3	0.4	20	*0.2*	4.5	0.4	20	*0.3*	6.1	0.5	20	*0.4*

Continued on next page

Appendix 1—table 2 continued

	Duration of 8-cell stage [h]				Duration of fourth wave of cleavages [h]				Duration of 16-cell stage [h]			
	Mean	SEM	Embryos	p value	Mean	SEM	Embryos	p value	Mean	SEM	Embryos	p value
mzMyh9; mzMyh10	10.3	1.4	8	*0.06*	2.0	0.8	3	*0.1*				
mzMyh9; mMyh10	8.1	1.4	6	*0.5*	4.3	1.1	3	*0.8*	NA			
mMyh9;mMyh10	9.3	1.0	8	*0.06*	3.6	0.7	5	*0.6*				

Appendix 1—table 3. Statistical analysis of periodic contraction data.
Mean amplitude of periodic movements and contact angle related to ***Figure 2H*** with associated SEM, embryo number, and p value from Mann-Whitney *U* test against WT.

		Maximum amplitude within 50–120 s oscillation period range [µm]			Contact angle [°]		
	Embryos	Mean	SEM	p value	Mean	SEM	p value
WT	21	0.146	0.009	NA	126	5	NA
mzMyh9	15	0.037	0.002	*0.000003*	78	3	*0.000003*
mMyh9	8	0.041	0.003	*0.00002*	82	6	*0.001*
mzMyh10	11	0.077	0.009	*0.004*	103	6	*0.02*
mMyh10	20	0.094	0.014	*0.007*	108	5	*0.02*

RESEARCH ARTICLE

Figures and figure supplements

Multiscale analysis of single and double maternal-zygotic *Myh9* and *Myh10* mutants during mouse preimplantation development

Markus Frederik Schliffka *et al*

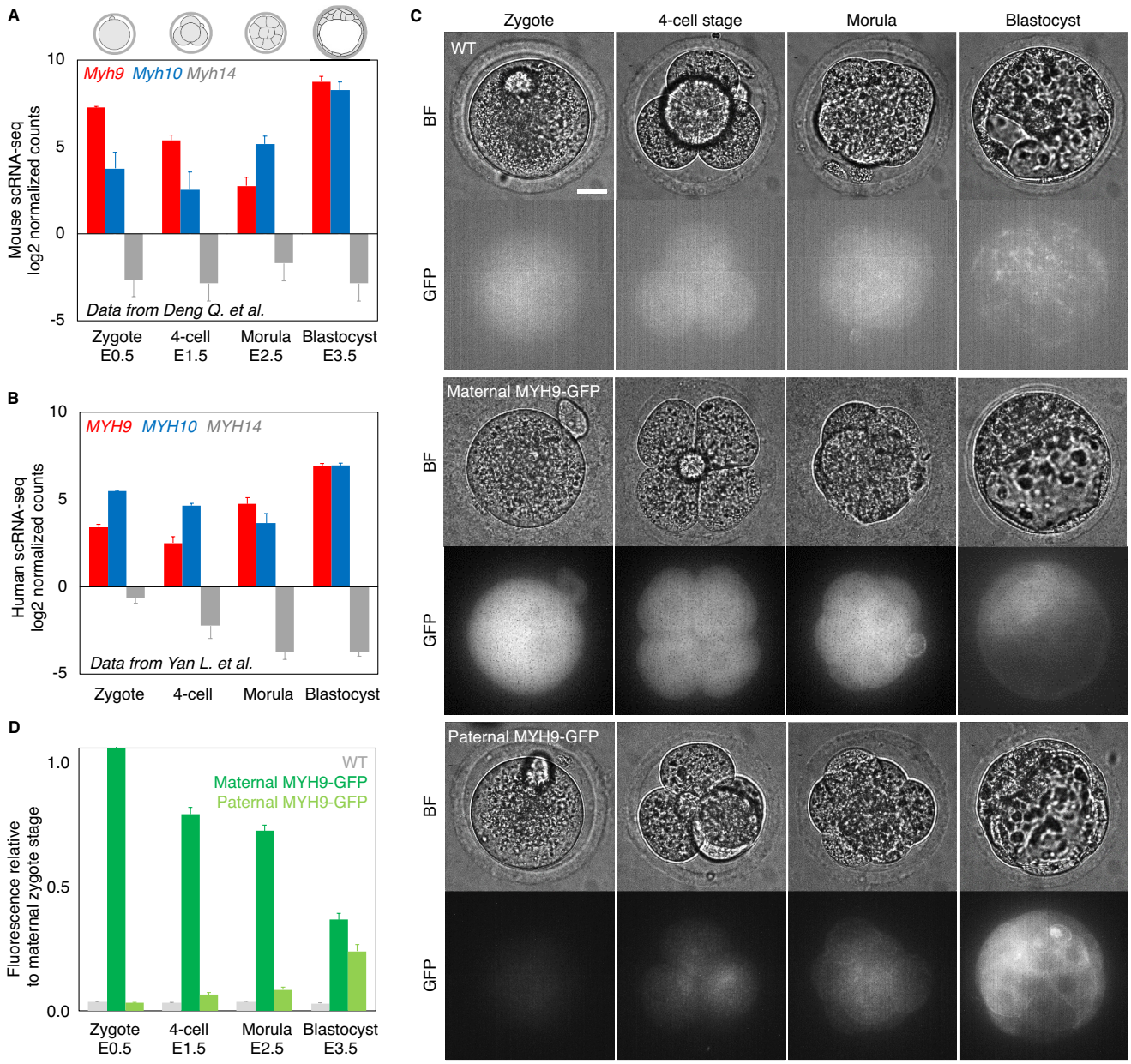

Figure 1—figure supplement 1. Analysis of the expression of non-muscle myosin II heavy chain (NMHC) paralogs during preimplantation development based on single cell RNA sequencing and MYH9-GFP fluorescence. (**A**) Mouse single cell RNA sequencing analysis adapted from ***Deng et al., 2014***, showing the expression levels of *Myh9* (red), *Myh10* (blue), and *Myh14* (grey) at the zygote, four-cell, morula, and blastocyst stages. Data show mean ± SEM. (**B**) Human single cell RNA sequencing analysis adapted from ***Yan et al., 2013***, showing the expression levels of *MYH9* (red), *MYH10* (blue), and *MYH14* (grey) at the zygote, four-cell, morula, and blastocyst stages. Data show mean ± SEM. (**C**) Representative images of WT (top) and transgenic embryos expressing a GFP-tagged version of MYH9 from their maternal (middle) or paternal (bottom) allele at the zygote, four-cell, morula, and blastocyst stages. LUT is adjusted to the brightest signal of each respective genotype. (**D**) MYH9-GFP fluorescent level normalized to maternal MYH9-GFP at the zygote stage. Data originate from three independent experiments for the WT (grey) from zygote to blastocyst stage (n = 6), maternal MYH9-GFP (dark green) zygote stage (n = 23), maternal MYH9-GFP from 4-cell stage to blastocyst stage (n = 24), and paternal MYH9-GFP (light green) from zygote to blastocyst stage (n = 22). Data show mean ± SEM. Scale bars, 20 μm.

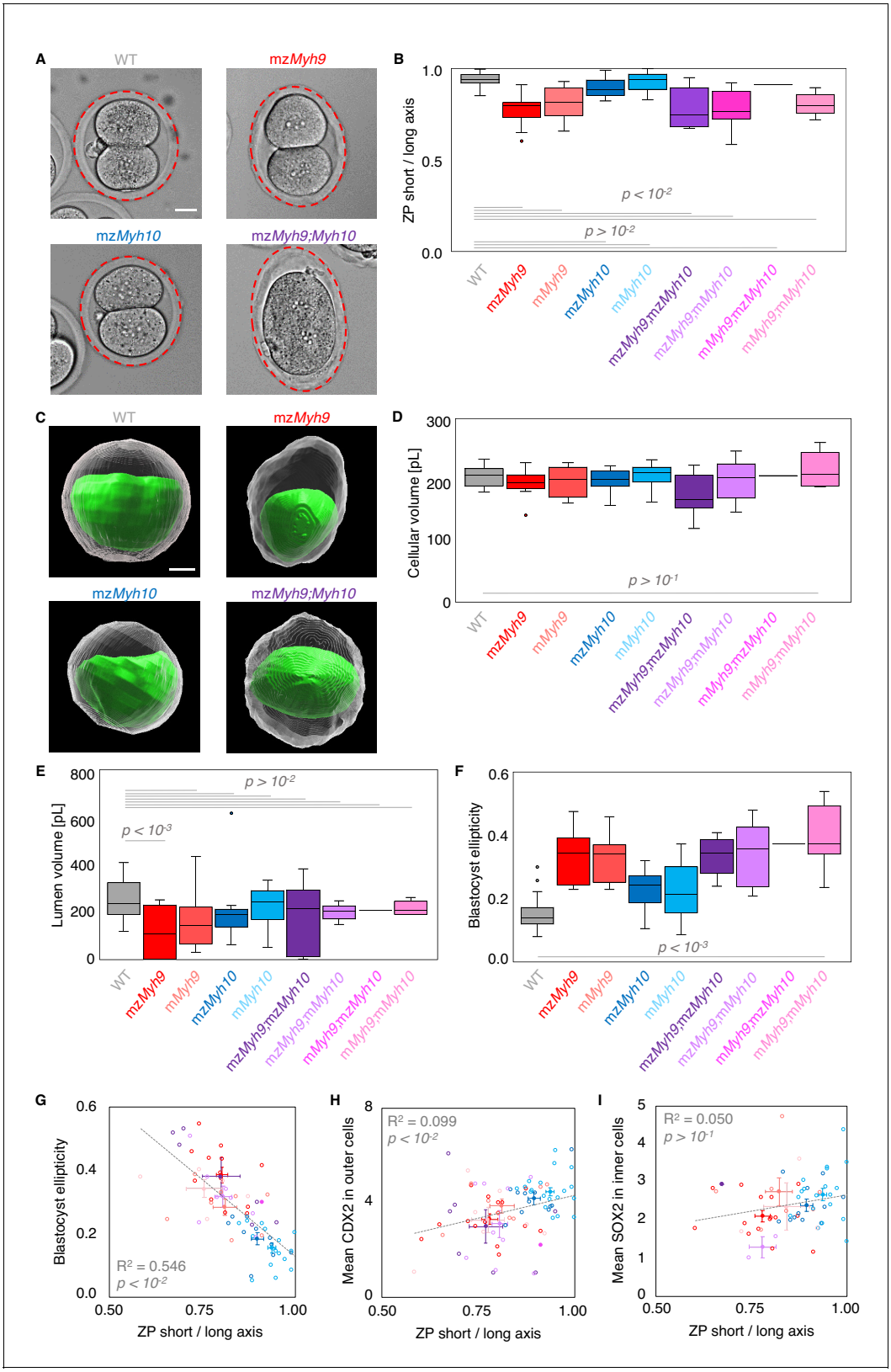

Figure 2—figure supplement 1. Macroscopic shape analysis of maternal-zygotic *Myh9* and *Myh10* mutant embryos. (**A**) Representative images of E1.5 WT, mz*Myh9*, mz*Myh10*, and mz*Myh9;*mz*Myh10* embryos. The zona pellucida is highlighted with a red ellipse. (**B**) Boxplot of the short/long axis ratio of

Figure 2—figure supplement 1 continued on next page

Figure 2—figure supplement 1 continued

an ellipse manually fitted onto the zona pellucida of E1.5 embryos that are WT (grey, n = 23), mz*Myh9* (red, n = 15), m*Myh9* (light red, n = 8), mz*Myh10* (blue, n = 11), m*Myh10* (light blue, n = 19), mz*Myh9;*mz*Myh10* (purple, n = 8), mz*Myh9;*m*Myh10* (lilac, n = 9), m*Myh9;*mz*Myh10* (pink, n = 1), and m*Myh9;* m*Myh10* (bubblegum, n = 7) mutants. (**C**) Representative images of segmented WT, mz*Myh9*, mz*Myh10*, and mz*Myh9;*mz*Myh10* blastocysts. The segmented lumen is shown in green. The cellular volume, shown in grey, results from subtracting the lumen volume from the segmented embryo volume. (**D-F**) Cellular (**D**) and lumen (**E**) volumes, and 3D oblate ellipticity (**F**) of segmented WT (grey, n = 23), mz*Myh9* (red, n = 13), m*Myh9* (light red, n = 8), mz*Myh10* (blue, n = 10), m*Myh10* (light blue, n = 16), mz*Myh9;*mz*Myh10* (purple, n = 6), mz*Myh9;*m*Myh10* (lilac, n = 8), m*Myh9;*mz*Myh10* (pink, n = 1), and m*Myh9;*m*Myh10* (bubblegum, n = 5) mutants. (**G-I**) Blastocyst ellipticity (**G**), CDX2 N/C ratio in outer cells (**H**), or SOX2 N/C ratio in inner cells (**I**) as a function of the ZP short/long axis at the 2-cell stage. mz*Myh9* (red, n = 13/15/15), m*Myh9* (light red, n = 8/8/7), mz*Myh10* (blue, n = 10/11/11), m*Myh10* (light blue, n = 16/19/19), mz*Myh9;*mz*Myh10* (purple, n = 6/7/1), mz*Myh9;*m*Myh10* (lilac, n = 8/9/2), m*Myh9;*mz*Myh10* (pink, n = 1/1/0), and m*Myh9;*m*Myh10* (bubblegum, n = 5/7/3) mutants. Open circles show individual embryos and filled circles give mean ± SEM of a given genotype. Pearson's R^2 and p value are indicated. Scale bars, 20 μm. Welch's *t* test p values compared to WT are shown.

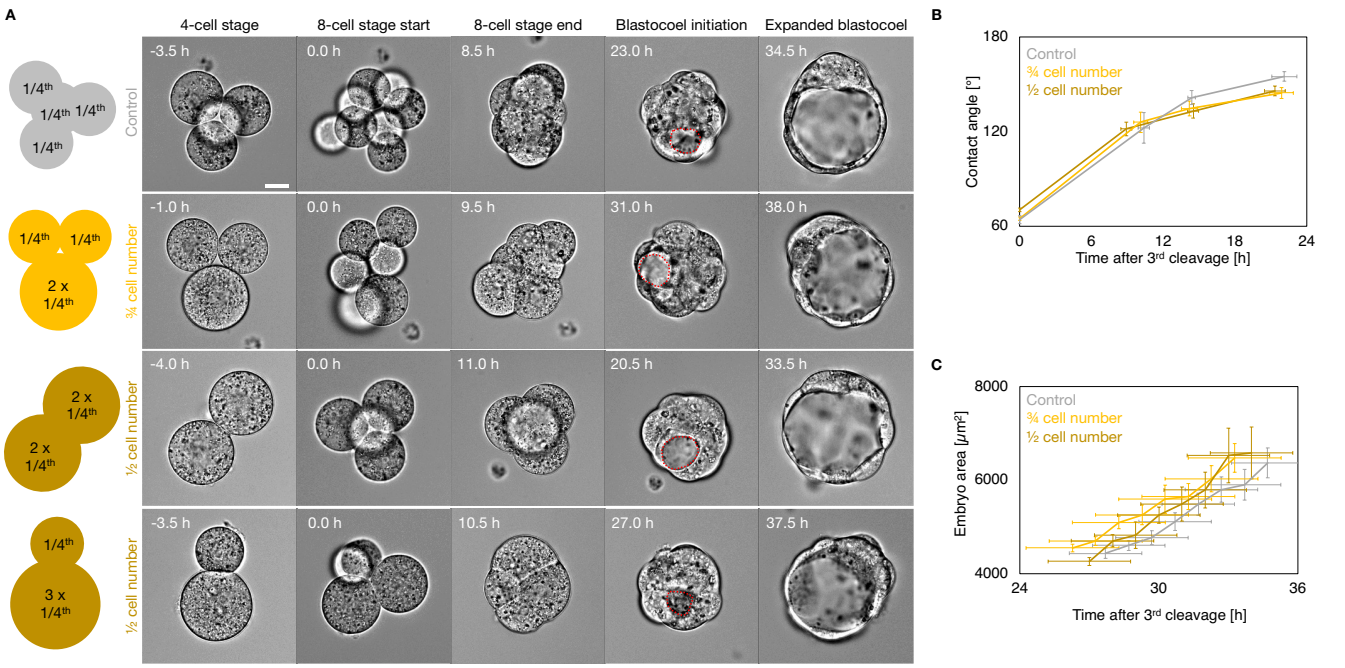

Figure 2—figure supplement 2. Morphogenesis of embryos with blastomeres fused at the 4-cell stage. (**A**) Schematic diagram of 4-cell stage embryos with four cells (control) or after fusion with three cells, two cells of equal or unequal sizes. Representative images of long-term time-lapse of embryos withfour cells (control), or after fusion with three cells, two cells of equal or unequal sizes at the end of the 4-cell stage, start and end of the 8-cell stage, at the initiation of blastocoel formation, and early blastocyst stage (***Figure 2—video 4***). Scale bar, 20 µm. Time in hours after the third cleavage. Dotted red lines indicate the nascent lumen. (**B**) Contact angle of control (grey, n = 12, 12, 12, 12), ¾ cell number (yellow, n = 12, 12, 12, 9), and ½ cell number (brown, n = 4, 4, 4, 4) embryos after the third cleavage, before and after the fourth cleavage, and before the fifth cleavage. Data show mean ± SEM. (**C**) Embryo growth during lumen formation for control (grey, n = 10), ¾ cell number (yellow, n = 11), and ½ cell number (brown, n = 4) embryos measured for seven continuous hours after a lumen of at least 20 µm is observed (as in blastocoel initiation of panel A). Data show mean ± SEM.

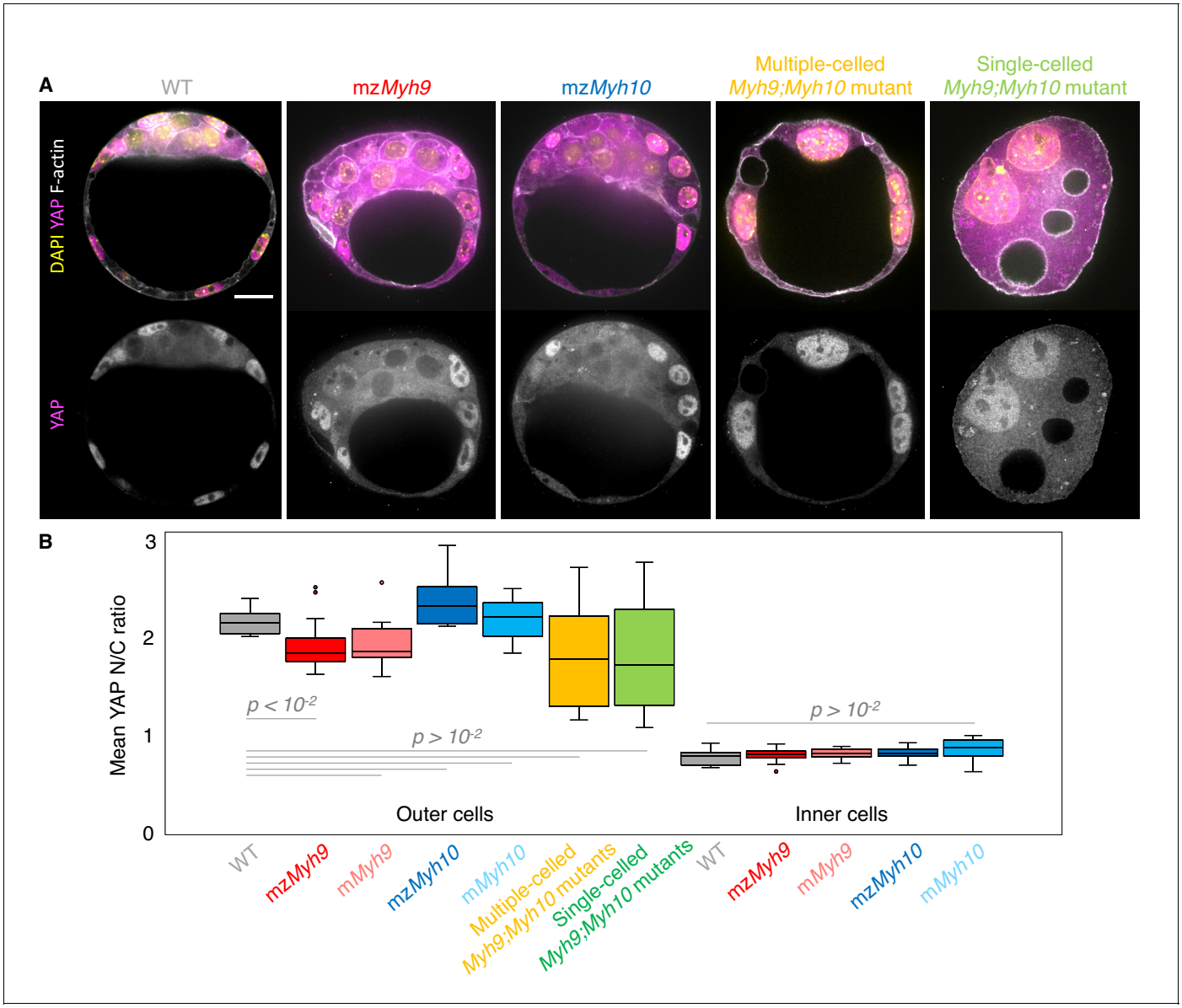

Figure 3—figure supplement 1. Analysis of YAP localization in maternal-zygotic *Myh9* and *Myh10* mutant embryos. (**A**) Representative images of WT, mz*Myh9*, mz*Myh10*, and multiple- or single-celled *Myh9;Myh10* mutant embryos stained for YAP (magenta), DAPI (yellow), and F-actin (grey). Scale bar, 20 µm. (**B**) Mean nuclear to cytoplasmic (N/C) ratio of YAP for outer and inner cells from WT (grey, n = 15), mz*Myh9* (red, n = 19), m*Myh9* (light red, n = 9), mz*Myh10* (blue, n = 6), m*Myh10* (light blue, n = 13) embryos and outer cells from multiple-celled *Myh9;Myh10* (yellow, n = 10) and single-celled *Myh9;Myh10* (green, n = 9) mutant embryos. Mann-Whitney *U* test p values compared to WT are indicated.

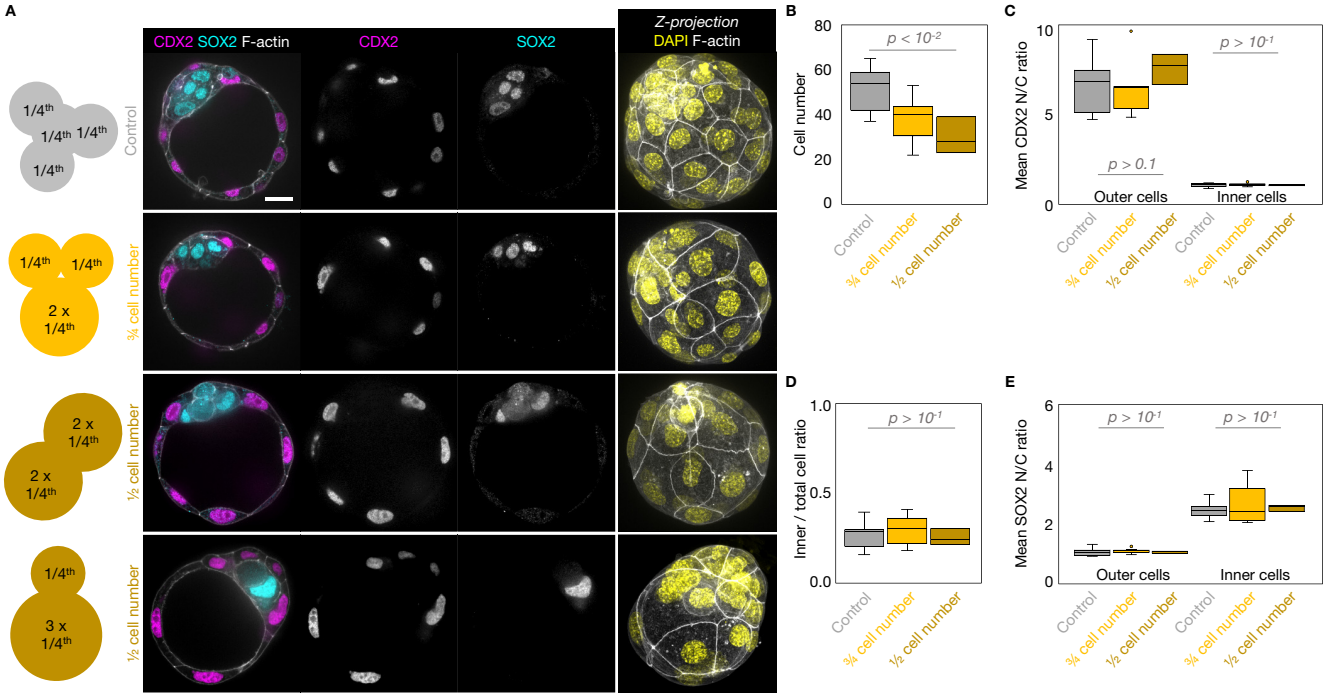

Figure 3—figure supplement 2. Lineage specification of embryos with blastomeres fused at the 4-cell stage. (**A**) Schematic diagram of 4-cell stage embryos with four cells (control) or after fusion with three cells, two cells of equal or unequal sizes. Representative images of embryos with four cells (control), or after fusion with three cells, two cells of equal or unequal sizes stained for TE and ICM markers CDX2 (magenta) and SOX2 (cyan). DAPI in yellow and F-actin in grey. The same fused embryos as in ***Figure 2—figure supplement 2A*** are shown. (**B-D**) Total cell number (**B**) and proportion of inner cells (**D**) in control (grey, n = 11), ¾ cell number (yellow, n = 9), and ½ cell number (brown, n = 3) embryos. (**C-E**) N/C ratio of CDX2 (**C**) and SOX2 (**E**) staining for outer (left) or inner (right) cells from control (grey, n = 11), ¾ cell number (yellow, n = 9), and ½ cell number (brown, n = 3) embryos. Scale bars, 20 µm. Mann-Whitney *U* test p values compared to WT are indicated.

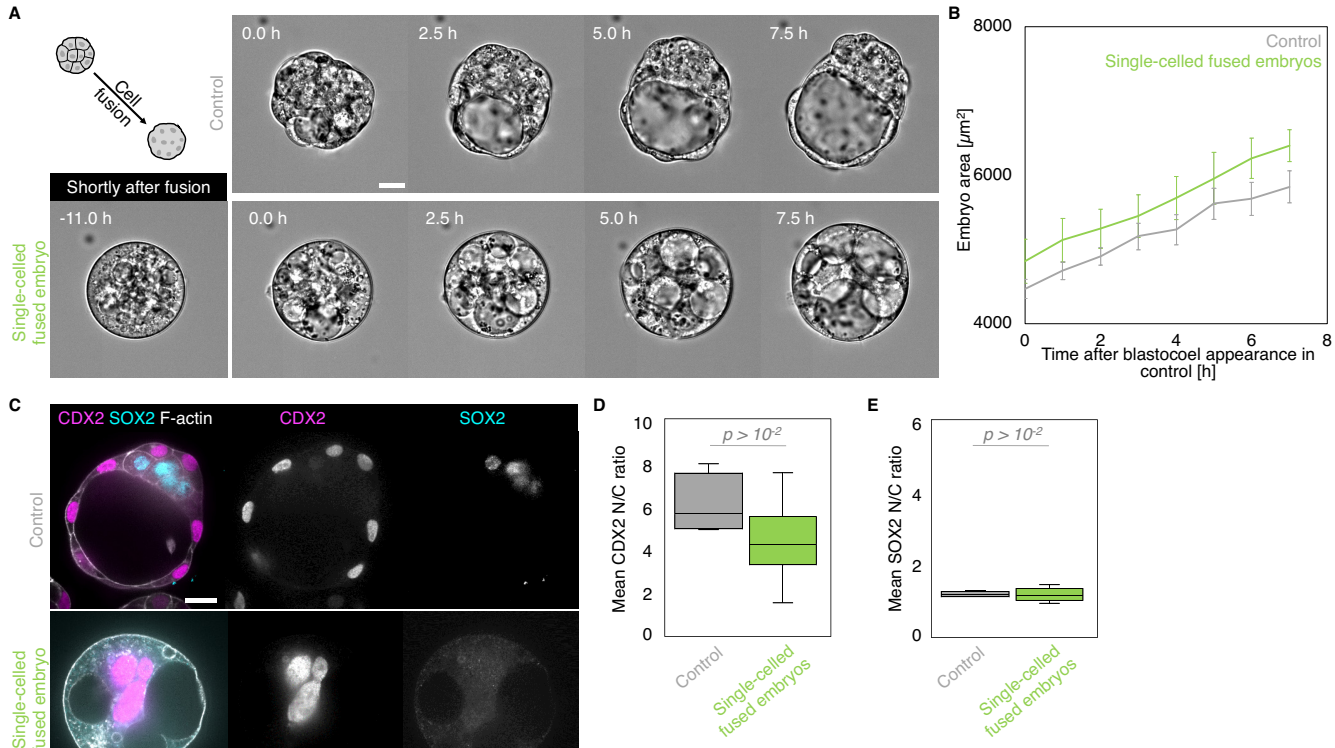

Figure 8—figure supplement 1. Morphogenesis and lineage specification of embryos with all blastomeres fused at the late morula stage. (**A**) Representative images of long-term time-lapse of control and fused single-celled embryos at the onset of fluid accumulation (***Figure 8—video 2***). A schematic diagram of the cell fusion process is shown, with a picture of the representative fused embryo shown right after the fusion. Scale bar, 20 µm. (**B**) Embryo growth curves during fluid accumulation for control (grey, n = 8) and fused single-celled (light green, n = 7) embryos measured for seven continuous hours after a lumen of at least 20 µm is observed. Data show mean ± SEM. (**C**) Representative images of control and fused single-celled embryos stained for TE and ICM markers CDX2 (magenta) and SOX2 (cyan), DAPI (yellow), and F-actin (grey). Scale bar, 20 µm. (**D-E**) N/C ratio of CDX2 (**D**) and SOX2 (**E**) staining for outer cells from averaged control (grey, n = 4) and fused single-celled (light green, n = 6) embryos. Mann-Whitney *U* test p values compared to control are indicated.

Legends for the movies pertaining to *Multiscale analysis of single and double maternal-zygotic Myh9 and Myh10 mutants during mouse preimplantation development*
https://elifesciences.org/articles/68536

Figure 2—video 1

Preimplantation development of WT, mz*Myh9*, and mz*Myh10* embryos.

Long-term time-lapse imaging of WT (left), mz*Myh9* (middle), and mz*Myh10* (right) embryos from the 4-cell stage onwards. Images are taken every 30 min; scale bar is 20 μm. Time is given in hours following the last division from the third wave of cleavages.

Figure 2—video 2

Periodic waves of contraction in WT, mz*Myh9*, mz*Myh10*, and mz*Myh9;*mz*Myh10* embryos.

Short-term time-lapse imaging of WT (top left), mz*Myh9* (top right), mz*Myh10* (bottom left), and mz*Myh9;*mz*Myh10* (bottom right) embryos. Images are taken every 5 s; scale bar is 20 μm.

Figure 2—video 3

Failed cleavage in mz*Myh9* embryos.

Long-term time-lapse imaging of an mz*Myh9* embryo during the third cleavage wave. Images are taken every 30 min; scale bar is 20 μm.

Figure 2—video 4

Preimplantation development of control, ¾, and ½ cell number embryos.

Long-term time-lapse imaging of control (top left), ¾ cell number (top right), and ½ cell number (after the fusion events of two pairs of blastomeres on bottom left or after the fusion of three blastomeres on bottom right) embryos from the 4-cell stage onwards. Images are taken every 30 min; scale bar is 20 μm. Time is given in hours following the last division from the third wave of cleavages.

Figure 5—video 1

Preimplantation development of mz*Myh9;*mz*Myh10* embryos.

Long-term time-lapse imaging of mz*Myh9;*mz*Myh10* embryos forming an ICM (left), or without ICM (right) from the equivalent of the 2-cell stage onwards. Images are taken every 30 min; scale bar is 20 μm. Time is given in hours following the last tentative division from the third wave of cleavages.

Figure 8—video 1

Preimplantation development of an m*Myh9;*m*Myh10* embryo failing all successive cleavages.

Long-term time-lapse imaging of an m*Myh9;*m*Myh10* embryo failing all successive cleavages. Images are taken every 30 min; scale bar is 20 μm. Time is given in hours following the last putative division from the third wave of cleavages.

Figure 8—video 2

Fluid accumulation in control and single-celled fused embryos.

Long-term time-lapse imaging of control (left) and single-celled fused (right) embryos around the time of the fifth wave of cleavage onwards. Images are taken every 30 min; scale bar is 20 μm. Time is given in hours following the time at which a lumen of about 20 μm is visible in the control embryo.

2.2 Research paper B: Inverse blebs operate as hydraulic pumps during mouse blastocyst formation

Background

With the formation of the blastocoel, the first lumen of mammalian development, the embryo is first confronted with the challenge to accommodate and direct intercellular fluid. As detailed in the introduction, the embryo forms the blastocoel in a process of hydraulic fracturing and coarsening, in which hundreds of microlumens compete for fluid until only the final blastocoel remains. The positioning of the embryo can be patterned by manipulation of adhesion and contractility patterns. While the entire lumen formation process takes around 5 h to complete, microlumen dynamics take place in the range of tens of minutes.

Aims

We asked how actomyosin contractility, which often manifests itself at a fast timescale in the mouse embryo [181,182], can influence microlumen dynamics which occur on a longer timescale. To this end, we performed confocal and light-sheet live imaging with high temporal resolution of the blastocoel formation process.

Results

We discovered short-lived membrane protrusions forming at cell-cell contacts which we call *inverse blebs*. Inverse blebs form during the microlumen phase of blastocoel formation and disappear as the final lumen forms. Using genetic and pharmacological perturbations of the embryo, we found that inverse blebs form due to pressure imbalances of the intercellular fluid, which are favored by local fluid confinement by cell-cell adhesion molecules (CDH1). After their formation and extension in ca. 15 s, inverse blebs retract within ca. 40 s due to the contractile action of actin and myosin, which are recruited to the inverse bleb membrane. We integrate our understanding of inverse bleb formation and retraction in a biophysical model. Within the embryo, we only observe inverse blebs at the contact of two cells, but not of multiple cells. By manipulation of the embryo topology, we identified multicellular junctions as pressure sinks and inverse blebs as a way for the cell to direct fluid away from bicellular contacts

towards multicellular microlumens, thereby promoting the coarsening process. Our findings highlight inverse blebs as a mechanism for the embryo to actively redistribute fluid within the microlumen network employing actomyosin contractility.

This manuscript has been prepared for publication. Movies referred to in the text can be found here:
https://www.dropbox.com/sh/9p24uvmo1ij8bgg/AACGNOG9Xwg02kDj3OEu8LrYa?dl=0
The movie legends can be found in the manuscript.

This study has been published as a non-peer reviewed preprint:
Markus F. Schliffka, Julien G. Dumortier, Diane Pelzer, Arghyadip Mukherjee and Jean-Léon Maître (2023): **Inverse blebs operate as hydraulic pumps during mouse blastocyst formation.**
https://doi.org/10.1101/2023.05.03.539105
https://www.biorxiv.org/content/10.1101/2023.05.03.539105v1

Contributions to the manuscript:
I performed all experiments in this manuscript with the following exceptions: Dextran inclusion in Figure 1E/Movie 3 was performed by J.G.D. Cdh1 gDNA design, cloning and injection, as well as Lap2B-GFP mRNA injection, were performed by D.P. I analyzed all data in this manuscript. The analysis of single bleb dynamics and actomyosin dynamics in Fig.1 and Extended Data Figure 1 was performed using a custom R script written by J.G.D. I participated in the conceptualization and experimental design of this project, in the acquisition of funds and the editing of the manuscript.

A.M. developed and wrote the biophysical theory presented in the supplementary note in the manuscript, based on the experimental data and observations that I provided. He developed the biophysical theory in constant exchange with me and J.-L.M.

Inverse blebs operate as hydraulic pumps during mouse blastocyst formation

Markus F. Schliffka[1,2], Julien G. Dumortier[1], Diane Pelzer[1], Arghyadip Mukherjee[3*] and Jean-Léon Maître[1*]

[1] Institut Curie, CNRS UMR3215, INSERM U934, PSL Research University, Sorbonne Université, Paris, France.
[2] Carl Zeiss SAS, Marly-le-Roy, France.
[3] Laboratoire de physique de l'École Normale Supérieure, CNRS UMR 8023, PSL Research University, Sorbonne Université, Université Paris Cité, Paris 75005, France.
*Correspondence to jean-leon.maitre@curie.fr and arghyadip.mukherjee@ens.fr

During preimplantation development, mouse embryos form a fluid-filled lumen, which sets their first axis of symmetry [1,2]. Pressurized fluid breaks open cell-cell contacts and accumulates into pockets, which gradually coarsen into a single lumen [3–5]. During coarsening, the adhesive and contractile properties of cells are thought to guide intercellular fluid (IF) but what cell behavior may control fluid movements is unknown. Here, we report large fluid-filled spherical membrane intrusions called inverse blebs [6,7] growing into cells at adhesive contacts. At the onset of lumen coarsening, we observed hundreds of inverse blebs throughout the embryo, each dynamically filling with IF and retracting within a minute. We find that inverse blebs grow due to pressure build-up resulting from luminal fluid accumulation and cell-cell adhesion, which locally confines fluid. Inverse blebs then retract due to actomyosin contraction, which effectively redistributes fluid within the intercellular space. Importantly, inverse blebs show topological specificity and only occur at contacts between two cells, not at contacts formed by multiple cells, which essentially serve as fluid sinks. Manipulating the topology of the embryo reveals that, in the absence of sinks, inverse blebs pump fluid into one another in a futile cycle. We propose that inverse blebs operate as hydraulic pumps to promote luminal coarsening, thereby constituting an instrument used by cells to control fluid movement.

All living cells are immersed in fluid [8]. Within animal tissues, the amount of fluid between cells varies greatly from blood, where plasma constitutes the majority of tissue volume, to dense tissues, where IF is hardly detected. During embryonic development or the formation of organoids, relocation of IF is suspected to influence tissue jamming [9–11] or topological transitions when fluid lumens form [12]. In some of the most striking relocations of IF, pressurized fluid can even fracture tissues [3,13,14]. In large fluid compartments, such as lumens, the movement of IF can be controlled by specialized cell protrusions called cilia [15], but in packed tissues we are only beginning to understand how cells control the fluid surrounding them [16].

During the formation of the first mammalian lumen, pressurized fluid fractures cell-cell contacts into hundreds of microlumens, which eventually coarsen into a single lumen called the blastocoel [3] (Fig. 1A). As observed in mouse embryos [3] and in a reconstituted in vitro model [17], fracturing follows the path of lowest cell-cell adhesion and, once trapped into microlumens, fluid follows gradients of pressure set by cell mechanics. Therefore, the physical properties of cells guide IF throughout the embryo and determine the position of the first mammalian lumen, which is key to set its dorsoventral axis [1,2]. How active cellular processes modulate pressure gradients and guide IF in a complex three-dimensional geometry remains unknown. Regulation of actomyosin activity is a likely mechanism to modulate hydrostatic pressure locally [4,18–20] and thus IF movements. However, the levels of actomyosin contractility are weak at cell-cell contacts, which translates into low tensions [3,21]. Moreover, actomyosin processes typically act on faster timescales (tens of seconds to minutes [22,23]) compared to the lifetime of microlumen networks (several hours) [3]. How cell contractility could act at cell-cell contacts is thus unclear.

To examine whether fast actomyosin processes occur during lumen positioning, we imaged 32-cell stage mouse embryos at the onset of lumen formation with high spatiotemporal resolution. Imaging the plasma membrane, we observed short-lived hemispherical intrusions at cell-cell contacts growing several microns into cells in ~15 s before retracting within ~40 s (Fig. 1B-D, Movie 1-2). Compared to microlumens growing ~1 μm for ~3 h between cell-cell contacts [3], such intrusions are larger and

shorter lived. Actin and non-muscle myosin II appear at these intrusions only as they retract, with actin detected shortly before reaching maximal size and myosin arriving ~5 s later (Fig. 1D and Extended Data Fig. 1A, Movie 1-2). Both actin and myosin signals increase, rapidly peaking ~20 s after the maximal extension of the intrusion, before they return to the weak basal level typical of cell-cell contacts [21] (Fig. 1A-C, Extended Data Fig. 1B, Movie 1-2). Such dynamics are characteristic of blebs, which are hemispherical protrusions growing without actin before being retracted by actomyosin within ~1 min [20,24,25]. Therefore, we will refer to these intrusions as *inverse blebs*, since contrary to classical outward blebs they grow into the cytoplasm. Inverse blebs have been described previously at the free apical surface of zebrafish endothelial cells [6] and of mouse hepatocytes [7]. Here, inverse blebs appear at basolateral cell-cell contacts. Importantly, inverse blebs forming at cell-cell contacts of mouse embryos do not result from a cell pushing an outward bleb into its neighbor. Rather, we observed decreased membrane signal intensity at the inverse bleb surface (Fig. 1D), indicating that plasma membranes from contacting cells locally detach and accumulate IF, as confirmed by labelling IF with a fluorescent dextran (Fig. 1E, Movie 3). Also, the intrusions are not secretory vesicles [26,27] since membrane could clearly be seen expanding from the cell-cell contact while IF fills them up (Fig. 1C, E), Movie 1-3). We also considered the possibility that intrusions would be macropinocytotic cups, which also fill up with IF [28]. However, macropinocytotic cups grow due to actin polymerization, which is not the case with the intrusions observed here expanding without actin (Fig. 1C-E, Movie 1-2). Taken together, these observations reveal inverse blebs operating at very fast timescales, inflating and retracting within a minute at the adhesive contacts of mouse embryos (Fig. 1D).

To investigate the link between short-lived inverse blebs and long-term blastocoel formation, we performed full volume light-sheet microscopy to image inverse blebs throughout lumen formation (Movie 4) and quantified their spatiotemporal dynamics. Inverse blebs can be observed for about 3 h during lumen formation, with a maximum of ~15 blebs per minute on average (Fig. 1F). The maximal blebbing activity precedes the rapid growth of the lumen. In fact, by the time the blastocoel reaches a size of ~5 pL, equivalent to the volume of a single 32-cell stage blastomere [3,29], over 80 % of

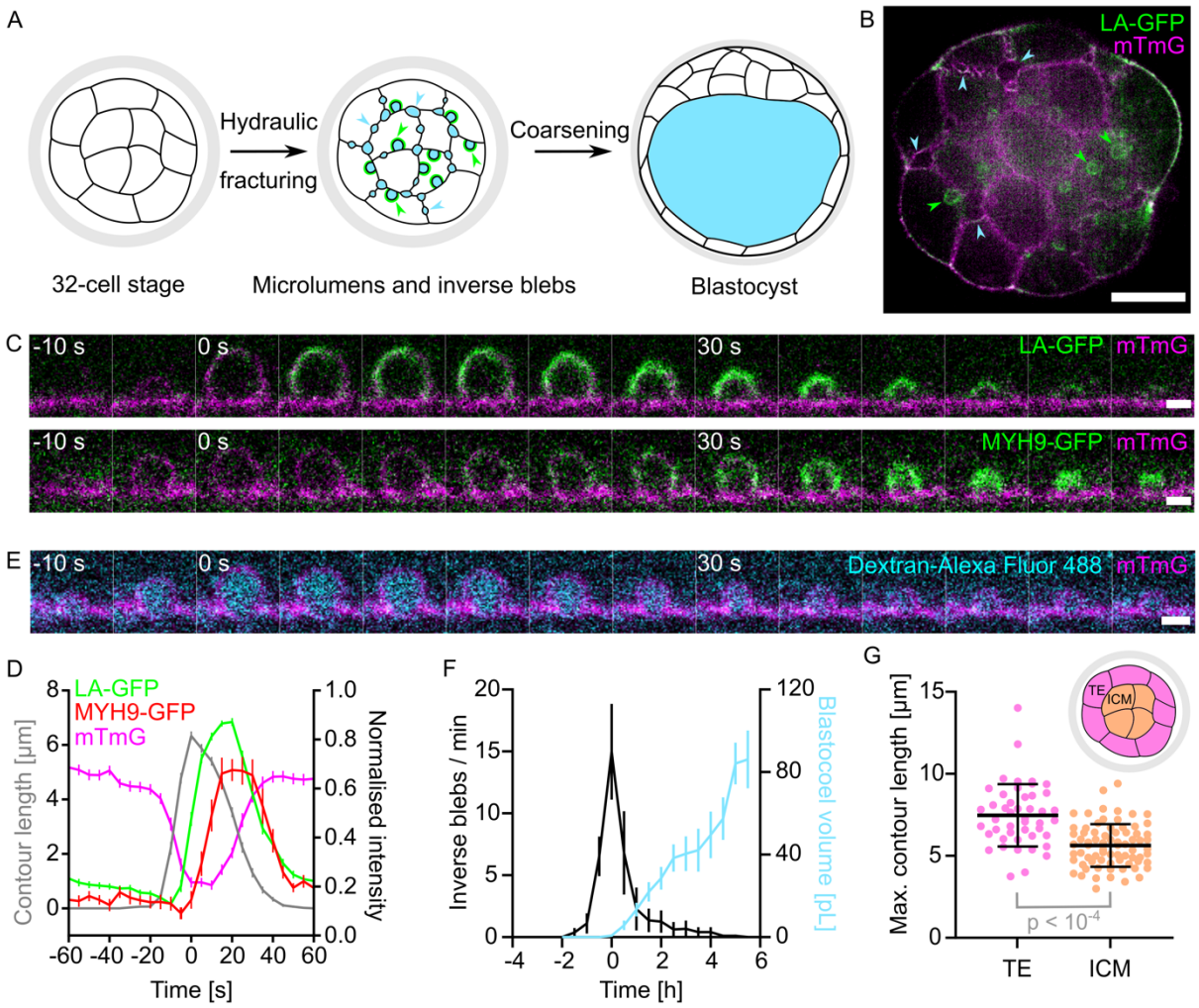

Figure 1: Inverse blebs at the onset of blastocoel formation

A) Schematic diagram of blastocyst lumen formation showing a 32-cell stage embryo before (left) and after (middle) hydraulic fracturing of cell-cell contacts and after the coarsening of fluid-filled (blue) pockets into a single lumen to form a blastocyst (right). After fracturing and before coarsening of the lumen, two types of fluid pockets can be observed: microlumens (blue arrowheads, symmetric, without actin in green) and inverse blebs (green arrowheads, asymmetric, coated with actin).

B) Equatorial plane of a 32-cell stage mouse embryo with LifeAct-GFP (LA-GFP) in green and mTmG in magenta (Movie 1). Green arrowheads point at LA-GFP positive inverse blebs and blue arrowheads at LA-GFP negative microlumens. Scale bar, 20 μm.

C) Still images following the lifetime of an inverse bleb shown with mTmG in magenta and LA-GFP (top, Movie 1) or MYH9-GFP (bottom, Movie 2) in green. Images taken every 5 s with time indicated relative to the maximal inverse bleb size. Scale bars, 2 μm.

D) Mean contour length (grey, n = 121 blebs from 18 embryos) and normalized LA-GFP (green, n = 100 blebs from 13 embryos), MYH9-GFP (red, n = 21 blebs from 5 embryos) or mTmG (magenta, n = 142 blebs from 23 embryos) intensity of inverse blebs synchronized to their maximal extension. Error bars show SEM.

E) Still images following the lifetime of an inverse bleb shown with Dextran-Alexa Fluor 488 (labelling intercellular fluid) in cyan and mTmG in magenta (Movie 3). Images taken every 5 s with time indicated relative to the maximal inverse bleb size. Scale bar, 2 μm.

(legend cont.)
F) Number of inverse blebs per minute observed in embryos imaged every 10 s for 5 min repeated every 30 min in their full volume using light-sheet microscopy (Movie 4) during blastocoel formation. The volume of the segmented blastocoel is shown in blue. Mean ± SEM values of 8 embryos are calculated after synchronizing embryos to the time of maximal inverse bleb number.
G) Maximal contour length of inverse blebs growing in trophectoderm (TE, pink, n = 46 blebs from 18 embryos) and inner cell mass (ICM, peach, n = 75 blebs from 18 embryos) cells. Mean and SD are shown in black bracket. p value results from Student's t test. Top-left: schematic diagram showing TE and ICM cells location in a 32-cell stage embryo.

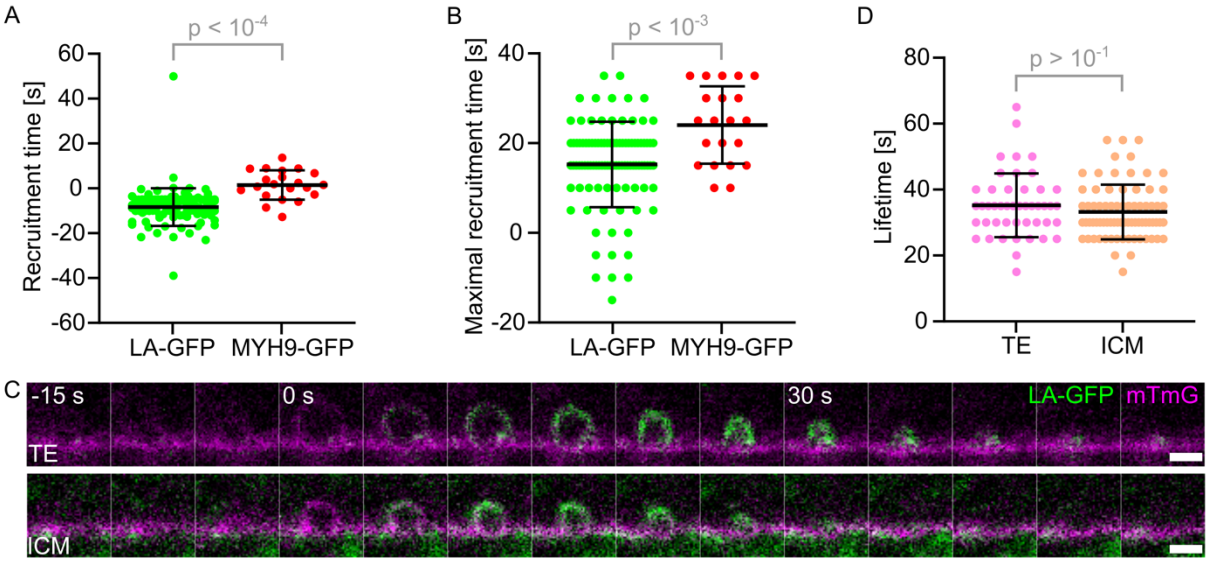

Extended Data Figure 1: Dynamics of individual inverse blebs
A) Initial recruitment time of LA-GFP (green, n = 100 blebs from 13 embryos) and MYH9-GFP (red, n = 21 blebs from 5 embryos) to inverse blebs. Mean and SD are shown in black bracket. p value results from Student's t test.
B) Maximal recruitment time of LA-GFP (green, n = 100 blebs from 13 embryos) and MYH9-GFP (red, n = 21 blebs from 5 embryos) to inverse blebs. Mean and SD are shown in black bracket. p value results from Student's t test.
C) Still images following the lifetime of an inverse blebs shown with LA-GFP in green and mTmG in magenta for a TE (top lane) and an ICM (bottom lane) cell. Images taken every 5 s with time indicated relative to the maximal inverse bleb size. Scale bars, 2 μm.
D) Inverse bleb lifetime in TE (pink, n = 46 blebs from 18 embryos) and ICM (peach, n = 75 blebs from 18 embryos) cells. Mean and SD are shown in black bracket. p value results from Student's t test.

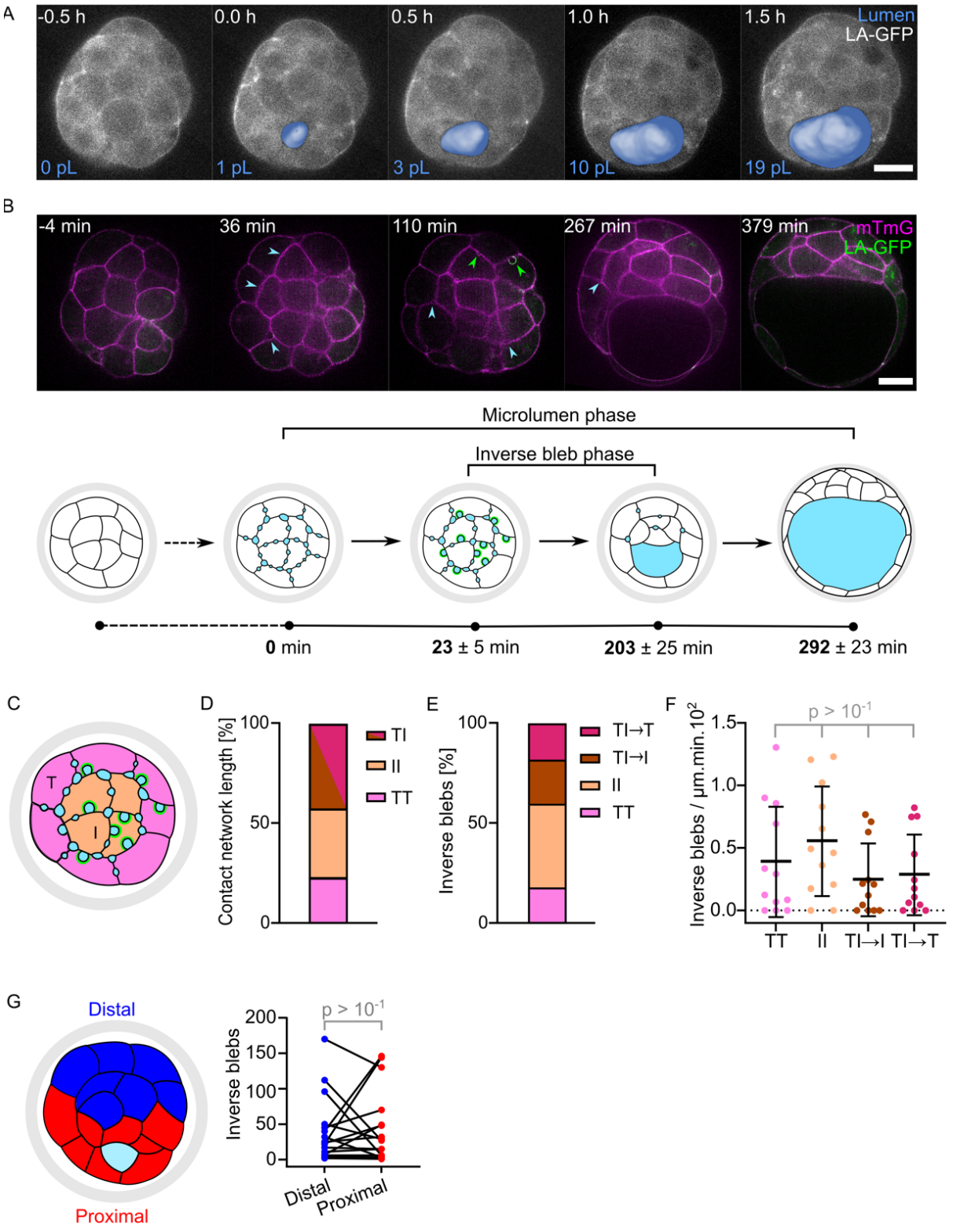

Extended Data Figure 2: Spatiotemporal dynamics of inverse blebs throughout blastocoel formation

A) Equatorial plane of a 32-cell stage embryo with the segmented lumen (blue) overlaid on LA-GFP (grey, Movie 4). The volume of the segmented lumen is indicated on the bottom left. Scale bar, 20 μm.

B) Top: equatorial plane of a 32-cell stage embryo with LA-GFP in green and mTmG in magenta (Movie 5) at distinct steps of lumen formation. Blue arrowheads point at LA-GFP negative

(legend cont.)
microlumens, green arrowheads point at LA-GFP positive inverse blebs. Scale bar, 20 μm. Bottom: schematic diagrams of the distinct steps leading to the formation of the blastocoel (large blue structure) with mean ± SEM characteristic times measured in 18 embryos relative to the apparition of microlumens (small blue pockets) in a 32-cell stage embryo enclosed in the zona pellucida (grey). The microlumen phase corresponds to the time during which microlumens can be detected while the inverse bleb phase represents the duration of observation of inverse blebs (blue pockets coated with green actin).
C) Schematic diagram of 32-cell stage embryo enclosed within the zona pellucida (grey) showing inverse blebs (asymmetric intrusions coated with green actomyosin and filled with blue luminal fluid) and microlumens (symmetric pockets of blue luminal fluid) between surface trophectoderm (pink, T) and inner cell mass cells (peach, I).
D) Proportion of contact length relative to the cell-cell contact network within the imaging plane for TE-TE (TT, pink), ICM-ICM (II, peach) or TE-ICM (TI, brown-purple) from 12 embryos.
E) Proportion of inverse blebs growing at TE-TE (pink), ICM-ICM (peach) and TE-ICM interfaces with the direction of growth into TE (brown) or ICM (purple) indicated for TE-ICM interfaces from 12 embryos.
F) Number of inverse blebs observed per minute normalized by the length of cell-cell contacts at given tissue interfaces in the optical slice of embryos imaged using spinning disk microscopy (Movie 5). Inverse blebs are captured growing between trophectoderm cells (TT, n = 57), inner cell mass cells (II, n = 129), into inner cell mass cells (TI->I, n = 72) or into trophectoderm cells (TI->T, n = 63) at the interface between trophectoderm and inner cell mass cells of 12 embryos. Mean and SD are shown in black bracket. p values result from Kruskal-Wallis and Dunn's multiple comparison tests.
G) Left: schematic diagram of 32-cell stage embryo within the zona pellucida (grey) where cells were labeled as proximal (red) or distal (dark blue) relative to the position of the growing blastocoel (light blue structure).
Right: Number of inverse blebs observed throughout development on the distal and proximal halves of 17 embryos. p value results from paired Student's t test.

blebs have already occurred (Fig. 1F, Extended Data Fig. 2A). Therefore, inverse blebs occur transiently during the nucleation phase of lumen formation. Using spinning disk confocal microscopy to resolve smaller microlumens, we systematically observed microlumens appearing ~20 min before the first inverse bleb and persisting ~90 min after the last inverse bleb (Extended Data Fig. 2B, Movie 5). Therefore, short-lived inverse blebs do not precede microlumens, but always coexist with them and share the same IF to inflate (Movie 3). Microlumens and inverse blebs form at the interface of both trophectoderm (TE) and inner cell mass (ICM) cells, the two cell lineages forming the blastocyst. Previously, we found that due to the different mechanics of TE and ICM cells, microlumens show distinct shapes at their respective interfaces [3]. Here, we measured larger inverse blebs in TE than in ICM cells (Fig. 1G, Extended Data Fig. 1C), which retract within the same time (Extended Data Fig. 1D). The

different growth could be explained by the lower pressure in TE cells compared to ICM cells [3,30] and indicates that an inverse bleb growing in TE cells displaces more fluid than when growing in ICM cells. We further observed that inverse blebs appear without significant bias at all types of cell-cell contacts: between two TE cells, two ICM cells or between a TE and an ICM cell (once corrected for contact type sampling, Extended Data Fig. 2C-F). Finally, counting inverse blebs throughout lumen formation and analyzing their position relative to the final location of the blastocoel revealed no clear relationship (Extended Data Fig. 2G). Taken together, we find that inverse blebs are temporally regulated and show lineage specific characteristics.

Unlike outward blebs and other inverse blebs observed so far, inverse blebs of preimplantation embryos grow at adhesive cell-cell contacts. On the one hand, adhesion could prevent the nucleation and growth of inverse blebs by keeping the intercellular space shut. On the other hand, adhesion molecules form clusters at the edges of microlumens [3] and at the neck of inverse blebs (Extended Data Fig. 3A-D, Movie 6), and thus could trap the fluid needed for the growth of inverse blebs. To explore the role of adhesion, we imaged embryos in which *Cdh1* is maternally knocked out (m*Cdh1*$^{+/-}$) [31]. m*Cdh1*$^{+/-}$ embryos form a blastocyst while displaying microlumens for a significantly shorter time than wildtype (WT) embryos (Extended Data Fig. 4A-B, Movie 7). In m*Cdh1*$^{+/-}$ embryos, we observed that microlumens tend to fuse into a single lumen instead of progressively coarsening by exchanging fluid at a distance as observed in WT embryos (Movie 7). This is consistent with cell-cell contacts being less adhesive and providing less mechanical resistance to the accumulation of pressurized fluid. Hence, reduced adhesion increases hydraulic compliance within the embryo, as evidenced in reconstituted in vitro settings [17]. In m*Cdh1*$^{+/-}$ embryos, we rarely observed inverse blebs and, if so, in reduced numbers compared to WT embryos (Fig. 2A-B, Extended Data Fig. 4C, Movie 8), which, as suggested above, indicates a critical role of adhesion in entrapment of fluid at cell-cell contacts needed for inverse bleb nucleation and/or growth. Since adhesion could promote the local accumulation of fluid in pockets of low adhesion, we tested the local effects of adhesion by generating chimeric embryos with half of the embryo expressing lower levels of CDH1. This was achieved by knocking out *Cdh1* zygotically (z*Cdh1*) via CRISPR/Cas9 microinjection

at the 2-cell stage (Extended Data Fig. 4D-E). As reported previously [3], chimeric embryos fractured cell-cell contacts and formed a lumen preferentially located on the hydraulically compliant z*Cdh1* side of chimeric embryos (Extended Data Fig. 4E). In z*Cdh1* chimeric embryos, we did not observe inverse blebbing on either the mutant or WT side of the embryo (Extended Data Fig. 4F), revealing that a regional reduction of adhesion can alter the global hydraulics of the embryo. Therefore, adhesion provides an essential local confinement of intercellular fluid, which promotes inverse blebbing and can alter the mode of lumen coarsening globally.

Outward blebs inflate because the cytoplasmic pressure is higher than the medium pressure, which results from the actomyosin cortex compressing the cytoplasm [19]. In the case of inverse blebs observed in zebrafish endothelial cells, inverse blebs inflate due to blood pressure [6]. In preimplantation embryos, we suspected that accumulation of luminal fluid could be responsible for the pressure increase necessary for inverse blebs. Luminal fluid accumulates by osmosis, to prevent this we blocked sodium transport by inhibiting sodium/proton exchangers with ethylisopropyl amiloride (EIPA) or the sodium/potassium pump with ouabain [32,33]. Either treatment prevented lumen formation in most embryos and inverse blebs could rarely be observed, and if so only when lumen formation would occur (Extended Data Fig. 5). To dynamically tune the accumulation of luminal fluid, we acutely treated blebbing embryos with EIPA, which caused inverse blebs to almost completely vanish within 15 min of treatment (Fig. 2C-D, Movie 9). Importantly, acutely treated embryos conserved their IF, microlumen network and small lumens that had formed before the treatment (Fig. 2C, Movie 9), indicating that there would be in principle enough fluid to inflate inverse blebs. Therefore, luminal fluid accumulation and the resulting build-up of hydrostatic pressure are required to inflate inverse blebs.

These initial observations hint at the following scenario: fluid accumulation, confined between adhesion pockets (Extended Data Fig. 3A-B), raises IF pressure until a first threshold is reached for microlumens to form (Extended Data Fig. 2B); further raising IF pressure above a second threshold nucleates inverse blebs, which stop when fluid ceases to accumulate (Fig. 2C-D) and does not need to occur in the absence of firm

adhesion throughout the embryo (Fig. 2A-B, Extended Data Fig. 4C-F); finally, once a sufficiently large lumen of a few pL has formed (Fig. 1F, Extended Data Fig. 2A), adhesion confinement is locally reduced and IF pressure drops, leading first to the disappearance of inverse blebs and then of microlumens (Extended Data Fig. 2B). To better conceptualize the roles of cell-cell adhesion and fluid accumulation in the nucleation of inverse blebs, we formulate a minimal physical model of fluid pockets confined between two cells, which could form both stable microlumens or dynamic inverse blebs (Supplementary Note). Taking into account the pressure build-up within the IF, the elasticity provided by clustered adhesion sites at the periphery and tensions

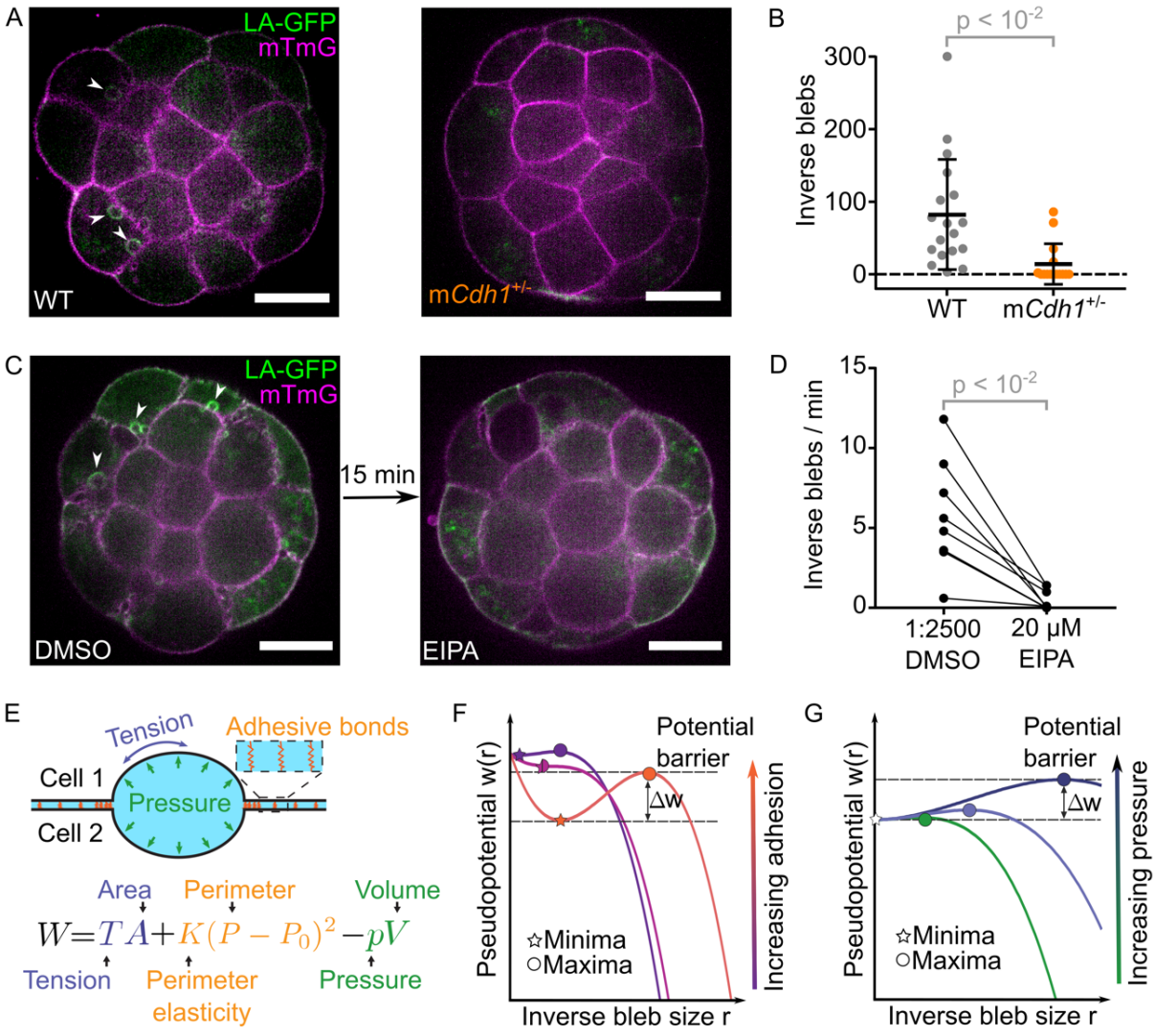

Figure 2: Inverse blebs formation requires cell-cell adhesion and fluid accumulation
A) Equatorial planes of WT (left) and m*Cdh1*$^{+/-}$ (right) embryos with LifeAct-GFP (LA-GFP) in green and mTmG in magenta (Movie 7). Arrowheads point at inverse blebs. Scale bars, 20 μm.

(legend cont.)

B) Number of inverse blebs observed at the equatorial plane of WT (grey, n = 18) and m*Cdh1*$^{+/-}$ (orange, n = 15) embryos imaged every 1 min using spinning disk microscopy. Mean and SD are shown in black bracket. p value results from Mann-Whitney U test.

C) Equatorial planes of embryos with LifeAct-GFP (LA-GFP) in green and mTmG in magenta in 1:2500 DMSO control medium and after 15 min of treatment with 20 μM EIPA (Movie 9). Arrowheads point at inverse blebs. Scale bars, 20 μm.

D) Number of inverse blebs observed per minute in the equatorial plane of 8 embryos in 1:2500 DMSO control medium and after 15 min of treatment with 20 μM EIPA. p value results from paired Wilcoxon test.

E) Schematic diagram of a fluid pocket trapped between two cells. The pseudopotential W characterizing the propensity of the fluid pocket to form an inverse bleb depends on the tension T at the surface of the pocket of area A, the perimeter elasticity K of the adhesion bonds (orange) around the pocket of perimeter P and resting perimeter P_0 and, the hydrostatic pressure p of the pocket of volume V.

F-G) Pseudopotential w as a function of the inverse bleb size r with varying adhesion strength k (F) or pressure p (G). Normalized units, see Supplementary Note. For each example, the minima (star) and maxima (circle) are indicated. Only conditions with sufficient adhesion or low pressure allow for a finite potential barrier Δw needed to maintain the coexistence of microlumens and inverse blebs.

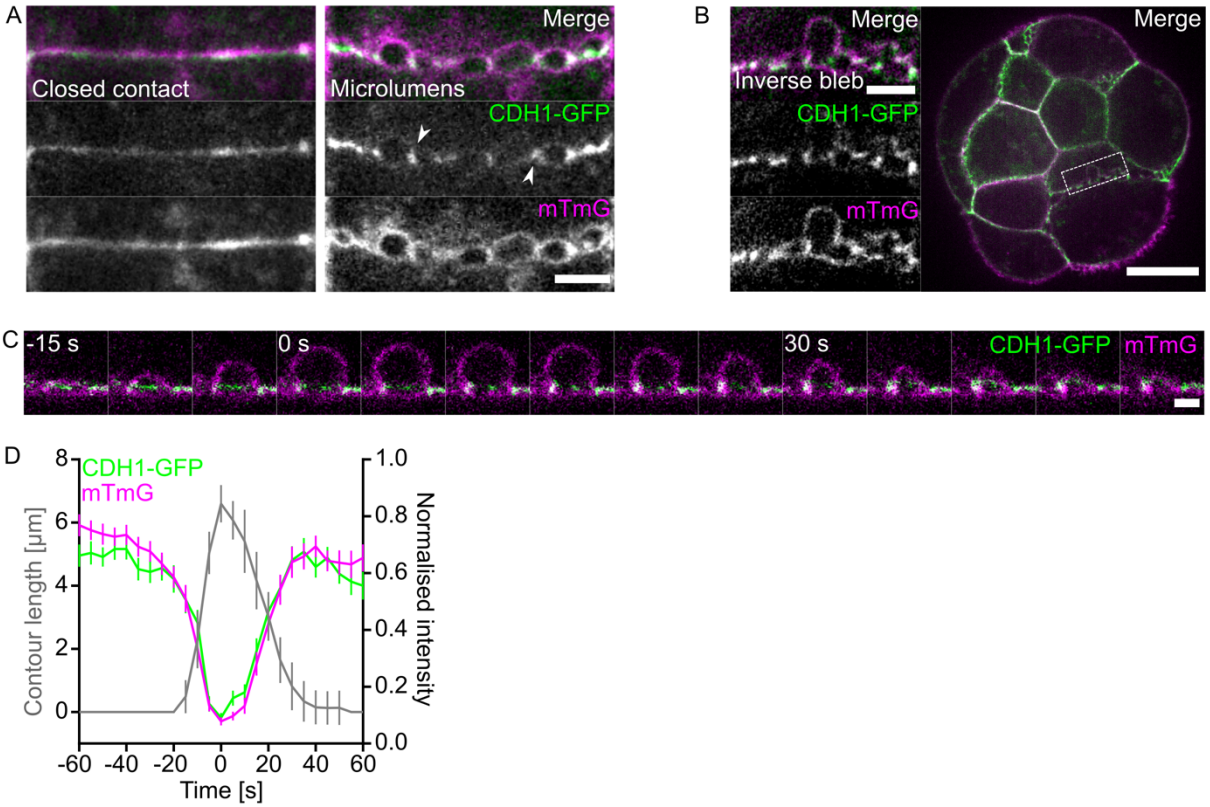

Extended Data Figure 3: Dynamics of adhesion molecules in individual inverse blebs

A) Still images showing cell-cell contacts before and after the formation of microlumens with CDH1-GFP in green and mTmG in magenta. Arrowheads point at foci of CDH1 around microlumens. Scale bar, 5 μm.

(legend cont.)

B) Equatorial plane of a 32-cell stage embryo with CDH1-GFP in green and mTmG in magenta (Movie 6). Scale bar, 20 μm. Dashed rectangle shows a cell-cell contact with an inverse bleb magnified on the left. Scale bar, 5 μm.

C) Still images following the lifetime of an inverse bleb shown with mTmG in magenta and CDH1-GFP in green. Images taken every 5 s with time indicated relative to the maximal inverse bleb size. Scale bar, 2 μm.

D) Mean contour length (grey), normalized CDH1-GFP (green) and mTmG (magenta) intensities of 31 inverse blebs from 7 embryos synchronized to their maximal extension. Error bars show SEM.

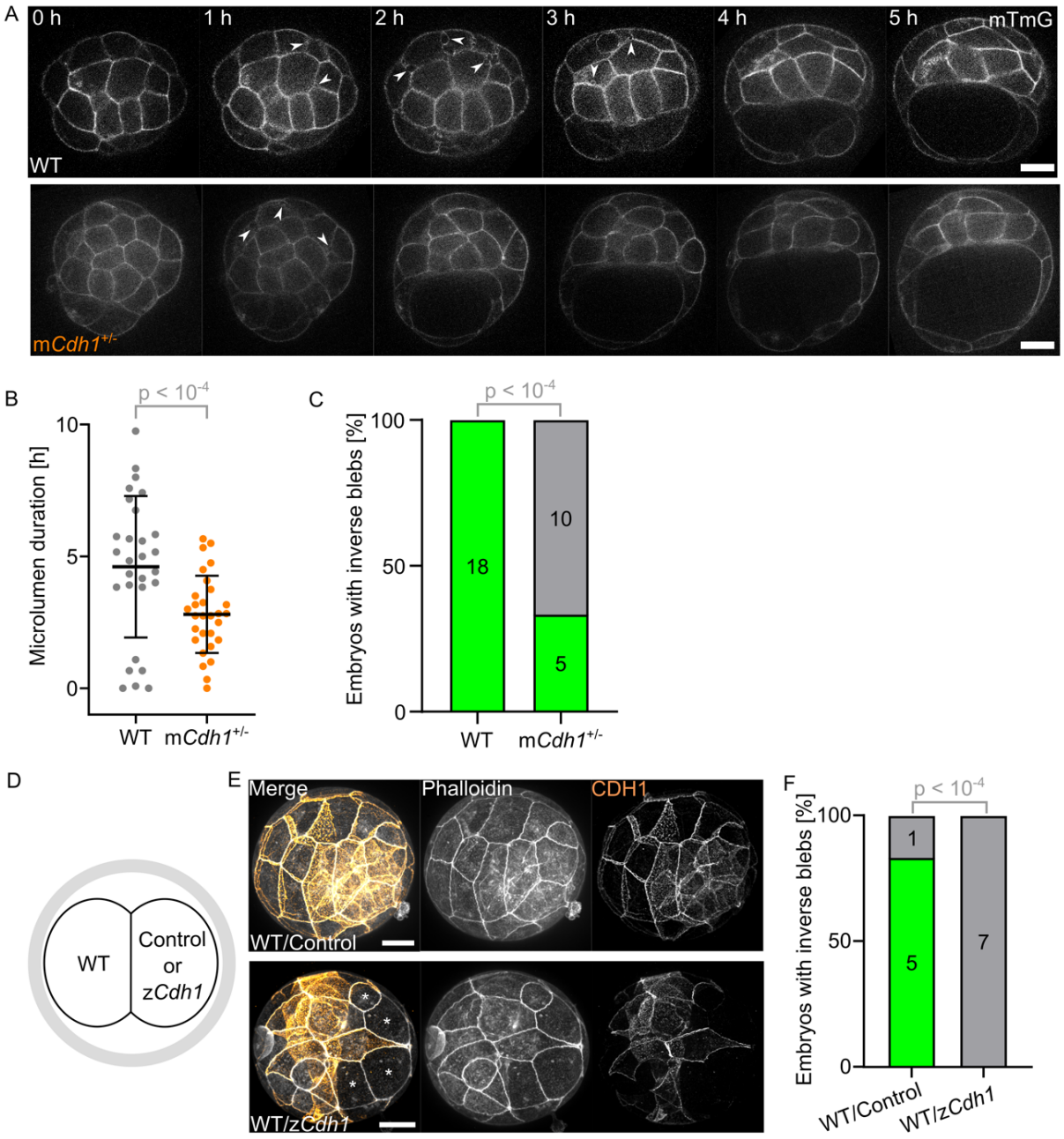

Extended Data Figure 4: Global and local effects of adhesion loss on microlumens and inverse blebs

(legend cont.)
A) Still images of mTmG in WT (top) and m*Cdh1*$^{+/-}$ (bottom) embryos during lumen formation (Movie 7). Arrows point at microlumens. Scale bars, 20 μm.
B) Duration of microlumens in WT (n = 28) and m*Cdh1*$^{+/-}$ (n = 29) embryos. Mean and SD are shown in black bracket. p value results from Welch's t test.
C) Proportion of WT (n = 18) and m*Cdh1*$^{+/-}$ (n = 15) embryos showing inverse blebs. p value results from Fisher's exact test.
D) Schematic diagram of 2-cell stage embryo where one blastomere is microinjected with either CRISPR/Cas9 targeting *Cdh1* (z*Cdh1*) or Cas9 alone (Control).
E) Immunostaining of embryos injected with Cas9 alone (Control) or Cas9 and CRISPR gRNA targeting *Cdh1* (z*Cdh1*) in one blastomere at the 2-cell stage with CDH1 shown in orange and actin in grey. Asterisks mark cells without CDH1. Scale bar, 20 μm.
F) Proportion of embryos showing inverse blebs after injection with CRISPR/Cas9 targeting *Cdh1* (z*Cdh1*, n = 7 embryos) or Cas9 alone (Control, n = 6 embryos) in one blastomere at the 2-cell stage. p value results from Fisher's exact test.

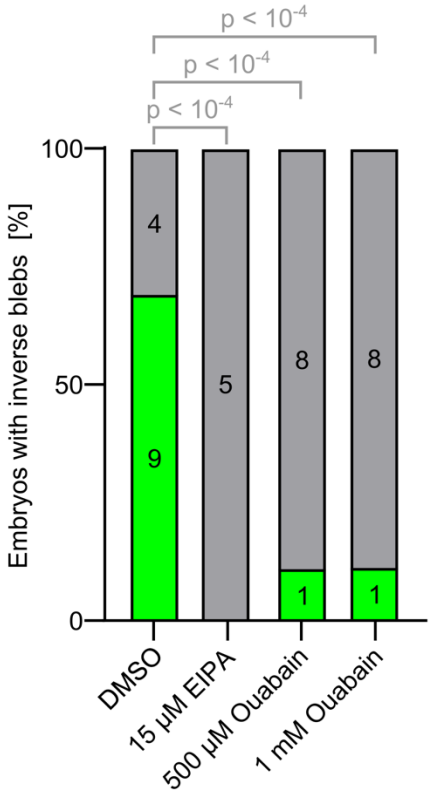

Extended Data Figure 5: Inverse blebs require accumulation of luminal fluid
Proportion of embryos showing inverse blebs in DMSO (1:100 or 1:200, 13 embryos), EIPA (15 μM, n = 5 embryos) or, 500 μM (n = 9 embryos) or 1 mM (n = 9 embryos) Ouabain treatments during the 32-cell stage. p values result from Fisher's exact test.

at the surface of fluid pockets (Fig. 2E, Supplementary Note), the mechanics of the system can be captured by a pseudopotential W (Fig. 2E-G). The minimum of the potential indicates mechanically stable fluid pockets with finite-sizes. This is also

depicted in a recent theoretical framework associated to in vitro reconstruction of microlumen formation [17]. Here, we also find that beyond a critical size, symmetric lens-shaped microlumens go through a hydraulic instability [34] leading to asymmetric hemispherical shapes, characteristic of inverse blebs (Supplementary Note). With sufficient adhesion, the model captures the coexistence of finite-sized and long-lived microlumens with dynamic inverse blebs (where pseudopotential is minimum at smaller sizes of fluid pockets in Fig. 2F). Here, the nucleation of inverse blebs is a potential barrier hopping phenomenon and lowering the potential barrier increases the susceptibility to nucleate inverse blebs. When adhesion is reduced, depending on the initial size, microlumens either shrink due to surface tension or grow to maximal size resulting in the absence of stable microlumens or inverse blebs (Supplementary Note), as observed when *Cdh1* is knocked out (Fig. 2A-B, Extended Data Fig. 4A-B). Similarly, the model suggests that more fluid accumulation and hence higher pressure build-up lowers the barrier (Fig. 2G). This is consistent with our experimental results where reducing fluid accumulation stops inverse bleb nucleation (Fig. 2C-D, Extended Data Fig. 5). Together, our theoretical framework qualitatively captures the effects of adhesion and pressure on the nucleation of inverse blebs that we observed experimentally.

Once inflated by pressurized luminal fluid, inverse blebs eventually stop growing and retract. To retract, outward blebs rely on the recruitment of actomyosin to contract the swollen protrusion [24]. To elucidate the role of actomyosin contractility on inverse bleb retraction, we used para-Nitroblebbistatin to acutely block all non-muscle myosin II heavy chains (NMHC) of blebbing mouse embryos. Inhibition of NMHCs increased the time taken to retract inverse blebs (Extended Data Fig. 6A-C, Movie 10), indicating that bleb retraction relies on actomyosin contractility. Among NMHC paralogs, outward bleb retraction is mediated by MYH9 [35], which we also detect at inverse blebs during their retraction (Fig. 1C-D, Extended Data Fig. 6J, Movie 2). We generated heterozygous mutants lacking the maternal allele of *Myh9* (m*Myh9*$^{+/-}$), which are able to form a blastocyst [36], and measured inverse bleb dynamics. Inverse blebs of m*Myh9*$^{+/-}$ embryos grow as large as in WT embryos but take longer to retract (Fig. 3A-C, Extended Data Fig. 6G, Movie 11). In contrast, embryos lacking the maternal allele

of *Myh10*, the other NMHC paralog expressed in the mouse preimplantation embryo [36], did not show altered inverse bleb dynamics (Fig. 3A-C, Movie 11). Therefore, like outward blebs [35], inverse blebs retract thanks to the recruitment of MYH9. Interestingly, inhibition of contractility did not affect actin recruitment dynamics or the growth and retraction profiles of inverse blebs (Fig. 3C, Extended Data Fig. 6C-I), unlike outward blebs, whose growth is impacted by reduced cytoplasmic pressure after contractility loss [19,35]. This further confirms our experimental and theoretical

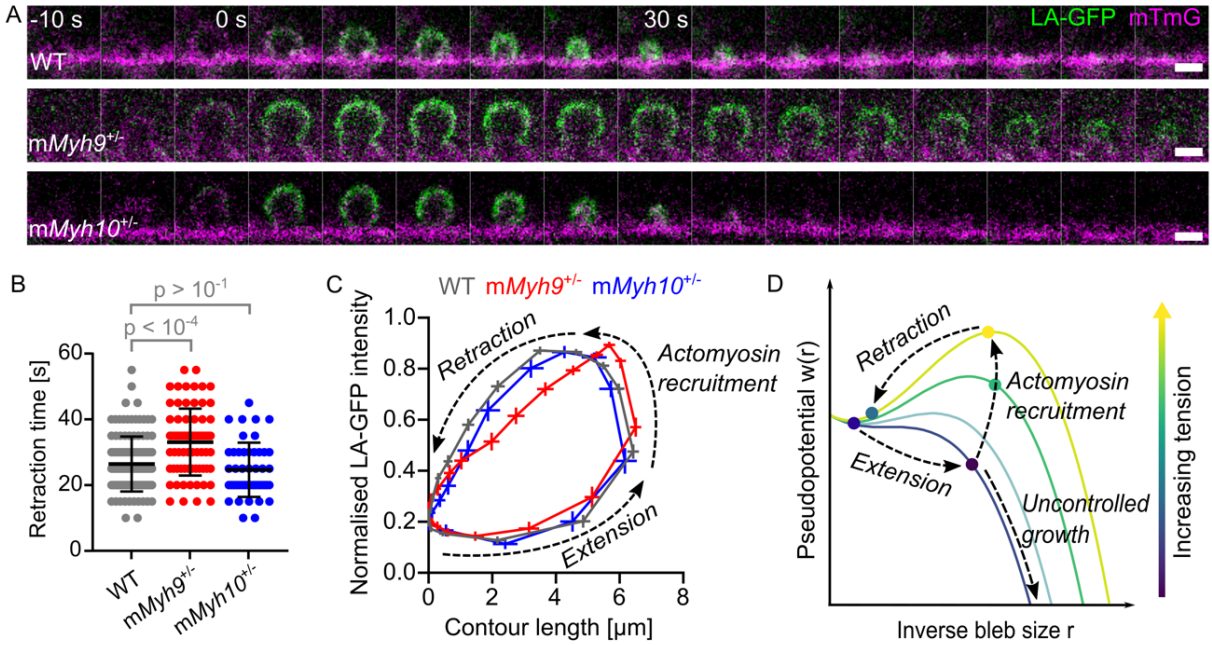

Figure 3: Inverse blebs retract with actomyosin contractility

A) Still images following the lifetime of an inverse blebs shown with LA-GFP in green and mTmG in magenta in WT (top), m*Myh9*$^{+/-}$ (middle) and m*Myh10*$^{+/-}$ (bottom) embryos (Movie 11). Images taken every 5 s with time indicated relative to the maximal inverse bleb size. Scale bars, 2 μm.

B) Duration of retraction of inverse blebs for WT (grey, n = 121 from 18 embryos), m*Myh9*$^{+/-}$ (red, n = 67 from 10 embryos) and m*Myh10*$^{+/-}$ (blue, n = 41 from 6 embryos) embryos. Mean and SD are shown in black bracket. p values result from ANOVA and Dunnett's tests.

C) Mean normalized LA-GFP intensity as a function of mean contour length of inverse blebs synchronized to their maximal extension for WT (grey, n = 100 from 13 embryos), m*Myh9*$^{+/-}$ (red, n = 67 from 10 embryos) and m*Myh*10$^{+/-}$ (blue, n = 41 from 6 embryos) embryos. Error bars show SEM. Arrows indicate the extension and retraction dynamics of inverse blebs.

D) Pseudopotential w as a function of the inverse bleb size r with varying tension. Normalized units, see Supplementary Note. Before actomyosin recruitment, fluid pockets undergo uncontrolled growth and extend into an inverse bleb. After actomyosin recruitment, the tension increases the pseudopotential w, stops the extension of the fluid pocket and eventually retracts it.

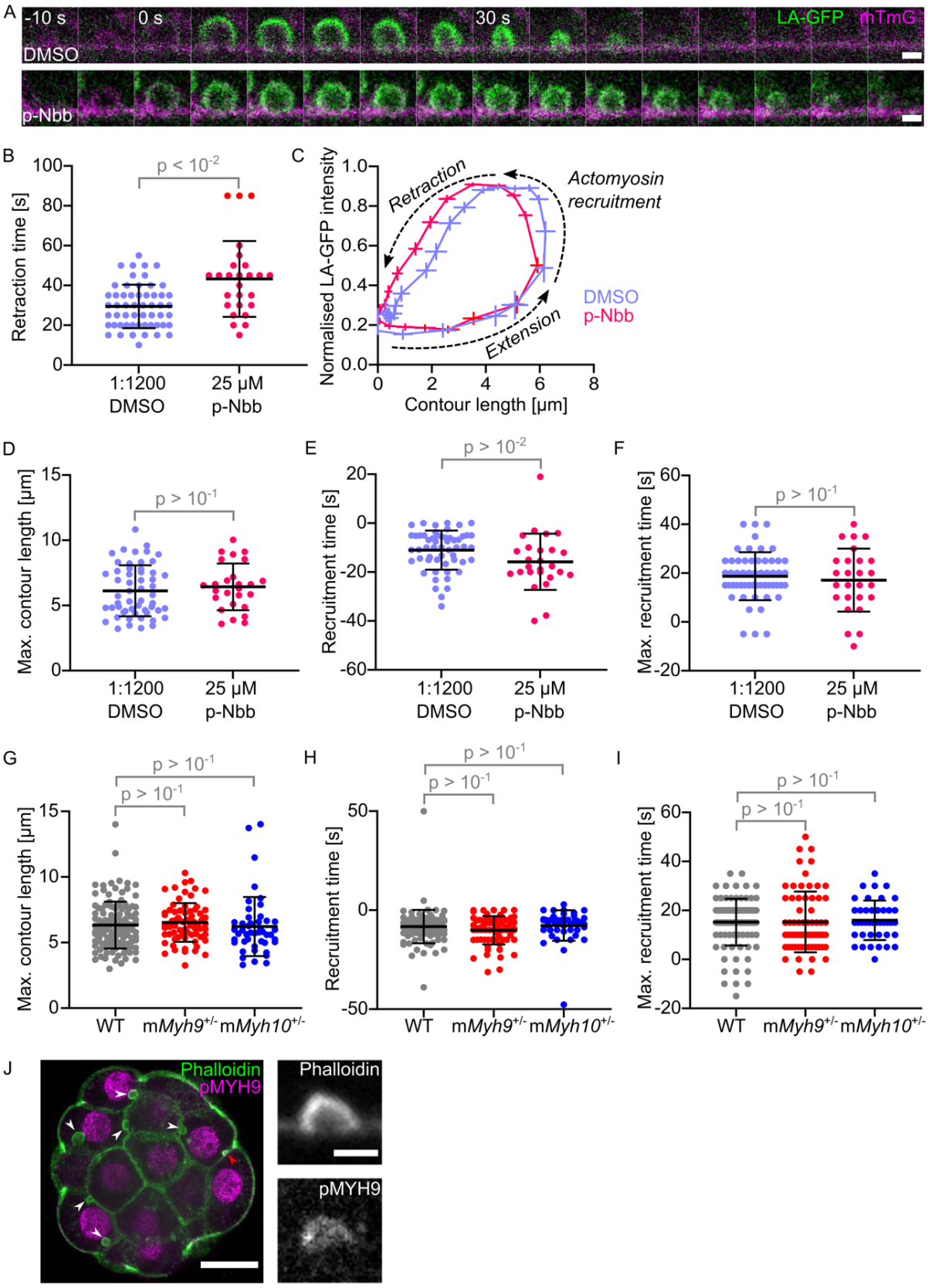

Extended Data Figure 6: Dynamics of individual inverse blebs with impaired actomyosin contractility

A) Still images following the lifetime of an inverse blebs shown with LifeAct-GFP (LA-GFP) in green and mTmG in magenta in 1:1200 DMSO (top) or 25 μM para-Nitroblebbistatin (pNbb, bottom)

(legend cont.)
media (Movie 10). Images taken every 5 s with time indicated relative to the maximal inverse bleb size. Scale bars, 2 μm.
B) Duration of retraction of inverse blebs for embryos treated with 1:1200 DMSO (purple, n = 55 from 6 embryos) or 25 μM para-Nitroblebbistatin (violet, n = 26 from 6 embryos) media. Mean and SD are shown in black bracket. p value results from Welch's t test.
C) Mean normalized LA-GFP intensity as a function of mean contour length of inverse blebs synchronized to their maximal extension for embryos treated with 1:1200 DMSO (purple, n = 55 from 6 embryos) or 25 μM para-Nitroblebbistatin (violet, n = 26 from 6 embryos) media. Error bars show SEM. Arrows indicate the extension and retraction dynamics of inverse blebs.
D-F) Maximal contour length, initial and maximal recruitment time of LA-GFP to inverse blebs of embryos treated with 1:1200 DMSO alone (purple, n = 55 blebs from 6 embryos) or with 25 μm para-Nitroblebbistatin (violet, n = 26 blebs from 6 embryos). Mean and SD are shown in black bracket. p values result from Welch's t test.
G-I) Maximal contour length, initial and maximal recruitment time of LA-GFP to inverse blebs of WT (grey, n = 100 blebs from 13 embryos), m*Myh9*$^{+/-}$ (red, n = 67 blebs from 10 embryos) or m*Myh10*$^{+/-}$ (blue, n = 41 blebs from 6 embryos) embryos. Mean and SD are shown in black bracket. p values result from ANOVA and Dunnett's multiple comparisons tests.
J) Left: immunostaining of 32-cell stage embryos showing Phalloidin (green) and the phosphorylated form of non-muscle myosin heavy chain IIA (pMYH9, magenta). Arrowheads point at fixed inverse blebs. Scale bar, 20 μm. Right: greyscale images on the right show separate signals of the inverse bleb pointed by the red arrowhead. Scale bar, 2 μm.

conclusions that inverse blebs inflate as a result of pressure from adhesive confinement and IF accumulation rather than from cell contractility (Fig. 2, Supplementary Note). In our theoretical framework, a time modulated increase of active tension, corresponding to the recruitment of actomyosin after inverse bleb extension, can change the underlying pseudopotential (Fig. 3D) and contract a growing inverse bleb. The resulting life cycle of inverse blebs can thus be depicted as an orbit in phase space of inverse bleb size and pseudopotential W, showing qualitative agreement between the model (Fig. 3D) and experimental data (Fig. 3C, Extended Data Fig. 6C).

Due to their life cycle of fast fluid accumulation/charge and shrinkage/discharge dynamics, inverse blebs act as *bona fide* hydraulic pumps able to quickly redistribute fluid within the three-dimensional intercellular space. Dispersed inverse bleb fluid may fuel the formation of new blebs, which makes the effectiveness of such pumps to redistribute intercellular fluid questionable. However, the transport of this dispersed bleb fluid depends on the geometry of the intercellular space of the embryo. The

intercellular space is made of three distinct topological entities: contacts between two cells or faces; tricellular contacts or edges; and multicellular junctions or vertices (Fig. 4A). Apart from their topology, these different types of contact sites likely differ vastly in their mechanics [3]. We had previously described two types of microlumens (Fig. 4A): bicellular microlumens, strictly confined between two cells (faces), and multicellular microlumens, which are surrounded by at least three cells (edges and vertices). Both bi- and multicellular microlumens grow and shrink during lumen formation but differ in size and dynamics [3]. We noted that inverse blebs form

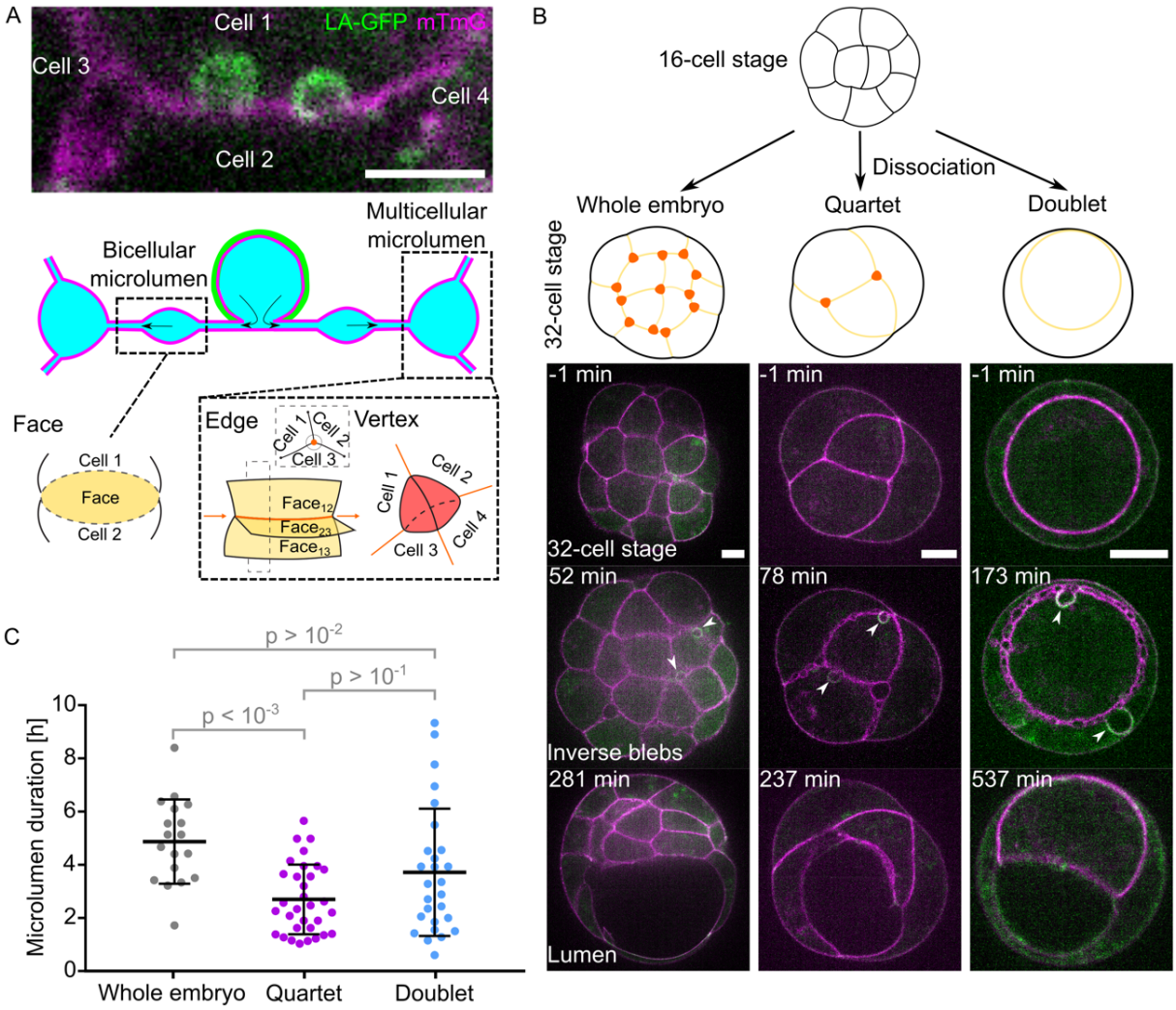

Figure 4: Inverse blebs pump fluid into topological sinks

A) Top: still image showing inverse blebs at a cell-cell contact bounded by two microlumens contained by multiple neighboring cells with LifeAct-GFP (LA-GFP) in green and mTmG in magenta. Middle: corresponding schematic diagram with cell membranes in magenta, actomyosin in green and IF in blue. Arrows indicate the fluid flows expected from the retraction of the inverse bleb. Bottom: Topological features associated with the microlumen network: contacts between two

(legend cont.)
cells constitute a face and show bi-cellular microlumens and inverse blebs; at the contact of three or more faces respectively, edges and vertices show multicellular microlumens.
B) Top: schematic diagram of a 16-cell stage embryo developing into a whole 32-cell stage embryo or into quartets and doublets after dissociation. Faces where bicellular microlumens form are shown in yellow. Edges and vertices where multicellular microlumens form are shown in red in whole embryos and quartets. Bottom: equatorial plane of a whole 32-cell stage embryo, quartet and doublet of 32-cell stage blastomeres with LA-GFP in green and mTmG in magenta (Movie 5, 12-13). Images are shown before microlumen appearance, during the presence of microlumens and inverse blebs and after their disappearance. Arrowheads point at inverse blebs. Scale bar, 10 μm.
C) Microlumen duration during lumen formation in whole embryos (grey, n = 18 embryos), quartets (purple, n = 32 quartets) and doublets (blue, n = 27 doublets). Mean and SD are shown in black bracket. p values result from Kruskal-Wallis and Dunn's multiple comparison tests.

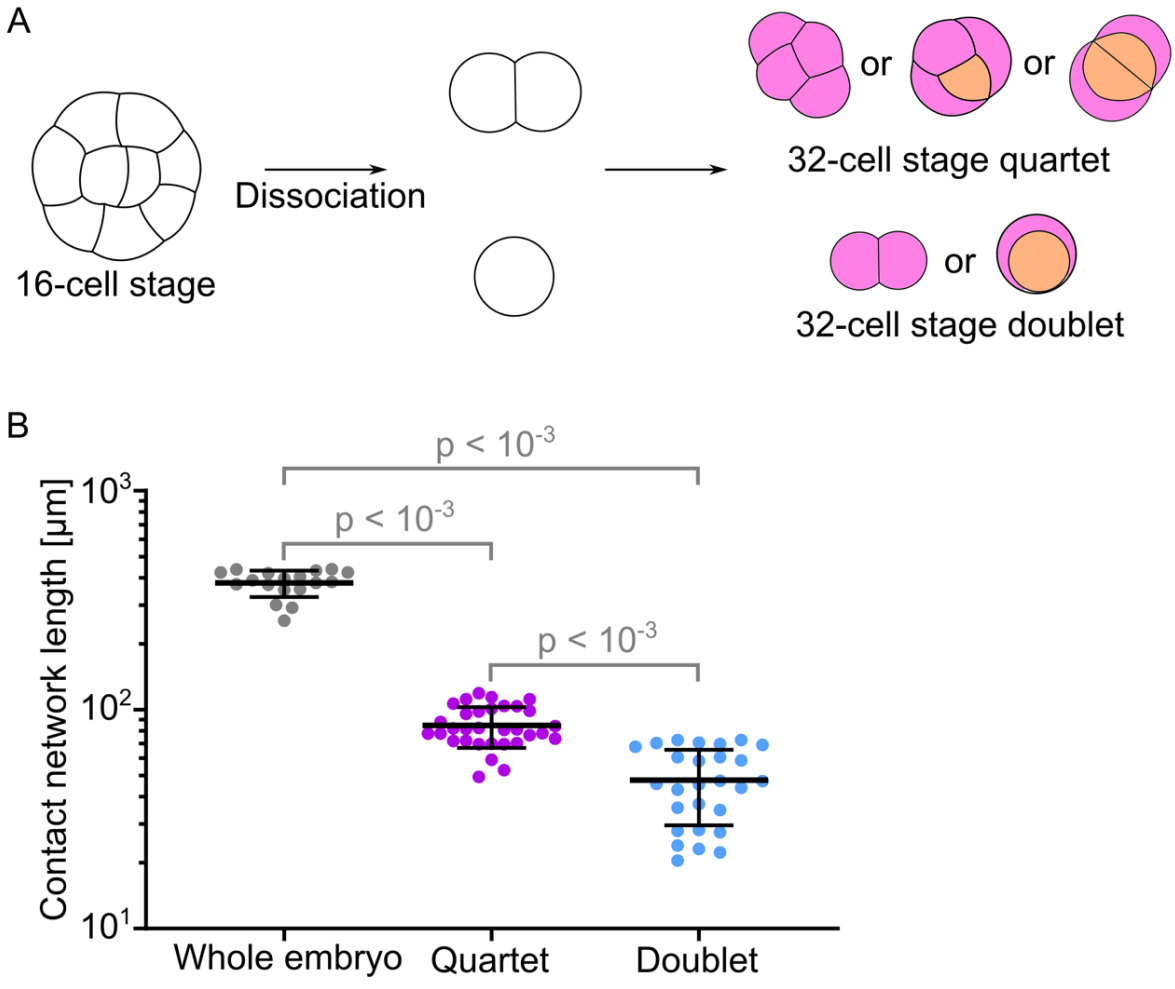

Extended Data Figure 7: Geometry and topology of reduced embryos
A) Schematic diagrams of the dissociation process used to produce quartets and doublets of 32-cell stage blastomeres. A 16-cell stage embryo is dissociated into singlets and doublets which then divide into doublets and quartets respectively. Quartets can adopt 3 different configurations: from left to right, 4 outer cells, 3 outer and 1 inner cell or 2 outer and 2 inner cells, which have at least

(legend cont.)
2 multicellular microlumens. Doublets can consist of 2 outer cells or 1 outer and 1 inner cells, which do not have multicellular microlumen.
B) Length of the network of cell-cell contact measured at the equatorial plane of whole embryos (n = 18), quartets (n = 32) or doublets (n = 27) shown with a logarithmic scale. p values result from ANOVA and Dunnett's multiple comparisons tests.

exclusively at the interface between two cells, both at bicellular microlumens and at seemingly closed cell-cell contacts, and do not appear at multicellular microlumens (Fig. 4A, Movie 1-3). This implies that multicellular microlumens situated at edges or vertices can behave as sinks, absorbing the fluid discharged by inverse blebs retraction. The presence of sinks makes inverse blebs effective hydraulic pumps, which could redistribute IF to promote the coarsening of the microlumen network.

To elucidate the interplay between inverse blebs and the topology of the intercellular space, we set out to modify the embryo geometry. In embryos with reduced cell number, there are fewer sinks that are also spatially located closer to each other compared to whole embryos. In this case, all discharged inverse bleb fluid should accumulate in these select nearby sinks, speeding up lumen formation. Contrarily, eliminating all such sinks would force all discharged inverse bleb fluid to circulate and nucleate new blebs, delaying the formation of the lumen. To test this idea, we dissociated embryos, creating doublets and quartets of 32-cell stage blastomeres to simplify the topology of the microlumen network (Fig. 4B, Extended Data Fig. 7A). With one eighth the cell number, quartets form microlumens within a smaller cell-cell contact network than whole embryos (Extended Data Fig. 7A-B). Topologically, quartets show a reduced number of channels and vertices (either 1 or 2 vertices), hence a reduced number of hydraulic sinks compared to whole embryos (Fig. 4B). We measured that microlumens persist twice as long in whole embryos as compared to quartets (Fig. 4C, Movie 5 and 12). Therefore, a simpler microlumen network with fewer sinks takes less time to coarsen. Following the same rationale, further reducing the cell number to a doublet, with only a single interface to coarsen microlumens at, should form a lumen faster than whole embryos and quartets. However, this is not the case (Fig. 4C, Movie 5 and 13). Unlike quartets, doublets do not have multicellular microlumens (Fig. 4B-C). Thus, all microlumens can form inverse blebs, pumping fluid back and forth between microlumens in a futile cycle (Movie 13). Altogether, we

conclude that inverse blebs act as hydraulic pumps that flush luminal fluid trapped at cell-cell contacts into topological sinks to foster the coarsening of the microlumen network into a single lumen.

Outward blebs have been observed in a variety of situations and were proposed to help the clearance of apoptotic cells [37], to act as signaling hubs [38], migratory protrusions [39], pressure valves [18], or, in the case of inverse blebs, as facilitators of apical membrane expansion [6]. Here, we find that inverse blebs are able to repair the damages of pressurized fluid percolating the tissue by pumping luminal fluid away from cell-cell contacts. We had noted previously that bicellular microlumens disappear before the multicellular ones during blastocoel formation [3]. The hydraulic pumping of inverse blebs into topological sinks contributes to the coarsening of the bicellular microlumens into multicellular ones. Therefore, inverse blebs provide a cellular mechanism explaining how contractility, which is weak at cell-cell contacts, can position the first mammalian lumen and first axis of symmetry of the mammalian embryo. More generally, inverse blebs constitute a unique mechanism for cells to handle IF in dense tissues where beating cilia may underperform. As such, in other dense tissues where pressure is elevated like the liver, kidney, swollen lymph nodes or wounded skin [7,14,40,41], inverse blebs could operate as hydraulic pumps redistributing the fluid permeating tissues.

References

1. Kurotaki Y, Hatta K, Nakao K, Nabeshima Y, Fujimori T: **Blastocyst Axis Is Specified Independently of Early Cell Lineage But Aligns with the ZP Shape**. *Science (80-)* 2007, **316**:719–723.
2. Takaoka K, Hamada H: **Cell fate decisions and axis determination in the early mouse embryo**. *Development* 2012, **139**:3–14.
3. Dumortier JG, Le Verge-Serandour M, Tortorelli AF, Mielke A, de Plater L, Turlier H, Maître J-L: **Hydraulic fracturing and active coarsening position the lumen of the mouse blastocyst**. *Science (80-)* 2019, **365**:465 LP – 468.
4. Collinet C, Lecuit T: **Programmed and self-organized flow of information during morphogenesis**. *Nat Rev Mol Cell Biol* 2021, **22**:245–265.
5. Le Verge-Serandour M, Turlier H: **A hydro-osmotic coarsening theory of biological cavity formation**. *PLOS Comput Biol* 2021, **17**:e1009333.
6. Gebala V, Collins R, Geudens I, Phng L, Gerhardt H: **Blood flow drives lumen formation by inverse membrane blebbing during angiogenesis in vivo**. 2016, **18**.
7. Gupta K, Li Q, Fan JJ, Fong ELS, Song Z, Mo S, Tang H, Ng IC, Ng CW, Pawijit P, et al.: **Actomyosin contractility drives bile regurgitation as an early response during obstructive cholestasis**. *J Hepatol* 2017, **66**:1231–1240.
8. Schliffka MF, Maître J-L: **Stay hydrated: basolateral fluids shaping tissues**. *Curr Opin Genet Dev* 2019, **57**:70–77.
9. Petridou NI, Grigolon S, Salbreux G, Hannezo E, Heisenberg C-P: **Fluidization-mediated tissue spreading by mitotic cell rounding and non-canonical Wnt signalling**. *Nat Cell Biol* 2019, **21**:169–178.
10. Mongera A, Rowghanian P, Gustafson HJ, Shelton E, Kealhofer DA, Carn EK, Serwane F, Lucio AA, Giammona J, Campàs O: **A fluid-to-solid jamming transition underlies vertebrate body axis elongation**. *Nature* 2018, **561**:401–405.
11. Krens SFG, Veldhuis JH, Barone V, Čapek D, Maître J-L, Brodland GW, Heisenberg C-P: **Interstitial fluid osmolarity modulates the action of differential tissue surface tension in progenitor cell segregation during gastrulation**. *Development* 2017, **144**:1798–1806.
12. Ishihara K, Mukherjee A, Gromberg E, Brugués J, Tanaka EM, Jülicher F: **Topological morphogenesis of neuroepithelial organoids**. *Nat Phys* 2023, **19**:177–183.
13. Munjal A, Hannezo E, Tsai TY-C, Mitchison TJ, Megason SG: **Extracellular hyaluronate pressure shaped by cellular tethers drives tissue morphogenesis**. *Cell* 2021, **184**:6313-6325.e18.
14. Kennard AS, Sathe M, Labuz EC, Prinz CK, Theriot JA: **Post-injury hydraulic fracturing drives fissure formation in the zebrafish basal epidermal cell layer**. *bioRxiv* 2022, doi:10.1101/2022.05.21.492930.
15. Katoh TA, Omori T, Mizuno K, Sai X, Minegishi K, Ikawa Y, Nishimura H, Itabashi T, Kajikawa E, Hiver S, et al.: **Immotile cilia mechanically sense the direction of fluid flow for left-right determination**. *Science (80-)* 2023, **379**:66–71.
16. Huljev K, Shamipour S, Pinheiro D, Preusser F, Steccari I, Sommer CM, Naik

S, Heisenberg C-P: **A hydraulic feedback loop between mesendoderm cell migration and interstitial fluid relocalization promotes embryonic axis formation in zebrafish**. *Dev Cell* 2023, **58**:582-596.e7.
17. Dinet C, Torres-Sánchez A, Arroyo M, Staykova M: **Patterning of membrane adhesion under hydraulic stress**. *bioRxiv* 2023, doi:10.1101/2023.01.04.522479.
18. Sedzinski J, Biro M, Oswald A, Tinevez J-Y, Salbreux G, Paluch E: **Polar actomyosin contractility destabilizes the position of the cytokinetic furrow**. *Nature* 2011, **476**:462–466.
19. Tinevez J-Y, Schulze U, Salbreux G, Roensch J, Joanny J-F, Paluch E: **Role of cortical tension in bleb growth**. *Proc Natl Acad Sci* 2009, **106**:18581–18586.
20. Charras GT, Yarrow JC, Horton MA, Mahadevan L, Mitchison TJ: **Non-equilibration of hydrostatic pressure in blebbing cells**. *Nature* 2005, **435**:365–369.
21. Maître J-L, Niwayama R, Turlier H, Nédélec F, Hiiragi T: **Pulsatile cell-autonomous contractility drives compaction in the mouse embryo**. *Nat Cell Biol* 2015, **17**:849–855.
22. Coravos JS, Mason FM, Martin AC: **Actomyosin Pulsing in Tissue Integrity Maintenance during Morphogenesis**. *Trends Cell Biol* 2017, **27**:276–283.
23. Özgüç Ö, Maître J-L: **Multiscale morphogenesis of the mouse blastocyst by actomyosin contractility**. *Curr Opin Cell Biol* 2020, **66**:123–129.
24. Charras G, Paluch E: **Blebs lead the way: how to migrate without lamellipodia**. *Nat Rev Mol Cell Biol* 2008, **9**:730–736.
25. Charras GT, Hu C-K, Coughlin M, Mitchison TJ: **Reassembly of contractile actin cortex in cell blebs** . *J Cell Biol* 2006, **175**:477–490.
26. Ebrahim S, Chen D, Weiss M, Malec L, Ng Y, Rebustini I, Krystofiak E, Hu L, Liu J, Masedunskas A, et al.: **Dynamic polyhedral actomyosin lattices remodel micron-scale curved membranes during exocytosis in live mice**. *Nat Cell Biol* 2019, **21**:933–939.
27. Ryan AQ, Chan CJ, Graner F, Hiiragi T: **Lumen Expansion Facilitates Epiblast-Primitive Endoderm Fate Specification during Mouse Blastocyst Formation**. *Dev Cell* 2019, **51**:684-697.e4.
28. Moreau HD, Blanch-Mercader C, Attia R, Maurin M, Alraies Z, Sanséau D, Malbec O, Delgado M-G, Bousso P, Joanny J-F, et al.: **Macropinocytosis Overcomes Directional Bias in Dendritic Cells Due to Hydraulic Resistance and Facilitates Space Exploration**. *Dev Cell* 2019, **49**:171–188.
29. Niwayama R, Moghe P, Liu Y-J, Fabrèges D, Buchholz F, Piel M, Hiiragi T: **A Tug-of-War between Cell Shape and Polarity Controls Division Orientation to Ensure Robust Patterning in the Mouse Blastocyst**. *Dev Cell* 2019, **51**:564-574.e6.
30. Maître J-L, Turlier H, Illukkumbura R, Eismann B, Niwayama R, Nédélec F, Hiiragi T: **Asymmetric division of contractile domains couples cell positioning and fate specification**. *Nature* 2016, **536**:344–348.
31. Stephenson RO, Yamanaka Y, Rossant J: **Disorganized epithelial polarity and excess trophectoderm cell fate in preimplantation embryos lacking E-cadherin**. *Development* 2010, **137**:3383–3391.
32. POWERS RD, BORLAND RM, BIGGERS JD: **Amiloride-sensitive rheogenic**

Na+ transport in rabbit blastocyst. *Nature* 1977, **270**:603–604.
33. Biggers JD, Borland RM, Lechene CP: **Ouabain-sensitive fluid accumulation and ion transport by rabbit blastocysts.** *J Physiol* 1978, **280**:319–330.
34. Chartier NT, Mukherjee A, Pfanzelter J, Fürthauer S, Larson BT, Fritsch AW, Amini R, Kreysing M, Jülicher F, Grill SW: **A hydraulic instability drives the cell death decision in the nematode germline**. *Nat Phys* 2021, **17**:920–925.
35. Taneja N, Burnette DT: **Myosin IIA drives membrane bleb retraction**. *Mol Biol Cell* 2019, **30**:1051–1059.
36. Schliffka MF, Tortorelli AF, Özgüç Ö, de Plater L, Polzer O, Pelzer D, Maître J-L: **Multiscale analysis of single and double maternal-zygotic Myh9 and Myh10 mutants during mouse preimplantation development**. *Elife* 2021, **10**:e68536.
37. Croft DR, Coleman ML, Li S, Robertson D, Sullivan T, Stewart CL, Olson MF: **Actin-myosin–based contraction is responsible for apoptotic nuclear disintegration** . *J Cell Biol* 2005, **168**:245–255.
38. Weems AD, Welf ES, Driscoll MK, Zhou FY, Mazloom-Farsibaf H, Chang B-J, Murali VS, Gihana GM, Weiss BG, Chi J, et al.: **Blebs promote cell survival by assembling oncogenic signalling hubs**. *Nature* 2023, **615**:517–525.
39. Blaser H, Reichman-Fried M, Castanon I, Dumstrei K, Marlow FL, Kawakami K, Solnica-Krezel L, Heisenberg C-P, Raz E: **Migration of Zebrafish Primordial Germ Cells: A Role for Myosin Contraction and Cytoplasmic Flow**. *Dev Cell* 2006, **11**:613–627.
40. Choudhury MI, Li Y, Mistriotis P, Vasconcelos ACN, Dixon EE, Yang J, Benson M, Maity D, Walker R, Martin L, et al.: **Kidney epithelial cells are active mechano-biological fluid pumps**. *Nat Commun* 2022, **13**:2317.
41. Assen FP, Abe J, Hons M, Hauschild R, Shamipour S, Kaufmann WA, Costanzo T, Krens G, Brown M, Ludewig B, et al.: **Multitier mechanics control stromal adaptations in the swelling lymph node**. *Nat Immunol* 2022, **23**:1246–1255.
42. Biggers JD, McGinnis LK, Raffin M: **Amino Acids and Preimplantation Development of the Mouse in Protein-Free Potassium Simplex Optimized Medium1**. *Biol Reprod* 2000, **63**:281–293.
43. Muzumdar MD, Tasic B, Miyamichi K, Li L, Luo L: **A global double-fluorescent Cre reporter mouse**. *genesis* 2007, **45**:593–605.
44. Riedl J, Flynn KC, Raducanu A, Gärtner F, Beck G, Bösl M, Bradke F, Massberg S, Aszodi A, Sixt M, et al.: **Lifeact mice for studying F-actin dynamics**. *Nat Methods* 2010, **7**:168–169.
45. Zhang Y, Conti MA, Malide D, Dong F, Wang A, Shmist YA, Liu C, Zerfas P, Daniels MP, Chan C-C, et al.: **Mouse models of MYH9-related disease: mutations in nonmuscle myosin II-A**. *Blood* 2012, **119**:238–250.
46. Kan NG, Stemmler MP, Junghans D, Kanzler B, de Vries WN, Dominis M, Kemler R: **Gene replacement reveals a specific role for E-cadherin in the formation of a functional trophectoderm**. *Development* 2007, **134**:31–41.
47. Jacobelli J, Friedman RS, Conti MA, Lennon-Dumenil A-M, Piel M, Sorensen CM, Adelstein RS, Krummel MF: **Confinement-optimized three-dimensional T cell amoeboid motility is modulated via myosin IIA–regulated adhesions**. *Nat Immunol* 2010, **11**:953–961.

48. Ma X, Takeda K, Singh A, Yu Z-X, Zerfas P, Blount A, Liu C, Towbin JA, Schneider MD, Adelstein RS, et al.: **Conditional Ablation of Nonmuscle Myosin II-B Delineates Heart Defects in Adult Mice**. *Circ Res* 2009, **105**:1102–1109.
49. Boussadia O, Kutsch S, Hierholzer A, Delmas V, Kemler R: **E-cadherin is a survival factor for the lactating mouse mammary gland**. *Mech Dev* 2002, **115**:53–62.
50. Pelzer D, Plater L de, Bradbury P, Eichmuller A, Bourdais A, Halet G, Maître J-L: **Ectopic activation of the polar body extrusion pathway triggers cell fragmentation in preimplantation embryos**. *bioRxiv* 2022, doi:10.1101/2022.12.22.521568.
51. Labun K, Montague TG, Krause M, Torres Cleuren YN, Tjeldnes H, Valen E: **CHOPCHOP v3: expanding the CRISPR web toolbox beyond genome editing**. *Nucleic Acids Res* 2019, **47**:W171–W174.
52. Cong L, Ran FA, Cox D, Lin S, Barretto R, Habib N, Hsu PD, Wu X, Jiang W, Marraffini LA, et al.: **Multiplex Genome Engineering Using CRISPR/Cas Systems**. *Science (80-)* 2013, **339**:819–823.
53. Muggeo VMR: **Estimating regression models with unknown break-points**. *Stat Med* 2003, **22**:3055–3071.
54. Machado S, Mercier V, Chiaruttini N: **LimeSeg: a coarse-grained lipid membrane simulation for 3D image segmentation**. *BMC Bioinformatics* 2019, **20**:2.

Movie legends

Movies can be found under the following link:
https://www.dropbox.com/sh/9p24uvmo1ij8bgg/AACGNOG9Xwg02kDj3OEu8LrYa?dl=0

Movie 1: Dynamic recruitment of actin during inverse blebs retraction.

Time lapse imaging at the equatorial plane of a 32-cell stage LifeAct-GFP (green), mTmG (magenta) embryo imaged every 5 s using spinning disk microscopy. Scale bar, 20 μm.

Movie 2: Dynamic recruitment of non-muscle myosin II during inverse blebs retraction.

Time lapse imaging at the equatorial plane of a 32-cell stage MYH9-GFP (green), mTmG (magenta) embryo imaged every 5 s using spinning disk microscopy. Scale bar, 20 μm.

Movie 3: Inverse blebs fill with intercellular fluid before flushing it back into the microlumen network.

Time lapse imaging at the equatorial plane of a 32-cell stage mTmG (grey) embryo incubated with Dextran-Alexa488 (cyan) at the 16-cell stage before sealing of tight junctions imaged every 5 s using spinning disk microscopy. Scale bar, 20 μm.

Movie 4: Inverse bleb activity peaks before lumen expansion.

Nested time lapse imaging of a LifeAct-GFP embryo imaged every 10 s for 5 min repeated every 30 min using light sheet microscopy. Equatorial plane is shown on the left and maximum projection on the right. Developmental time is indicated relative to peak blebbing activity measured throughout the entire embryo volume. Scale bar, 20 μm.

Movie 5: Inverse blebs coexist with microlumens throughout lumen formation.
Time lapse imaging at the equatorial plane of a LifeAct-GFP (green), mTmG (magenta) embryo imaged every minute using spinning disk microscopy. Scale bar, 20 μm.

Movie 6: Dynamics of adhesion molecules during inverse blebs.
Time lapse imaging at the equatorial plane of a 32-cell stage CDH1-GFP (green), mTmG (magenta) embryo imaged every 5 s using spinning disk microscopy. Scale bar, 20 μm.

Movie 7: m*Cdh1*$^{+/-}$ embryos form their lumen quicker than WT embryos.
Time lapse imaging of 32-cell stage mTmG WT and m*Cdh1*$^{+/-}$ embryos imaged every 5 min using spinning disk microscopy. Embryos are imaged throughout their entire volume to synchronize them to the time of appearance of microlumens. The equatorial plane is shown. Scale bar, 20 μm.

Movie 8: m*Cdh1*$^{+/-}$ embryos rarely form inverse blebs unlike WT embryos.
Time lapse imaging at the equatorial plane of 32-cell stage LifeAct-GFP (green), mTmG (magenta) WT and m*Cdh1*$^{+/-}$ embryos imaged every minute using spinning disk microscopy. Embryos are synchronized to the time of appearance of microlumens at the equatorial plane. Scale bar, 20 μm.

Movie 9: EIPA treatment acutely stops inverse blebs.
Time lapse imaging at the equatorial plane of a 32-cell stage LifeAct-GFP (green) mTmG (magenta) embryo imaged every 5 s using spinning disk microscopy. The embryo is first treated with 1:2500 DMSO containing medium (left), then with 20 μM EIPA for 15 min before the start of the time lapse (right). Scale bar, 20 μm.

Movie 10: para-Nitroblebbistatin treatment acutely slows inverse bleb retraction.
Time lapse imaging at the equatorial plane of a LifeAct-GFP (green), mTmG (magenta) embryo imaged every 5 s using spinning disk microscopy. Treatment with 25 μM para-Nitroblebbistatin (p-Nbb) for 15 min before the start of the time lapse

causes inverse blebs retraction to slow down compared to DMSO treatment. Scale bar, 20 μm.

Movie 11: m*Myh9*$^{+/-}$ embryos retract inverse blebs slower than WT and m*Myh10*$^{+/-}$ embryos.

Time lapse imaging at the equatorial plane of WT, m*Myh9*$^{+/-}$ or m*Myh10*$^{+/-}$ LifeAct-GFP (green), mTmG (magenta) embryos imaged every 5 s using spinning disk microscopy. Scale bar, 20 μm.

Movie 12: quartets of 32-cell stage blastomeres form a lumen rapidly.

Time lapse imaging at the equatorial plane of a LifeAct-GFP (green), mTmG (magenta) quartet of 32-cell stage blastomeres imaged every min using spinning disk microscopy. Time is indicated relative to the appearance of microlumens at the equatorial plane. Scale bar, 20 μm.

Movie 13: doublets of 32-cell stage blastomeres do not form a lumen rapidly.

Time lapse imaging at the equatorial plane of a LifeAct-GFP (green), mTmG (magenta) doublet of 32-cell stage blastomeres imaged every min using spinning disk microscopy. Time is indicated relative to the appearance of microlumens at the equatorial plane. Scale bar, 20 μm.

Methods

Embryo work

All animal work is performed in the animal facility at the Institut Curie, with permission by the institutional veterinarian overseeing the operation (APAFIS #11054-2017082914226001 and APAFIS #39490-2022111819233999 v2). The animal facilities are operated according to international animal welfare rules.

Embryos are isolated from superovulated female mice mated with male mice. Superovulation of female mice is induced by intraperitoneal injection of 5 international units (IU) pregnant mare's serum gonadotropin (PMSG, Ceva, Syncro-part), followed by intraperitoneal injection of 5 IU human chorionic gonadotropin (hCG, MSD Animal Health, Chorulon) 44-48 hours later. Embryos are recovered at E1.5 or E2.5 by flushing oviducts or/and uteri from plugged females with 37°C FHM (LifeGlobal, ZEHP-050 or Millipore, MR-122-D) using a modified syringe (Acufirm, 1400 LL 23).

Embryos are handled using an aspirator tube (Sigma, A5177-5EA) equipped with a glass pipette pulled from glass micropipettes (Blaubrand intraMark or Warner Instruments).

Embryos are placed in KSOM (LifeGlobal, ZEKS-050 or Millipore, MR-107-D) supplemented with 0.1 % BSA (Sigma, A3311) in 10 µL droplets covered in mineral oil (Sigma, M8410 or Acros Organics). Embryos are cultured in an incubator with a humidified atmosphere supplemented with 5% CO_2 at 37°C.

To remove the zona zellucida (ZP), embryos are incubated for 45-60 s in pronase (Sigma, P8811).

To dissociate blastomeres, embryos are incubated in EDTA containing Ca^{2+} free KSOM [42] at the 16-cell stage for 3-5 minutes, followed by repeated aspiration into a smoothened glass capillary and dissociation into single 16-cell blastomeres or 16-cell blastomere doublets, which results, after development in KSOM, in the formation of 32-cell stage doublets or quartets, respectively.

For imaging, embryos are placed in 5 mm glass-bottom dishes (MatTek).

Mouse lines

Mice are used from 5 weeks old on.

To visualize plasma membranes and F-actin, (Gt(ROSA)26Sor $^{tm4(ACTB-tdTomato,-EGFP)Luo)}$;Tg(CAG-EGFP)#Rows mice [43,44] are used.

To visualize plasma membranes and MYH9, (Gt(ROSA)26Sor $^{tm4(ACTB-tdTomato,-EGFP)Luo}$;*Myh9* $^{tm8.1RSad}$ mice [43,45] are used.

To visualize plasma membranes and CDH1 (Gt(ROSA)26Sor $^{tm4(ACTB-tdTomato,-EGFP)Luo}$; Cdh-GFP) mice [3,43] are used.

To remove LoxP sites specifically in oocytes, *Zp3*-cre (Tg(*Zp3*-cre)93Knw) mice [46] are used.

To generate m*Myh9*$^{+/-}$ embryos, *Myh9* ^{tm5RSad} mice [47] are used to breed *Myh9* $^{tm5RSad/tm5RSad}$; *Zp3* $^{Cre/+}$ females [46,47].

To generate m*Myh10*$^{+/-}$ embryos, *Myh10*^{tm7Rsad} mice are used to breed *Myh10*$^{tm7Rsad/tm7Rsad}$; *Zp3* $^{Cre/+}$ females [46,48].

To generate m*Cdh1*$^{+/-}$ embryos, *Cdh1*^{tm2kem} mice [49] are used to breed *Cdh1*$^{tm2kem/tm2kem}$; *Zp3*$^{Cre/+}$ females [46,49].

Mouse strain	**RRID**
Gt(ROSA)26Sor$^{tm4(ACTB-tdTomato,-EGFP)Luo}$	IMSR_JAX:007676
Tg(CAG–EGFP)#Rows	MGI:4831036
Myh9$^{tm8.1RSad}$	MGI:5499741
Tg(Zp3-cre)93Knw	MGI:3835429
Myh9$^{tm5RSad/tm5RSad}$	MGI:4838530
Myh10$^{tm7Rsad/tm7Rsad}$	MGI:4443040
Cdh1$^{tm2kem/tm2kem}$	IMSR_JAX:005319

Zygotic Cdh1 knockout in 2-cell embryos

To knock out *Cdh1*, we used the same approach as previously [50]. To target *Cdh1* a set of two gRNAs for each gene targeting close to the start codon are designed using the web tool CHOPCHOP [51], namely GCGCGGAAAAGCTGCGGCAC and GCAGGAGCGCGGAAAAGCTG. For RNA transcription, the gRNA target sequences are cloned into pX458 (Addgene, 48138) as previously described [52]. Briefly, following digestion of the plasmid with BbsI, two annealed oligos encoding the gRNA target region, containing the 5' overhang AAAC and the 3' overhang CACCG are

phosphorylated and cloned into pX458. The gRNA and its backbone are amplified by PCR with a fwd primer containing a T7 site. Following PCR purification RNA is transcribed using the MEGAshortscript T7 transcription kit (Invitrogen, AM1354). The RNA is then purified using the MEGAclear kit (Invitrogen, AM1908). Glass capillaries (Harvard Apparatus glass capillaries with 780 μm inner diameter) are pulled using a needle puller and microforge to build a holding pipette and an injection needle. The resulting injection needles are filled with RNA/protein solution diluted in injection buffer (5mM Tris-HCl pH 7.4, 0.1 mM EDTA) to the following concentrations: To knock out *Cdh1*, 2-cell embryos are injected with 300 ng/μL Cas9 protein (IDT, 1081058) and 80 ng/μL of each gRNA diluted in injection buffer. To visualize injected cells, mRNA encoding lamin associated protein 2 fused to GFP (Lap2b-GFP) is added to the injection mix at 200 ng/μL [50]. Lap2b-GFP mRNA is transcribed using the mMESSAGE mMACHINE SP6 Kit (Invitrogen, AM1340) according to manufacturer's instructions and resuspended in RNase-free water.

The filled needle is positioned on a micromanipulator (Narishige MMO-4) and connected to a positive pressure pump (Eppendorf FemtoJet 4i). Control embryos were injected with Cas9 protein and Lap2b-GFP mRNA only.

Embryos are placed in FHM drops covered with mineral oil under Leica TL Led microscope. 2-cell embryos are injected while holding with holding pipette connected to a Micropump CellTram Oil.

To verify the effectiveness of zygotic *Cdh1* knockout, immunostaining of chimeric embryo against CDH1 allows discerning the WT and knocked out halves of the embryos.

Confocal microscopy

Live imaging of embryos is performed using a Viventis Microscopy LS1 Live microscope. Fluorescence excitation is achieved with a dual illumination scanned Gaussian beam light sheet of ~1.1 µm full width 30% using a 488 nm laser. Signal is collected with a Nikon CFI75 Apo LWD 25x/1.1 objective and through a 488 nm long pass filter onto an Andor Zyla 4.2 Plus sCMOS camera. The microscope is equipped with an incubation chamber to keep the sample at 37°C and supply the atmosphere with 5% CO_2. Embryos are sampled using a custom Python script every 10 s for 5 min,

repeated every 30 min and the full volume of the embryo is acquired with a 76 μm z-stack with 2 μm step size.

Live imaging is performed using an inverted Zeiss Observer Z1 microscope with a CSU-X1 spinning disk unit (Yokogawa). Excitation is achieved using 488 and 561 nm laser lines through a 63x/1.2 C Apo Korr water immersion objective. Emission is collected through 525/50 and 595/50 band pass filters onto an ORCA-Flash 4.0 camera (C11440, Hamamatsu).

Alternatively, a Celldiscoverer 7 (Zeiss) with a CSU-X1 spinning disc unit (Yokogawa) is used. Excitation is achieved using 488 and 561 nm laser lines through a 50x/1.2 water immersion objective. Emission is collected through 514/30 and 592/25 band pass filters onto an ORCA-Flash 4.0 camera (C11440, Hamamatsu).

Both microscopes are equipped with an incubation chamber to keep the sample at 37°C and supply the atmosphere with 5% CO_2.

In order to capture the dynamics of inverse blebs, WT embryos expressing LifeAct-GFP and mTmG or MYH9-GFP and mTmG, m*Myh9*$^{+/-}$ or m*Myh10*$^{+/-}$ embryos expressing LifeAct-GFP and mTmG are imaged every 5 s for 5 min at their equatorial plane, which is repeated every 1 h from late E2.5 to E3.5 using a custom Metamorph journal (Molecular Devices). A 60 μm z-stack with a 5 μm step size is acquired before every time lapse to discern TE and ICM cells.

To measure microlumen duration in WT and m*Cdh1*$^{+/-}$ embryos, embryos expressing mTmG are imaged every 5 min for from E2.5 to E3.5, capturing a z-stack of 28 μm of the upper half of each embryo with a 4 μm step size.

In order to simultaneously track inverse bleb number and microlumens, WT or m*Cdh1*$^{+/-}$ embryos, doublets or quartets are imaged at the equatorial plane every 1 min from before microlumen initiation until lumen formation is completed.

Fluorescent dextran inclusion

3 kDa dextran coupled to Alexa Fluor 488 (Sigma, D34682) is added to KSOM at 0.1 g/L. Embryos are placed in labelled medium at the 16-cell stage before tight junctions fully seal.

EIPA treatment

5-(N-Ethyl-N-isopropyl)-amiloride (EIPA) (Sigma, A3085) 50 mM DMSO stock is diluted to 20 μM in KSOM. A 1:2500 DMSO in KSOM dilution is used as control.

For acute EIPA treatment of embryos, embryos are cultured in the control medium and checked for the presence of inverse blebs. Embryos in the inverse bleb phase are imaged every 5 s for 10 min at their equatorial plane in the control medium. Embryos are then transferred to 20 μM EIPA medium and incubated for 15 min before being imaged in the same manner.

para-Nitroblebbistatin treatment

Para-Nitroblebbistatin (Cayman Chemical) 50 mM DMSO stock is diluted to 25 μM in FHM without mineral oil. A 1:1200 DMSO in FHM dilution is used as control. Inverse blebbing embryos are either incubated in the control medium or para-Nitroblebbistatin medium for 15 min. Embryos are then imaged every 5 s for 10 to 30 min at their equatorial plane.

Immunostaining

Embryos in the inverse bleb phase were fixed in 2% PFA (Euromedex, 2000-C) for 10 min at 37°C, washed in PBS, and permeabilized with 0.01% Triton X-100 (Euromedex, T8787) in PBS (PBT) at room temperature before being placed in blocking solution (PBT with 3% BSA) at 4°C for 2–4 h. Primary antibodies were applied in blocking solution at 4°C overnight. After washes in PBT at room temperature, embryos were incubated with secondary antibodies and phalloidin in blocking solution at room temperature for 1 h. Embryos were washed in PBT and imaged immediately after.

Antibodies and dyes	**Dilution**	**Provider**	**RRID**
phospho-MYH9 (Ser1943)	1:200	Cell Signaling, 5026	AB_10576567
CDH1	1:500	eBioscience,14-3249-82	
Alexa Fluor 546 anti-mouse	1:200	Invitrogen, A11003	AB_2534071
Alexa Fluor Plus 488 anti-rabbit	1:200	Invitrogen, A32731	AB_2633280

Alexa Fluor 633 phalloidin	1:200	Invitrogen, A22284	

Data analysis

Data are analyzed using Microsoft Excel and R. Data are plotted using Graphpad Prism.

Inverse bleb count

The inverse bleb number in confocal and light-sheet time lapses is manually counted. A bleb is defined as a transient hemispherical actin-positive intrusion appearing at cell-cell contacts.

When embryos are imaged every min continuously throughout lumen formation, the number of blebs is provided as such.

When embryos are sampled with nested time-lapses (brief acquisition every 5 or 10 s for 5 or 10 min repeated every 30-60min), the number of blebs is provided per min.

Inverse blebs are allocated to TE or ICM cells based on the position of the cells: TE cells contact the surface of the embryo while ICM cells are surrounded by other cells.

Inverse blebs are allocated into a distal and proximal half by determining the site of blastocoel formation in the equatorial plane and bisecting the embryo in two equal halves.

Duration of the microlumen phase

Microlumen duration of embryos, quartets and doublets is determined as the time between the appearance of the first and disappearance of the last microlumens as detected visually.

Dynamics of individual inverse blebs

Inverse bleb dynamics are measured using FIJI by tracing the outline of inverse blebs using a line width of 1 μm. Before and after inverse bleb formation and retraction, a line corresponding to the opening width of the inverse bleb is measured. For each inverse bleb, measurements are taken 60 s before and after reaching their maximum size (90 s after size maximum for para-Nitroblebbistatin treatment).

The time of maximal size of each inverse bleb is taken as a reference time point. Intensity values of LifeAct-GFP, MYH9-GFP, CDH1-GFP and mTmG are first normalized to 60 s before inverse bleb size maximum and then to their minimal and maximal values. The lifetime of an inverse bleb is taken as the time during which a visible membrane protrusion is seen extending at a cell-cell contact until the time it is no longer visible. The retraction time is taken as the time of inverse bleb duration from its maximal size to its disappearance.

Using R segmented package [53], the LifeAct-GFP and MYH9-GFP recruitment times are calculated using iterative linear regression on the intensity data taken until the maximum value to find the breakpoint between the stable intensity and intensity increase.

Blastocoel volume

Blastocoel volume is measured on full-volume light sheet z-stacks using the FIJI plugin LimeSeg [54]. The blastocoel is traced back from the expanded blastocyst and measured as soon as a lumen is present (smallest segmented lumen < 1 pL). Before that, blastocoel volume is assumed to be 0 pL.

Statistics

Statistical test were performed using GraphPad Prism 9.5.1. Statistical significance is considered when $p < 10^{-2}$.

The sample size was not predetermined and simply results from the repetition of experiments. No sample was excluded. No randomization method was used. The investigators were not blinded during experiments.

Data availability

The raw microscopy data, regions of interests (ROI), analysis codes and analyses will be made available on the following repository under a CC BY- NC-SA license: https://ressources.curie.fr/inversebleb/.

Acknowledgements

We thank the imaging platform of the Genetics and Developmental Biology Unit at the Institut Curie (PICT-IBiSA@BDD, member of the French National Research Infrastructure France-BioImaging ANR-10-INBS-04) for their outstanding support, in particular Olivier Leroy for his help writing Metamorph journals; the animal facility of the Institut Curie for their invaluable help. We thank Viventis Microscopy for custom Python scripts for the LS1 Live. We thank Maria Almonacic and Marie-Hélène Verlhac for generously sharing the Lap2b-GFP plasmid. We thank Yohanns Bellaïche, Carles Blanch-Mercader and members of the Maître lab for critical reading of the manuscript. Research in the lab of J.-L.M. is supported by the Institut Curie, the Centre National de la Recherche Scientifique (CNRS), the Institut National de la Santé Et de la Recherche Médicale (INSERM), and is funded by grants from the Fondation Schlumberger pour l'Éducation et la Recherche via the Fondation pour la Recherche Médicale, the European Research Council Starting Grant ERC-2017-StG 757557, the Agence Nationale de la Recherche (ANR-21-CE13-0027-01), the European Molecular Biology Organization Young Investigator program (EMBO YIP), the INSERM transversal program Human Development Cell Atlas (HuDeCA), Paris Sciences Lettres (PSL) QLife (17-CONV-0005) grant and Labex DEEP (ANR-11-LABX-0044) which are part of the IDEX PSL (ANR-10-IDEX-0001-02). M.F.S. is funded by a Convention Industrielle de Formation pour la Recherche (No 1113 2019/0253) between the Agence Nationale de la Recherche and Carl Zeiss SAS; as well as La Ligue contre le cancer. M.F.S. thanks the support from La Fondation des Treilles. A.M. acknowledges funding from the QBio Junior Research Chair programme of the QBio initiative of ENS-PSL and the Parisante Campus.

Author contributions

M.F.S., J.G.D. and D.P. performed experiments and prepared data for analyses. M.F.S. J.G.D. and J.-L.M. designed the project, analyzed the data. A.M. developed the theoretical analysis. M.F.S., A.M. and J.-L.M. wrote the manuscript. M.F.S. and J.-L.M. acquired funding.

Conflict of interest

During this project M.F.S. was partly employed by Carl Zeiss SAS via a public PhD program Conventions Industrielles de Formation par la Recherche (CIFRE) co-funded by the Association Nationale de la Recherche et de la Technologie (ANRT).

Supplementary Note: Inverse blebs operate as hydraulic pumps during mouse blastocyst formation

Markus F. Schliffka[1,2], Julien G. Dumortier[1], Diane Pelzer[1], Arghyadip Mukherjee[3,*], Jean-Léon Maitre[1,*]

[1]Institut Curie, CNRS UMR3215, INSERM U934,
PSL Research University, Sorbonne Université, Paris, France.

[2]Carl Zeiss SAS, Marly-le-Roy, France.

[3]Laboratoire de physique de l'École Normale Supérieure, CNRS UMR 8023,
PSL Research University, Sorbonne Université, Université Paris Cité, Paris 75005, France.

*Correspondance to jean-leon.maitre@curie.fr and arghyadip.mukherjee@ens.fr

In this note we briefly describe the minimal physical model for the formation and dynamics of intercellular fluid pockets situated at the interface of two adhering cells, henceforth referred to as fluid pockets. To capture the mechanics of these fluid pockets with volume V, surface area A and perimeter P, we propose an effective pseudopotential W where we consider the effects of surface tension T_0 acting on the area, pressure build-up p and effect of adhesion at the periphery (Figure 1A). The surface tension seeks to shrink the fluid pockets while the pressure seeks to inflate them. Inside the fluid pockets, the cell membranes are detached but at the periphery there is enrichment of immobile adhesive bonds (within the timescale of $\sim$ 1 min), which can be thought of as elastic springs connecting the two plasma membranes (*1*). As more area detaches, more bonds detach and accumulate at the periphery (based on our experimental observations, also see (*2*)). The increased contraction from such elastic springs resist the increase in perimeter, while steric repulsion from increased number of adhesive bonds prefer to expand the perimeter. The balance of these two opposing effects set a preferred perimeter P_0 and the mechanics can be captured by an effective perimeter elasticity with elastic coefficient k and rest perimeter P_0 (see Appendix to the note). The pseudopotential W is then given by $W = T_0A + k(P - P_0)^2 - pV$, and we also recast the rest perimeter as $P_0 = 2\pi R_0$. For simplicity let us consider a spherical fluid pocket of radius R which yields

$$W(R) = 4\pi R^2 T_0 + k(2\pi R - 2\pi R_0)^2 - \frac{4\pi}{3}R^3 p \quad . \tag{1}$$

Note that here we consider an effective pressure p and do not explicitly take into account osmotic effects that may play a role at larger length and timescales (*3*). We nondimensionalize using the length scale R_0 and tension T_0 to define in relative units $r = R/R_0, \bar{k} = \pi k/T_0, \bar{p} = pR_0/3T_0$. The nondimensional pseudopotential,

$$w(r) = \frac{W(R)}{4\pi R_0^2 T_0} = \left(\frac{R}{R_0}\right)^2 + \frac{\pi k}{T_0}\left(\left(\frac{R}{R_0}\right) - 1\right)^2 - \frac{pR_0}{3T_0}\left(\frac{R}{R_0}\right)^3 \tag{2}$$

$$= r^2 + \bar{k}(r-1)^2 - \bar{p}r^3 \quad . \tag{3}$$

Size of intercellular fluid pockets.– The stable states of the system are captured by the minima of the pseudopotential $w(r)$, which informs us of the mechanically stable size. The potential $w(r)$ has a

minima (r_l) and a maxima (r_h) at a finite r (see Fig.1A), given by the solution of $dw/dr = 0$ and is

$$r_{l,h} = \left(1 + \bar{k} \mp \sqrt{(1+\bar{k})^2 - 6\bar{p}\bar{k}}\right)/3\bar{p} \quad \text{for} \quad \bar{k} > 0. \tag{4}$$

Near the minima r_l the fluid pockets relax to attain size r_l, while beyond the maxima the fluid pockets grow indefinitely to maximal possible size (Figure 1B). In the *absence* of adhesion ($\bar{k} = 0$), the minima $r_l = 0$. Hence, finite-sized fluid pockets are transient and should disappear at experimental timescales. Based on their initial size being larger or smaller than $r_h = 2/3\bar{p}$, they will either grow very large (due to inflation) or shrink away (due to tension). This is similar to the nucleation mechanism of droplets and soap bubbles (*4*).

For $\bar{k} > 0$, finite sized fluid pockets can exist at r_l given by Eq.(4) and for small $\bar{k}$ we find that the stable radius $r_l \simeq \bar{k}$. On the other hand, the maximum of the potential $w(r)$ presents the barrier to nucleate a large-growing fluid pocket. This barrier is located at r_h and is given by Eq.(4). For small $\bar{k}$ we can approximate $r_h \simeq 2/3\bar{p} - (1 - 2/3\bar{p})\bar{k}$. Due to fluctuations and continuous fluid pumping, a fluid pocket can cross over this potential barrier. Hence, for finite adhesion, stable fluid pockets of finite size and growing large fluid pockets of undetermined size can coexist. Note that the coexistence of stable fluid pockets and growing fluid pockets depends on the existence of distinct non-zero minimum r_l and maximum r_h and hence a finite barrier Δw. As evident from Eq.(4), this is satisfied as long as $(1+\bar{k})^2 > 6\bar{p}\bar{k}$. This allows us to derive a phase diagram as shown in Figure 2A. The propensity (or rate)

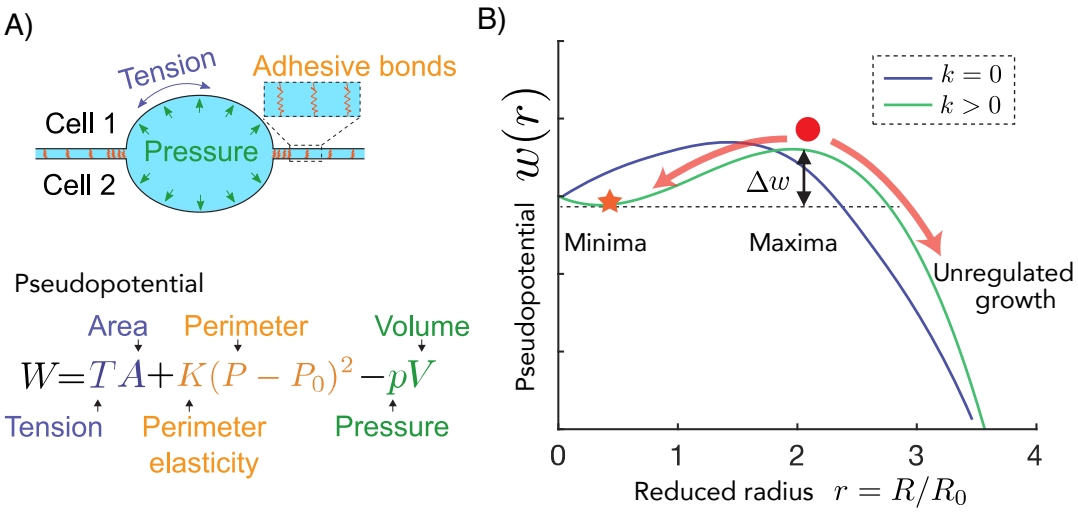

Figure 1: **Mechanics of fluid pockets:** A) Top: An intercellular fluid pocket situated between cell 1 and cell 2 is schematically depicted. Elastic adhesive bonds at the periphery of the fluid pocket are shown in the inset. Bottom: Energetic contributions from different mechanical parameters and geometric variables in the pseudopotential are depicted. B) Example normalised pseudopotential $w(r) - w(0)$ are shown as a function of reduced radius r (see text). For $k = 0$ (violet), the minima lies at $r = 0$ implying no stable finite sized fluid pocket, while for $k > 0$ (green) a stable finite minima can be found (large orange star), implying coexistence of finite-sized fluid pockets with growing fluid pockets. The maxima is shown with a red dot. A potential barrier of height Δw (the difference in w between the minima and maxima) is indicated for both cases.

to form such growing fluid pockets depends on the size of the potential barrier $\Delta w = w(r_h) - w(r_l)$. The lower the potential barrier, the higher is the probability to cross over the barrier. Δw depends on $\bar{k}$ and $\bar{p}$ as

$$\Delta w = \frac{4}{27\bar{p}^2}\left((1+\bar{k})^2 - 6\bar{p}\bar{k}\right)^{3/2} \quad . \tag{5}$$

Note that Δw is a decreasing function of relative pressure $\bar{p}$ (see main text, Fig. 2G), which implies that build-up of pressure due to pumping lowers the barrier and helps the formation of growing fluid pockets. On the other hand, Δw is an increasing function of relative perimeter elasticity $\bar{k}$, implying that adhesion inhibits barrier crossing (see maintext and Fig. 2F). Again, the barrier disappears when $(1+\bar{k})^2 < 6\bar{p}\bar{k}$, where the minima and the maxima fuse into an inflection point.

Shape and symmetry of intercellular fluid pockets.– We observe experimentally a characteristic difference in shape between the finite-sized fluid pockets and growing large fluid pockets. While the stable fluid pockets are typically symmetric and have a lens-like shape, the growing fluid pockets are asymmetric and resemble a spherical cap. To discuss whether a spontaneous symmetry breaking can take place in the course of the growth of the fluid pockets, we consider a spherical fluid pocket made of two hemispherical parts of radius R_1 and R_2 with identical tension T_0 and perimeter elasticity k. The volumes $V_i = (2\pi/3)R_i^3$, areas $A_i = 2\pi R_i^2$ and perimeters $P_i = 2\pi R_i$ for $i = 1, 2$. The mechanics can be captured with a pseudopotential similar to the previous section,

$$W(R_1, R_2) = T_0(A_1 + A_2) + \frac{k}{2}[(P_1 - P_0)^2 + (P_2 - P_0)^2] - p_1V_1 - p_2V_2 \tag{6}$$

$$= 4\pi(R_1^2 + R_2^2)\frac{T_0}{2} + \frac{k}{2}4\pi^2[(R_1 - R_0)^2 + (R_2 - R_0)^2] - \frac{2\pi}{3}R_1^3p_1 - \frac{2\pi}{3}R_2^3p_2 \quad . \tag{7}$$

Note that here the hydrostatic pressure plays the role of a Lagrange multiplier (constraint force) to maintain separate but connected volumes. We can estimate the pressures p_1 and p_2 quasi-statically by seeking $dW/dR_j = 0$ for $j = 1, 2$ and find

$$p_j = \frac{2(T_0 + \pi k)}{R_j} - \frac{2\pi k R_0}{R_j^2} \ , \text{ for } j = 1, 2 \quad . \tag{8}$$

Note that for $k = 0$ we recover Laplace's law. The volume balance in each of the hemispheres can be written as

$$\frac{dV_1}{dt} = sA_1 - J_{1\to2}\bar{A} \quad \text{and} \quad \frac{dV_2}{dt} = sA_2 + J_{1\to2}\bar{A} \quad , \tag{9}$$

where $\bar{A} \simeq (A_1 + A_2)/2$, s is pumping activity per unit area and $J_{1\to2}$ is a unit volume current from hemisphere 1 to hemisphere 2 due to change of shape. The current is described by a linear response law $J_{1\to2} = \mu(p_1 - p_2)$ where the hydraulic mobility μ is a function of the sphere radii R and dynamic viscosity η given by $\mu \simeq R/3\eta$. To study the symmetry breaking we study the dynamics of the relative volume difference $\nu = (V_1 - V_2)/(V_1 + V_2)$, given by

$$\frac{d\nu}{dt} = (V_1 + V_2)^{-1}\left(\frac{d(V_1 - V_2)}{dt} - \nu\frac{d(V_1 + V_2)}{dt}\right) \quad . \tag{10}$$

Note that $\nu = 0$ is the symmetric configuration where both hemispheres are identical while $\nu = \pm 1$ present the limiting cases where the entire volume is encapsulated either in hemisphere 1 or hemisphere 2. We consider a perturbation around the symmetric case (where $R_1 = R_2 = R$) in terms of the radii of the form $R_1 = R(1 + \psi)$ and $R_2 = R(1 - \psi)$ and perform a linear stability analysis. To linear order, the

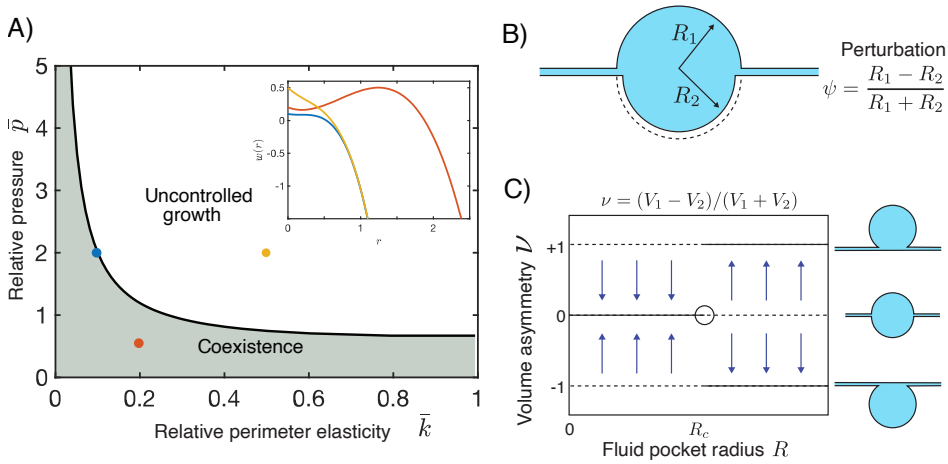

Figure 2: **Phases and symmetries of fluid pockets:** A) A phase diagram for coexistence of stable or growing fluid pockets is shown as function of relative adhesion $\bar{k}$ and relative pressure $\bar{p}$. Shaded grey region indicates region of parameter space where coexistence is found. In the inset, pseudopotential $w(r)$ is shown for colour coded parameter points. B) A shape perturbation scheme is depicted with two hemispheres of radius $R_1 > R_2$. C) A bifurcation diagram is shown for volume asymmetry ν as a function of system size/fluid pocket radius R. Below critical size R_c, the symmetric shape $\nu = 0$ is stable while above R_c the symmetric configuration $\nu = 0$ is unstable and the system adopts the asymmetric state $\nu = \pm 1$. The corresponding configurations are depicted on the right.

reduced volume difference $\nu = 3\psi + \mathcal{O}[\psi^3]$ and the linearised dynamics can be captured by

$$\frac{d\psi}{dt} \simeq \left(\frac{\pi k + T_0}{3\eta R} - \frac{s}{R} - \frac{8\pi k R_0}{3\eta R^2} \right) \psi + \mathcal{O}[\psi^3] = g(R)\psi \quad . \tag{11}$$

The asymmetry ψ grows when the growth rate $g(R)$ is positive, leading to a symmetry breaking while for $g(R) < 0$ symmetry is restored. Beyond a critical size R_c,

$$R > R_c = \frac{8\pi k}{\pi k + T_0 - 3\eta s} R_0 \quad , \tag{12}$$

an instability (*5*) occurs where the symmetric state $\nu = \psi = 0$ becomes unstable and relative differences between the two hemispheres diverge (see Fig. 2B). As a result we obtain an asymmetric configuration as depicted in Fig. 2B. On the other hand it implies that below R_c, small asymmetries will decay and enforce symmetric shape of fluid pockets. Hence, fluid pockets during their growth can obtain their characteristic asymmetric shape via a growth induced mechanical instability leading to clear morphological distinction between symmetric microlumens and larger asymmetric inverse blebs.

Retraction of inverse blebs.– Inverse blebs grow fast and, following an enrichment of actomyosin, shrink away. Here we consider the effect of a time-modulated active tension $t_a = T_a/T_0$ in terms of actin enrichment $\Delta\rho(t)$ and study the resulting dynamics. The dynamics of the reduced radii r can be expressed as a relaxation process in potential $w(r)$ with timescale τ and given as

$$\tau \frac{dr}{dt} = -\frac{dw}{dr} = 3\bar{p}r^2 + 2\bar{k} - 2(1 + \bar{k} + t_a(t))r \quad . \tag{13}$$

Surpassing the growth phase a transition from growing to shrinking can only occur for active tensions beyond a threshold given by

$$t_a > \frac{3}{2}\bar{p}r + \frac{\bar{k}}{r} - 1 - \bar{k} \quad . \tag{14}$$

To satisfy this criteria, either an enrichment of actomyosin or a reduction in $\bar{p}$ is necessary. Experimentally, we observe a sharp enrichment of actomyosin localisation in the retraction phase of the inverse bleb.

Appendix

Perimeter elasticity due to adhesive bonds. Consider a freshly nucleated spherical fluid pocket of radius R, where N_a number of adhesive bonds detached in the process of nucleation and accumulated at the periphery. If the surface density of adhesive sites prior to the detachment is ρ_s, then $N_a \simeq 2\pi R^2 \rho_s$. We can treat each of such adhesive bonds as an elastic spring with length e, rest length e_0 and stiffness k_e . Due to this enrichment, the density of adhesive bonds at the periphery ρ_p can be high. At high densities, interaction of molecules give rise to steric effects and cause repulsion. To capture the repulsive effects of such accumulation, we use the simplest energetic term Π/ρ_p that originates from a two dimensional steric pressure(similar to ideal gas). Note that the $\rho_p = N_a/2\pi Rd = R\rho_s/d$, where d is the thickness of the peripheral region. The mechanics can be presented with an pseudopotential,

$$\begin{aligned} \delta W &= \frac{k_e}{2}(e-e_0)^2 N_a + \Pi/\rho_p \\ &= \left[\pi k_e \rho_s (e-e_0)^2\right] R^2 + \left[\frac{\Pi d}{\rho_s}\right]\frac{1}{R} = AR^2 + \frac{B}{R} \quad , \end{aligned} \tag{15}$$

where $A = \pi k_e \rho_s (e-e_0)^2$ and $B = \Pi d/\rho_s$. The balance of these two effects sets a minima at

$$R_0 = \left(\frac{B}{2A}\right)^{1/3} = \left(\frac{\Pi d \rho_s^{-2}}{2\pi(e-e_0)^2}\right)^{1/3} \quad . \tag{16}$$

Around R_0, we can perform an expansion up to the leading order term and we find an effective perimeter elasticity $k(P-P_0)^2$ with $k = 3k_e\rho_s(e-e_0)^2/4\pi$,

$$\delta W \simeq 3\left(\frac{AB^2}{4}\right)^{1/3} + 3A\left(R-R_0\right)^2 + \mathcal{O}[\epsilon^3] = \delta W_0 + k(2\pi R - 2\pi R_0)^2 = \delta W_0 + k(P-P_0)^2 \quad . \tag{17}$$

References

1. Sabyasachi Dasgupta, Kapish Gupta, Yue Zhang, Virgile Viasnoff, and Jacques Prost. Physics of lumen growth. *Proceedings of the National Academy of Sciences*, 115(21):E4751–E4757, 2018.

2. Diana Pinheiro, Edouard Hannezo, Sophie Herszterg, Floris Bosveld, Isabelle Gaugue, Maria Balakireva, Zhimin Wang, Inês Cristo, Stéphane U Rigaud, Olga Markova, et al. Transmission of cytokinesis forces via e-cadherin dilution and actomyosin flows. *Nature*, 545(7652):103–107, 2017.

3. Mathieu Le Verge-Serandour and Hervé Turlier. A hydro-osmotic coarsening theory of biological cavity formation. *PLoS Computational Biology*, 17(9):e1009333, 2021.

4. F Weinhaus and W Barker. On the equilibrium states of interconnected bubbles or balloons. *American Journal of Physics*, 46(10):978–982, 1978.

5. Nicolas T Chartier, Arghyadip Mukherjee, Julia Pfanzelter, Sebastian Fürthauer, Ben T Larson, Anatol W Fritsch, Rana Amini, Moritz Kreysing, Frank Jülicher, and Stephan W Grill. A hydraulic instability drives the cell death decision in the nematode germline. *Nature Physics*, 17(8):920–925, 2021.

2.3 Additional results pertaining to Research paper B: Inverse blebs operate as hydraulic pumps during mouse blastocyst formation

The data in this chapter expand on the findings on inverse blebs during blastocoel formation. They were not included in the manuscript for publication because they remain at this stage preliminary. However, they are included here as they might serve for further discussion and directions.

2.3.1 Localization and growth directionality of inverse blebs

When analyzing the global distribution of inverse blebs throughout the embryo, we found no bias for any cell or contact type to form more inverse blebs (Inverse bleb manuscript, Extended Data Fig. 2). Especially, we did not observe a bias at the interface of TE and ICM cells, which are thought to have different surface tensions [115,250]. Therefore, global differences between the cells seem unlikely to bias inverse bleb directionality. For outward membrane blebs, local defects in the cell cortex can initiate bleb formation [137]. We hypothesized that likewise in the mouse embryo, local weaknesses in the cell cortex could cause inverse blebs to form at a certain site at the cell-cell contact and determine the blastomere into which it will inflate. To test this idea, we created chimeric embryos with contacts of heterotypic contractility by grafting an 8-cell stage WT blastomere on a m*Myh9*$^{+/-}$ host morula at the same developmental stage and then imaged lumen formation to observe a potential bias in the orientation of the inverse blebs (Figure 8A). Indeed, inverse blebs at the contact of a m*Myh9*$^{+/-}$ host and a WT graft extend overwhelmingly into the host blastomere, while this is not the case for homotypic control grafts (Figure 8B,C). This could indicate that the weaker actomyosin cortex or the reduced tension and cytoplasmic pressure of the m*Myh9*$^{+/-}$ blastomeres can direct inverse bleb orientation.

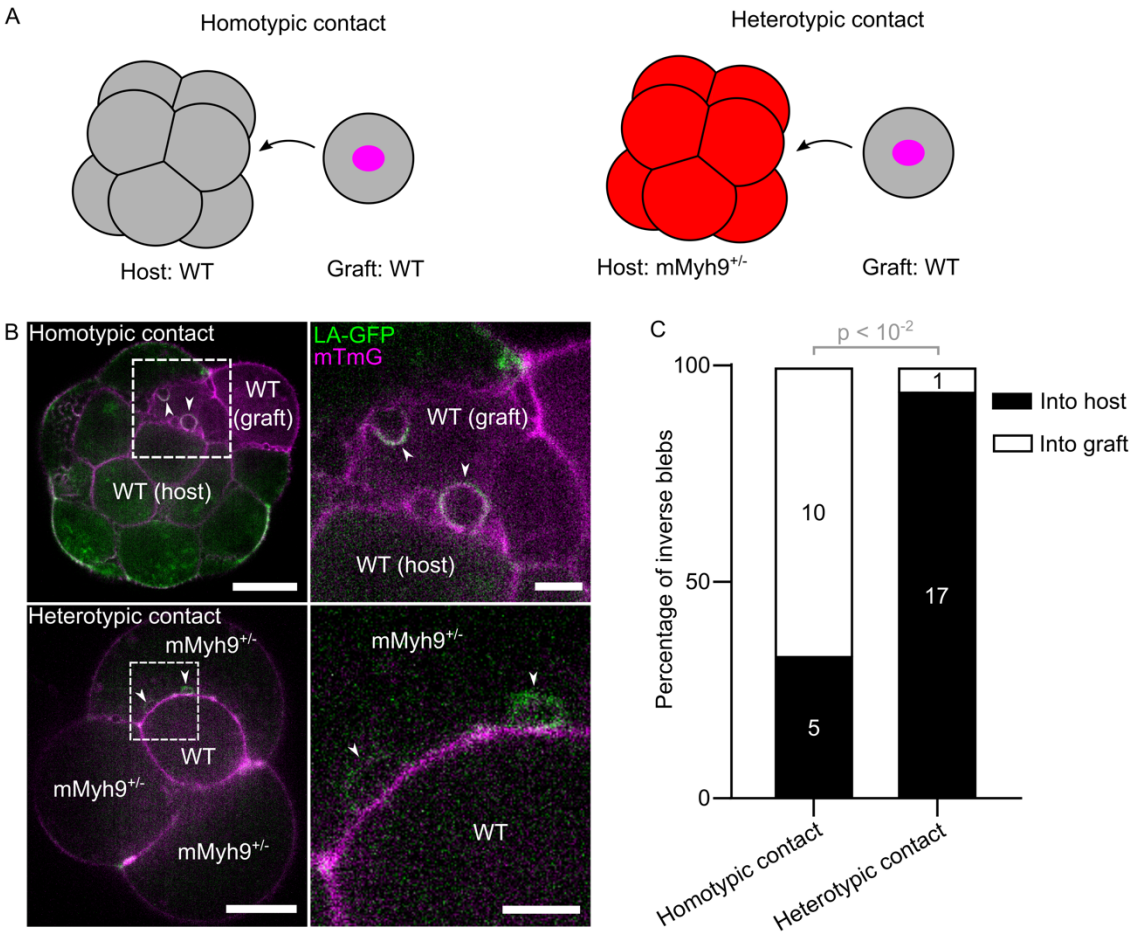

Figure 8: Inverse blebs at heterotypically contractile contacts. *A*) Creation of contacts with heterotypic contractility. 8-cell stage WT blastomeres expressing Lifeact-GFP, mTmG and H2B-mCherry (to distinguish them from the host blastomeres) were grafted on either a WT 8-cell stage host morula expressing LifeAct-GFP and mTmG as a control, or on an m*Myh9*$^{+/-}$ host morula expressing LifeAct-GFP and mTmG to create heterotypic contacts. Note that m*Myh9*$^{+/-}$ embryos do not always have a cell number equal to WT embryos at the same stage due to division defects (see chapter 2.1). Chimeras were imaged for 5 min every 5 s at the equatorial plane which was repeated every 1 h during the blastocoel formation process. B) Examples of inverse bleb formation at homo- (top) or heterotypic (bottom) contacts during lumen formation. Left images show the equatorial plane of the chimera, right images show the inset. Scale bar left, 20 μm. Scale bar right, 5 μm. C) Percentage of observed inverse blebs at the host/graft contact. Inset numbers indicate the absolute inverse bleb number. Data are from 7 / 3 chimeras from 4 / 2 experiments for homotypic / heterotypic contacts. The p value results from Fisher's exact test.

2.3.2 Inverse bleb size in the context of reduced luminal fluid accumulation

When investigating the role of pressure in inverse bleb formation, we acutely treated embryos in the inverse bleb phase with 20 μm EIPA and saw a decrease of inverse blebs formation within 15 min (Inverse bleb manuscript, Fig. 2). We hypothesized that

reducing the fluid influx into the intercellular space might result in a lower intercellular pressure which might cause the inverse blebs that still manage to form in the EIPA treatment condition to inflate to smaller sizes due to the reduced pressure. However, when measuring the maximal inverse bleb contour lengths in control and treatment condition, we could not detect a difference in their sizes (Figure 9). This might indicate that once the intercellular pressure reaches a threshold high enough to trigger an inverse bleb, its size does not depend on the absolute fluid pressure.

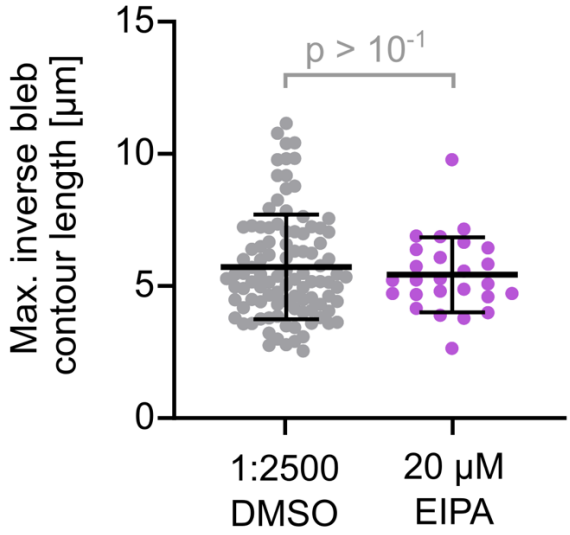

Figure 9: Comparison of maximal inverse bleb contour length in DMSO control condition and after 15 min of 20 µM EIPA treatment. Bars show average and bracket SD. n = 100/26 inverse blebs from 3 / 4 embryos from 3 experiments. The p value results from Student's t test.

2.3.3 Molecular characterization of inverse blebs by immunostaining

After inverse blebs extend, actin and myosin are recruited to the inverse bleb membrane to effect its retraction (Inverse bleb manuscript, Fig. 3). The mechanism for this specific recruitment is unclear, but it stands to reason that actin polymerization is driven by actin-nucleating factors like for outward blebs [139]. Inverse blebs were immunostained for various transmembrane proteins and actin-organizing factors (Figure 10) The transmembrane protein Na^+/K^+-ATPase localizes to both the apical and basolateral membrane. It is present in the inverse bleb membrane, indicating that transmembrane proteins do not change their localization after microlumen or inverse bleb formation and participate in the membrane movement. Although a transmembrane protein, CDH1 is not detectable in the inverse bleb membrane, since

it is mostly enriched where membranes are opposed to one another. This is in accordance with the observation in live embryos expressing CDH1-GFP, which accumulates in microlumen-/inverse bleb-adjacent foci (Inverse bleb manuscript, Extended Data Fig. 3). Considering the recruitment of the actomyosin cytoskeleton, we tested Arp2, which is a component of the Arp2/3 actin nucleation complex, and cortactin, which is also an actin nucleation factor. While cortactin has been implied in outward bleb retraction [147], the Arp2/3 complex does not seem to play a role in outward bleb retraction [139], but is nevertheless an important actin organizing factor in many processes. Both factors could be detected at the apical membrane of TE cells, showing that the protein is expressed during the preimplantation stages. However, both are absent from the inverse bleb membrane. Therefore, there is no evidence that they are involved in actin recruitment to the inverse blebs. Finally, we stained for the cortex-membrane linking complex consisting of ERM proteins in its phosphorylated state. The ERM complex localizes to the membrane of outward blebs prior to the recruitment of actin [139]. As for Arp2 and cortactin, the pERM complex almost exclusively localizes to the apical surface of the mouse embryo, and is absent from the inverse bleb membrane. This opens the question of how the newly polymerized actomyosin cortex attaches to the inverse bleb membrane. The testing of further markers will be required to discover which factors enable the recruitment of actin and myosin to the inverse blebs after inflation.

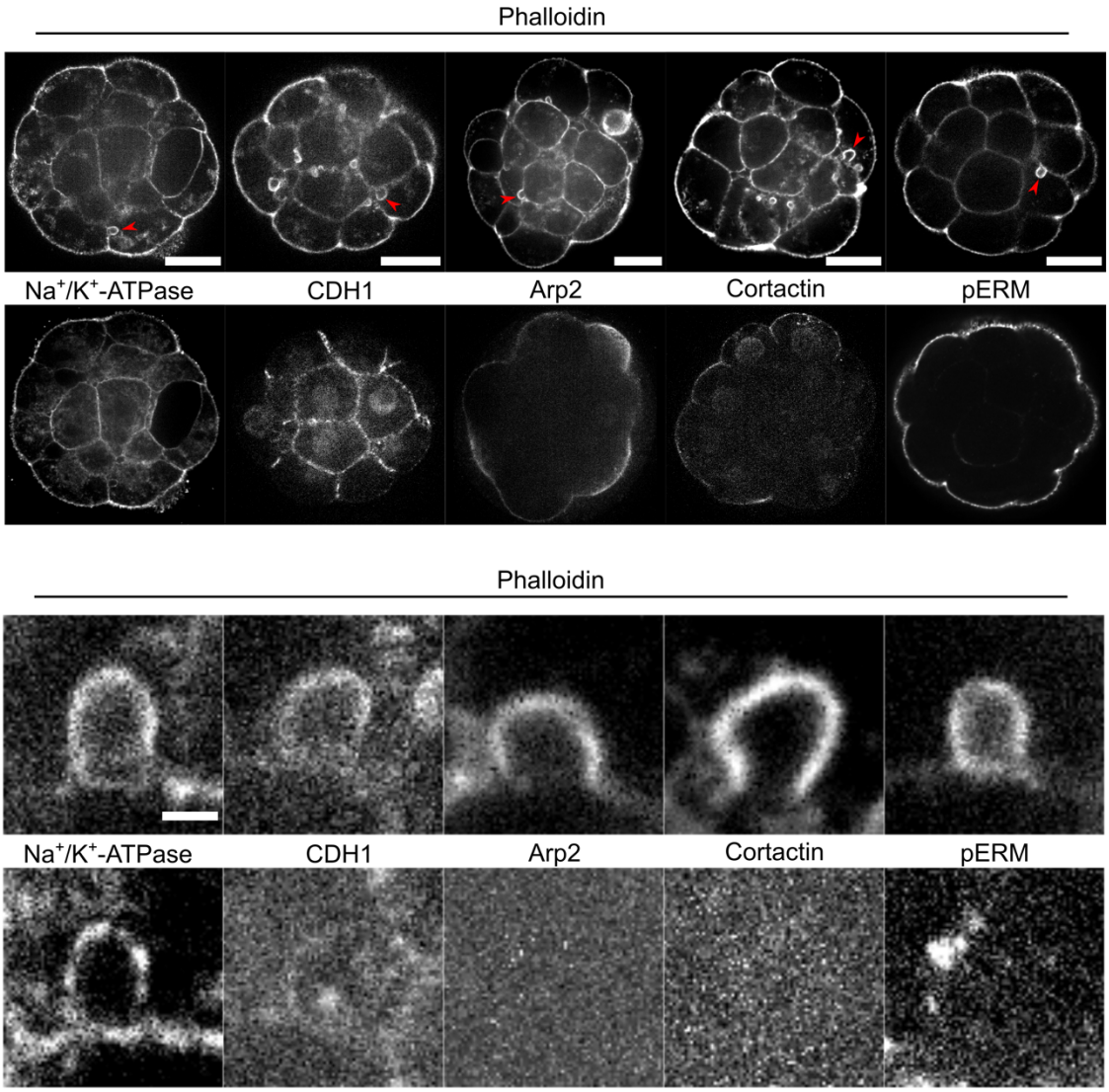

Figure 10: Immunostaining of membrane proteins and actin organizers in inverse blebs. Top: Single focal planes of mouse embryos fixed during the inverse bleb phase. Upper row shows F-actin stained with phalloidin, lower row shows the indicated proteins. Bottom: Detail of inverse blebs indicated by a red arrowhead in the top images. Scale bar for top images, 20 μm. Scale bar for bottom images, 5 μm, same scale for all magnified inverse blebs.

2.3.4 Inverse bleb number in doublets and quartets

In the context of our experiments with lumen formation in quartets and doublets, we compared the duration of microlumens (Inverse bleb manuscript, Fig. 4C). Here, we also consider the number of inverse blebs in these respective configurations. Whole embryos, quartets and doublets were imaged every 1 min at their equatorial plane and inverse blebs were counted during the lumen formation process. As expected from the reduced cell number and microlumen duration, quartets and doublets on average

show a reduced absolute inverse bleb number compared with whole embryos (Figure 11A). Nevertheless, it should be noted that even doublets with 1/16th the cell number of whole embryos are able to reach the same absolute number of inverse blebs. When normalizing the inverse bleb number for the cell number in the imaging plane, quartets and doublets show higher average inverse bleb numbers (albeit not statistically significant) (Figure 11B). The lower normalized inverse bleb number in the whole embryo might be a consequence of the many multicellular microlumens which can absorb fluid, while this is not possible in a setting of reduced topological pressure sinks.

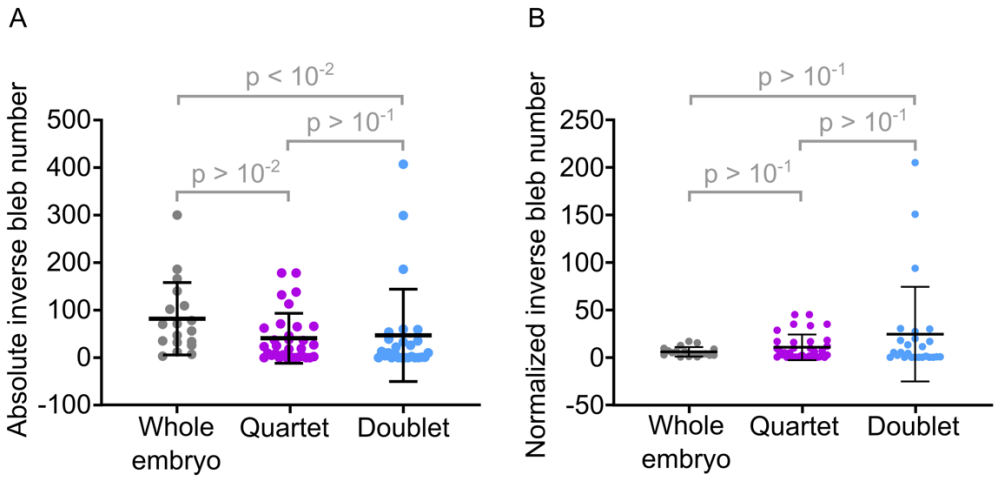

Figure 11: **Inverse bleb number in whole embryos, quartets and doublets**. A) Absolute inverse bleb number based on time-lapses in which the equatorial plane was imaged every 1 min. B) Inverse bleb number of (A) normalized for the cell number in the focal plane. Bars show average and bracket SD. n = 18/32/27. p values result from Kruskal-Wallis and Dunn's multiple comparison tests.

3. DISCUSSION

3.1 Additional discussion for Research paper A: Multiscale analysis of single and double maternal-zygotic mutants during mouse preimplantation development

Preimplantation development is a unique opportunity to study mammalian morphogenesis, as its autonomous development allows prolonged live imaging, manipulation and biophysical measurement of the embryo [152,282,283]. As the main driver of animal morphogenesis, actomyosin contractility has been the focus of recent studies on the mouse embryo which investigated its role in the regulation of cortical tension enabling morphogenesis [179], blastomere polarization [281], cortical oscillations and compaction [181,182], internalization [115,284,285], tight junction formation [272], blastocoel formation [250] and blastocyst size regulation [286]. These works have identified numerous roles for actomyosin contractility in cell shaping, positioning, lumen formation and lumen homeostasis. Recent studies have also advanced our understanding of the role of actomyosin contractility in the compaction of human embryos, showing that human embryos employ a similar, but quantitatively different strategy of compaction [164]. However, no study so far had been conducted investigating the complete loss of actomyosin contractility and its effect on early mouse embryonic development. Manipulation of actomyosin contractility in the studies listed above relied on partial genetic myosin knockout [115,286], siRNA-mediated knockdown [272,285] or pharmacological treatment [281]. While the role of the mammalian NMHC paralogs MYH9, MYH10 and MYH14 in development had been previously characterized using zygotic knockouts of their respective genes, their specific role in preimplantation development had not been analyzed yet.

In our study *Multiscale analysis of single and double maternal-zygotic Myh9 and Myh10 mutants during mouse preimplantation development,* we investigated how a partial or complete loss of actomyosin contractility affects preimplantation development by maternal-zygotically knocking out the two expressed NMHC paralog genes *Myh9* and *Myh10*, either separately or combined. In summary, this showed that MYH9 is the dominant paralog in mouse preimplantation development, and its maternal-zygotic loss leads to cell cycle delay, reduced cell number through

cytokinesis defects, lower compaction and impacted, yet correct lineage differentiation. By contrast, loss of *Myh10* had little impact on the embryonic phenotype. However, MYH10 seems to compensate to a large extent for the loss of *Myh9* in mz*Myh9*$^{-/-}$ embryos, as the phenotype of double knockout embryos is again more severe than loss of *Myh9* only. With their extremely reduced cell number, double knockout embryos still manage to apicobasally polarize and form a lumen with comparable growth rates as WT embryos. In the most extreme case, this happens in a single-celled embryo, as we confirm by complete embryo fusion.

The findings of this study and their implications have been extensively discussed in the article text (Chapter 2.1). The phenotypes observed in the NMHC knockout embryos highlight the highly regulative nature of early mammalian development [287], where genetic or physical perturbations still result in the robust formation of a blastocyst that can develop into a viable mouse. Indeed, m*Myh9*$^{+/-}$;m*Myh10*$^{+/-}$ embryos, which consistently show severely reduced cell number and differentiation, can develop into a viable mouse without observable phenotype. We observe frequent cytokinesis failures in *Myh9* and double knockout embryos, resulting in aneuploid cells. Aneuploidies are common in human development and result in developmental defects [288]. However, the analysis of early human embryos has shown that the number of aneuploid cells can be reduced by the embryo, suggesting a mechanism for exclusion of these cells [289]. Since m*Myh9*$^{+/-}$ and m*Myh9*$^{+/-}$;m*Myh10*$^{+/-}$ embryos result in viable mice, aneuploid cells must also be excluded from the fetal tissues at some point in development. Therefore, these mutant embryos may serve as a model for investigating how aneuploid cells are excluded from the cells that give rise to the fetal tissues in human embryos.

The findings of this study provide a global overview of the role actomyosin plays in shaping the mouse preimplantation embryo. In this, it complements the other studies referred to above which investigate the role of actomyosin in specific processes. While our findings confirm many previous observations, such as the vital role of MYH9 in cortical oscillations and compaction [181], we could not confirm e.g. the requirement of contractility for apicobasal polarization [281] (as even double knockout embryos can

form a functional epithelium that effects fluid transport), or a role for contractility in blastocoel expansion which has been suggested previously [256].

To what extent our findings can be generalized in mammalian development is up for debate. Most studies about the different organismic roles of NMHC paralogs have used the mouse as a model system. We also analyzed NMHC paralog expression in human preimplantation embryos based on published scRNA-seq data, which showed a more equal expression of MYH9 and MYH10 from the zygote stage onward. This might hint at a more equal contribution of the two paralogs in early human development. Indeed, human preimplantation morphogenesis is similar, but not completely equal to that in mice. The human embryo undergoes the same morphogenetic steps and employs actomyosin in comparable, but ultimately slightly different strategies than mouse embryos, e.g. during human compaction [164]. Further research is required to demonstrate the role of different NMHC paralogs in other species.

3.2 Characterization of inverse blebs during blastocoel formation

While the role of actomyosin contractility has been studied in detail for the preimplantation morphogenetic processes of compaction and internalization, as well as for cortical contractile waves [115,181,182], it was hitherto less clear what controls the dynamics of the blastocoel formation process. As a basolateral lumen, the blastocoel forms in a process of hydraulic fracturing and coarsening over several hours. While the growth and shrinkage dynamics of microlumens have been studied, as well as how adhesion and contractility patterns globally position the blastocoel, it remained unclear what controls fluid dynamics in the microlumen network. Since actomyosin often acts on the timescale of seconds rather than minutes or hours, we decided to image embryos during lumen formation at the timescale of seconds, which led to the discovery of inverse blebs in the early mouse embryo. Here, we are the first to describe inverse blebs at adhesive cell-cell interfaces that form due to pressurized fluid which is locally confined by adhesion molecules. In the wake of these findings, several questions remain about the dynamics and function of inverse blebs.

Having initially observed short-lived membrane protrusions that are covered in actin and myosin, we could confidently characterize them as inverse blebs. Like outward membrane blebs, they grow without actin, followed by actomyosin recruitment and retraction within ca. 1 min [136]. The process that we identify as inverse blebs in the mouse preimplantation embryo has been previously described as a process of exocytotic vesicles delivering fluid into the intercellular space [290]. However, this is not the case as we see the plasma membrane extending from the cell-cell contact during inverse bleb growth and before actomyosin recruitment (Inverse bleb manuscript, Fig. 1). Also, high temporal resolution imaging indicated no vesicle transport at the basolateral membrane. Interestingly, there are cases of exocytosis of large, micron-sized vesicles which need the formation of an actin coating for successful exocytosis of their content [291], which indeed look similar to inverse blebs. But as stated above, the extension of membrane from the contact and the fact that an inverse bleb fills with labelled intercellular fluid argue against an exocytotic process. Also, the observed process is unlikely to be a macropinocytotic process, as macropinocytotic cups grow with actin from the beginning, which is not what we observe for inverse blebs [292].

Inverse blebs differ from microlumens in their size, lifetime and symmetry. While microlumens grow to a diameter of ca. 1 μm, inverse blebs can reach diameters of 3 μm and more. Microlumens are stable on the timescale of minutes to hours and symmetrically extend into both adjacent blastomeres, inverse blebs extend and retract in under 1 min. One of their most striking features is, of course, that they selectively extend into one blastomere while the second one is not affected by the inverse bleb. Potential reasons for this are discussed in chapter 3.3.

3.3 Factors enabling inverse bleb formation and positioning

Inverse blebs are triggered by an increase in intercellular pressure combined with a local fluid confinement provided by CDH1. Either stopping the pressure increase or reducing the adhesion in the morula leads to the disappearance of inverse blebs

(Inverse bleb manuscript, Fig. 2). The observation that a preimplantation embryo with reduced adhesion (m*Cdh1*$^{+/-}$ embryos) can form a blastocyst without inverse blebs shows that these are not absolutely required for blastocyst formation. Additionally, m*Cdh1*$^{+/-}$ embryos go from morula to blastocyst in half the time as WT embryos (Inverse bleb manuscript, Extended Data Fig.4), and microlumens appear to undergo coalescence by merging rather than coarsening. This temporally more efficient strategy begs the question why WT embryos were selected for a higher adhesion level that entails the formation of inverse blebs. While m*Cdh1*$^{+/-}$ embryos show a reduced compaction phenotype during the morula stage, they seem to develop normally later and result in viable animals. The benefit of WT adhesion levels therefore remains an open question. The role of intercellular fluid pressure in the formation of inverse blebs seems to be analogous to cytosolic pressure in outward blebs [137,138] as they are necessary for bleb inflation and lowering of either pressure leads to disappearance of the respective blebs. Of course, the source of pressure differs in both cases: While inverse blebs are inflated by the pressurized intercellular fluid that accumulates in the microlumens due to the osmotic gradient that the embryo establishes, outward blebs inflate by the cytosol which is pressurized by cortical contractility.

Inverse blebs grow at all cell-cell contacts of the preimplantation embryo, with equal occurrences into TE and ICM cells when normalizing for the sampled contact lengths (Inverse bleb manuscript, Extended Data Fig. 2). It is unclear why inverse blebs form at certain points of the cell-cell contacts, while at other points only microlumen form or contacts remain closed. Globally, no bias for a specific inverse bleb localization can be detected and inverse bleb localization does not correlate with the final localization of the blastocoel (Inverse bleb manuscript, Extended Data Fig. 2). Thus, the factors determining inverse bleb localization and directionality are probably determined locally and not globally. For outward blebs, there are at least three theories about how they are triggered: (1) the cell cortex is locally weakened which leads to a detachment of the membrane, (2) the linker proteins attaching the cortex to the membrane are locally decreased, (3) a local contraction of the actomyosin cortex causes a local increase in pressure that detaches the membrane from the cortex [131]. Similar factors might play a role in determining where an inverse bleb forms. Local weaknesses in the

submembrane cortex might predestine a contact region for inverse bleb formation, and also determine the directionality of the bleb which would intrude into the cell with the locally weaker cortex. The observations made in WT-m*Myh9*$^{+/-}$ grafted embryos would support this concept (Chapter 2.3.1, Figure 8). The same scenario can be imagined for a unilateral local depletion of cortex-membrane connecting proteins on a cell-cell contact which would bias bleb position and directionality. However, the argument speaking against these two factors is that the actomyosin cortex at the basolateral contacts of the 32-cell stage embryo is comparatively weak. Myosin mostly localizes to the apical junction of the TE cells [227] and only accumulates at the basolateral membrane during inverse bleb retraction. Also, cortex-tethering proteins, such as ERM proteins, localize overwhelmingly to the apical membrane [196] and are only sparsely present at the basolateral contacts (Chapter 2.3.3, Figure 10). Therefore, it is doubtful if the cortex stability or its anchoring plays a substantial role in determining the site of inverse bleb formation. With the same reasoning, local contractions of the cortex are unlikely to disconnect it from the membrane to allow membrane expansion into the cytosol (analogously to theory 3 of outward bleb formation). It is possible that the directionality bias in WT-m*Myh9*$^{+/-}$ grafted embryos results from a global difference in cytosolic pressure between WT and m*Myh9*$^{+/-}$ cells, but that differences between WT blastomeres alone are not sufficient to bias inverse bleb directionality.

3.4 Mechanism of actomyosin recruitment

During the extension of inverse blebs, actin and myosin start to be recruited to the intruding membrane (Inverse bleb manuscript, Fig. 1 and 3). This happens very selectively since this accumulation cannot be observed at either microlumens or closed contacts adjacent to inverse blebs. Thus, actomyosin recruitment must follow a cue specific to the inverse bleb. While the nature of this recruitment cue remains unclear at this point, several scenarios as to how actomyosin is recruited are imaginable: Firstly, inverse blebs are strongly negatively curved membrane structures that bulge into the cell. As such, they might be recognized by curvature-sensing proteins. Classical curvature sensing proteins, such as BAR proteins, can sense and induce membrane curvature at the nanometer scale [293,294]. This is of course not

applicable for the size scale of inverse blebs, which reach diameters of up to 3 μm. However, members of the septin family of cytoskeletal proteins have been reported to recognize negative curvature on the micrometer scale [295], which are size ranges comparable to inverse blebs. Indeed, a recent report showed the recruitment of septins to the curved neck of outward membrane blebs in cancer cells, which has been implied in a signaling function [144]. The bleb neck in this scenario has a similar curvature geometry to inverse blebs. Septins interact with the actomyosin components of the cytoskeleton [296–298] and therefore might be candidate proteins for how the curvature of the inverse bleb is recognized and leads to actomyosin recruitment. A curvature-dependent mechanism would imply that actomyosin is recruited differently in outward and inverse blebs, as these two kinds of blebs have opposite membrane curvature geometries and would need to employ different protein machineries to bind to their respectively curved membrane. In a second scenario, the stretching of membrane, which coincides with dilution of residual CDH1 molecules in the membrane, could lead to reinforced actomyosin recruitment. Indeed, CDH1 dilution has been identified as a factor that can enable actomyosin accumulation [299]. Further investigation of inverse blebs might include testing the expression and localization of septins as potential curvature sensors, and other organizers of the actomyosin cytoskeleton that have been implied in the retraction of outward blebs, such as RhoA, actinin, ezrin [139] and formins [300]. However, while the recruitment of these factors to outward blebs can be clearly observed, the cue for their specific local recruitment, which reestablishes the cortex and leads to bleb retraction, also remains unclear. Mechanical deformation of the blastomere membrane to induce negative curvature on the same size scales as inverse blebs could give insight if curvature alone is sufficient to recruit actin and myosin in the case of inverse blebs.

3.5 Mechanism of inverse bleb retraction

The recruitment of actin and myosin leads to inverse bleb retraction. This process occurs analogously in outward membrane blebs. In both cases, actin is recruited to the bleb membrane before myosin [139]. Maternal knockout of either *Myh9* or *Myh10* showed that inverse blebs retract more slowly in m*Myh9*$^{+/-}$ embryos, but behave the

same in m*Myh10*$^{+/-}$ and WT embryos (Inverse bleb manuscript, Fig.3). On the one hand, this reflects the findings from our NMHC paralog knockout study (Chapter 2.1) where we saw that MYH9 is the dominant NMHC paralog whose knockout leads to a more severe phenotype. On the other hand, this is in line with findings from studies on outward bleb retraction, in which knockdown of *Myh9* slows down bleb retraction, but not *Myh10* (or *Myh14*) knockdown [140], suggesting a similar reliance on MYH9-mediated contractility in outward and inverse blebs. A similar delay in retraction of inverse blebs was seen when NMHCs were globally inhibited with para-Nitroblebbistatin. In cell culture, Blebbistatin treatment leads to a stop of outward bleb formation [106], presumably because cortex contractility is required for generating the intracellular pressure required to trigger blebs. Although this might require further quantification, we see no indication for a reduction of the inverse bleb number in m*Myh9*$^{+/-}$ or para-Nitroblebbistatin treated embryos. This reinforces the concept that the intercellular fluid pressure in cooperation with adhesion molecules triggers inverse blebs, while actomyosin-generated cytosolic pressure probably does not influence their formation. Interestingly, myosin knockout and inhibition did not alter the size to which inverse blebs grow, implying that myosin-mediated contractility does not stop inverse bleb growth per se. Instead, the factors determining inverse bleb size might be the pressure gradient that triggers the inverse bleb and that, once equilibrated, cannot lead to further expansion. Also, the extent to which the basolateral membrane of blastomeres can be stretched during inverse bleb extension might be limited, so that the amount of available membrane material may limit how far inverse blebs can acutely extend. However, the inverse blebs that still could be observed after EIPA treatment of inverse blebbing embryos (this treatment presumably stops pressure build-up in the intercellular space) were of comparable sizes to those in the control condition (Chapter 2.3.2, Figure 9). This would speak against a scalable influence of the intercellular pressure on inverse bleb size, and rather indicate that inverse blebs are triggered if the intercellular fluid reaches a certain threshold value. Since inverse bleb size differ between TE and ICM cells (Inverse bleb manuscript, Extended Data Fig.1), the respective surface tension and pressure of the two cell types also seem to play a role in setting the inverse blebs size. Alternatively, actin recruitment, whose dynamics are not altered in NMHC knockout / inhibition, might be sufficient to stop

inverse bleb growth prior to a delayed retraction by sufficiently counteracting the intruding membrane. This might be tested by a suitable manipulation of actin assembly dynamics. However, preliminary experiments in that regard using Latranculin B or Jasplakinolide led to the complete disappearance of inverse blebs so that this hypothesis could not be tested.

3.6 Function of inverse blebs in fluid distribution

At the 32-cell stage, the basolateral contacts of the blastomeres can be separated into bi- and multicellular contacts, which topologically correspond to faces (bicellular contacts) and channels / vertices (multicellular contacts). We have observed a topological exclusiveness for inverse blebs which appear only at bicellular junctions (Inverse bleb manuscript, Fig. 4). In the lumen formation process, bi- and multicellular microlumens show different coarsening behaviors, and the final blastocoel likely always emerges from a multicellular contact [250]. Coarsening of the microlumen network is thought to occur because of pressure differences between microlumens and fluid exchange through the connecting intercellular space which ultimately results in the disappearance of all microlumens except the final blastocoel [250,301]. However, this coarsening principle was conceptualized based on 1D or 2D microlumen chains and networks in which fluid exchange happens freely through connecting tubes [301]. In the 32-cell stage mouse embryo, the microlumens form a complex 3D network in which individual microlumens are separated by foci of adhesion molecules, which form when the cell contacts are separated by hydraulic fracturing. The complex 3D architecture in concert with the delimiting adhesion molecules may hinder free exchange of fluid between microlumens. As observed in the adhesion-reduced m*Cdh1*$^{+/-}$ embryos, the blastocoel formation duration is reduced by half compared to WT embryos, and inverse blebs are rarely observed (Inverse bleb manuscript, Fig.2, Extended Data Fig.4). Also, the experiments of chimeric *Cdh1* knockout have shown that local adhesion reduction is actually sufficient to stop inverse bleb formation on the level of the entire embryo. Our understanding is that a local pressure increase above a certain threshold, enabled by adhesion molecule confinement, triggers inverse bleb formation. Considering the whole microlumen network, this would mean that inverse

blebs form in regions in which pressure equilibration by fluid exchange between microlumens cannot occur efficiently, leading to the local entrapment of fluid. As we observe inverse bleb formation only at bicellular junctions, the necessary fluid entrapment and pressure build-up would only occur at bicellular cell-cell interfaces. Therefore, adhesion molecules might effectively impede fluid exchange between microlumens caused by pressure differences, as put forward in the coarsening model, leading to the formation of inverse blebs. The retraction of inverse blebs would then serve as an active way for the cell to redistribute fluid in the intercellular network and effect the fluid exchange between neighboring microlumens which had previously failed, making the inverse bleb an active fluid pumping mechanism.

The absence of inverse blebs at multicellular microlumens led to the hypothesis that the latter could act as pressure sinks into which coarsening is directed. Our experiments involving lumen formation in the context of a reduced cell number showed the influence of topological features on the coarsening process. Counterintuitively, doublets, with half the cell number as quartets, took on average a longer time to coarsen their microlumen network. We attribute this observation to the fact that in a doublet, fluid cannot accumulate in a multicellular microlumen, which would be supported by inverse blebs at the bicellular contacts. Instead, fluid expelled after inverse bleb retraction in doublets would always be reintroduced into the surrounding bicellular microlumens, potentially generating new inverse blebs. In the larger quartets, all cell-cell contacts contact at least one multicellular microlumen, which can serve as a pressure sink in the coarsening process, thus reducing the time to resolve the microlumen network. However, the differences in the number of inverse blebs between the whole embryo, quartets and doublets are less clear. Quartets show fewer inverse blebs in absolute numbers on average compared to the whole embryo, but not to a statistically significant degree as would be expected from the eightfold smaller cell number (Chapter 2.3.4, Figure 11A). The doublets show a high degree of variation in inverse bleb number, ranging from no inverse blebs to several hundred in just two cells. Therefore, the absence of a multicellular contact does not forcibly result in more inverse blebs. Only when normalizing for the cell number in the imaging plane, doublets show on average a higher, albeit not statistically significantly different inverse

bleb number. To what extent the number of inverse blebs can influence the speed of coarsening remains to be investigated.

Apart from these discrepancies of inverse bleb numbers between whole and reduced embryos, whole WT embryos on their own show a large variability in inverse bleb number (Inverse bleb manuscript, Fig. 2B) (Chapter 2.3.4, Figure 11), and inverse blebs do not always appear in all blastomeres of the embryo. Thus, WT levels of adhesion do not necessarily result in inverse bleb formation at all cell contacts, and lumen formation can proceed solely through coarsening of microlumens. This makes it still unclear to what extent inverse blebs are able to influence the coarsening process. Further manipulations of the adhesion levels in the preimplantation embryo could inform us how adhesion strength and patterning can influence inverse bleb formation. A desirable test as to how blastocoel formation might be impacted if blastomeres did not actively counteract the rapid fluid accumulation observed in inverse bleb growth, would be to specifically inhibit inverse bleb retraction while not compromising fluid accumulation and the microlumen network architecture. This might result in substantial bicellular fluid accumulation and impeded coarsening. However, such an experiment would require an exact understanding and manipulation of the actomyosin recruitment mechanism as discussed in chapters 3.4 and 3.5. Also, to test the hypothesis that inverse blebs direct fluid into multicellular microlumens, it might be interesting to label and track fluid within the microlumen network. However, this would require a selective labelling e.g. by photoconversion of a fluid subset, ideally on the scale of a single inverse bleb to track the resulting fluid movement.

3.7 Inverse blebs beyond the mouse preimplantation embryo

Beyond the mouse embryo, inverse blebs have been previously described in other lumen-related contexts. During zebrafish vasculature development, inverse blebs appear at the tip of sprouting blood vessels and are thought to facilitate apical membrane expansion of the sprouting blood vessel [302]. In this case, inverse blebs form at the apical surface of endothelial cells at the cell-lumen interface and are triggered by the luminal pressure of the blood vessel. The reported dynamics of

inverse bleb formation and retraction are very similar to the ones we found in the mouse embryo, and retraction also depends on actomyosin recruitment. In the zebrafish vasculature, inverse bleb formation seems to depend on the organization and stability of the apical cortex, as laser ablation [302] or overexpression of the actin-binding protein Marcksl1 [303] can induce inverse blebs. In this, they show similarities to outward membrane blebs which can be induced likewise by ablating the cortex [137] and support a model of bleb formation that proposes local weaknesses of the cortex as the cause for membrane detachment. As discussed in chapter 3.3, it is unclear to what extent these findings about cortex stability as the cause of inverse blebs can be transferred to our observations in the mouse embryo. Another instance of inverse bleb formation was found in the mouse bile duct, where inverse blebs were observed at the hepatocyte-bile interface [273]. Similar to the inverse blebs in zebrafish, they form at the apical cell-lumen interface and are retracted after actomyosin recruitment. Interestingly, these inverse blebs can sometimes pinch off the plasma membrane and internalize as vesicles, leading to the conclusion that they serve as a pressure relieve mechanism in case of excess bile accumulation [273]. This phenomenon cannot be clearly observed in the mouse embryo.

The main difference between these previously described inverse blebs and the ones described in this thesis is that in the mouse embryo, they form at adhesive, basolateral cell-cell contacts, and not at apical cell-lumen interfaces. Pressurized fluid in microlumens is able to trigger inverse bleb formation, but not the final blastocoel itself. This suggests that the pressure locally applied on the blastomere in a microlumen is sufficient to force inverse bleb intrusion, but not the pressure of the blastocoel. In the two other cases of inverse blebs described above, the global luminal pressure seems to be sufficiently high to trigger local inverse bleb formation. For outward membrane blebs, it has been suggested that local intracellular pressure imbalances in the framework of a poroelastic model of the cytosol can serve as a trigger for blebs [304]. In this model, pressure would also act locally on the cell membrane, analogously to the microlumens, showing that local action of pressure on the cell membrane is sufficient to trigger blebs. For the other types of inverse blebs at apical membranes on which the global pressure of the lumen acts, other reasons for inverse bleb formation

seem more likely, such as local cortex weaknesses, which have also been suggested for outward bleb formation [137].

3.8 Inverse blebs as a mechanism of fluid management in hydraulically fractured tissues

Inverse blebs in the mouse preimplantation embryo occur during the microlumen phase of blastocyst formation and cannot be observed before or afterwards. The microlumen phase is an instance of hydraulic fracturing in which pressurized fluid in the intercellular space breaks open cell-cell contacts. Since inverse blebs disappear after the blastocoel has formed, their formation likely depends on the presence of microlumens. Recently, similar tissue fracturing has been reported in other systems: When kidney cell layers are exposed to pressurized fluid, they form transient, actin-positive intrusions between which might be akin to inverse blebs [305]. Another interesting instance of tissue fracturing occurs during the wounding of fish skin, where extraorganismic fluid enters into the tissue following an osmotic gradient and thus breaks open the intercellular space [306]. This process results in small fluid pockets resembling microlumens between the skin cells, and might perhaps also cause actomyosin-retracted membrane intrusion into the cells, similar to inverse blebs. Further investigation in these and similar systems will show if the principles that we have found to cause inverse bleb formation and retraction in the mouse embryo also apply to other systems.

Ultimately, inverse blebs are a mechanism for cells to actively manage intercellular fluid. Animal organisms have a variety of ways at their disposal to move intercellular fluid. On the most macroscopic level, the heart as a muscle-powered fluid pump causes blood circulation. On a smaller scale, cilia beating can actively and directionally move fluid, e.g. in the laterality organs of vertebrates [279,307] or during spinal cord development [308]. In the zebrafish embryo, intercellular fluid displacement has been observed to occur solely due to tissue rearrangement [309]. On the smallest scale, osmotic gradients control fluid movement as is obviously the case in the blastocyst, but also in other lumen formation processes and importantly the movement of

interstitial fluid between blood vessels, the interstitial space and lymph vessels [310]. As discussed in chapter 3.6, inverse blebs in the early mouse embryo may serve as an active pumping mechanism to redistribute fluid in the microlumen network. So far, few instances of inverse blebs in organismic contexts have been observed. Further research might show if a fluid movement mechanism comparable to inverse blebs is also employed by cells in other situations. Since the observation of this short-lived, subcellular phenomenon requires live imaging with a high temporal and spatial resolution, current advanced microscopy techniques such as light-sheet or lattice light-sheet imaging may prove very useful for discovering them in other settings.

3.9 Outlook

Altogether, the work presented in this PhD thesis has increased our understanding of the morphogenetic processes that shape the early mammalian embryo. As in many other instances in animal development [311], actomyosin contractility is a main driver of preimplantation morphogenesis [179], and our studies allowed us to investigate both the global, long-term role of contractility from fertilization to blastocyst formation, and its manifestation on the short timescale as inverse blebs. This highlights how morphogenesis occurs on multiple temporal and spatial scales. Beyond the role of the actomyosin cytoskeleton in sculpting the early embryo, our findings have given us insight into the management of extracellular fluid by the embryo. The single-celled, fluid-accumulating NMHC mutant embryos gave us interesting insights into the regulation of transepithelial fluid accumulation, and inverse blebs show the fascinating interplay of contractility, cell-cell adhesion and intercellular fluid pressure. While the findings of these studies are specific to the mouse preimplantation embryo, the underlying principles will hopefully serve to increase our general understanding of embryonic morphogenesis.

4. REFERENCES

1. Steinberg MS: **Reconstruction of Tissues by Dissociated Cells**. *Science (80-)* 1963, **141**:401–408.
2. Chen J, Xu N, Huang H, Cai T, Xi R: **A feedback amplification loop between stem cells and their progeny promotes tissue regeneration and tumorigenesis**. *Elife* 2016, **5**:e14330.
3. Wang JH-C, Thampatty BP, Lin J-S, Im H-J: **Mechanoregulation of gene expression in fibroblasts**. *Gene* 2007, **391**:1–15.
4. Lecuit T, Lenne P-F: **Cell surface mechanics and the control of cell shape, tissue patterns and morphogenesis**. *Nat Rev Mol Cell Biol* 2007, **8**:633–644.
5. Pilot F, Lecuit T: **Compartmentalized morphogenesis in epithelia: From cell to tissue shape**. *Dev Dyn* 2005, **232**:685–694.
6. Théry M, Bornens M: **Cell shape and cell division**. *Curr Opin Cell Biol* 2006, **18**:648–657.
7. Mak M, Spill F, Kamm RD, Zaman MH: **Single-Cell Migration in Complex Microenvironments: Mechanics and Signaling Dynamics**. *J Biomech Eng* 2016, **138**.
8. Stock J, Pauli A: **Self-organized cell migration across scales – from single cell movement to tissue formation**. *Development* 2021, **148**:dev191767.
9. Nelson MR, King JR, Jensen OE: **Buckling of a growing tissue and the emergence of two-dimensional patterns**. *Math Biosci* 2013, **246**:229–241.
10. Nelson CM: **Geometric control of tissue morphogenesis**. *Biochim Biophys Acta - Mol Cell Res* 2009, **1793**:903–910.
11. Maître J-L, Berthoumieux H, Frederik S, Krens G, Salbreux G, Jülicher F, Paluch E, Heisenberg C: **Adhesion Functions in Cell Sorting by Mechanically Coupling the Cortices of Adhering Cells**. *Science (80-)* 2012, **338**:253–257.
12. Friedl P, Gilmour D: **Collective cell migration in morphogenesis, regeneration and cancer**. *Nat Rev Mol Cell Biol* 2009, **10**:445–457.
13. Szabó A, Mayor R: **Mechanisms of Neural Crest Migration**. *Annu Rev Genet* 2018, **52**:43–63.
14. Chuang P-T, McMahon AP: **Branching morphogenesis of the lung: new molecular insights into an old problem**. *Trends Cell Biol* 2003, **13**:86–91.
15. Patel VN, Rebustini IT, Hoffman MP: **Salivary gland branching morphogenesis**. *Differentiation* 2006, **74**:349–364.
16. Carmeliet P: **Angiogenesis in health and disease**. *Nat Med* 2003, **9**:653–660.
17. LaBarbera M: **Principles of Design of Fluid Transport Systems in Zoology**. *Science (80-)* 1990, **249**:992–1000.
18. Essner JJ, Amack JD, Nyholm MK, Harris EB, Yost HJ: **Kupffer's vesicle is a ciliated organ of asymmetry in the zebrafish embryo that initiates left-right development of the brain, heart and gut**. *Development* 2005, **132**:1247–1260.
19. Kim YS, Fan R, Kremer L, Kuempel-Rink N, Mildner K, Zeuschner D, Hekking L, Stehling M, Bedzhov I: **Deciphering epiblast lumenogenesis reveals proamniotic cavity control of embryo growth and patterning**. *Sci Adv* 2023, **7**:eabe1640.
20. Sigurbjörnsdóttir S, Mathew R, Leptin M: **Molecular mechanisms of de novo**

lumen formation. *Nat Rev Mol Cell Biol* 2014, **15**:665–676.
21. Xiao L, Kumazawa Y, Okamura H: **Cell death, cavitation and spontaneous multi-differentiation of dental pulp stem cells-derived spheroids in vitro: A journey to survival and organogenesis**. *Biol Cell* 2014, **106**:405–419.
22. Datta A, Bryant DM, Mostov KE: **Molecular Regulation of Lumen Morphogenesis**. *Curr Biol* 2011, **21**:R126–R136.
23. Lane MC, Koehl MAR, Wilt F, Keller R: **A role for regulated secretion of apical extracellular matrix during epithelial invagination in the sea urchin**. *Development* 1993, **117**:1049–1060.
24. Kyprianou C, Christodoulou N, Hamilton RS, Nahaboo W, Boomgaard DS, Amadei G, Migeotte I, Zernicka-Goetz M: **Basement membrane remodelling regulates mouse embryogenesis**. *Nature* 2020, **582**:253–258.
25. Shahbazi MN, Scialdone A, Skorupska N, Weberling A, Recher G, Zhu M, Jedrusik A, Devito LG, Noli L, Macaulay IC, et al.: **Pluripotent state transitions coordinate morphogenesis in mouse and human embryos**. *Nature* 2017, **552**:239–243.
26. Copp AJ, Adzick NS, Chitty LS, Fletcher JM, Holmbeck GN, Shaw GM: **Spina bifida**. *Nat Rev Dis Prim* 2015, **1**:15007.
27. Murray JC: **Gene/environment causes of cleft lip and/or palate**. *Clin Genet* 2002, **61**:248–256.
28. O'Donnell A, Yutzey KE: **Mechanisms of heart valve development and disease**. *Development* 2020, **147**:dev183020.
29. Malcoe LH, Shaw GM, Lammer EJ, Herman AA: **The effect of congenital anomalies on mortality risk in white and black infants.** *Am J Public Health* 1999, **89**:887–892.
30. Fletcher DA, Mullins RD: **Cell mechanics and the cytoskeleton**. *Nature* 2010, **463**:485–492.
31. Hoyt MA, Hyman AA, Bähler M: **Motor proteins of the eukaryotic cytoskeleton**. *Proc Natl Acad Sci* 1997, **94**:12747–12748.
32. Cao TT, Chang W, Masters SE, Mooseker MS: **Myosin-Va Binds to and Mechanochemically Couples Microtubules to Actin Filaments**. *Mol Biol Cell* 2003, **15**:151–161.
33. Gavin RH: **Synergy of Cytoskeleton Components: Cytoskeletal polymers exhibit both structural and functional synergy**. *Bioscience* 1999, **49**:641–655.
34. Rizzelli F, Malabarba MG, Sigismund S, Mapelli M: **The crosstalk between microtubules, actin and membranes shapes cell division**. *Open Biol* 2020, **10**:190314.
35. Salbreux G, Charras G, Paluch E: **Actin cortex mechanics and cellular morphogenesis**. *Trends Cell Biol* 2012, **22**:536–545.
36. Korkmazhan E, Dunn AR: **The membrane-actin linker ezrin acts as a sliding anchor**. *Sci Adv* 2023, **8**:eabo2779.
37. Bennett V, Lorenzo DN: **Chapter Five - An Adaptable Spectrin/Ankyrin-Based Mechanism for Long-Range Organization of Plasma Membranes in Vertebrate Tissues**. In *Dynamic Plasma Membranes*. Edited by Bennett VBT-CT in M. Academic Press; 2016:143–184.
38. Chugh P, Paluch EK: **The actin cortex at a glance**. *J Cell Sci* 2018, **131**:jcs186254.

39. Xia S, Lim YB, Zhang Z, Wang Y, Zhang S, Lim CT, Yim EKF, Kanchanawong P: **Nanoscale Architecture of the Cortical Actin Cytoskeleton in Embryonic Stem Cells**. *Cell Rep* 2019, **28**:1251-1267.e7.
40. Ramanathan SP, Helenius J, Stewart MP, Cattin CJ, Hyman AA, Muller DJ: **Cdk1-dependent mitotic enrichment of cortical myosin II promotes cell rounding against confinement**. *Nat Cell Biol* 2015, **17**:148–159.
41. Kumar R, Saha S, Sinha B: **Cell spread area and traction forces determine myosin-II-based cortex thickness regulation**. *Biochim Biophys Acta - Mol Cell Res* 2019, **1866**:118516.
42. Clark AG, Dierkes K, Paluch EK: **Monitoring Actin Cortex Thickness in Live Cells**. *Biophys J* 2013, **105**:570–580.
43. Chugh P, Clark AG, Smith MB, Cassani DAD, Dierkes K, Ragab A, Roux PP, Charras G, Salbreux G, Paluch EK: **Actin cortex architecture regulates cell surface tension**. *Nat Cell Biol* 2017, **19**:689–697.
44. Elzinga M, Collins JH, Kuehl WM, Adelstein RS: **Complete Amino-Acid Sequence of Actin of Rabbit Skeletal Muscle**. *Proc Natl Acad Sci* 1973, **70**:2687–2691.
45. Chesarone MA, Goode BL: **Actin nucleation and elongation factors: mechanisms and interplay**. *Curr Opin Cell Biol* 2009, **21**:28–37.
46. Carlier M-F, Pantaloni D: **Control of actin dynamics in cell motility**. *J Mol Biol* 1997, **269**:459–467.
47. Kang F, Purich DL, Southwick FS: **Profilin Promotes Barbed-end Actin Filament Assembly without Lowering the Critical Concentration ***. *J Biol Chem* 1999, **274**:36963–36972.
48. Ono SBT-IR of C: **Mechanism of Depolymerization and Severing of Actin Filaments and Its Significance in Cytoskeletal Dynamics**. Academic Press; 2007:1–82.
49. Koestler SA, Auinger S, Vinzenz M, Rottner K, Small JV: **Differentially oriented populations of actin filaments generated in lamellipodia collaborate in pushing and pausing at the cell front**. *Nat Cell Biol* 2008, **10**:306–313.
50. Lamb MC, Tootle TL: **Fascin in Cell Migration: More Than an Actin Bundling Protein**. *Biology (Basel)* 2020, **9**.
51. Hill TL: **Microfilament or microtubule assembly or disassembly against a force.** *Proc Natl Acad Sci* 1981, **78**:5613–5617.
52. Borisy GG, Svitkina TM: **Actin machinery: pushing the envelope**. *Curr Opin Cell Biol* 2000, **12**:104–112.
53. Sellers JR: **Myosins: a diverse superfamily**. *Biochim Biophys Acta - Mol Cell Res* 2000, **1496**:3–22.
54. Wu X, Bowers B, Rao K, Wei Q, Hammer III JA: **Visualization of Melanosome Dynamics within Wild-Type and Dilute Melanocytes Suggests a Paradigm for Myosin V Function In Vivo** . *J Cell Biol* 1998, **143**:1899–1918.
55. Fili N, Toseland CP: **Unconventional Myosins: How Regulation Meets Function**. *Int J Mol Sci* 2020, **21**.
56. Cook AW, Gough RE, Toseland CP: **Nuclear myosins – roles for molecular transporters and anchors**. *J Cell Sci* 2020, **133**:jcs242420.
57. Golomb E, Ma X, Jana SS, Preston YA, Kawamoto S, Shoham NG, Goldin E,

Conti MA, Sellers JR, Adelstein RS: **Identification and Characterization of Nonmuscle Myosin II-C, a New Member of the Myosin II Family ***. *J Biol Chem* 2004, **279**:2800–2808.
58. Sellers JR, Heissler SM: **Nonmuscle myosin-2 isoforms**. *Curr Biol* 2019, **29**:R275–R278.
59. SOMLYO AP, SOMLYO A V: **Ca2+ Sensitivity of Smooth Muscle and Nonmuscle Myosin II: Modulated by G Proteins, Kinases, and Myosin Phosphatase**. *Physiol Rev* 2003, **83**:1325–1358.
60. Matsumura F: **Regulation of myosin II during cytokinesis in higher eukaryotes**. *Trends Cell Biol* 2005, **15**:371–377.
61. Tan I, Yong J, Dong JM, Lim L, Leung T: **A Tripartite Complex Containing MRCK Modulates Lamellar Actomyosin Retrograde Flow**. *Cell* 2008, **135**:123–136.
62. Garrido-Casado M, Asensio-Juárez G, Vicente-Manzanares M: **Nonmuscle Myosin II Regulation Directs Its Multiple Roles in Cell Migration and Division**. *Annu Rev Cell Dev Biol* 2021, **37**:285–310.
63. Matsumura F, Hartshorne DJ: **Myosin phosphatase target subunit: Many roles in cell function**. *Biochem Biophys Res Commun* 2008, **369**:149–156.
64. Vicente-Manzanares M, Ma X, Adelstein RS, Horwitz AR: **Non-muscle myosin II takes centre stage in cell adhesion and migration**. *Nat Rev Mol Cell Biol* 2009, **10**:778.
65. Even-Faitelson L, Ravid S: **PAK1 and aPKCζ Regulate Myosin II-B Phosphorylation: A Novel Signaling Pathway Regulating Filament Assembly**. *Mol Biol Cell* 2006, **17**:2869–2881.
66. Dulyaninova NG, Malashkevich VN, Almo SC, Bresnick AR: **Regulation of Myosin-IIA Assembly and Mts1 Binding by Heavy Chain Phosphorylation**. *Biochemistry* 2005, **44**:6867–6876.
67. Clark K, Middelbeek J, Lasonder E, Dulyaninova NG, Morrice NA, Ryazanov AG, Bresnick AR, Figdor CG, van Leeuwen FN: **TRPM7 Regulates Myosin IIA Filament Stability and Protein Localization by Heavy Chain Phosphorylation**. *J Mol Biol* 2008, **378**:790–803.
68. Kiehart DP, Lutz MS, Chan D, Ketchum AS, Laymon RA, Nguyen B, Goldstein LS: **Identification of the gene for fly non-muscle myosin heavy chain: Drosophila myosin heavy chains are encoded by a gene family.** *EMBO J* 1989, **8**:913–922.
69. Bao J, Jana SS, Adelstein RS: **Vertebrate Nonmuscle Myosin II Isoforms Rescue Small Interfering RNA-induced Defects in COS-7 Cell Cytokinesis***. *J Biol Chem* 2005, **280**:19594–19599.
70. Vicente-Manzanares M, Zareno J, Whitmore L, Choi CK, Horwitz AF: **Regulation of protrusion, adhesion dynamics, and polarity by myosins IIA and IIB in migrating cells** . *J Cell Biol* 2007, **176**:573–580.
71. Maupin P, Phillips CL, Adelstein RS, Pollard TD: **Differential localization of myosin-II isozymes in human cultured cells and blood cells**. *J Cell Sci* 1994, **107**:3077–3090.
72. Kolega J: **Cytoplasmic dynamics of myosin IIA and IIB: spatial 'sorting' of isoforms in locomoting cells**. *J Cell Sci* 1998, **111**:2085–2095.
73. Kim K-Y, Kovács M, Kawamoto S, Sellers JR, Adelstein RS: **Disease-associated Mutations and Alternative Splicing Alter the Enzymatic and**

Motile Activity of Nonmuscle Myosins II-B and II-C*. *J Biol Chem* 2005, **280**:22769–22775.
74. Kovács M, Thirumurugan K, Knight PJ, Sellers JR: **Load-dependent mechanism of nonmuscle myosin 2**. *Proc Natl Acad Sci* 2007, **104**:9994–9999.
75. Wang F, Kovács M, Hu A, Limouze J, Harvey E V, Sellers JR: **Kinetic Mechanism of Non-muscle Myosin IIB: FUNCTIONAL ADAPTATIONS FOR TENSION GENERATION AND MAINTENANCE***. *J Biol Chem* 2003, **278**:27439–27448.
76. Kovács M, Wang F, Hu A, Zhang Y, Sellers JR: **Functional Divergence of Human Cytoplasmic Myosin II: KINETIC CHARACTERIZATION OF THE NON-MUSCLE IIA ISOFORM***. *J Biol Chem* 2003, **278**:38132–38140.
77. Yamamoto K, Otomo K, Nemoto T, Ishihara S, Haga H, Nagasaki A, Murakami Y, Takahashi M: **Differential contributions of nonmuscle myosin IIA and IIB to cytokinesis in human immortalized fibroblasts**. *Exp Cell Res* 2019, **376**:67–76.
78. Taneja N, Bersi MR, Baillargeon SM, Fenix AM, Cooper JA, Ohi R, Gama V, Merryman WD, Burnette DT: **Precise Tuning of Cortical Contractility Regulates Cell Shape during Cytokinesis**. *Cell Rep* 2020, **31**.
79. Heuzé ML, Sankara Narayana GHN, D'Alessandro J, Cellerin V, Dang T, Williams DS, Van Hest JCM, Marcq P, Mège R-M, Ladoux B: **Myosin II isoforms play distinct roles in adherens junction biogenesis**. *Elife* 2019, **8**:e46599.
80. Smutny M, Cox HL, Leerberg JM, Kovacs EM, Conti MA, Ferguson C, Hamilton NA, Parton RG, Adelstein RS, Yap AS: **Myosin II isoforms identify distinct functional modules that support integrity of the epithelial zonula adherens**. *Nat Cell Biol* 2010, **12**:696–702.
81. Conti MA, Even-Ram S, Liu C, Yamada KM, Adelstein RS: **Defects in Cell Adhesion and the Visceral Endoderm following Ablation of Nonmuscle Myosin Heavy Chain II-A in Mice**. *J Biol Chem* 2004, **279**:41263–41266.
82. Tullio AN, Accili D, Ferrans VJ, Yu Z-X, Takeda K, Grinberg A, Westphal H, Preston YA, Adelstein RS: **Nonmuscle myosin II-B is required for normal development of the mouse heart**. *Proc Natl Acad Sci* 1997, **94**:12407 LP – 12412.
83. Ma X, Jana SS, Anne Conti M, Kawamoto S, Claycomb WC, Adelstein RS: **Ablation of Nonmuscle Myosin II-B and II-C Reveals a Role for Nonmuscle Myosin II in Cardiac Myocyte Karyokinesis**. *Mol Biol Cell* 2010, **21**:3952–3962.
84. Wang A, Ma X, Conti MA, Adelstein RS: **Distinct and redundant roles of the non-muscle myosin II isoforms and functional domains**. *Biochem Soc Trans* 2011, **39**:1131 LP – 1135.
85. Wang A, Ma X, Conti MA, Liu C, Kawamoto S, Adelstein RS: **Nonmuscle myosin II isoform and domain specificity during early mouse development**. *Proc Natl Acad Sci* 2010, **107**:14645 LP – 14650.
86. Meng W, Takeichi M: **Adherens Junction: Molecular Architecture and Regulation**. *Cold Spring Harb Perspect Biol* 2009, **1**.
87. Saito M, Tucker DK, Kohlhorst D, Niessen CM, Kowalczyk AP: **Classical and desmosomal cadherins at a glance**. *J Cell Sci* 2012, **125**:2547–2552.

88. Shapiro L, Weis WI: **Structure and Biochemistry of Cadherins and Catenins**. *Cold Spring Harb Perspect Biol* 2009, **1**.
89. Yamada S, Nelson WJ: **Localized zones of Rho and Rac activities drive initiation and expansion of epithelial cell–cell adhesion** . *J Cell Biol* 2007, **178**:517–527.
90. Shewan AM, Maddugoda M, Kraemer A, Stehbens SJ, Verma S, Kovacs EM, Yap AS: **Myosin 2 Is a Key Rho Kinase Target Necessary for the Local Concentration of E-Cadherin at Cell–Cell Contacts**. *Mol Biol Cell* 2005, **16**:4531–4542.
91. Ivanov AI, Bachar M, Babbin BA, Adelstein RS, Nusrat A, Parkos CA: **A Unique Role for Nonmuscle Myosin Heavy Chain IIA in Regulation of Epithelial Apical Junctions**. *PLoS One* 2007, **2**:e658.
92. Maître J-L, Heisenberg C-P: **Three Functions of Cadherins in Cell Adhesion**. *Curr Biol* 2013, **23**:R626–R633.
93. Sawyer JM, Harrell JR, Shemer G, Sullivan-Brown J, Roh-Johnson M, Goldstein B: **Apical constriction: A cell shape change that can drive morphogenesis**. *Dev Biol* 2010, **341**:5–19.
94. Munjal A, Lecuit T: **Actomyosin networks and tissue morphogenesis**. *Development* 2014, **141**:1789–1793.
95. Zihni C, Mills C, Matter K, Balda MS: **Tight junctions: from simple barriers to multifunctional molecular gates**. *Nat Rev Mol Cell Biol* 2016, **17**:564–580.
96. Fanning AS, Jameson BJ, Jesaitis LA, Anderson JM: **The Tight Junction Protein ZO-1 Establishes a Link between the Transmembrane Protein Occludin and the Actin Cytoskeleton ***. *J Biol Chem* 1998, **273**:29745–29753.
97. Hartsock A, Nelson WJ: **Adherens and tight junctions: Structure, function and connections to the actin cytoskeleton**. *Biochim Biophys Acta - Biomembr* 2008, **1778**:660–669.
98. Citi S: **The mechanobiology of tight junctions**. *Biophys Rev* 2019, **11**:783–793.
99. DeLeon-Pennell KY, Barker TH, Lindsey ML: **Fibroblasts: The arbiters of extracellular matrix remodeling**. *Matrix Biol* 2020, **91–92**:1–7.
100. Chanet S, Martin AC: **Chapter Thirteen - Mechanical Force Sensing in Tissues**. In *Mechanotransduction*. Edited by Engler AJ, Kumar SBT-P in MB and TS. Academic Press; 2014:317–352.
101. Hood JD, Cheresh DA: **Role of integrins in cell invasion and migration**. *Nat Rev Cancer* 2002, **2**:91–100.
102. Molè MA, Weberling A, Fässler R, Campbell A, Fishel S, Zernicka-Goetz M: **Integrin β1 coordinates survival and morphogenesis of the embryonic lineage upon implantation and pluripotency transition**. *Cell Rep* 2021, **34**.
103. Strangeways TSP, Hardy WB: **Observations on the changes seen in living cells during growth and division**. *Proc R Soc London Ser B, Contain Pap a Biol Character* 1922, **94**:137–141.
104. Fischer-Friedrich E, Hyman AA, Jülicher F, Müller DJ, Helenius J: **Quantification of surface tension and internal pressure generated by single mitotic cells**. *Sci Rep* 2014, **4**:6213.
105. Vadnjal N, Nourreddine S, Lavoie G, Serres M, Roux PP, Paluch EK:

Proteomic analysis of the actin cortex in interphase and mitosis. *J Cell Sci* 2022, **135**:jcs259993.
106. Straight AF, Cheung A, Limouze J, Chen I, Westwood NJ, Sellers JR, Mitchison TJ: **Dissecting Temporal and Spatial Control of Cytokinesis with a Myosin II Inhibitor**. *Science (80-)* 2003, **299**:1743–1747.
107. Finegan TM, Bergstralh DT: **Division orientation: disentangling shape and mechanical forces**. *Cell Cycle* 2019, **18**:1187–1198.
108. Wang Y, Xu Y, Liu Q, Zhang Y, Gao Z, Yin M, Jiang N, Cao G, Yu B, Cao Z, et al.: **Myosin IIA-related Actomyosin Contractility Mediates Oxidative Stress-induced Neuronal Apoptosis** . *Front Mol Neurosci* 2017, **10**.
109. Croft DR, Coleman ML, Li S, Robertson D, Sullivan T, Stewart CL, Olson MF: **Actin-myosin–based contraction is responsible for apoptotic nuclear disintegration** . *J Cell Biol* 2005, **168**:245–255.
110. Atieh Y, Wyatt T, Zaske AM, Eisenhoffer GT: **Pulsatile contractions promote apoptotic cell extrusion in epithelial tissues**. *Curr Biol* 2021, **31**:1129-1140.e4.
111. Levayer R, Lecuit T: **Biomechanical regulation of contractility: spatial control and dynamics**. *Trends Cell Biol* 2012, **22**:61–81.
112. Martin AC, Kaschube M, Wieschaus EF: **Pulsed contractions of an actin–myosin network drive apical constriction**. *Nature* 2009, **457**:495–499.
113. Solon J, Kaya-Çopur A, Colombelli J, Brunner D: **Pulsed Forces Timed by a Ratchet-like Mechanism Drive Directed Tissue Movement during Dorsal Closure**. *Cell* 2009, **137**:1331–1342.
114. Behrndt M, Salbreux G, Campinho P, Hauschild R, Oswald F, Roensch J, Grill SW, Heisenberg C-P: **Forces Driving Epithelial Spreading in Zebrafish Gastrulation**. *Science (80-)* 2012, **338**:257–260.
115. Maître J-L, Turlier H, Illukkumbura R, Eismann B, Niwayama R, Nédélec F, Hiiragi T: **Asymmetric division of contractile domains couples cell positioning and fate specification**. *Nature* 2016, **536**:344–348.
116. Iijima N, Sato K, Kuranaga E, Umetsu D: **Differential cell adhesion implemented by Drosophila Toll corrects local distortions of the anterior-posterior compartment boundary**. *Nat Commun* 2020, **11**:6320.
117. Bao M, Cornwall-Scoones J, Sanchez-Vasquez E, Chen D-Y, De Jonghe J, Shadkhoo S, Hollfelder F, Thomson M, Glover DM, Zernicka-Goetz M: **Stem cell-derived synthetic embryos self-assemble by exploiting cadherin codes and cortical tension**. *Nat Cell Biol* 2022, **24**:1341–1349.
118. Krieg M, Puech P, Käfer J, Graner F, Müller DJ, Heisenberg C: **Tensile forces govern germ-layer organization in zebrafish**. 2008, **10**:429–436.
119. Fagotto F, Kashkooli L, Zarour E, Canty L, François P: **Sorting at embryonic boundaries requires high heterotypic interfacial tension**. *Nat Commun* 2017, **8**.
120. Major RJ, Irvine KD: **Localization and requirement for Myosin II at the dorsal-ventral compartment boundary of the Drosophila wing**. *Dev Dyn* 2006, **235**:3051–3058.
121. Skoglund P, Rolo A, Chen X, Gumbiner BM, Keller R: **Convergence and extension at gastrulation require a myosin IIB-dependent cortical actin network**. *Development* 2008, **135**:2435–2444.
122. Shindo A, Wallingford JB: **PCP and Septins Compartmentalize Cortical**

Actomyosin to Direct Collective Cell Movement. *Science (80-)* 2014, **343**:649–652.
123. Rauzi M, Lenne P-F, Lecuit T: **Planar polarized actomyosin contractile flows control epithelial junction remodelling**. *Nature* 2010, **468**:1110–1114.
124. Wallingford JB, Fraser SE, Harland RM: **Convergent Extension: The Molecular Control of Polarized Cell Movement during Embryonic Development**. *Dev Cell* 2002, **2**:695–706.
125. Rauzi M, Hočevar Brezavšček A, Ziherl P, Leptin M: **Physical Models of Mesoderm Invagination in Drosophila Embryo**. *Biophys J* 2013, **105**:3–10.
126. Bailles A, Collinet C, Philippe J-M, Lenne P-F, Munro E, Lecuit T: **Genetic induction and mechanochemical propagation of a morphogenetic wave**. *Nature* 2019, **572**:467–473.
127. Sherrard K, Robin F, Lemaire P, Munro E: **Sequential Activation of Apical and Basolateral Contractility Drives Ascidian Endoderm Invagination**. *Curr Biol* 2010, **20**:1499–1510.
128. Nishimura T, Takeichi M: **Shroom3-mediated recruitment of Rho kinases to the apical cell junctions regulates epithelial and neuroepithelial planar remodeling**. *Development* 2008, **135**:1493–1502.
129. Andrew DJ, Ewald AJ: **Morphogenesis of epithelial tubes: Insights into tube formation, elongation, and elaboration**. *Dev Biol* 2010, **341**:34–55.
130. Wang S, Matsumoto K, Lish SR, Cartagena-Rivera AX, Yamada KM: **Budding epithelial morphogenesis driven by cell-matrix versus cell-cell adhesion**. *Cell* 2021, **184**:3702-3716.e30.
131. Schick J, Raz E: **Blebs—Formation, Regulation, Positioning, and Role in Amoeboid Cell Migration** . *Front Cell Dev Biol* 2022, **10**.
132. Innocenti M: **New insights into the formation and the function of lamellipodia and ruffles in mesenchymal cell migration**. *Cell Adh Migr* 2018, **12**:401–416.
133. Choi CK, Vicente-Manzanares M, Zareno J, Whitmore LA, Mogilner A, Horwitz AR: **Actin and α-actinin orchestrate the assembly and maturation of nascent adhesions in a myosin II motor-independent manner**. *Nat Cell Biol* 2008, **10**:1039–1050.
134. Jurado C, Haserick JR, Lee J: **Slipping or Gripping? Fluorescent Speckle Microscopy in Fish Keratocytes Reveals Two Different Mechanisms for Generating a Retrograde Flow of Actin**. *Mol Biol Cell* 2004, **16**:507–518.
135. Charras G, Paluch E: **Blebs lead the way: how to migrate without lamellipodia**. *Nat Rev Mol Cell Biol* 2008, **9**:730–736.
136. Charras GT, Coughlin M, Mitchison TJ, Mahadevan L: **Life and Times of a Cellular Bleb**. *Biophys J* 2008, **94**:1836–1853.
137. Tinevez J-Y, Schulze U, Salbreux G, Roensch J, Joanny J-F, Paluch E: **Role of cortical tension in bleb growth**. *Proc Natl Acad Sci* 2009, **106**:18581–18586.
138. Maugis B, Brugués J, Nassoy P, Guillen N, Sens P, Amblard F: **Dynamic instability of the intracellular pressure drives bleb-based motility**. *J Cell Sci* 2010, **123**:3884–3892.
139. Charras GT, Hu C-K, Coughlin M, Mitchison TJ: **Reassembly of contractile actin cortex in cell blebs** . *J Cell Biol* 2006, **175**:477–490.

140. Taneja N, Burnette DT: **Myosin IIA drives membrane bleb retraction**. *Mol Biol Cell* 2019, **30**:1051–1059.
141. Blaser H, Reichman-Fried M, Castanon I, Dumstrei K, Marlow FL, Kawakami K, Solnica-Krezel L, Heisenberg C-P, Raz E: **Migration of Zebrafish Primordial Germ Cells: A Role for Myosin Contraction and Cytoplasmic Flow**. *Dev Cell* 2006, **11**:613–627.
142. Paluch EK, Raz E: **The role and regulation of blebs in cell migration**. *Curr Opin Cell Biol* 2013, **25**:582–590.
143. Laster SM, Mackenzie Jr. JM: **Bleb formation and F-actin distribution during mitosis and tumor necrosis factor-induced apoptosis**. *Microsc Res Tech* 1996, **34**:272–280.
144. Weems AD, Welf ES, Driscoll MK, Zhou FY, Mazloom-Farsibaf H, Chang B-J, Murali VS, Gihana GM, Weiss BG, Chi J, et al.: **Blebs promote cell survival by assembling oncogenic signalling hubs**. *Nature* 2023, **615**:517–525.
145. Sedzinski J, Biro M, Oswald A, Tinevez J-Y, Salbreux G, Paluch E: **Polar actomyosin contractility destabilizes the position of the cytokinetic furrow**. *Nature* 2011, **476**:462–466.
146. Erickson CA, Trinkaus JP: **Microvilli and blebs as sources of reserve surface membrane during cell spreading**. *Exp Cell Res* 1976, **99**:375–384.
147. Mercer J, Helenius A: **Vaccinia Virus Uses Macropinocytosis and Apoptotic Mimicry to Enter Host Cells**. *Science (80-)* 2008, **320**:531–535.
148. Molè MA, Weberling A, Zernicka-Goetz M: **Chapter Four - Comparative analysis of human and mouse development: From zygote to pre-gastrulation**. In *Gastrulation: From Embryonic Pattern to Form*. Edited by Solnica-Krezel LBT-CT in DB. Academic Press; 2020:113–138.
149. Lawitts JA, Biggers JDBT-M in E: **[9] Culture of preimplantation embryos**. In *Guide to Techniques in Mouse Development*. . Academic Press; 1993:153–164.
150. Rivera-Pérez JA, Jones V, Tam PPL: **Chapter 11 - Culture of Whole Mouse Embryos at Early Postimplantation to Organogenesis Stages: Developmental Staging and Methods**. In *Guide to Techniques in Mouse Development, Part A: Mice, Embryos, and Cells, 2nd Edition*. Edited by Wassarman PM, Soriano PMBT-M in E. Academic Press; 2010:185–203.
151. Aguilera-Castrejon A, Oldak B, Shani T, Ghanem N, Itzkovich C, Slomovich S, Tarazi S, Bayerl J, Chugaeva V, Ayyash M, et al.: **Ex utero mouse embryogenesis from pre-gastrulation to late organogenesis**. *Nature* 2021, **593**:119–124.
152. Maître JL: **Mechanics of blastocyst morphogenesis**. *Biol Cell* 2017, **109**:323–338.
153. Phifer-Rixey M, Nachman MW: **Insights into mammalian biology from the wild house mouse Mus musculus**. *Elife* 2015, **4**:e05959.
154. Rossant J: **Making the Mouse Blastocyst: Past, Present, and Future**. *Curr Top Dev Biol* 2016, **117**:275–288.
155. ONUMA H, Maurer RR, Foote RH: **In-vitro culture of rabbit ova from early cleavage stages to the blastocyst stage**. *Reproduction* 1968, **16**:491–493.
156. Bouchereau W, Jouneau L, Archilla C, Aksoy I, Moulin A, Daniel N, Peynot N, Calderari S, Joly T, Godet M, et al.: **Major transcriptomic, epigenetic and metabolic changes underlie the pluripotency continuum in rabbit**

preimplantation embryos. *Development* 2022, **149**:dev200538.
157. Boroviak T, Stirparo GG, Dietmann S, Hernando-Herraez I, Mohammed H, Reik W, Smith A, Sasaki E, Nichols J, Bertone P: **Single cell transcriptome analysis of human, marmoset and mouse embryos reveals common and divergent features of preimplantation development**. *Development* 2018, **145**:dev167833.
158. Wang X, Liu D, He D, Suo S, Xia X, He X, Han J-DJ, Zheng P: **Transcriptome analyses of rhesus monkey preimplantation embryos reveal a reduced capacity for DNA double-strand break repair in primate oocytes and early embryos**. *Genome Res* 2017, **27**:567–579.
159. Hurst PR, Jefferies K, Eckstein P, Wheeler AG: **An ultrastructural study of preimplantation uterine embryos of the rhesus monkey**. *J Anat* 1978, **126**:209–220.
160. Cavazza T, Takeda Y, Politi AZ, Aushev M, Aldag P, Baker C, Choudhary M, Bucevičius J, Lukinavičius G, Elder K, et al.: **Parental genome unification is highly error-prone in mammalian embryos**. *Cell* 2021, **184**:2860-2877.e22.
161. So C, Menelaou K, Uraji J, Harasimov K, Steyer AM, Seres KB, Bucevičius J, Lukinavičius G, Möbius W, Sibold C, et al.: **Mechanism of spindle pole organization and instability in human oocytes**. *Science (80-)* 2023, **375**:eabj3944.
162. Niakan KK, Han J, Pedersen RA, Simon C, Pera RAR: **Human pre-implantation embryo development**. *Development* 2012, **139**:829–841.
163. Fogarty NME, McCarthy A, Snijders KE, Powell BE, Kubikova N, Blakeley P, Lea R, Elder K, Wamaitha SE, Kim D, et al.: **Genome editing reveals a role for OCT4 in human embryogenesis**. *Nature* 2017, **550**:67–73.
164. Firmin J, Ecker N, Danon DR, Lange VB, Turlier H, Patrat C, Maitre J-L: **Mechanics of human embryo compaction**. *bioRxiv* 2022, doi:10.1101/2022.01.09.475429.
165. Meistermann D, Bruneau A, Loubersac S, Reignier A, Firmin J, François-Campion V, Kilens S, Lelièvre Y, Lammers J, Feyeux M, et al.: **Integrated pseudotime analysis of human pre-implantation embryo single-cell transcriptomes reveals the dynamics of lineage specification**. *Cell Stem Cell* 2021, **28**:1625-1640.e6.
166. Macklon NS, Geraedts JPM, Fauser BCJM: **Conception to ongoing pregnancy: the 'black box' of early pregnancy loss**. *Hum Reprod Update* 2002, **8**:333–343.
167. Koot YEM, Teklenburg G, Salker MS, Brosens JJ, Macklon NS: **Molecular aspects of implantation failure**. *Biochim Biophys Acta - Mol Basis Dis* 2012, **1822**:1943–1950.
168. Firmin J, Maître J-L: **Morphogenesis of the human preimplantation embryo: bringing mechanics to the clinics**. *Semin Cell Dev Biol* 2021, **120**:22–31.
169. Georgadaki K, Khoury N, Spandidos A. D, Zoumpourlis V: **The molecular basis of fertilization (Review)**. *Int J Mol Med* 2016, **38**:979–986.
170. Thowfeequ S, Srinivas S: **Embryonic and extraembryonic tissues during mammalian development: shifting boundaries in time and space**. *Philos Trans R Soc B Biol Sci* 2022, **377**:20210255.
171. Braden AWH, Austin CR, David HA: **The Reaction of the Zona Pellucida to**

Sperm Penetration. *Aust J Biol Sci* 1954, **7**:391–410.
172. Mintz B: **Experimental Study of the Developing Mammalian Egg: Removal of the Zona Pellucida**. *Science (80-)* 1962, **138**:594–595.
173. Honda H, Motosugi N, Nagai T, Tanemura M, Hiiragi T: **Computer simulation of emerging asymmetry in the mouse blastocyst**. *Development* 2008, **135**:1407–1414.
174. Kurotaki Y, Hatta K, Nakao K, Nabeshima Y, Fujimori T: **Blastocyst Axis Is Specified Independently of Early Cell Lineage But Aligns with the ZP Shape**. *Science (80-)* 2007, **316**:719–723.
175. Maemura M, Taketsuru H, Nakajima Y, Shao R, Kakihara A, Nogami J, Ohkawa Y, Tsukada Y: **Totipotency of mouse zygotes extends to single blastomeres of embryos at the four-cell stage**. *Sci Rep* 2021, **11**:11167.
176. TARKOWSKI AK: **Mouse Chimæras Developed from Fused Eggs**. *Nature* 1961, **190**:857–860.
177. Rossant J: **Investigation of the determinative state of the mouse inner cell mass. II. The fate of isolated inner cell masses transferred to the oviduct.** *J Embryol Exp Morphol* 1975, **33 4**:991–1001.
178. Suwińska A, Czołowska R, Ożdżeński W, Tarkowski AK: **Blastomeres of the mouse embryo lose totipotency after the fifth cleavage division: Expression of Cdx2 and Oct4 and developmental potential of inner and outer blastomeres of 16- and 32-cell embryos**. *Dev Biol* 2008, **322**:133–144.
179. Özgüç Ö, Maître J-L: **Multiscale morphogenesis of the mouse blastocyst by actomyosin contractility**. *Curr Opin Cell Biol* 2020, **66**:123–129.
180. Kelly SJ: **Studies of the developmental potential of 4- and 8-cell stage mouse blastomeres**. *J Exp Zool* 1977, **200**:365–376.
181. Maître J-L, Niwayama R, Turlier H, Nédélec F, Hiiragi T: **Pulsatile cell-autonomous contractility drives compaction in the mouse embryo**. *Nat Cell Biol* 2015, **17**:849–855.
182. Özgüç Ö, de Plater L, Kapoor V, Tortorelli AF, Clark AG, Maître J-L: **Cortical softening elicits zygotic contractility during mouse preimplantation development**. *PLOS Biol* 2022, **20**:e3001593.
183. Ducibella T, Anderson E: **Cell shape and membrane changes in the eight-cell mouse embryo: Prerequisites for morphogenesis of the blastocyst**. *Dev Biol* 1975, **47**:45–58.
184. Ducibella T, Ukena T, Karnovsky M, Anderson E: **Changes in cell surface and cortical cytoplasmic organization during early embryogenesis in the preimplantation mouse embryo** . *J Cell Biol* 1977, **74**:153–167.
185. Vestweber D, Gossler A, Boller K, Kemler R: **Expression and distribution of cell adhesion molecule uvomorulin in mouse preimplantation embryos**. *Dev Biol* 1987, **124**:451–456.
186. Hyafil F, Morello D, Babinet C, Jacob F: **A cell surface glycoprotein involved in the compaction of embryonal carcinoma cells and cleavage stage embryos**. *Cell* 1980, **21**:927–934.
187. Shirayoshi Y, Okada TS, Takeichi M: **The calcium-dependent cell-cell adhesion system regulates inner cell mass formation and cell surface polarization in early mouse development**. *Cell* 1983, **35**:631–638.
188. Stephenson RO, Yamanaka Y, Rossant J: **Disorganized epithelial polarity**

and excess trophectoderm cell fate in preimplantation embryos lacking E-cadherin. *Development* 2010, **137**:3383–3391.
189. Fierro-González JC, White MD, Silva JC, Plachta N: **Cadherin-dependent filopodia control preimplantation embryo compaction**. *Nat Cell Biol* 2013, **15**:1424–1433.
190. Crozet F, Letort G, Bulteau R, Da Silva C, Eichmuller A, Tortorelli AF, Blévinal J, Belle M, Dumont J, Piolot T, et al.: **Filopodia-like protrusions of adjacent somatic cells shape the developmental potential of oocytes**. *Life Sci Alliance* 2023, **6**:e202301963.
191. Aslan Öztürk S, Cincik M, Donmez Cakil Y, Sayan S, Selam B: **Early Compaction Might Be a Parameter to Determine Good Quality Embryos and Day of Embryo Transfer in Patients Undergoing Intracytoplasmic Sperm Injection**. *Cureus* 2022, **14**:e23593.
192. Bowerman B, Shelton CA: **Cell polarity in the early Caenorhabditis elegans embryo**. *Curr Opin Genet Dev* 1999, **9**:390–395.
193. Chang P, Pérez-Mongiovi D, Houliston E: **Organisation of Xenopus oocyte and egg cortices**. *Microsc Res Tech* 1999, **44**:415–429.
194. Ziomek CA, Johnson MH: **Cell surface interaction induces polarization of mouse 8-cell blastomeres at compaction**. *Cell* 1980, **21**:935–942.
195. Reeve WJD, Ziomek CA: **Distribution of microvilli on dissociated blastomeres from mouse embryos: evidence for surface polarization at compaction**. *Development* 1981, **62**:339–350.
196. Louvet S, Aghion J, Santa-Maria A, Mangeat P, Maro B: **Ezrin Becomes Restricted to Outer Cells Following Asymmetrical Division in the Preimplantation Mouse Embryo**. *Dev Biol* 1996, **177**:568–579.
197. Vinot S, Le T, Ohno S, Pawson T, Maro B, Louvet-Vallée S: **Asymmetric distribution of PAR proteins in the mouse embryo begins at the 8-cell stage during compaction**. *Dev Biol* 2005, **282**:307–319.
198. Alarcon VB: **Cell Polarity Regulator PARD6B Is Essential for Trophectoderm Formation in the Preimplantation Mouse Embryo1**. *Biol Reprod* 2010, **83**:347–358.
199. Korotkevich E, Niwayama R, Courtois A, Friese S, Berger N, Buchholz F, Hiiragi T: **The Apical Domain Is Required and Sufficient for the First Lineage Segregation in the Mouse Embryo**. *Dev Cell* 2017, **40**:235–247.
200. Johnson MH, Ziomek CA: **The foundation of two distinct cell lineages within the mouse morula**. *Cell* 1981, **24**:71–80.
201. Hirate Y, Hirahara S, Inoue K, Suzuki A, Alarcon VB, Akimoto K, Hirai T, Hara T, Adachi M, Chida K, et al.: **Polarity-Dependent Distribution of Angiomotin Localizes Hippo Signaling in Preimplantation Embryos**. *Curr Biol* 2013, **23**:1181–1194.
202. Stephenson RO, Yamanaka Y, Rossant J: **Disorganized epithelial polarity and excess trophectoderm cell fate in preimplantation embryos lacking E-cadherin**. *Development* 2010, **137**:3383–3391.
203. Pomp O, Lim HYG, Skory RM, Moverley AA, Tetlak P, Bissiere S, Plachta N: **A monoastral mitotic spindle determines lineage fate and position in the mouse embryo**. *Nat Cell Biol* 2022, **24**:155–167.
204. Dard N, Louvet-Vallée S, Maro B: **Orientation of Mitotic Spindles during the 8- to 16-Cell Stage Transition in Mouse Embryos**. *PLoS One* 2009,

4:e8171.
205. Samarage CR, White MD, Álvarez YD, Fierro-González JC, Henon Y, Jesudason EC, Bissiere S, Fouras A, Plachta N: **Cortical Tension Allocates the First Inner Cells of the Mammalian Embryo**. *Dev Cell* 2015, **34**:435–447.
206. Anani S, Bhat S, Honma-Yamanaka N, Krawchuk D, Yamanaka Y: **Initiation of Hippo signaling is linked to polarity rather than to cell position in the pre-implantation mouse embryo**. *Development* 2014, **141**:2813–2824.
207. Tarkowski AK, Wróblewska J: **Development of blastomeres of mouse eggs isolated at the 4- and 8-cell stage**. *Development* 1967, **18**:155–180.
208. Sasaki H: **Roles and regulations of Hippo signaling during preimplantation mouse development**. *Dev Growth Differ* 2017, **59**:12–20.
209. Vassilev A, Kaneko KJ, Shu H, Zhao Y, DePamphilis ML: **TEAD/TEF transcription factors utilize the activation domain of YAP65, a Src/Yes-associated protein localized in the cytoplasm**. *Genes Dev* 2001, **15**:1229–1241.
210. Hong W, Guan K-L: **The YAP and TAZ transcription co-activators: Key downstream effectors of the mammalian Hippo pathway**. *Semin Cell Dev Biol* 2012, **23**:785–793.
211. Nishioka N, Yamamoto S, Kiyonari H, Sato H, Sawada A, Ota M, Nakao K, Sasaki H: **Tead4 is required for specification of trophectoderm in pre-implantation mouse embryos**. *Mech Dev* 2008, **125**:270–283.
212. Yagi R, Kohn MJ, Karavanova I, Kaneko KJ, Vullhorst D, DePamphilis ML, Buonanno A: **Transcription factor TEAD4 specifies the trophectoderm lineage at the beginning of mammalian development**. *Development* 2007, **134**:3827–3836.
213. Hirate Y, Cockburn K, Rossant J, Sasaki H: **Tead4 is constitutively nuclear, while nuclear vs. cytoplasmic Yap distribution is regulated in preimplantation mouse embryos**. *Proc Natl Acad Sci* 2012, **109**:E3389–E3390.
214. Nishioka N, Inoue K, Adachi K, Kiyonari H, Ota M, Ralston A, Yabuta N, Hirahara S, Stephenson RO, Ogonuki N, et al.: **The Hippo Signaling Pathway Components Lats and Yap Pattern Tead4 Activity to Distinguish Mouse Trophectoderm from Inner Cell Mass**. *Dev Cell* 2009, **16**:398–410.
215. Ibar C, Kirichenko E, Keepers B, Enners E, Fleisch K, Irvine KD: **Tension-dependent regulation of mammalian Hippo signaling through LIMD1**. *J Cell Sci* 2018, **131**:jcs214700.
216. Zhao B, Li L, Lu Q, Wang LH, Liu C-Y, Lei Q, Guan K-L: **Angiomotin is a novel Hippo pathway component that inhibits YAP oncoprotein**. *Genes Dev* 2011, **25**:51–63.
217. Wang W, Huang J, Chen J: **Angiomotin-like Proteins Associate with and Negatively Regulate YAP1***. *J Biol Chem* 2011, **286**:4364–4370.
218. Dupont S, Morsut L, Aragona M, Enzo E, Giulitti S, Cordenonsi M, Zanconato F, Le Digabel J, Forcato M, Bicciato S, et al.: **Role of YAP/TAZ in mechanotransduction**. *Nature* 2011, **474**:179–183.
219. Panciera T, Azzolin L, Cordenonsi M, Piccolo S: **Mechanobiology of YAP and TAZ in physiology and disease**. *Nat Rev Mol Cell Biol* 2017, **18**:758–770.

220. Aragona M, Panciera T, Manfrin A, Giulitti S, Michielin F, Elvassore N, Dupont S, Piccolo S: **A Mechanical Checkpoint Controls Multicellular Growth through YAP/TAZ Regulation by Actin-Processing Factors**. *Cell* 2013, **154**:1047–1059.
221. Rossant J: **Genetic Control of Early Cell Lineages in the Mammalian Embryo**. *Annu Rev Genet* 2018, **52**:185–201.
222. Wicklow E, Blij S, Frum T, Hirate Y, Lang RA, Sasaki H, Ralston A: **HIPPO Pathway Members Restrict SOX2 to the Inner Cell Mass Where It Promotes ICM Fates in the Mouse Blastocyst**. *PLOS Genet* 2014, **10**:e1004618.
223. Strumpf D, Mao C-A, Yamanaka Y, Ralston A, Chawengsaksophak K, Beck F, Rossant J: **Cdx2 is required for correct cell fate specification and differentiation of trophectoderm in the mouse blastocyst**. *Development* 2005, **132**:2093–2102.
224. Wu G, Gentile L, Fuchikami T, Sutter J, Psathaki K, Esteves TC, Araúzo-Bravo MJ, Ortmeier C, Verberk G, Abe K, et al.: **Initiation of trophectoderm lineage specification in mouse embryos is independent of Cdx2**. *Development* 2010, **137**:4159–4169.
225. Young RA: **Control of the Embryonic Stem Cell State**. *Cell* 2011, **144**:940–954.
226. Posfai E, Petropoulos S, de Barros FRO, Schell JP, Jurisica I, Sandberg R, Lanner F, Rossant J: **Position- and Hippo signaling-dependent plasticity during lineage segregation in the early mouse embryo**. *Elife* 2017, **6**:e22906.
227. Zenker J, White MD, Gasnier M, Alvarez YD, Lim HYG, Bissiere S, Biro M, Plachta N: **Expanding Actin Rings Zipper the Mouse Embryo for Blastocyst Formation**. *Cell* 2018, **173**:776–791.
228. Eckert JJ, Fleming TP: **Tight junction biogenesis during early development**. *Biochim Biophys Acta - Biomembr* 2008, **1778**:717–728.
229. Ducibella T, Albertini DF, Anderson E, Biggers JD: **The preimplantation mammalian embryo: Characterization of intercellular junctions and their appearance during development**. *Dev Biol* 1975, **45**:231–250.
230. van Meer G, Simons K: **The function of tight junctions in maintaining differences in lipid composition between the apical and the basolateral cell surface domains of MDCK cells.** *EMBO J* 1986, **5**:1455–1464.
231. Blasky AJ, Mangan A, Prekeris R: **Polarized Protein Transport and Lumen Formation During Epithelial Tissue Morphogenesis**. *Annu Rev Cell Dev Biol* 2015, **31**:575–591.
232. Strilić B, Eglinger J, Krieg M, Zeeb M, Axnick J, Babál P, Müller DJ, Lammert E: **Electrostatic Cell-Surface Repulsion Initiates Lumen Formation in Developing Blood Vessels**. *Curr Biol* 2010, **20**:2003–2009.
233. Manejwala FM, Cragoe EJ, Schultz RM: **Blastocoel expansion in the preimplantation mouse embryo: Role of extracellular sodium and chloride and possible apical routes of their entry**. *Dev Biol* 1989, **133**:210–220.
234. Kawagishi R, Tahara M, Sawada K, Morishige K, Sakata M, Tasaka K, Murata Y: **Na+/H+ Exchanger-3 is involved in mouse blastocyst formation**. *J Exp Zool Part A Comp Exp Biol* 2004, **301A**:767–775.

235. Barr KJ, Garrill A, Jones DH, Orlowski J, Kidder GM: **Contributions of Na+/H+ exchanger isoforms to preimplantation development of the mouse**. *Mol Reprod Dev* 1998, **50**:146–153.
236. Robinson DH, Bubien JK, Smith PR, Benos DJ: **Epithelial Sodium Conductance in Rabbit Preimplantation Trophectodermal Cells**. 1991, **321**:313–321.
237. Miller, JG; Schultz G: **Amino acid transport in mouse blastocyst compartments**. *J Embryol Exp Morphol* 1985,
238. DiZio SM, Tasca RJ: **Sodium-dependent amino acid transport in preimplantation mouse embryos: III. Na+□K+-ATPase-linked mechanism in blastocysts**. *Dev Biol* 1977, **59**:198–205.
239. Watson AJ, Damsky CH, Kidder GM: **Differentiation of an epithelium: Factors affecting the polarized distribution of Na+,K+-ATPase in mouse trophectoderm**. *Dev Biol* 1990, **141**:104–114.
240. Madan P, Rose K, Watson AJ: **Na/K-ATPase β1 subunit expression is required for blastocyst formation and normal assembly of trophectoderm tight junction-associated proteins**. *J Biol Chem* 2007, **282**:12127–12134.
241. Vorbrodt A, Konwinski M, Solter D, Koprowski H: **Ultrastructural cytochemistry of membrane-bound phosphatases in preimplantation mouse embryos**. *Dev Biol* 1977, **55**:117–134.
242. Wiley LM: **Cavitation in the mouse preimplantation embryo: Na K-ATPase and the origin of nascent blastocoele fluid**. *Dev Biol* 1984, **105**:330–342.
243. Watson AJ, Kidder GM: **Immunofluorescence assessment of the timing of appearance and cellular distribution of Na/K-ATPase during mouse embryogenesis**. *Dev Biol* 1988, **126**:80–90.
244. Tokhtaeva E, Sachs G, Souda P, Bassilian S, Whitelegge JP, Shoshani L, Vagin O: **Epithelial Junctions Depend on Intercellular Trans-interactions between the Na,K-ATPase β$_1$ Subunits ***. *J Biol Chem* 2011, **286**:25801–25812.
245. Zhao Y, Doroshenko PA, Alper SL, Baltz JM: **Routes of Cl–Transport across the Trophectoderm of the Mouse Blastocyst**. *Dev Biol* 1997, **189**:148–160.
246. Biggers JD, Bell JE, Benos DJ: **Mammalian blastocyst: transport functions in a developing epithelium**. *Am J Physiol Physiol* 1988, **255**:C419–C432.
247. Bell CE, Larivière NMK, Watson PH, Watson AJ: **Mitogen-activated protein kinase (MAPK) pathways mediate embryonic responses to culture medium osmolarity by regulating Aquaporin 3 and 9 expression and localization, as well as embryonic apoptosis**. *Hum Reprod* 2009, **24**:1373–1386.
248. Barcroft LC, Offenberg H, Thomsen P, Watson AJ: **Aquaporin proteins in murine trophectoderm mediate transepithelial water movements during cavitation**. *Dev Biol* 2003, **256**:342–354.
249. Marikawa Y, Alarcon VB: **Creation of Trophectoderm, the First Epithelium, in Mouse Preimplantation Development BT - Mouse Development: From Oocyte to Stem Cells**. In Edited by Kubiak JZ. Springer Berlin Heidelberg; 2012:165–184.
250. Dumortier JG, Le Verge-Serandour M, Tortorelli AF, Mielke A, de Plater L, Turlier H, Maître J-L: **Hydraulic fracturing and active coarsening position the lumen of the mouse blastocyst**. *Science (80-)* 2019, **365**:465 LP – 468.

251. D J Durian, D A Weitz, D J Pine: **Dynamics and coarsening in three-dimensional foams**. *J Phys Condens Matter* 1990, **2**:SA433.
252. Motosugi N, Bauer T, Polanski Z, Solter D, Hiiragi T: **Polarity of the mouse embryo is established at blastocyst and is not prepatterned**. *Genes Dev* 2005, **19**:1081–1092.
253. Christodoulou N, Weberling A, Strathdee D, Anderson KI, Timpson P, Zernicka-Goetz M: **Morphogenesis of extra-embryonic tissues directs the remodelling of the mouse embryo at implantation**. *Nat Commun* 2019, **10**:3557.
254. Simon CS, Rahman S, Raina D, Schröter C, Hadjantonakis A-K: **Live Visualization of ERK Activity in the Mouse Blastocyst Reveals Lineage-Specific Signaling Dynamics**. *Dev Cell* 2020, **55**:341-353.e5.
255. Niimura S: **Time-Lapse Videomicrographic Analyses of Contractions in Mouse Blastocysts**. *J Reprod Dev Reprod Dev* 2003, **49**:413–423.
256. Chan CJ, Costanzo M, Ruiz-Herrero T, Mönke G, Petrie RJ, Bergert M, Diz-Muñoz A, Mahadevan L, Hiiragi T: **Hydraulic control of mammalian embryo size and cell fate**. *Nature* 2019, **571**:112–116.
257. Leonavicius K, Royer C, Preece C, Davies B, Biggins JS, Srinivas S: **Mechanics of mouse blastocyst hatching revealed by a hydrogel-based microdeformation assay**. *Proc Natl Acad Sci* 2018, **115**:10375–10380.
258. Rossant J, Chazaud C, Yamanaka Y: **Lineage allocation and asymmetries in the early mouse embryo**. *Philos Trans R Soc London Ser B Biol Sci* 2003, **358**:1341–1349.
259. Bassalert C, Valverde-Estrella L, Chazaud C: **Chapter Five - Primitive Endoderm Differentiation: From Specification to Epithelialization**. In *Cell Fate in Mammalian Development*. Edited by Plusa B, Hadjantonakis A-KBT-CT in DB. Academic Press; 2018:81–104.
260. Guo G, Huss M, Tong GQ, Wang C, Li Sun L, Clarke ND, Robson P: **Resolution of Cell Fate Decisions Revealed by Single-Cell Gene Expression Analysis from Zygote to Blastocyst**. *Dev Cell* 2010, **18**:675–685.
261. Ohnishi Y, Huber W, Tsumura A, Kang M, Xenopoulos P, Kurimoto K, Oleå AK, Araúzo-Bravo MJ, Saitou M, Hadjantonakis AK, et al.: **Cell-to-cell expression variability followed by signal reinforcement progressively segregates early mouse lineages**. *Nat Cell Biol* 2014, **16**:27–37.
262. Yamanaka Y, Lanner F, Rossant J: **FGF signal-dependent segregation of primitive endoderm and epiblast in the mouse blastocyst**. *Development* 2010, **137**:715–724.
263. Kang M, Garg V, Hadjantonakis A-K: **Lineage Establishment and Progression within the Inner Cell Mass of the Mouse Blastocyst Requires FGFR1 and FGFR2**. *Dev Cell* 2017, **41**:496-510.e5.
264. Filimonow K, Saiz N, Suwińska A, Wyszomirski T, Grabarek JB, Ferretti E, Piliszek A, Plusa B, Maleszewski M: **No evidence of involvement of E-cadherin in cell fate specification or the segregation of Epi and PrE in mouse blastocysts**. *PLoS One* 2019, **14**:e0212109.
265. Moore R, Tao W, Meng Y, Smith ER, Xu X-X: **Cell adhesion and sorting in embryoid bodies derived from N- or E-cadherin deficient murine embryonic stem cells**. *Biol Open* 2014, **3**:121–128.

266. Moore R, Cai KQ, Escudero DO, Xu X-X: **Cell adhesive affinity does not dictate primitive endoderm segregation and positioning during murine embryoid body formation**. *genesis* 2009, **47**:579–589.
267. Meilhac SM, Adams RJ, Morris SA, Danckaert A, Le Garrec J-F, Zernicka-Goetz M: **Active cell movements coupled to positional induction are involved in lineage segregation in the mouse blastocyst**. *Dev Biol* 2009, **331**:210–221.
268. Yanagida A, Corujo-Simon E, Revell CK, Sahu P, Stirparo GG, Aspalter IM, Winkel AK, Peters R, De Belly H, Cassani DAD, et al.: **Cell surface fluctuations regulate early embryonic lineage sorting**. *Cell* 2022, **185**:777-793.e20.
269. Su-Mi K, Jong-Soo K: **A Review of Mechanisms of Implantation**. *Dev Reprod* 2017, **21**:351–359.
270. Weberling A, Zernicka-Goetz M: **Trophectoderm mechanics direct epiblast shape upon embryo implantation**. *Cell Rep* 2021, **34**.
271. Bardot ES, Hadjantonakis A-K: **Mouse gastrulation: Coordination of tissue patterning, specification and diversification of cell fate**. *Mech Dev* 2020, **163**:103617.
272. Zenker J, White MD, Gasnier M, Alvarez YD, Lim HYG, Bissiere S, Biro M, Plachta N: **Expanding Actin Rings Zipper the Mouse Embryo for Blastocyst Formation**. *Cell* 2018, **173**:776–791.
273. Gupta K, Li Q, Fan JJ, Fong ELS, Song Z, Mo S, Tang H, Ng IC, Ng CW, Pawijit P, et al.: **Actomyosin contractility drives bile regurgitation as an early response during obstructive cholestasis**. *J Hepatol* 2017, **66**:1231–1240.
274. Lizama CO, Zovein AC: **Polarizing pathways: Balancing endothelial polarity, permeability, and lumen formation**. *Exp Cell Res* 2013, **319**:1247–1254.
275. Thottacherry JJ, Chen J, Johnston DS: **Apical-basal polarity in the gut**. *Semin Cell Dev Biol* 2023, doi:https://doi.org/10.1016/j.semcdb.2022.12.007.
276. Verschuren EHJ, Castenmiller C, Peters DJM, Arjona FJ, Bindels RJM, Hoenderop JGJ: **Sensing of tubular flow and renal electrolyte transport**. *Nat Rev Nephrol* 2020, **16**:337–351.
277. Carleton AE, Duncan MC, Taniguchi K: **Human epiblast lumenogenesis: From a cell aggregate to a lumenal cyst**. *Semin Cell Dev Biol* 2022, **131**:117–123.
278. McGrath J, Somlo S, Makova S, Tian X, Brueckner M: **Two Populations of Node Monocilia Initiate Left-Right Asymmetry in the Mouse**. *Cell* 2003, **114**:61–73.
279. Essner JJ: **Kupffer's vesicle is a ciliated organ of asymmetry in the zebrafish embryo that initiates left-right development of the brain, heart and gut**. *Development* 2005, **132**:1247–1260.
280. Hava D, Forster U, Matsuda M, Cui S, Link BA, Eichhorst J, Wiesner B, Chitnis A, Abdelilah-Seyfried S: **Apical membrane maturation and cellular rosette formation during morphogenesis of the zebrafish lateral line**. *J Cell Sci* 2009, **122**:687–695.
281. Zhu M, Leung CY, Shahbazi MN, Zernicka-Goetz M: **Actomyosin polarisation through PLC-PKC triggers symmetry breaking of the mouse**

embryo. *Nat Commun* 2017, **8**:921.
282. Reichmann J, Eguren M, Lin Y, Schneider I, Ellenberg J: **Chapter 15 - Live imaging of cell division in preimplantation mouse embryos using inverted light-sheet microscopy**. In *Mitosis and Meiosis Part B*. Edited by Maiato H, Schuh MBT-M in CB. Academic Press; 2018:279–292.
283. Guevorkian K, Maître J-L: **Chapter 10 - Micropipette aspiration: A unique tool for exploring cell and tissue mechanics in vivo**. In *Cell Polarity and Morphogenesis*. Edited by Lecuit TBT-M in CB. Academic Press; 2017:187–201.
284. Anani S, Bhat S, Honma-Yamanaka N, Krawchuk D, Yamanaka Y: **Initiation of Hippo signaling is linked to polarity rather than to cell position in the pre-implantation mouse embryo**. *Development* 2014, **141**:2813 LP – 2824.
285. Samarage CR, White MD, Álvarez YD, Fierro-González JC, Henon Y, Jesudason EC, Bissiere S, Fouras A, Plachta N: **Cortical Tension Allocates the First Inner Cells of the Mammalian Embryo**. *Dev Cell* 2015, **34**:435–447.
286. Chan CJ, Costanzo M, Ruiz-Herrero T, Mönke G, Petrie RJ, Bergert M, Diz-Muñoz A, Mahadevan L, Hiiragi T: **Hydraulic control of mammalian embryo size and cell fate**. *Nature* 2019, **571**:112–116.
287. Dietrich J-E, Hiiragi T: **Stochastic patterning in the mouse pre-implantation embryo**. *Development* 2007, **134**:4219–4231.
288. Shahbazi MN, Wang T, Tao X, Weatherbee BAT, Sun L, Zhan Y, Keller L, Smith GD, Pellicer A, Scott RT, et al.: **Developmental potential of aneuploid human embryos cultured beyond implantation**. *Nat Commun* 2020, **11**:3987.
289. Yang M, Rito T, Metzger J, Naftaly J, Soman R, Hu J, Albertini DF, Barad DH, Brivanlou AH, Gleicher N: **Depletion of aneuploid cells in human embryos and gastruloids**. *Nat Cell Biol* 2021, **23**:314–321.
290. Ryan AQ, Chan CJ, Graner F, Hiiragi T: **Lumen Expansion Facilitates Epiblast-Primitive Endoderm Fate Specification during Mouse Blastocyst Formation**. *Dev Cell* 2019, **51**:684-697.e4.
291. Ebrahim S, Chen D, Weiss M, Malec L, Ng Y, Rebustini I, Krystofiak E, Hu L, Liu J, Masedunskas A, et al.: **Dynamic polyhedral actomyosin lattices remodel micron-scale curved membranes during exocytosis in live mice**. *Nat Cell Biol* 2019, **21**:933–939.
292. Moreau HD, Blanch-Mercader C, Attia R, Maurin M, Alraies Z, Sanséau D, Malbec O, Delgado M-G, Bousso P, Joanny J-F, et al.: **Macropinocytosis Overcomes Directional Bias in Dendritic Cells Due to Hydraulic Resistance and Facilitates Space Exploration**. *Dev Cell* 2019, **49**:171–188.
293. Simunovic M, Voth GA, Callan-Jones A, Bassereau P: **When Physics Takes Over: BAR Proteins and Membrane Curvature**. *Trends Cell Biol* 2015, **25**:780–792.
294. Kozlov MM, Taraska JW: **Generation of nanoscopic membrane curvature for membrane trafficking**. *Nat Rev Mol Cell Biol* 2023, **24**:63–78.
295. Cannon KS, Woods BL, Crutchley JM, Gladfelter AS: **An amphipathic helix enables septins to sense micrometer-scale membrane curvature**. *J Cell Biol* 2019, **218**:1128–1137.
296. Mavrakis M, Azou-Gros Y, Tsai F-C, Alvarado J, Bertin A, Iv F, Kress A,

Brasselet S, Koenderink GH, Lecuit T: **Septins promote F-actin ring formation by crosslinking actin filaments into curved bundles**. *Nat Cell Biol* 2014, **16**:322–334.
297. Dolat L, Hunyara JL, Bowen JR, Karasmanis EP, Elgawly M, Galkin VE, Spiliotis ET: **Septins promote stress fiber–mediated maturation of focal adhesions and renal epithelial motility**. *J Cell Biol* 2014, **207**:225–235.
298. Norden C, Liakopoulos D, Barral Y: **Dissection of septin actin interactions using actin overexpression in Saccharomyces cerevisiae**. *Mol Microbiol* 2004, **53**:469–483.
299. Pinheiro D, Hannezo E, Herszterg S, Bosveld F, Gaugue I, Balakireva M, Wang Z, Cristo I, Rigaud SU, Markova O, et al.: **Transmission of cytokinesis forces via E-cadherin dilution and actomyosin flows**. *Nature* 2017, **545**:103–107.
300. Eisenmann KM, Harris ES, Kitchen SM, Holman HA, Higgs HN, Alberts AS: **Dia-Interacting Protein Modulates Formin-Mediated Actin Assembly at the Cell Cortex**. *Curr Biol* 2007, **17**:579–591.
301. Le Verge-Serandour M, Turlier H: **A hydro-osmotic coarsening theory of biological cavity formation**. *PLOS Comput Biol* 2021, **17**:e1009333.
302. Gebala V, Collins R, Geudens I, Phng L, Gerhardt H: **Blood flow drives lumen formation by inverse membrane blebbing during angiogenesis in vivo**. 2016, **18**.
303. Kondrychyn I, Kelly DJ, Carretero NT, Nomori A, Kato K, Chong J, Nakajima H, Okuda S, Mochizuki N, Phng L-K: **Marcksl1 modulates endothelial cell mechanoresponse to haemodynamic forces to control blood vessel shape and size**. *Nat Commun* 2020, **11**:5476.
304. Charras GT, Yarrow JC, Horton MA, Mahadevan L, Mitchison TJ: **Non-equilibration of hydrostatic pressure in blebbing cells**. *Nature* 2005, **435**:365–369.
305. Choudhury MI, Li Y, Mistriotis P, Vasconcelos ACN, Dixon EE, Yang J, Benson M, Maity D, Walker R, Martin L, et al.: **Kidney epithelial cells are active mechano-biological fluid pumps**. *Nat Commun* 2022, **13**:2317.
306. Kennard AS, Sathe M, Labuz EC, Prinz CK, Theriot JA: **Post-injury hydraulic fracturing drives fissure formation in the zebrafish basal epidermal cell layer**. *bioRxiv* 2022, doi:10.1101/2022.05.21.492930.
307. Yoshiba S, Shiratori H, Kuo IY, Kawasumi A, Shinohara K, Nonaka S, Asai Y, Sasaki G, Belo JA, Sasaki H, et al.: **Cilia at the Node of Mouse Embryos Sense Fluid Flow for Left-Right Determination via Pkd2**. *Science (80-)* 2012, **338**:226 LP – 231.
308. Grimes DT, Boswell CW, Morante NFC, Henkelman RM, Burdine RD, Ciruna B: **Zebrafish models of idiopathic scoliosis link cerebrospinal fluid flow defects to spine curvature**. *Science (80-)* 2016, **352**:1341 LP – 1344.
309. Huljev K, Shamipour S, Pinheiro D, Preusser F, Steccari I, Sommer CM, Naik S, Heisenberg C-P: **A hydraulic feedback loop between mesendoderm cell migration and interstitial fluid relocalization promotes embryonic axis formation in zebrafish**. *Dev Cell* 2023, **58**:582-596.e7.
310. Swartz MA, Fleury ME: **Interstitial Flow and Its Effects in Soft Tissues**. *Annu Rev Biomed Eng* 2007, **9**:229–256.
311. Heisenberg C-P, Bellaïche Y: **Forces in Tissue Morphogenesis and**

Patterning. *Cell* 2013, **153**:948–962.

5. RESUME / ABSTRACT

RÉSUMÉ

Étude multi-échelle de la morphogenèse de l'embryon préimplantatoire

Au cours du développement embryonnaire, les animaux suivent une séquence complexe de changements de forme provoqués par des forces issues de la contractilité cellulaire, générées par le cytosquelette de l'actomyosine. Chez l'embryon de mammifère, la morphogenèse débute dès la phase préimplantatoire, qui commence par la fécondation et aboutit à la formation du blastocyste, la structure qui s'implante dans l'utérus maternel. Ainsi, l'embryon préimplantatoire suit une série de mouvements morphogénétiques contrôlés par la contractilité qui aboutissent avec la formation du premier lumen au sein du blastocyste.

Nous avons mené la première étude examinant l'effet de la perte complète de contractilité sur le développement préimplantatoire. Nous avons généré les mutants maternels-zygotiques simples et double des gènes *Myh9* et *Myh10*, codants pour les chaînes lourdes de la myosine non musculaire de type II, ce qui nous a permis d'étudier la contribution relative de ces deux paralogues dans la génération de la contractilité cellulaire. Nous avons constaté que MYH9 est le principal contributeur dans ce processus, car sa perte entraîne un retard du cycle cellulaire, une réduction du nombre de cellules, de la compaction et de la différenciation. La perte de *Myh10* n'a pas d'impact fort par rapport aux embryons de type sauvage. Néanmoins, un phénotype plus sévère a pu être observé chez les embryons double mutants dont la cytocinèse échoue dans la plupart des cas, suggérant une compensation par MYH10 dans les mutants *Myh9*. Malgré le manque de cellules, la différenciation et la formation du lumen se poursuivent dans les double mutants. Dans les cas les plus extrêmes, des embryons composés d'une seule et unique cellule accumulent du fluide dans des compartiments intracellulaires, ce qui indique que le programme préimplantatoire est exécuté indépendamment du nombre de cellules.

Dans les embryons sauvages, le blastocyste se forme suivant un processus de fracturation hydraulique produisant un réseau de microlumens qui murit en un lumen unique entourée de plusieurs cellules. Bien que le mécanisme global de ce processus soit compris, on ne sait toujours pas comment les cellules régulent localement la dynamique des microlumens. Ici, nous décrivons des blebs inversés aux contacts entre cellules. Les blebs inversés sont des invaginations membranaires de courte durée qui gonflent dans le cytoplasme avant d'être

repoussées par la contractilité cellulaire. Les blebs inversés se forment à la suite de l'augmentation globale de la pression du fluide intercellulaire et du confinement local du fluide par l'adhésion cellulaire. Nous proposons que les blebs inversés agissent comme des pompes hydrauliques pour diriger le fluide au sein du réseau de microlumens, promouvant ainsi son murissement.

Ces résultats approfondissent notre compréhension moléculaire, cellulaire et biophysique de la façon dont la contractilité cellulaire façonne l'embryon de mammifère

MOTS CLÉS

embryon préimplantatoire – morphogenèse – imagerie en temps réel

ABSTRACT

Multiscale study of mouse preimplantation morphogenesis

During development, embryos undergo a complex sequence of morphogenetic shape changes powered by cellular contractile forces which allow the embryo to correctly form tissues and organs. Contractile cellular forces in morphogenesis are chiefly generated by the actomyosin cytoskeleton. In the mammalian embryo, morphogenesis begins during preimplantation development, which commences with fertilization and leads up to the formation of the blastocyst, the structure that implants into the maternal uterus. During preimplantation development, the embryo undergoes a series of contractility-driven morphogenetic steps that culminate in the positioning of the first lumen of development in the blastocyst.

Here, we conducted the first study investigating the effect of complete contractility loss on preimplantation development. We performed single and double maternal-zygotic knockout of the non-muscle myosin heavy chain genes *Myh9* and *Myh10*, which allowed us to study the relative contribution of these two paralogs to contractility generation in preimplantation development. We found that MYH9 is the main contributor in this process, as its maternal-zygotic loss results in cell cycle delay, reduced cell number, compaction and differentiation. Loss of *Myh10* did not have a strong detectable impact compared to wildtype embryos. Nevertheless, a more severe phenotype could be observed in *Myh9* and *Myh10* double

knockout embryos as cytokinesis failed in most cases, suggesting some compensation by MYH10 in *Myh9* single mutants. Despite severely reduced cell number, differentiation and lumen formation still somehow continued in double knockout embryos. In the most extreme cases, single-celled embryos accumulated fluid in intracellular compartments, indicating that the preimplantation developmental program is executed independently of cell number.

In WT embryos, the blastocyst forms in a process of hydraulic fracturing producing hundreds of microlumen followed by their coarsening into a single lumen surrounded by multiple cells. While the global mechanism of this process is understood, it remains unclear how cells regulate microlumen dynamics locally. Here, we describe inverse blebs at cell-cell contacts during microlumen formation. Inverse blebs are short-lived membrane protrusions expanding into the cytoplasm before being retracted by actomyosin contraction. We show that inverse blebs form due to a global increase in intercellular fluid pressure and require local fluid confinement by cell-cell adhesion. We propose that inverse blebs serve as hydraulic pumps to push the fluid within the microlumen network, thereby supporting the coarsening of the first mammalian lumen.

Together, these finding expand our molecular, cellular and physical understanding of how cell contractility shapes the early mammalian embryo.

KEYWORDS

preimplantation embryo – morphogenesis – live imaging